FALLING-FILM EVAPORATION OVER HORIZONTAL RECTANGULAR TUBES

A Dissertation
Presented to
The Academic Faculty

by

John G. Bustamante

In Partial Fulfillment
of the Requirements for the Degree
Doctor of Philosophy in the
George W. Woodruff School of Mechanical Engineering

Georgia Institute of Technology
August 2014

FALLING-FILM EVAPORATION OVER
HORIZONTAL RECTANGULAR TUBES

Approved by:

Dr. Srinivas Garimella, Advisor
George W. Woodruff School of
Mechanical Engineering
Georgia Institute of Technology

Dr. S. Mostafa Ghiaasiaan
George W. Woodruff School of
Mechanical Engineering
Georgia Institute of Technology

Dr. Satish Kumar
George W. Woodruff School of
Mechanical Engineering
Georgia Institute of Technology

Dr. Thomas Fuller
School of Chemical and Biomolecular
Engineering
Georgia Institute of Technology

Dr. Laurence Jacobs
School of Civil and Environmental
Engineering
Georgia Institute of Technology

Date Approved: June 30, 2014

To my family

ACKNOWLEDGEMENTS

First and foremost, I would like to thank my advisor, Dr. Srinivas Garimella, for his support and guidance throughout my time at Georgia Tech. I am grateful for his advice, criticism, insights, and patience during my time at STSL. He has been instrumental in my development as an engineer.

I would also like to thank the past and present members of STSL for their support, friendship, and many interesting discussions. In particular, I would like to acknowledge Todd Bandhauer, Brian Fronk, Dhruv Hoysall, Brendon Keinath, Matthew Laderer, Adrienne Little, Malcolm Macdonald, Jeff Milkie, Anand Nagavarapu, and Alex Rattner for their assistance and guidance.

I am also grateful to the many other professors that have contributed to my education and personal growth. In particular, I want to thank Dr. Schimmels and Dr. Goldsborough at Marquette, who introduced me to research, and my dissertation reading committee, for the time they devoted to reviewing my work and providing their insights and guidance. In addition, I would like to thank Dr. Rodriguez and Dr. Johnson, who I had the privilege to work with at JPL and introduced me to cryogenics.

Finally, I am grateful to my family, for their love and support, as well as my friends—I would be remiss not to mention Chris Babuska, Tom Coyne, Evan Davey, Carley Shulman, Adam Offenbacher, Scott and Beth Brombosz, Chip and Jess Humphries, Chris and Diane Butch, Anthony Baldridge, and Nick Haase. Lastly, I must thank Emily Wille, who I am blessed to have in my life.

TABLE OF CONTENTS

LIST OF TABLES

LIST OF FIGURES

NOMENCLATURE

a	empirical constant, [-]
A	surface area, [m^2]
AD	average deviation, [%]
AAD	absolute average deviation, [%]
Ar	Archimedes number, $g\,\rho^2\,d^3\,\mu^{-2}$, [-]
b	empirical constant, [-]
Bo	Bond number, $\rho\,g\,f_d\,f_s\,\sigma^{-1}$, [-]
c_p	specific heat, [kJ kg^{-1} K^{-1}]
d	diameter, [m]
d_h	hydraulic diameter, [m]
e	intensive energy, [kJ kg^{-1}]
f	fin dimension, [m]
F	force, [N]
g	gravitational constant, [m s^{-2}]
$G_{t\text{-}s}$	tube-specific empirical parameter, [-]
Ga	modified Galileo number (or Kapitza number), $\sigma^3\rho\,g^{-1}\mu^{-4}$, [-]
h	heat transfer coefficient, [W m^{-2} K^{-1}]
H	liquid distributor height, [m]
i_{fg}	latent heat of vaporization, [kJ kg^{-1}]
K_{ff}	falling-film factor, [-]
k	thermal conductivity, [W m^{-1} K^{-1}]
L	length, [m]

LR	air ingression rate, [Pa hr^{-1}]
m	mass, [kg]
ṁ	mass flow rate, [kg s^{-1}]
N	number, [-]
Nu	Nusselt number, $h\,k^{-1}\,(\mu^2\,\rho^{-2}\,g^{-1})^{1/3}$, [-]
p	tube pitch, [m]
P	pressure, [Pa]
P$_e$	perimeter, [m]
Pr	Prandtl number, $c_p\,\mu\,k^{-1}$, [-]
q"	heat flux, [W m^{-2}]
Q	heat input, [W]
R	radius, [m]
Re	film Reynolds number, $4\,\Gamma\,\mu^{-1}$, [-]
s	tube or test section spacing, [m]
S	intensive entropy, [kJ kg^{-1} K^{-1}]
t	time, [s]
T	temperature, [°C]
u	internal energy, [kJ kg^{-1}]
U	velocity, [m s^{-1}]
V	volume, [m^3]
W	unit width, [m]
We	Weber number, $\rho\,v^2\,D\,\sigma^{-1}$, [-]
WR	wetting ratio, $A_{wet}\,A^{-1}$, [-]
x	distance from axis, [m]
y	distance, [m]

z	height, [m]

Greek Symbols

δ	film thickness, [m]
ε	emissivity, [-]
Γ	mass flow rate per unit length on one side of tube, [kg m^{-1} s^{-1}]
λ	wavelength, [m]
μ	dynamic viscosity, [kg m^{-1} s^{-1}]
v	kinematic viscosity, $\mu\,\rho^{-1}$, [m^{2} s^{-1}]
ρ	density, [kg m^{-3}]
σ	surface tension, [N m^{-1}]
θ	angle around tube measured from stagnation point, [radians]
τ	time, [s]
ξ	capillary length, $\sigma^{0.5}\rho^{-0.5}g^{-0.5}$, [m]

Subscripts and Superscripts

0	baseline value
avg	average
bundle	with a tube bundle
c	characteristic
C	chamber
crit	critical
cs	cross-sectional
cv	convective
D	droplet
d	depth
dry	with partial dryout

en	enhanced
eq	equivalent
exp	experimental
ff	falling-film
f,T	film on the tube
G	gravitational
J	jet
l	liquid
lv	liquid-vapor interface
min	minimum
nb	nucleate boiling
NF	Nusselt film
pb	pool boiling
pr	profiled tube
pred	predicted
pr,0	profiled tube with baseline fin spacing
r	reduced
rad	radiation
sat	saturation
s	spacing
s,0	baseline fin spacing
S	sheet
σ	surface tension
T	transition
trans	transitional

TS	test section
TS,*i*	local to one area of test section
w	width
wall,*i*	local to one area of wall
wv	wave
wet	fully wetted
We=0	at a Weber number of zero
v	vapor

SUMMARY

The present study is the first investigation of falling-film evaporation over horizontal rectangular tubes. This geometry is representative of the external profile of microchannel tubes. Incorporating these designs into shell-and-tube heat exchangers has the potential to provide compact, high-performance components for a wide range of applications. This fluid flow was investigated experimentally, targeting three areas: measurements of heat transfer coefficients, quantification of flow characteristics, and the performance of flow distributors. Falling-film evaporation experiments were conducted using water on a rectangular test section with dimensions of $203 \times 1.42 \times 27.4$ mm (length × width × height), measuring heat transfer coefficients over a range of saturation temperatures (10 to 30°C), test section spacings (5 to 15 mm), heat fluxes (10 to 20 kW m^{-2}), and film Reynolds numbers (50 to 550). This was supported by a flow visualization study that quantified droplet and wave parameters using image analysis of high speed videos. Finally, the performance of eight liquid distributors, which are used to establish falling-film flows, was quantified and the size of the generated droplets and jets was measured. Three models were developed to predict the flow regime, wetted tube area, and heat transfer coefficient. The flow regime model is based on a thermodynamic analysis, while the wetted tube area is found with a hydrodynamic model based on idealized flow assumptions. Finally, the heat transfer model relies on a relationship with the classic Nusselt (1916) film theory. Each of these models demonstrated good agreement with the experimental data, as well as trends in the literature. The increased understanding of falling-film evaporation gained in this study will enable the accurate design of shell-and-tube heat exchangers with microchannel tubes.

CHAPTER 1: INTRODUCTION

Economic and environmental considerations continue to drive strong interest in increasing the efficiency of thermal systems. In many cases, this is achieved by improving the performance of heat exchangers. In widely used shell-and-tube heat exchangers, conventional flooded evaporator designs fill the shell-side area with working fluid. One alternative is designs based on falling-film evaporation, which maintain only a thin liquid film over the tubes. This leads to a reduced working fluid inventory, higher heat transfer coefficients with negligible pressure drops, and closer approach temperatures, yielding more compact designs with potentially lower costs and improved heat transfer performance. Ultimately, this increases cycle efficiencies while reducing the required working fluid charge, which lowers capital costs and environmental impact. This has led to their usage in the refrigeration, petrochemical, and desalination industries.

Falling-film evaporator designs are typically based on films falling over horizontal or vertical round tubes. Recently, horizontal tube designs have demonstrated several advantages over vertical units, including higher heat transfer coefficients, external tube enhancements, and closer approach temperatures (Thome, 2009). These horizontal tube designs have focused on the usage of round tubes, while a second promising geometry, external falling films over flat microchannel tubes with internal microchannels ($d_h \sim 1$ mm), has received little attention. In an evaporator utilizing microchannel tubes, the tubes can be orientated horizontally in a vertical array with in-tube cooling and an external evaporating thin film, as seen in Figure 1.1. Microchannel tubes possess several characteristics that make them ideal for such a configuration: high surface area-to-volume
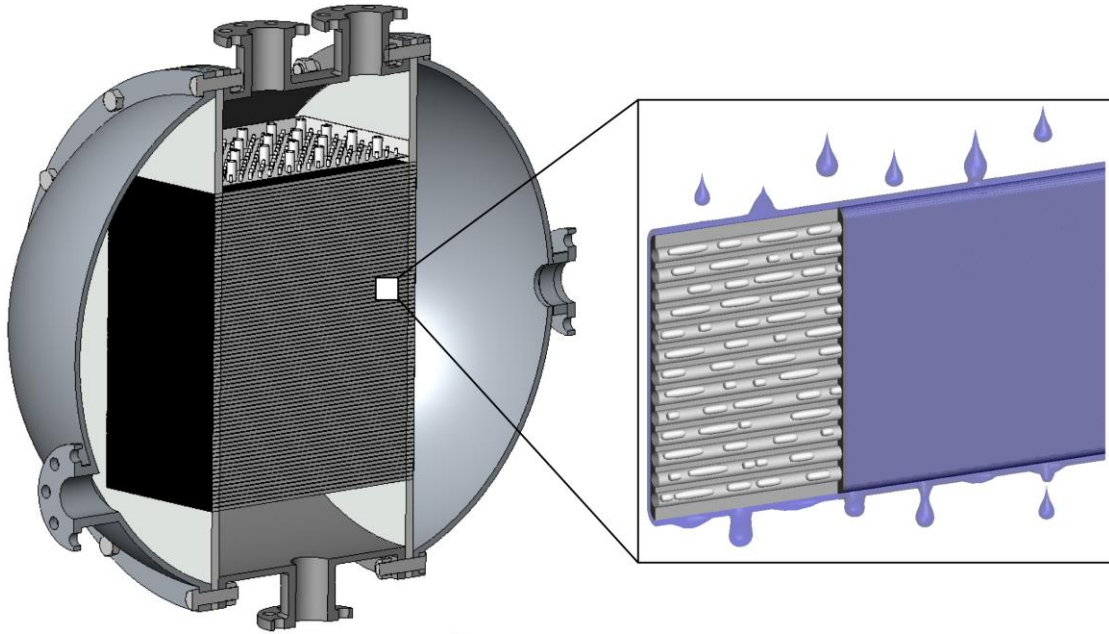
Figure 1.1. Section view of a shell-and-tube heat exchanger using flat, microchannel tube banks with a zoomed view of a single tube

ratios, the ability to withstand high internal pressures, and a low working fluid charge. The small hydraulic diameters lead to high internal heat transfer coefficients, while falling-film evaporation over the microchannel tubes is expected to provide high external heat transfer coefficients by enhancing thin-film heat transfer on a vertical surface with waves. The internal pressure drop can be maintained at reasonable levels by using parallel channel configurations, while the shell side provides gravity driven liquid film flow and a large vapor space to maintain minimal pressure drop during the evaporation process. Overall, this design has the potential to yield high-performance, compact heat exchangers.

Accurate heat transfer models are necessary to effectively design falling-film evaporators. Although previous studies have investigated heat transfer in horizontal and vertical round tube configurations, examining a wide range of fluid properties, flow rates, geometries, and tube surfaces, very limited information is available on heat transfer for

external films falling over microchannel tube geometries. Only Wang *et al.* (2010, 2011) have studied falling films over rectangular tube geometries, representative of the external surface of microchannel tubes, and their studies were limited to an examination of flow transitions at adiabatic conditions and measurements of sensible heat transfer coefficients. No models capable of predicting the heat transfer performance of films falling over rectangular tube geometries are currently available. To develop these models, heat transfer data and information on the key flow mechanisms are needed.

In the present study, experiments are conducted to measure the heat transfer coefficients during falling-film evaporation using water at subatmospheric pressures over a range of saturation temperatures, heat fluxes, tube spacings, and flow rates. In addition, a flow visualization study is conducted to measure key flow characteristics. Image analysis of high-speed video quantified droplet and wave characteristics, and the flow regimes are identified. A supporting study that quantitatively compares flow distributors, which establish the falling-film flow, is also conducted. Ultimately, these results advance the knowledge of heat transfer under these conditions, allowing the development of a new heat transfer model for falling-film evaporation over horizontal rectangular tubes.

The working fluid and flow conditions selected for this study were based on a prior study by Garimella *et al*. (2011) that designed a novel waste heat recovery system for a naval ship application using a cascaded absorption/compression cooling cycle. This system coupled a lithium bromide-water absorption cycle with a carbon dioxide vapor compression cycle to provide simultaneous cooling at 5°C directly from the absorption cycle and cooling down to -40°C from the bottoming cycle with an overall electrically-based COP of 5.7. Compared to an equivalent standard vapor compression system, it
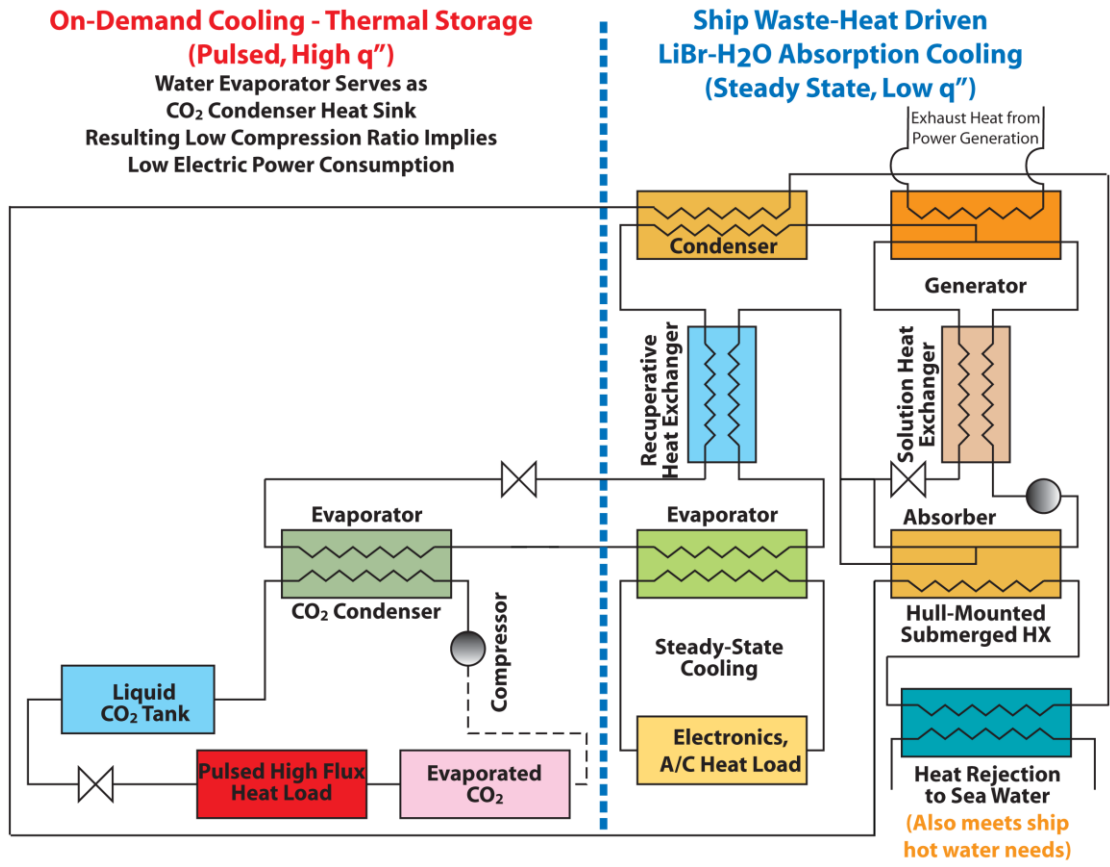
Figure 1.2. Cascaded absorption/vapor-compression cycle schematic (Garimella *et al.*, 2011)

would save up to 31% of the required electrical input. However, one key component of this system, the heat exchanger coupling the two cycles, has several challenging requirements. It must couple the high pressure (4280 kPa) CO_2 condensation with low pressure (0.9 kPa) water evaporation without excessive wall thicknesses, accommodate the large specific volume of water with minimal pressure drop for both fluids, and transfer MW-scale heat loads across a small (3 K nominal) temperature difference in a compact geometry. These challenging requirements can all be met with a heat exchanger of shell-and-tube configuration utilizing the flat, rectangular microchannel tubes described above.

4

The dissertation is organized as follows:

- Chapter 2 reviews the relevant literature on falling-film evaporation experiments, modeling, and flow distributors.

- Chapter 3 describes the experimental facility developed to investigate falling-film evaporation, and reviews the experimental procedures and test matrix.

- Chapter 4 presents the data analysis techniques and results from the flow visualization study, the flow distributor comparison, and in the heat transfer study.

- Chapter 5 compares the results from the present study with models available in the literature, and presents the development of a new flow regime and heat transfer model.

- Chapter 6 presents the conclusions from this work, as well as recommendations for further study.

CHAPTER 2: LITERATURE REVIEW

A review of the literature on experimental techniques used in falling-film evaporation studies, flow mode transition studies, studies examining flow characteristics, experimental heat transfer studies, and heat transfer models is presented here. This is followed by an identification of several research needs that are addressed by the present study.

Prior related reviews of the literature have been compiled by Thome (1999; 2009), Ribatski and Jacobi (2005), Mitrovic (2005), and Fernández-Seara and Pardiñas (2013). Thome (1999) provided an overview of significant articles prior to 1994 and a more detailed discussion of studies published from 1994 to 1999. A later publication (Thome, 2009) expanded on this review with additional discussion on the advantages and disadvantages of horizontal tube falling-film evaporators, thermal design considerations, falling-film modes, and recent work by his research group. Ribatski and Jacobi (2005) critically examined the literature on flow pattern studies, plain tubes, enhanced surfaces, tube bundles, and mathematical and empirical models for heat transfer, with a focus on studies related to refrigeration applications. Mitrovic (2005) provided a review focusing on flow pattern correlations, and included a discussion of the Reynolds numbers and other dimensionless numbers used by different authors. Fernández-Seara and Pardiñas (2013) reviewed the falling-film literature related to refrigerants, and compared falling-film evaporation with pool boiling.

2.1 Experimental Techniques

Although the details of the experimental setups used in falling-film evaporation studies vary, a number of similar features and considerations are described here. In particular, this section discusses test section design, differences in the description of flow rate, and liquid distributors.

2.1.1 <u>Test Sections</u>

Test sections in previous works have used geometries consisting of a single tube, a vertical array of tubes, or a tube bundle. Heating is typically provided with an internal electric resistance heater or internal fluid flow, although some designs electrically heat a thin foil on the surface of the tube. Internal electric heating has the advantage of simple implementation, low uncertainties in heat duty, and direct control of heat duty. Meanwhile, fluid heating is beneficial because it more closely duplicates conditions found in real applications, and there is less uncertainty regarding possible internal contact resistances and temperature variation across the tube surface. In test facilities with internal fluid flow, the internal heat transfer coefficient is often enhanced with enhanced tube features. For example, Habert and Thome (2010a) add an internal tube with a helically wound wire to increase heat transfer coefficient, enhance mixing, and reduce entrance effects. Test sections typically have a specified uniform surface finish, which can be either a plain smooth surface or have surface structures to enhance heat transfer. The supporting structure holding and aligning the test section is designed to minimize conductive losses to the extent possible.

To calculate heat transfer coefficients, the temperature of the test section surface must be determined. In test sections with electric heating, this is often accomplished by

placing thermocouples on the surface of the test section. Placement may be in grooves on the actual outside surface of the tube, or inside internal features of the tube. In both cases, care is taken to minimize the impact on the external surface features and surface finish, as well as contact resistances. Normally a series of thermocouples is located on each test section, often arranged to either capture axial variation, radial variation, or a combination of the two. In situations with internal fluid flow, many investigations simply locate thermocouples at the inlet and outlet of the test section and use simple resistance networks to determine the test section surface temperature. Special care is taken to level the test section. Poorly leveled test sections result in poor flow distribution, and can also impact the type of flow observed. For instance, Dhir and Taghavi-Tafreshi (1981) observed that fluid jets maintained themselves in static locations if the tubes were correctly leveled and the liquid was well distributed, but deviation in either aspect resulted in unstable jets. Although the method of leveling the tubes is often not described and presumably involves standard leveling equipment, Ruan *et al.* (2009) has suggested circulating fluid in the column mode and adjusting the tubes until the columns fall from fixed locations and do not move in either direction. Finally, vibrations in the test section can lead to unstable flow patterns (Armbruster and Mitrovic, 1994), and should be suppressed.

2.1.2 <u>Definition of Film Flow Rate</u>

The definitions of the film flow rate, Γ, and Reynolds number, *Re*, vary from author to author, complicating comparisons of the results between studies. The film flow rate, Γ, can be defined as either the flow rate per unit width over one side of the tube, or the flow over both sides of the tube. Furthermore, the film Reynolds number can be

defined using either of the above film flow rate definitions, and is usually defined using the hydraulic diameter as the characteristic length, although the film thickness has also been used. A more complete description of these options was provided by Mitrovic (2005). The present study uniformly uses the flow rate per unit width over one side of the tube to determine the film flow rate, as shown in Equation (2.1), and defines the film Reynolds number using the hydraulic diameter as the characteristic length, as shown in Equations (2.2) and (2.3). The hydraulic diameter is equal to four times the film thickness, found by taking four times the cross-sectional flow area divided by the wetted perimeter.

$$\Gamma = \frac{\dot{m}}{2L_{\mathrm{TS}}} \tag{2.1}$$

$$d_{\mathrm{h}} = \frac{4A_{\mathrm{cs}}}{P_{\mathrm{e}}} = \frac{4L_{\mathrm{TS}}\delta}{L_{\mathrm{TS}}} = 4\delta \tag{2.2}$$

$$Re = \frac{\rho U d_{\mathrm{h}}}{\mu} = \frac{4\rho U \delta}{\mu} = \frac{4\Gamma}{\mu} \tag{2.3}$$

2.1.3 Liquid Distributors

In horizontal tube falling-film heat transfer experiments, the liquid distributor, also known as the liquid feeder or flow distributor, is used to deliver fluid to the test section. The goal of these devices is to establish an even fluid flow along the length of the horizontal tube, and to simulate the performance of a tube above the test section in experimental facilities. By establishing this initial fluid flow, liquid distributors can have a strong influence on the local heat transfer coefficient by varying local film thickness, waviness, and flow characteristics (such as film breakdown and dryout). Despite their importance, liquid distributors are typically only evaluated visually based on observations

of full tube wetting or other general flow characteristics, with few studies focusing on quantifying their performance.

Liquid distributors can be broadly classified as low and high momentum designs. Low momentum distributors are driven by gravity or a low driving pressure, and are aligned directly above the top row of evaporator tubes with free-fall between the distributor and horizontal tubes. High momentum designs, meanwhile, use spray nozzles to deliver fluid to the tubes. Spray nozzles usually generate higher local heat transfer coefficients, but require higher supply pressures and significant liquid overfeed to prevent dryout. The present study uses low momentum designs.

Low momentum designs can be broadly classified as tube-based or box-based designs, as seen in Figure 2.1. Tube-based distributor designs rely on a single tube or two concentric tubes with pressure supplied by a pump or gravitational head from a feeding tank. Fluid enters from one or both sides of the tube, and exits through an array of holes, a slot, or a porous structure. Meanwhile, box-based designs typically consist of a rectangular box with pressure generated by gravitational head. Fluid either enters the box
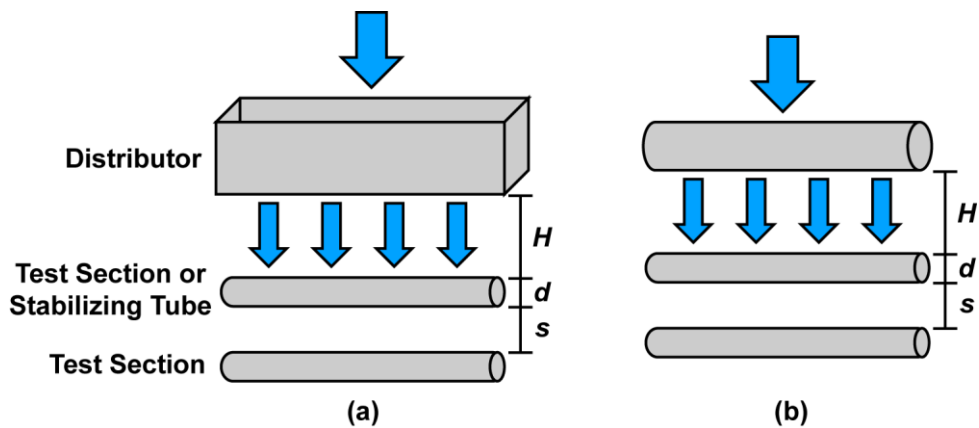
Figure 2.1. Schematic of a simple (a) box-based and (b) tube-based distributor design with test section

10

directly or through a tube that provides an initial distribution, referred to as a feeder tube in this study, and exits through a slot or array of holes. In some designs, foam or other material within the box aids in creating a better distribution at low flow rates. For both tube-based and box-based configurations, many designs also include an unheated tube directly below the initial distributor to aid in replicating the flow pattern created by having a tube above the heated test section. These tubes have been referred to as stabilizing tubes, levelizing tubes, spray tubes, or adiabatic tubes, and will be uniformly referred to as stabilizing tubes in this work.

The following sections provide an overview of low momentum designs from previous studies. This includes a summary of tube-based distributor designs, box-based distributor designs, and the available liquid distributor assessments and comparisons. An overview of these liquid distributor designs is provided in Table 2.1.

Tube-based Distributor Designs

A number of tube-based designs have been used in prior studies. Danilova and Burkin (1976) observed uniform distribution with a concentric tube design with holes in both the inner and outer tubes. The fluid entered from both sides of the inner tube, and exited through holes on the top of the outer tube. Mitrovic (1986) found good performance with a single-tube design where liquid entered from both ends of the tube and exited through an array of holes to a stabilizing tube below. After considering several distributor designs by Fletcher (1975), Parken (1975), Dhir and Taghavi-Tafreshi (1981), and Honda *et al.* (1987), Hu and Jacobi (1996a) later replicated Mitrovic's (1986) design with a modified hole size and spacing, and reported that it provided uniform flow. Chyu and Bergles (1987) designed a single-tube distributor that included an interior heater to

11

bring the fluid to saturation conditions, with the liquid then exiting through a slot at the top of the tube. Honda *et al.* (1991) used a concentric tube design with the fluid entering from only one end of the inner tube. The inner tube had an array of holes on the top of the tube with larger spacing near the fluid entrance, and an outer tube with an exit slot at its bottom. Fujita and Tsutsui (1995b, 1996, 1998) examined a number of tube-based distributor designs, including a porous sintered tube and a tube with holes. The hole pitch, orientation, and diameter, as well as the presence and number of stabilizing tubes, were varied. Tatara and Payvar (2001) chose to combine a tube-based liquid distributor with spray nozzles, using an array of seven tubes with a simple array of downward-facing holes over a tube bundle, combined with two spray tubes located centrally in the tube bundle. They reported an even flow distribution and good spraying pattern. Killion and Garimella (2004a) designed a concentric tube distributor where the inner tube had a widely spaced array of upward-facing small holes, and an outer tube with the bottom half cut away. The small holes would ensure minimal maldistribution due to header effects, while the cutaway tube let flow leave the distributor such that similar flow patterns could develop on subsequent tubes. Yang and Shen (2008) chose to use a simple single-tube distributor with an array of downward-facing holes, but sealed both ends and had fluid entering through a hole centered in the top.

Box-based Distributor Designs

There is a similar variety of box-based designs fabricated for prior studies. Parken (1990) used a distributor with fluid entering the box through a centrally located pipe, and exiting through a narrow slot with a narrow gap before the heated test tube. Liu and Zhu (2005) designed a similar distributor with an angled exit slot, but including an angled

plate above the slot to generate an initial fluid distribution. Armbruster and Mitrovic's (1994) design had fluid entering from fittings on both end walls of the box, and leaving through an array of small holes on the bottom of the box. The bottom plate of the box had a rounded profile on its bottom, and a stabilizing tube was placed below the exit holes. Roques and Thome (2003) selected a distributor design with fluid entering the top of a box, and leaving through an array of small holes on the bottom of the box. This design was modified by Roques *et al.* (2002), who included a grid with foam to the middle of the chamber for low viscosity fluids. Roques and Thome (2007a) designed a distributor with the fluid entering an initial tube with upward-facing holes. It then passed into a box with two layers of foam, with the second layer having a smaller pore diameter to increase pressure drop and improve lateral fluid distribution. Then, the fluid exited through an array of holes on the bottom plate. Habert and Thome (2010a) improved the performance of this design at low flow rates by including a half tube below the distributor, with the bottom part of the tube machined to form a sharp edge and forcing the liquid to fall on the center of the first test tube. Ruan *et al.* (2009) fabricated a box-based distributor with the fluid entering from both sides of an initial distribution tube with an array of holes on the bottom. The fluid then exited the box through an array of smaller holes on the bottom plate. In tests with horizontal flat tubes, Wang *et al.* (2010) observed good performance using the same distributor, but adding a stabilizing tube below the rectangular box.

Table 2.1. Summary of liquid distributor designs

Study	Flow Mode	Fluid	Tube Diameter / Length [mm]	# of Tubes in Bank	Type of Distributor
Tube-based Distributor Designs					
Danilova *et al.* (1976)	-	R-12, R-22, R-113	18 / 330	5 – 60	Concentric tubes: both with holes
Mitrovic (1986)	D, J, S	Water, Alcohol	18 / 300	1	Tube with holes, stabilizing tube
Chyu and Bergles (1987)	D, J	Water	25.4 / 152	1	Tube with slot at top, internal heater
Honda *et al.* (1991)	D, J	R-113	15.9 / 100	45	Concentric tubes: inner holes and outer slot
Hu and Jacobi (1996a)	D, J, S	Water, Glycol, Oil, Alcohol	9.5, 12.7, 15.9, 19.0, 22.2 / 229	1	Tube with holes on bottom, stabilizing tube
Fujita and Tsutsui (1995b, 1996, 1998)	D, J, S	R-11	25 / 130	5	Porous sintered tube; tube with holes; box with holes
Tatara and Payvar (2001)	D, J, S	R-11	19.1 / 205	40	Tube with holes and spray tubes in bundle
Killion and Garimella (2004a)	D	Aqueous LiBr	15.9 / 500	9	Concentric tubes: inner holes and split outer
Yang and Shen (2008)	D	Water, Seawater	14 / 500	2	Tube with holes
Li *et al.* (2010)	D, D-J	Water	15.88 / 700	12	Tube with holes
Box-based Distributor Designs					
Parken *et al.* (1990)	S	Water	25.4, 50.8 / 305	1	Box with thin slot
Armbruster and Mitrovic (1994)	D, J, S	Water, Alcohol	18 / 260	1	Box with holes, stabilizing tube
Liu and Yi (2001)	S	Water, R-11	18 / 120	3	Box with angled slot, curved plate
Roques *et al.* (2002)	D, J, S	Water, Glycol	12.7, 19.1 / 200	3	Box with holes, foam at low flow rates
Roques and Thome (2003)	D, J, S	Water, Glycol	19.05 / 200	3	Box with holes
Liu and Zhu (2005)	S	Water	13, 20, 30 / 130, 200, 300	3	Box with angled slot, curved plate
Roques and Thome (2007a)	D, J, S	R-134a	19.05 / 550	6 – 10	Box with holes, feeder tube, 2 foam layers
Ruan *et al.* (2009)	D, J, S	Water, Glycol	25.4 / 50 – 295	3	Box with holes, feeder tube
Habert and Thome (2010a) , Christians (2010)	D, J, S	R-134a, R-236fa	19.1 / 554	10 – 30	Box with holes, feeder tube, 2 foam layers, half stabilizing tube

Table 2.1. Summary of liquid distributor designs (continued)

Study	Flow Mode	Fluid	Tube Diameter / Length [mm]	# of Tubes in Bank	Type of Distributor
Wang *et al.* (2010)	D, J, S	Water, Glycol	3.2×25.4 (flat) / 400	2	Box with holes, feeder tube

Abbreviations: D = Droplet, J = Column/Jet, S = Sheet

Liquid Distributor Performance Comparisons

Although many studies have only reported the performance of a single distributor in qualitative terms, several studies have chosen to examine the impact of varying distributor parameters or compared the performance of distributor designs. Several studies have noted that increasing the height of the distributor above the first tube results in higher heat transfer coefficients (Chyu and Bergles, 1987; Mitrovic, 1986; Yang and Shen, 2008). This is generally attributed to the higher impact velocity of the fluid. However, this impact appears to be less significant, perhaps negligible, in the boiling regime (Chyu, 1984), and large distributor heights result in poor fluid coverage of the tube and lower heat transfer coefficients (Yang and Shen, 2008) or unstable flow (Wang *et al.*, 2010). Ruan *et al.* (2009) observed that the liquid distribution length, which was varied from 75 to 295 mm in their study, impacted the flow mode transitions. This distribution length effect was most significant for the jet to jet-sheet transition with a low Galileo number fluid, reducing the transitional flow rate by 25%, and was attributed to edge effects contributing to the sheet formation and break-up process.

Fujita and Tsutsui (1995b, 1996, 1998) investigated the performance of three liquid feeders designs in six configurations with R-11 at a pressure of 0.2 MPa. This included a porous sintered tube, a perforated tube with holes facing upwards or

downwards, and a box with holes and 1, 2 or 3 stabilizing tubes. They observed that the type of distributor had a substantial impact on the flow pattern observed over the tubes, and measured substantial axial flow rate variation at the first tube under the distributor. These variations were damped as the fluid flowed over subsequent tubes, with an almost even distribution after three tubes. This resulted in Nusselt number variation of approximately 20% between some distributor designs.

2.2   Flow Mode Transitions

The flow of films falling over horizontal tubes is typically considered to be in one of three primary flow modes: droplets, jets, and sheets. In addition, many authors note the existence of transition modes between these primary modes, often referred to as the droplet-jet and jet-sheet modes. The jet mode is also referred to as the column mode, but
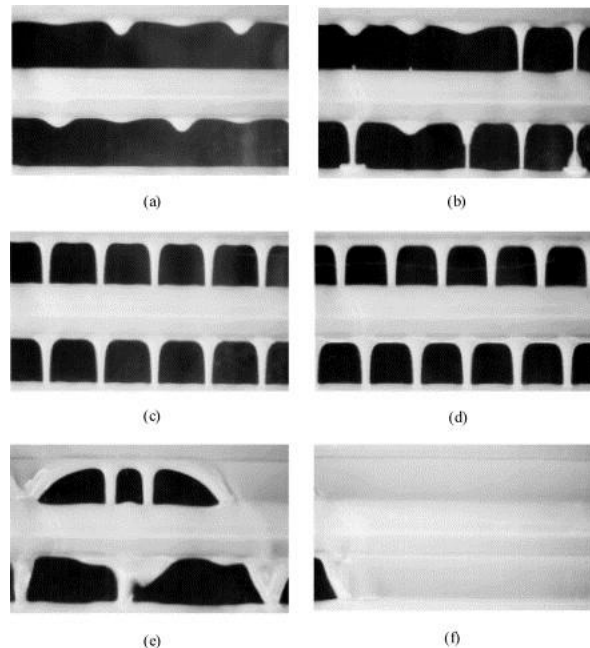
Figure 2.2. Falling-film flow modes: (a) droplet mode, (b) droplet-jet mode, (c) inline jet mode, (d) staggered jet mode, (e) jet-sheet mode, and (f) sheet mode (Hu and Jacobi, 1996a)

16

is uniformly referred to as the jet mode in the present study. Representations of these flow modes are shown in Figure 2.2. The figure shows the droplet mode (a), droplet-jet mode (b), jet mode (c, d), jet-sheet mode (e), and sheet mode (f). In this case, note that the jet mode was subdivided into in-line jets (c) and staggered jets (d). These flow modes influence the fluid flow over each tube, and are expected to have an impact on the heat transfer characteristics of falling-film flow. This section discusses the criteria used to distinguish between flow modes, the influence of relevant parameters on the transitional flow rates, and models developed to predict flow mode transitions.

2.2.1   Transition criteria

The quantification of flow mode transitions is an inherently subjective process. Each investigator chooses which flow modes to include in the classification, and also how to differentiate between them. Initially, these classifications were based on visual observations, but recent studies have taken videos of the transitions and differentiated between flow modes using quantitative criteria. For instance, Roques *et al.* (2002) divided the intertube flow modes into the standard droplet, droplet-jet, jet, jet-sheet, and sheet modes with analysis based on video at 30 fps. They stated that the droplet mode exists when only droplets fall between tubes, and there are no continuous liquid bridges across the intertube region. The transition to droplet-jet occurs when droplets are still present, but a liquid jet, defined as a continuous link between the tubes, exists for at least 1 to 2 seconds. In the jet mode, only liquid jets are present. The transition to jet-sheet mode occurs when a small sheet, formed by the merging of two liquid jets, is present. Finally, the sheet mode occurs when the fluid flows as a single liquid sheet between tubes.

There are many variations of the above flow mode definitions. In addition, many authors simply use different designations for the flow modes. Dhir and Taghavi-Tafresi (1981) only categorized the flow mode using the primary flow modes—droplet, jet, and sheet—while increasing the flow rate, but included unstable sheet mode and unstable jet mode when the decreasing flow rate. Honda *et al.* (1987) included the droplet-jet flow mode in the droplet mode, but maintained the transitional jet-sheet mode between jet and sheet modes. Fujita and Tsutsui (1995b, 1996) described the observed flow patterns using five flow modes: discrete droplets, droplets, columns, disturbed columns, and sheets. Droplets with nonuniform sizes and moving generation sites were considered to constitute the discrete droplet mode, while droplets that originate as columns that break into droplets before reaching the next tube were considered to be the droplet mode. The disturbed column mode has breakup and branching between columns, while the column mode has uniform liquid streams between the tubes. Hu and Jacobi (1996a) defined droplet, droplet-jet, in-line jet, staggered jet, unsteady jet, jet-sheet, and sheet flow modes. The in-line jet mode indicates that jets between subsequent tubes are aligned horizontally, while in staggered jet mode, the jets are located at the midpoint between two jets in the tube above. Unsteady jets were not present at all conditions, but indicate that the jet departure sites were not at steady locations. Wang *et al.* (2010) split the sheet flow mode into whole sheet mode and torn sheet mode, where torn sheet mode indicates that the film does not form a single sheet, but no jets are present. Finally, several investigators differentiate between transitions with increasing and decreasing flow rates to capture possible hysteresis effects. For instance, Hu and Jacobi (1996a) refer to the transition

between droplet mode and droplet-jet mode as droplet/droplet-jet when the flow rate is increasing, and droplet-jet/droplet when the flow rate is decreasing.

2.2.2 **Influence of Parameters**

A number of factors have been proposed to influence the flow rate at which flow mode transitions occur, including fluid properties, tube spacing, tube surface, tube diameter, tube shape, vapor shear, additives, type of liquid feeder, gravitational acceleration, and the presence of boiling. Generally, it has been observed that flow is in the sheet mode when inertial effects are dominant, the droplet mode when gravity and surface tension are more significant, with jet mode occurring due to a combination of these forces and viscous effects (Hu and Jacobi, 1996a).

Fluid Properties

There is wide agreement that fluid properties are the dominant influence on transitional flow rate (Armbruster and Mitrovic, 1994; Honda *et al.*, 1987; Hu and Jacobi, 1996a; Roques and Thome, 2007b; Roques *et al.*, 2002; Ruan *et al.*, 2009; Wang *et al.*, 2012). These studies found that the transitional Reynolds number increases as surface tension or liquid density increases, and decreases as viscosity increases. However, viscosity has a minimal influence on the transitional mass flow rate, so the influence of viscosity on transitional Reynolds number is due to the dynamic viscosity term in the Reynolds number definition. This is supported by the experimental results of Dhir and Taghavi-Tafreshi (1981) and Honda *et al.* (1987), although Roques and Thome (2007b) have suggested that a higher viscosity also results in less distinct flow modes. A study by Dhir and Taghavi-Tafreshi (1981) also found that the transitional flow rate is largely

independent of surface tension, which contradicted other results, and may be due to a limited experimental range.

Tube Spacing

A variety of trends has been reported about the influence of tube spacing on mode transition flow rates. Fujita and Tsutsui (1995b, 1996) found that the droplet-to-jet transition depends on tube spacing, but considered it a secondary effect compared to flow rate. Meanwhile, Hu and Jacobi (1996a) observed that tube spacing has a minimal influence in the range considered, but suggested that tube spacing would limit the applicable range of flow mode transition correlations. Roques *et al.* (2002) reported a tube spacing effect, but found that the impact on flow mode transitions varied with tube spacing. At large tube spacings, the tube spacing had relatively little impact on the transitional flow rate; at moderate tube spacings, the transitional Reynolds number increased; and at small tube spacings, the transitional Reynolds number decreased. The effect was found to be most significant at small tube spacings. In tests with rectangular tubes, Wang *et al.* (2010) observed that the flow rates required for mode transition increased as tube spacing increased. The differing trends observed in these studies can be attributed to the scope of each study, which examined different fluid properties and flow rates. It appears that tube spacing has an impact on the flow rates required for flow mode transitions, but this influence is not as strong as that of fluid properties, and may not be apparent in all studies. In addition, increasing tube spacing can lead to other undesirable phenomena, such as splashing, and also decrease the surface area provided per unit volume in a heat exchanger, limiting its potential as a design variable in practical applications.

Structured Surfaces

Structured surfaces exhibit the same flow modes as smooth tubes (Honda *et al.*, 1987; Roques and Thome, 2003; Roques *et al.*, 2002), but surface features influence the flow rate at which mode transitions occur. Roques *et al.* (2002) examined the flow transitions on plain, low-finned, enhanced boiling, and enhanced condensation tubes. The transitions on enhanced boiling tubes occur at flow rates similar to those for plain tubes, but all other structured surfaces shifted the transitional Reynolds numbers. A second study (Roques and Thome, 2003) expanded this study to additional low-finned tubes. Tubes with 40 fpi had transitional flow rates similar to those for plain tubes, but both 19 and 26 fpi tubes required higher flow rates to undergo flow mode transitions. This is attributed to the destabilizing effect an increased pitch between fins causes, influencing the departure sites of jets and other features.

Vapor Shear

Vapor shear can be directed in either co-current or counter-current orientation to the liquid film flow. In tests with film condensation on low-finned tube bundles, Honda *et al.* (1991) observed that co-current vapor flow shifted the onset of the sheet mode to higher flow rates by breaking the film up into small droplets. Hu and Jacobi (1996a) tested co-current gas flow with Weber numbers up to 200, and found that it did not impact the jet-sheet to sheet transition, but that high modified Galileo number transitions for droplet mode were affected. These contrary results can be attributed to the different test conditions and limited ranges of each study, and further experimental data would be needed to fully assess the impact of co-current vapor flow on flow mode transitions. Ruan *et al.* (2009) examined the impact of counter-current gas flow on flow mode

transitions and observed that most flow mode transitions occurred at higher Reynolds numbers as Weber number increased, but that this is not the case for all transitions. There was little impact on the jet-sheet to sheet transition, and the jet to jet-sheet transition occurred at a lower Reynolds number. In addition, the hysteresis in mode transitions decreased as Weber number increased. They attributed these differences to the thickening of the liquid film, jets, and sheets due to shear, as well as unsteadiness caused by the vapor flow. As the gas flow rate increased further, the flow became unsteady.

Additives

The presence of additives can substantially influence the flow modes present. Moeykens *et al.* (1995a) observed that adding polyol-ester lubricant in concentrations of 1.0%, 2.0%, and 3.0% all caused substantial foaming of the film. Meanwhile, Ruan and Jacobi (2011) found that fluids with aluminum oxide nanoparticles in concentrations of 0.05%, 0.5%, 1%, and 2% exhibited the same transitions as flow without nanoparticles, but flow mode transitions occurred at higher Reynolds numbers as the concentration of the nanofluid increased. The flow mode transitions occurred at higher Reynolds numbers than predicted by correlations accounting for the macroscopic property effects of the nanoparticles, making the cause of the influence unclear.

Heat Flux

Heat flux does not have a direct impact on the transitional flow rate. However, increasing heat flux leads to nucleate boiling in the flow. Roques and Thome (2007b) found that the transitions are shifted to higher flow rates when nucleate boiling is present. In addition, it has been noted that the film may travel as a two-phase bubbly layer when boiling is present (Habert and Thome, 2010a). The higher transitional flow rates can be

attributed to both the bubble formation sites and the bubbly nature of the film delaying the formation of stable jets and sheets. Increasing heat flux can also lead to film breakdown and partial dryout, which can modify the flow mode.

Liquid Distributor

Fujita and Tsutsui (1995b, 1996) examined the influence of six liquid feeding methods on transitional flow rates using R-11 at a pressure of 0.2 MPa. They observed that the discrete droplet mode, unique to their flow mode definitions, was not impacted by the feeding method, but the feeding method had a substantial effect on the flow rate at which all other transitions occurred. Meanwhile, Ruan *et al.* (2009) considered different feeding lengths, from 75 to 295 mm, using a single feeder design. The impact on transitional flow rates was most significant for the jet to jet-sheet transition with a low Galileo number fluid, and reduced the transitional flow rate by 25%. This is attributed to edge effects contributing to the sheet formation and break-up process. In tests with rectangular tubes, Wang *et al.* (2010) found that the distributor height also impacted flow patterns, but the influence was not consistent through all flow modes. The transitions from jet mode to sheet mode occurred at higher flow rates as the distributor height increased, but the droplet to droplet-jet transition occurred at a lower flow rate. In addition, a large distributor height can lead to unstable flow on the tube.

Tube Diameter

With round tubes, the tube diameter has no impact on transitional flow rates (Dhir and Taghavi-Tafreshi, 1981; Hu and Jacobi, 1996a), although Hu and Jacobi (1996a) suggested that it may have an impact on the jet regime due to momentum interactions between neighboring jets. However, Wang *et al.* (2010) found that flat, horizontal tubes

23

with dimensions of $400 \times 25.4 \times 3.18$ mm have substantially different flow regime transitions than round tubes. Flat tubes have a much smaller range during which the jet flow mode is present, and the jet-sheet flow mode was not always observed when decreasing flow rates. In addition, they note that flat tubes may not exhibit the Taylor instability driven droplet spacing observed on round tubes, and gravitational and shear forces could lead to different liquid velocity profiles.

Hysteresis

Several studies have observed that increasing or decreasing flow rate results in hysteresis between flow mode transitions. Armbruster and Mitrovic (1994) observed minimal hysteresis for the droplet to jet transition, but far more significant hysteresis for the jet to sheet mode transition. In addition, the jet-sheet transition region was minimal when flow rate was decreasing. Dhir and Taghavi-Tafreshi (1981) found similar results, with the jet-sheet transition occurring at almost twice the flow rate when the flow rate was increasing rather than decreasing. Hu and Jacobi (1996a) observed hysteresis in the transitions between all flow regimes, but found that it was a relatively minor influence. Neglecting hysteresis increased the maximum root-mean-squared deviation of their correlations from 8.5 to 11.2 percent, and they suggested that it may be neglected for many purposes within their experimental range. Finally, Roques *et al.* (2002) observed minimal hysteresis for plain and enhanced tubes, and suggested that it should be neglected for practical reasons, as the trend in flow rate may not be known for an operating heat exchanger.

2.2.3   Flow Mode Transition Models

The transitions between each flow regime have been predicted using empirical and theoretical approaches. This section presents an overview of the usage of each of these options in the literature.

Empirical Correlations

Empirical correlations relate the transitional flow rate to nondimensionalized fluid properties and other parameters. Several investigators (Armbruster and Mitrovic, 1994; Honda *et al.*, 1987; Hu and Jacobi, 1996a; Roques and Thome, 2007b; Roques *et al.*, 2002) have reported good agreement using the form

$$Re = a_0 Ga^{a_1} \tag{2.4}$$

where *Re* is the Reynolds number, *Ga* is the modified Galileo number, sometimes replaced with the Kapitza number, and a_0 and a_1 are empirical constants. The empirical constants are defined separately for each flow mode transition, and also defined separately for increasing and decreasing flow rates for situations where hysteresis is being considered. The exponent a_1 is typically near, or sometimes fixed at, a value of 0.25.

Modifications to this form have been used to incorporate other factors. For instance, Ruan *et al.* (2009) accounted for vapor flow by modifying the calculated transitional Reynolds number using an equation of the form

$$Re = Re_{\mathrm{We}=0} \left\{ 1 + \left[(a_0 + a_1 We) + (a_2 + a_3 We) Ga^{-0.25} \right] We \right\} \tag{2.5}$$

where a_0, a_1, a_2, and a_3 are empirical constants. Although this correlation shows good agreement with their data, they acknowledge that it has no physical basis. Meanwhile,

Roques *et al.* (2002) captured a tube spacing effect by expanding the empirical coefficient a_0 into a third order polynomial that non-dimensionalized intertube spacing with the tube diameter. Honda *et al.* (1987) also recommended that tube spacing may be a relevant study, but did not collect sufficient data to include its influence in their correlation. In a study with rectangular tube geometries, Wang *et al.* (2012) captured this tube spacing effect with an equation of the form

$$Re = a_0 + a_1(s/\xi)^{a_2} Ga^{a_3} \tag{2.6}$$

with empirical constants a_0, a_1, a_2, and a_3.

Theoretical Approaches

Yung *et al.* (1980) suggested that the onset of the droplet-to-column transition could be predicted by setting the droplet production frequency equal to the capillary wave oscillation frequency, resulting in the form

$$\Gamma = a_0 \frac{\rho_l}{\lambda} \frac{\pi d^3}{6} \left(\frac{2\pi\sigma}{\rho_l \lambda^3} \right)^{0.5} \tag{2.7}$$

where the wavelength λ is determined using the Taylor instability analysis by Bellman and Pennington (1954). The empirical coefficient a_0 is fit to transition data collected for ethyl alcohol and water. The experiments were run with a single generation site on a single tube fed by a buret. A value of 0.405 was fit to the data, predicting the collected experimental data to within ±10%.

Wang and Jacobi (2014) developed a theoretical approach for determining mode transitions based on a thermodynamic analysis. The point of thermodynamic equilibrium between the two modes is determined, at which point either mode is available and a

26

transition can occur. This analysis results in the same relationship for both the droplet-to-jet transition and the jet-to-sheet transition, shown in Equation (2.8).

$$Re \sim Ga^{0.25}(s/\xi)^{0.5} \tag{2.8}$$

This approach successfully explains the relationship between Reynolds number and modified Galileo number that many previous investigations have used as the basis of empirical correlations, and also predicts a tube-spacing effect usually not included in empirical correlations. This formulation was evaluated using data collected in several previous studies by their research group (Hu and Jacobi, 1996a; Ruan and Jacobi, 2011; Ruan *et al.*, 2009; Wang *et al.*, 2010; Wei and Jacobi, 2002). Compared to correlations without the tube spacing effect, this relationship showed an overall improvement in performance, although two of the transitions—from jet-sheet to jet mode and droplet-jet to droplet mode—showed worse agreement. However, the authors acknowledged that these limited data sets were not intended to examine the influence of tube spacing, and further investigation would be necessary to support this relationship.

Table 2.2. Summary of flow mode transition studies

Study	Fluid	d [mm]	H [mm]	s [mm]	$\Gamma \times 10^3$ [kg m^{-1} s^{-1}]	q'' [kW m^{-2}]	Regimes
Yung *et al.* (1980)	Water, Ethyl Alcohol	-	-	-	-	0	D, J
Mitrovic (1986)	Water, Isopropyl Alcohol	18	4.5–87	30–90	38–130	9.4, 18.4	discrete D, J, laminar S, turbulent S
Honda *et al.* (1987)	R-113, Methanol, Propanol	15.8	6.2, 28.2	6.2, 28.2	-	0	D, J, J-S, S
Honda *et al.* (1991)	R-113	15.6–16.1	5.9–6.4	5.9–6.4	-	-	D, J, J-S, S
Armbruster and Mitrovic (1994)	Water, Isopropyl Alcohol	18	22.5–126	22.5–126	5–120	0	D, D-J, J, disturbed J, S
Fujita and Tsutsui (1995b)	R-11	25	25	25	1–180	0.5–2.5	D, D-J, J, disturbed J, S
Fujita and Tsutsui (1996)	R-11	25	25	25	1–180	0.5–2.5	D, D-J, inline J, staggered J, unsteady J, J-S, S
Hu and Jacobi (1996a)	Water, Ethylene Glycol, Water/Glycol, Oil, Alcohol	9.5–22.2	5–50	5–50	0–110	0	D, D-J, J, J-S, S
Roques *et al.* (2002)	Water, Ethylene Glycol, Water/Glycol	12.7, 19.1	-	3.2–24.9	-	0	D, D-J, J, J-S, S
Roques and Thome (2007b)	R-134a	19.1	-	3.2–24.9	0–187	0–60	D, D-J, J, J-S, S
Ruan *et al.* (2009)	Water, Ethylene Glycol	25.4	1	11–45	0–150	0	D, D-J, J, J-S, S
Wang *et al.* (2010)	Water, Ethylene Glycol	25.4 × 3.2	2.0, 6.4	4.8–24.9	0–145	0	D, D-J, J, J-S, S
Ruan and Jacobi (2011)	Water, Water with Nanoparticles	19.1	1	10	10–185	0–29	D, D-J, J, J-S, S
Wang *et al.* (2012)	Oil, Water, Ethylene Glycol, Water/Glycol	25.4 × 3.2	2.0, 6.4	4.8–24.9	0–145	0	D, D-J, J, J-S, torn S, whole S

Note: D = Droplet, J = Jet, S = Sheet

2.3   Flow Characteristics

In addition to studies on flow transitions, a number of investigations have focused on characteristics of the falling-film flow, including droplet size, droplet and jet spacing, and film thickness. In a qualitative study focusing on absorption systems, Killion and Garimella (2003) described the complex fluid behavior over horizontal round tubes in the droplet mode, highlighting the deviations from idealized film behavior during droplet and wave development, and discussing the implications of this behavior on heat and mass transfer performance. Information on this film behavior is important to the development of accurate, mechanistic models of these processes.

Droplet Size

The size of droplets in falling-film systems has been examined by several studies. Yung *et al.* (1980) examined the diameter of droplets falling over adiabatic tubes with a diameter of 38 mm using water and ethyl alcohol. Given that the liquid breakup is a function of gravity and surface tension, they recommended the expression

$$d = a_0 \sqrt{\frac{\sigma}{\rho_1 g}} \qquad (2.9)$$

where the constant a_0 was found to be 3.0 for their experiments. They also measured the diameter of the smaller secondary droplets, finding these to have 24 to 46% of the diameter of the primary droplets. They recommended that droplet size information be used to design evaporators such that droplet entrainment did not lead to film breakdown and limit performance.

In a study focusing on falling-film absorption, Killion and Garimella (2004a) examined the development of droplet surface area and volume over time using high-

29

speed video, measuring droplet characteristics with an image analysis program. They observed continuous increases in surface area and volume until the point of impact. However, the surface area-to-volume ratio was highest in the region after impact, with satellite droplets providing additional surface area for the same overall liquid droplet volume. In their study using aqueous lithium-bromide solutions over 15.9 mm tubes, maximum droplet surface areas and volumes of 180 mm^2 and 200 mm^3 were measured, respectively. An additional study (Killion and Garimella, 2004b) found that the droplet formation and impact process could be predicted well by numerical simulation with the volume of fluid method. Good agreement was found between the experiments and computational results both visually and with the surface area and volume data.

Droplet and Jet Spacing

There is wide agreement that the droplet and jet generation site spacing on horizontal round tubes is related to Taylor instabilities, which occur when a more dense fluid is above a less dense fluid. Most studies have reported this spacing to be regular, although Mitrovic (1995) observed that at very low flow rates, the droplets break off at random positions and only leave from fixed positions at higher flow rates.

Bellman and Pennington (1954) found that for inviscid, incompressible fluids the most dangerous wavelength, which is the distance between the unstable disturbances that will grow most rapidly and generate droplets is given by

$$\lambda = 2\pi \sqrt{\frac{a_0 \sigma}{g(\rho_l - \rho_v)}} \tag{2.10}$$

where the constant a_0 is equal to 3. Yung *et al.* (1980) later recommended the same form, but found that for water, ethyl alcohol, and ammonia, setting the constant a_0 equal to a

value of 2 gave the best agreement with their data, but that for thicker liquid layers $a_0 = 3$ is still more accurate. In tests with condensing R-113, methanol, and propanol, Honda *et al.* (1987) found good agreement with Yung *et al.*'s wavelength predictions in the jet regime, but that it significantly underpredicted the droplet spacing.

Later studies have suggested that the tube diameter and flow rate, among other factors, have an impact, which is not captured by this approach. In a study examining bubble departure from film boiling on a cylinder, Lienhard and Wong (1964) found that the most dangerous wavelength could be predicted by

$$\lambda = \frac{2\pi\sqrt{3}}{\sqrt{g(\rho_l - \rho_v)/\sigma + 2/d^2}} \qquad (2.11)$$

This showed good agreement with data taken using benzene and isopropanol on cylindrical heaters with diameters of 0.0508 to 1.290 mm. In experiments with silicone oils, ethylene glycol, and glycerol over horizontal tubes with diameters of 1 to 19 mm, Dhir and Taghavi-Tafreshi (1981) found that Lienhard and Wong's correlation showed good agreement at low tube diameters, but predicted wavelengths 18% higher than most of their data. Dhir and Taghavi-Tafreshi also observed that the jet spacing was lower than the droplet spacing. They suggested that this may correspond to the critical wavelength, equal to the most dangerous wavelength divided by the square root of 3, because this shorter unstable wavelength provides more locations of liquid to exit the tube as the flow rate is increased. Mitrovic (1986) also observed jet spacings between the critical and most dangerous wavelengths predicted by the Lienhard and Wong (1964) correlation. In addition, he noted that the jets on each tube have the same spacing, but are offset from one another by $\lambda/2$. This was attributed to axial flow along each tube away from the

31

stagnation point of each jet meeting in the center of the jet-to-jet spacing and then flowing downwards. In tests with water and isopropyl alcohol, Armbruster and Mitrovic (1994) found that Lienhard and Wong's correlation performed well, but adjusted it by an empirical factor of 0.75 to improve agreement with their data.

Hu and Jacobi (1998) conducted experiments to measure droplet and jet spacing with water, ethylene glycol, a water-glycol mixture, and hydraulic oil for a range of tube spacings, tube diameters, and flow rates. They observed that the droplet and jet spacing decreased as Reynolds number increased for high Galileo number fluids, but there was a minimal impact for fluids with a low Galileo number. Meanwhile, tube diameter only had an influence for small diameter tubes, and tube spacing had a minimal impact, although it modified the qualitative appearance of the flow. In addition, they noted that as Reynolds number approached zero, their data were predicted well by the Bellman and Pennington (1954) correlation, Equation (2.10). Given these results, they proposed two correlations, Equations (2.12) and (2.13). Equation (2.12) is applicable to flow with $Re < 50$, and Equation (2.13) is applicable to flow with $Re > 100$.

$$\lambda = 0.836 \frac{2\pi\sqrt{3}}{\sqrt{g\rho_1/\sigma + 2/d^2}} - 0.863 \frac{\xi Re}{Ga^{0.25}} \tag{2.12}$$

$$\lambda = 0.75 \frac{2\pi\sqrt{3}}{\sqrt{g\rho_1/\sigma + 2/d^2}} - 0.85 \frac{\xi}{Ga^{0.25}} \tag{2.13}$$

As can be seen, these equations adapt the Lienhard and Wong (1964) approach with an additional term accounting for the flow rate and fluid properties. This predicted the experimental data with a maximum root-mean-squared error of 8%. They also found good performance with a single, more complex correlation that blends Equations (2.12) and (2.13).

Although these studies of droplet and jet spacing have encompassed increasingly large experimental ranges, there are still no correlations available with wide applicability. There is, however, agreement that Taylor instabilities largely determine the spacing. In addition, in practical applications with a bank of tubes, it is not clear whether the predicted tube spacing persists throughout the tube bank. Mitrovic (1986) reported that jets on subsequent tubes have the same spacing, but Honda *et al.* (1987) found that the jet spacing broke down on lower tubes in an array.

Film Thickness

A number of methods have been used to measure the thickness of liquid films, including contact methods, adding radioactive additives, light absorption, capacitance methods, electrical conductivity, shadow methods, fluorescence methods, and other optical methods (Lel *et al.*, 2005). In horizontal tube studies, relatively good agreement has been observed with the classic Nusselt film theory (Nusselt, 1916), which provides the expression

$$\delta = \left(\frac{3\mu_l \Gamma}{\rho_l \left(\rho_l - \rho_v \right) g \, \sin\left(\theta \right)} \right)^{1/3}$$

(2.14)

where θ is the angle around the tube measured from the stagnation point. This approach predicts the lowest film thickness at 90 degrees, with thicker films near the top and bottom of the tube.

Rogers and Goindi (1989) examined the film thickness over tubes with a diameter of 132 mm using dial point gauge measurements at 45, 90, and 135 degrees. Measurements were taken with water at film Reynolds numbers up to 2000. Measured thicknesses for films in the laminar regime were approximately 30% higher than the

theoretical predictions by Nusselt film theory. However, their contact measurement method would measure the maximum film thickness, which would be increased by film waviness. Therefore, higher values would be expected. Based on these measurements, they recommended Equation (2.15) for best agreement with their data.

$$\frac{\delta}{d} = 3.716\, Re^{0.174} Ar^{-1/3} \left(\sin\theta\right)^{-1/3} \tag{2.15}$$

In experiments with water, ethylene glycol, and a mixture of the two fluids, Gstoehl *et al.* (2004) examined the film thickness over 19.05 mm diameter tubes with spacings from 3.2 mm to 19.4 mm. Measurements were made using laser-induced fluorescence and laser tomography, allowing film thickness measurements at 5 degree increments over time, although the method did not allow for film thickness measurements near 90 degrees. Fluctuations of the film thickness over time were small relative to the film thickness, staying under 12% in the examined range. The film thickness measurements showed reasonable agreement with Nusselt theory, with two notable deviations. The agreement decreased at high Reynolds numbers, and with the smallest tube size, the film thickness fell sharply after 90 degrees. No explanation for these lower film thicknesses was suggested. To improve agreement with the data, they recommend using a modified Nusselt film theory, where Nusselt film theory is applied to the upper part of the tube (up to 90 degrees), and then a constant film thickness is assumed beginning at that point. In tests with an inclined plate using chromatic confocal imaging and fluorescence intensity, Lel *et al.* (2005) also observed deviation from Nusselt theory at large Reynolds numbers. Their measurements found close agreement between the two techniques in tests with silicone fluids for Reynolds numbers from 2 to 700, and they

recommended a new correlation to improve the fit with their data throughout the measured range:

$$\delta \left(\frac{g}{\nu^2} \sin\theta \right)^{1/3} = 1 + 0.615 Re^{0.47} \qquad (2.16)$$

Additional investigations on film thickness over horizontal tubes have examined the distribution of the film thickness and the impact of gas flow. Xu *et al.* (2003) found that the film thickness did not change with tube diameter, but that the film thickness distribution narrowed as tube diameter increased. In other words, a wider range of film thicknesses was measured with smaller tubes. Meanwhile, Ruan *et al.* (2011) used a theoretical analysis to account for the impact of counter-current gas flow, which may have an impact in tube bundle studies. It was found that the vapor shear caused film thickness to increase as gas velocity increases.

2.4 Experimental Heat Transfer Studies

This section includes studies on the falling-film evaporation heat transfer coefficients. These studies have been conducted with plain and enhanced tubes, under sub-cooled and saturation conditions, as well as during convective evaporation and boiling heat transfer. This section organizes these studies based on the impact of each parameter. This includes a discussion of the effects of flow rate, dryout, heat flux, temperature, liquid distributor and tube spacing, the angle around the tube, tube diameter, vapor flow, enhanced tube surfaces, and tube bundles. A summary of these influences is given in Table 2.3, and the conditions for each experimental heat transfer study are shown in Table 2.5.

Table 2.3. Influences on heat transfer coefficient

Parameter	Influence on h as Parameter Increases	Physical Explanation	Studies
Convective Evaporation Regime			
Flow Rate	Increase, decrease, and increase again	Initial increase as dryout decreases, decrease due to thickening laminar film, and increase due to turbulence or boundary layer development	(Brumfield and Theofanous, 1976; Chyu and Bergles, 1987; Conti, 1978; Fujita and Tsutsui, 1998; Lee *et al.*, 2012; Li *et al.*, 2011a; Liu and Yi, 2001; Liu *et al.*, 2002; Lorenz and Yung, 1979; Mitrovic, 1986; Owens, 1978; Parken and Fletcher, 1982; Parken *et al.*, 1990; Putilin *et al.*, 1996; Rifert *et al.*, 1992; Rogers *et al.*, 1995; Tan *et al.*, 1990; Zeng *et al.*, 1995)
Dryout	Decrease	Very low local h in dry areas	(Fujita and Ueda, 1978; Ganić and Getachew, 1986; Gross, 1994; Li *et al.*, 2011a; Li *et al.*, 2011b; Li *et al.*, 2010)
Heat Flux	No effect	No mechanism to influence h	(Conti, 1978; Fujita and Tsutsui, 1995b, 1996, 1998; Li *et al.*, 2011b; Liu and Yi, 2001, 2002; Liu *et al.*, 2002; Owens, 1978; Parken, 1975; Parken and Fletcher, 1982; Parken *et al.*, 1990)
Temperature	Increase	Decreased liquid viscosity decreases film thickness	(Kocamustafaogullari and Chen, 1988; Liu, 1975; Owens, 1978; Parken, 1975; Parken and Fletcher, 1982; Parken *et al.*, 1990)
Distributor Height / Tube Spacing	Increase	Increased local heat transfer coefficient at point of fluid impact, but at high spacings reduces film coverage	(Chyu, 1984; Chyu and Bergles, 1985, 1987; Liu, 1975; Liu and Yi, 2002; Mitrovic, 1986; Parken, 1975)
Angle Around Tube	Decrease	Fluid impingement and thermal boundary layer growth	(Hu and Jacobi, 1996b; Mitrovic, 1986; Putilin *et al.*, 1996; Rifert *et al.*, 1989; Rifert *et al.*, 1992; Rogers and Goindi, 1989; Tan *et al.*, 1990)
Tube Diameter	Decrease	Tube angle effects apply to larger portion of small diameter tubes	(Liu and Zhu, 2005; Parken, 1975; Parken and Fletcher, 1982; Parken *et al.*, 1990)
Vapor Flow	Increase, decrease, or no net effect	Increase due to waviness or reduced film thickness; decrease due to thicker film, entrainment or deflection, and dryout	(Garcia *et al.*, 1992; Liu, 1975; Ribatski and Jacobi, 2005; Yung *et al.*, 1980)

Table 2.3. Influences on heat transfer coefficient (continued)

Parameter	Influence on *h* as Parameter Increases	Physical Explanation	Studies
Surface Enhancement	Increase	Increased tube surface area, film waviness or tube coverage, decreased film thickness, modified velocity profile and boundary layer development	(Chien and Chen, 2012; Chien and Tsai, 2011; Lee *et al.*, 2012; Li *et al.*, 2011b; Liu and Yi, 2001, 2002; Putilin *et al.*, 1996; Rifert *et al.*, 1989; Rifert *et al.*, 1992; Sabin and Poppendiek, 1978)
Tube Bundle	Decrease or no effect	Minimal effect with complete wetting, but substantial decrease if film breakdown occurs	(Fujita and Tsutsui, 1998; Lorenz and Yung, 1982; Zeng *et al.*, 1997)
Boiling Regime			
Flow Rate	Increase, then no effect or increase	Initial increase as dryout decreases, no effect in areas of tube dominated by boiling, but convective effects persist	(Chien and Chen, 2012; Chien and Tsai, 2011; Chyu and Bergles, 1985, 1987; Habert and Thome, 2010a; He *et al.*, 2011; Moeykens, 1994; Moeykens and Pate, 1994; Parken, 1975; Parken *et al.*, 1990; Roques and Thome, 2007a; Yang and Shen, 2008; Zeng *et al.*, 1995)
Dryout	Decrease	Very low local *h* in dry areas	(Armbruster and Mitrovic, 1995; Christians and Thome, 2012a; Fujita and Tsutsui, 1998; Habert and Thome, 2010a; Roques and Thome, 2007a, 2007b),
Heat Flux	Increase	Increased nucleation site density and boiling over larger portion of tube	(Chien and Chen, 2012; Chien and Tsai, 2011; Fletcher *et al.*, 1974; Fletcher *et al.*, 1975; Habert, 2009; Habert and Thome, 2010a; He *et al.*, 2011; Liu and Yi, 2001, 2002; Moeykens, 1994; Moeykens and Pate, 1994; Parken, 1975; Parken *et al.*, 1990; Roques, 2004; Roques and Thome, 2007a; Yang and Shen, 2008; Zeng *et al.*, 1995)
Temperature	Increase	Decreased film thickness and increased nucleation site density	(Chien and Chen, 2012; Chien and Tsai, 2011; Fletcher *et al.*, 1974; Fletcher *et al.*, 1975; Parken, 1975; Zeng *et al.*, 1995)
Distributor Height / Tube Spacing	No effect	Possible increased local heat transfer coefficients at point of impact, but minor influence relative to boiling	(Chyu, 1984; Chyu and Bergles, 1985, 1987; Danilova *et al.*, 1976; Roques and Thome, 2007b; Yang and Shen, 2008; Zeng *et al.*, 1995)

Table 2.3. Influences on heat transfer coefficient (continued)

Parameter	Influence on *h* as Parameter Increases	Physical Explanation	Studies
Angle Around Tube	Decrease then increase	Fluid impingement at top of tube and boiling at bottom	(Parken and Fletcher, 1982; Parken *et al.*, 1990)
Tube Diameter	Decrease or increase	With high boiling *h*, increase due to more boiling area, otherwise convective evaporation trend is observed	(Fletcher *et al.*, 1974; Moeykens, 1994; Moeykens and Pate, 1994; Parken, 1975; Parken *et al.*, 1990)
Vapor Flow	Increase, decrease, or no net effect	Increase due to waviness or reduced film thickness; decrease due to thicker film, entrainment or deflection, dryout, and suppressed bubble nucleation	(Parken, 1975; Ribatski and Jacobi, 2005)
Surface Enhancement	Increase	Provides bubble nucleation sites and possible convective enhancement	(Bukin *et al.*, 1982; Chien and Chen, 2012; Chien and Tsai, 2011; Christians and Thome, 2012a; Chyu *et al.*, 1982; Chyu and Bergles, 1989; Habert and Thome, 2010a; Moeykens *et al.*, 1995a; Roques and Thome, 2007a; Tan *et al.*, 1990; Zeng *et al.*, 1998)
Tube Bundle	Decrease or no effect	Minimal effect with complete wetting, but substantial decrease if film breakdown occurs	(Chang and Chiou, 1999; Christians and Thome, 2012a; Habert and Thome, 2010a; Moeykens and Pate, 1995; Roques and Thome, 2007a)

2.4.1 <u>Flow Rate</u>

In the convective evaporation regime, several heat transfer coefficient trends have been observed with increasing flow rate. The heat transfer coefficient first increases, reaches a local maximum, then decreases to a local minima and begins increasing again. There is general agreement that the initial increase in heat transfer coefficient is due to reduced levels of dryout on the tube. Then, when the tube is fully wetted, this trend reverses as the laminar thin film becomes thicker, decreasing the heat transfer coefficient. The final increase in heat transfer coefficient as flow rate continues to rise has often been attributed to turbulence (Chyu, 1984; Fujita and Tsutsui, 1995b, 1998), although Brumfield and Theofanous (1976) noted that this turbulence may begin at different flow rates for the film and wave regions. However, several other studies have suggested that the dominant influence in this region is not turbulence, and should instead be attributed to the increasing importance of the thermal entrance region and a decrease of the developing boundary layer thickness (Lorenz and Yung, 1979; Putilin *et al.*, 1996; Rogers *et al.*, 1995).

These conflicting influences of flow rate on heat transfer coefficient have resulted in a number of trends being observed in experimental studies. Several groups have found that the heat transfer coefficient first decreases, and then begins increasing (Chyu, 1984; Chyu and Bergles, 1985, 1987; Conti, 1978; Fujita and Tsutsui, 1995b, 1996, 1998; Lee *et al.*, 2012; Liu and Yi, 2001). Meanwhile, other studies have only observed heat transfer coefficient increasing with flow rate (Mitrovic, 1986; Parken, 1975; Parken and Fletcher, 1982; Parken *et al.*, 1990; Putilin *et al.*, 1996; Rifert *et al.*, 1989; Rifert *et al.*, 1992; Tan *et al.*, 1990; Zeng *et al.*, 1995). Finally, Li *et al.* (2011a; 2010) observed the

heat transfer coefficient first increasing, and then decreasing. In addition, several studies have noted trends that do not agree with the above general descriptions. Owens (1978) observed that the heat transfer first decreased, but then remained approximately independent of flow rate for Reynolds numbers of 1000 to 10000. This was attributed to the increasing film thickness being offset by an increase in turbulence. Additional experiments have found that the heat transfer coefficient is almost independent of Reynolds number in the range considered (Chyu *et al.*, 1982; Liu, 1975; Liu *et al.*, 2002; Sabin and Poppendiek, 1978), or that the trend is insignificant enough to be neglected.

Although these differing trends may be attributed to the fluid properties and flow rates being examined in each study, it should also be noted that characteristics of the experimental approach could be responsible for some of these findings. For instance, some liquid feeding mechanisms may not have uniform performance across the full range of flow rates being examined, leading to maldistribution of the fluid or modifying the impact region or waviness of the film. Similarly, in experiments relying on electrical heating with the surface temperature being measured by thermocouples, the thermocouple placement could influence these trends. If all of the thermocouples are at a single location along the length of the tube, the experiment would not capture the influence of dryout accurately.

Under boiling conditions, dryout still has a detrimental effect on heat transfer coefficient at low flow rates. At flow rates high enough to maintain full wetting, two primary trends have been observed. Several studies have observed no influence of flow rate on heat transfer coefficient (Chyu and Bergles, 1985, 1987; Habert and Thome, 2010a; Moeykens, 1994; Moeykens and Pate, 1994; Roques and Thome, 2007a; Zeng *et*

al., 1995), although Habert and Thome (2010a) found that it can cause scatter in the data due to droplet/column deflection or splashing. Meanwhile, other experiments have found that heat transfer coefficient increases as flow rate increases (Chien and Chen, 2012; Chien and Tsai, 2011; He *et al.*, 2011; Parken, 1975; Parken *et al.*, 1990; Yang and Shen, 2008). These conflicting trends may be due to the continued influence of convection heat transfer on tubes with boiling. Flow rate does not appear to influence heat transfer coefficient in areas where nucleate boiling occurs, but if boiling does not occur across the entire tube surface, the overall heat transfer coefficient will still be impacted by flow rate due to the convective effects discussed above.

2.4.2   <u>Dryout</u>

Dryout, where portions of the tube are not fully wetted, causes substantially lower local heat transfer coefficients that lead to lower overall heat transfer coefficients. In situations with convective evaporation, the formation of dryout appears to be related to the thickness of the film, while dryout may be caused by dry areas forming underneath bubbles during boiling conditions (Roques and Thome, 2007b). Gross (1994) found that in cases without boiling, the formation of dryout was influenced by liquid inertial forces, surface tension forces, the Marangoni effect, vapor inertial forces, and interfacial shear stress. Liquid inertial forces encourage rewetting of dry patches, while surface tension forces, the Marangoni effect, and vapor inertial forces tend to increase dryout. Interfacial shear stress can potentially lead to either situation, as it promotes rewetting of the leading edge of dry areas but also acts to extend dryout at the trailing edge. Several experimental studies have also observed that there are distinct conditions at which unstable dry patches

are first created, and the conditions at which dry patches become permanent (Fujita and Ueda, 1978; Ganić and Getachew, 1986).

There is widespread agreement that the onset of dryout can be reached by reducing flow rate or increasing heat flux (Armbruster and Mitrovic, 1995; Christians, 2010; Christians and Thome, 2012a; Fujita and Tsutsui, 1998; Habert, 2009; Habert and Thome, 2010a; Roques, 2004; Roques and Thome, 2007a), although in conditions without boiling, Li *et al.* (2011a; 2011b; 2010) found that the onset of dryout occurred at a set Reynolds number. Several studies have recommended empirical correlations of the form

$$Re = a_0 + a_1 q''^{a_2} \tag{2.17}$$

for both evaporation and boiling conditions (Fujita and Tsutsui, 1998; Roques and Thome, 2007b). Additional studies have recommended modifying this form to include the influence of fluid properties such as density, viscosity, and the latent heat of vaporization, as well as the tube diameter or a tube surface parameter (Christians and Thome, 2012a, 2012b; Habert and Thome, 2010b; Ribatski and Thome, 2007). In addition to these influences on dryout formation, Ganić and Roppo (1980) found that tube spacing impacts the onset of dryout, and Sabin and Poppendiek (1978) observed significant dryout during startup, with full wetting only being achieved after 500 minutes of operation. The presence of dryout during startup was not noted by other studies, although many studies include a substantial startup time at high flow rate to reach steady-state conditions. More theoretical approaches that either examine a force balance on a dry patch stagnation point or a minimum film thickness have been proposed, but are typically limited in their predictive capabilities in many actual applications because such an

analysis requires knowledge of the contact angle and other factors that are not readily available (Bohn and Davis, 1993; El-Genk and Saber, 2001; Hartley and Murgatroyd, 1964).

In addition to directly lowering the heat transfer coefficient, dryout can also adversely affect liquid flow. Conti (1978) and Sabin and Poppendiek (1978) observed that under dryout conditions the fluid ran as rivulets that coalesced and overshot the bottom of the tube, leaving off the side of the tube and potentially not impacting tubes below. Meanwhile, Yung *et al*. (1980) noted that there is less splashing off of tubes when they are fully wetted. More generally, it may be said that dryout leads to additional film breakdown on lower tubes in an array, further decreasing the heat transfer performance of the overall tube array.

2.4.3 <u>Heat Flux</u>

During convective evaporation conditions, there is wide agreement that heat flux does not affect the heat transfer coefficient (Conti, 1978; Fujita and Tsutsui, 1995b, 1996, 1998; Li *et al.*, 2011b; Liu and Yi, 2001, 2002; Liu *et al.*, 2002; Owens, 1978; Parken, 1975; Parken and Fletcher, 1982; Parken *et al.*, 1990). Under these conditions, where heat is transferred through the film via conduction and convection, causing evaporation at the film surface, there is no mechanism for heat flux to increase heat transfer coefficient. However, during boiling conditions, there is similar agreement that the heat transfer coefficient increases as the heat flux increases (Chien and Chen, 2012; Chien and Tsai, 2011; Fletcher *et al.*, 1974; Fletcher *et al.*, 1975; Habert, 2009; Habert and Thome, 2010a; He *et al.*, 2011; Liu and Yi, 2001, 2002; Moeykens, 1994; Moeykens and Pate, 1994; Parken, 1975; Parken *et al.*, 1990; Roques, 2004; Roques and Thome, 2007a; Yang

and Shen, 2008; Zeng *et al.*, 1995), although the opposite trend has been observed for some enhanced tube designs (Habert and Thome, 2010a; Roques and Thome, 2007a). This is attributed to an increased nucleation site density and boiling occurring over a larger portion of the tube surface due to the increased film temperature. This is consistent with the observations of Parken *et al.* (1975; 1990), who found that at low heat fluxes, bubble generation takes place near the bottom of the tube, but as heat flux is increased, the location shifts higher on the tube.

It should be noted that high levels of heat flux will cause dryout, which supersedes both of the above trends and drastically decreases the overall heat transfer coefficient. In convective conditions, Li *et al.* (2011b) found that at low Reynolds numbers, high heat fluxes evaporated enough liquid to make dry patches appear, decreasing the overall heat transfer coefficient. Similarly, Chien and Chen (2012) noted that under boiling conditions, high heat fluxes only increase the heat transfer coefficient until the critical heat flux is reached, after which dry patches appear and the heat transfer coefficient decreases.

2.4.4 <u>Temperature</u>

Under convective evaporation conditions, the heat transfer coefficient increases as saturation temperature increases (Kocamustafaogullari and Chen, 1988; Liu, 1975; Owens, 1978; Parken, 1975; Parken and Fletcher, 1982; Parken *et al.*, 1990). This is generally attributed to the liquid viscosity decreasing with increasing temperature, which decreases the thickness of the film. However, in tests with water at subatmospheric pressures and Reynolds numbers of 10 to 100, Li *et al.* (2011a; 2010) observed that the heat transfer coefficient first decreased sharply with temperature before increasing. They

suggested that this was due to either sensible heating of the fluid, or a decreased temperature difference between the fluid and heating source, increasing the thickness of the film.

Under boiling conditions, the heat transfer coefficient generally increases as saturation temperature increases (Chien and Chen, 2012; Chien and Tsai, 2011; Fletcher *et al.*, 1974; Fletcher *et al.*, 1975; Parken, 1975; Zeng *et al.*, 1995). The increasing temperature reduces viscosity and thus film thickness, and can increase the bubble nucleation site density, both of which increase the heat transfer coefficient. However, higher temperatures can also slow bubble growth because the reduced film thickness requires a steeper temperature profile (Cerza and Sernas, 1985), which reduces the heat transfer coefficient. In addition, several studies have noted a relationship between tube diameter and the influence of temperature on heat transfer coefficient. Fletcher *et al.* (1974; 1975) found that heat transfer coefficients increased with temperature for tubes with a 25.4 mm diameter, but did not do so for tubes with a 50.8 mm diameter. In addition, they noted that at low temperatures, the nucleation frequency was low and bubbles grew quickly, while at higher temperatures the bubbles were smaller with a higher frequency. Parken *et al.* (1990) observed that with water films on 25.4 mm tubes, the saturation temperature did not impact the heat transfer coefficient below 100°C, but increased the heat transfer slightly above this temperature. Meanwhile, with 50.8 mm diameter tubes, the heat transfer coefficient increased up to 100°C, and then decreased. They attributed this to a lower heat flux generating fewer bubble nucleation sites.

2.4.5 <u>Liquid Distributor Height and Tube Spacing</u>

The effects of increasing the liquid distributor height or tube spacing are generally similar, as they both increase the impingement velocity on the tubes below. Under convective evaporation conditions, the heat transfer coefficient increases as either the liquid distributor height or tube spacing increases (Chyu, 1984; Chyu and Bergles, 1985, 1987; Liu, 1975; Mitrovic, 1986; Parken, 1975). This is attributed to a higher heat transfer coefficient in the impact region, as well as possibly due to a larger developing flow region or increasing film waviness. Depending on the conditions, studies have found that this increase can be limited to the impact region (Parken, 1975) or extend around the whole tube perimeter (Liu, 1975; Mitrovic, 1986). In addition, Mitrovic (1986) found that this influence was minimal at low flow rates, but more substantial at high flow rates. Other studies (Liu and Yi, 2002; Liu *et al.*, 2002) have found that this impact is relatively minimal, and considered it secondary to the other influences on heat transfer coefficient. In addition, it has been noted that increasing liquid distributor height or tube spacing will eventually lead to significant fluid loss due to splashing and other phenomena, which can cause film breakdown and much lower heat transfer coefficients (Liu and Yi, 2002).

Under boiling conditions, the liquid distributor height and tube spacing are found to have a weak effect on heat transfer coefficient (Chyu, 1984; Chyu and Bergles, 1985, 1987; Danilova *et al.*, 1976; Roques and Thome, 2007b; Yang and Shen, 2008; Zeng *et al.*, 1995). In different studies, increasing spacing was observed to cause the heat transfer coefficient to increase slightly (Yang and Shen, 2008), decrease slightly (Roques and Thome, 2007b), or to have no impact (Danilova *et al.*, 1976). This is generally attributed to the nucleate boiling phenomena having a much larger influence on the heat transfer

coefficients (Chyu, 1984). However, as in cases with evaporation conditions, increasing the tube spacing or liquid distributor height beyond a certain point results in substantial dryout and very low heat transfer coefficients (Yang and Shen, 2008).

2.4.6   <u>Angle Around Tube</u>

For both convective and boiling conditions with sensible heat transfer or evaporative conditions, the highest heat transfer coefficients are found at the top of the tube (Hu and Jacobi, 1996b; Mitrovic, 1986; Parken and Fletcher, 1982; Parken *et al.*, 1990; Putilin *et al.*, 1996; Rifert *et al.*, 1989; Rifert *et al.*, 1992; Rogers and Goindi, 1989; Tan *et al.*, 1990). This is the case in the droplet, jet, and sheet flow modes, although the droplet and jet modes exhibit higher axial variation than the sheet mode (Hu and Jacobi, 1996b). This is attributed to the fluid impinging on the tube and the resulting film agitation, as well as thermal boundary layer growth, with the heat transfer coefficient being enhanced by a factor of approximately 2 to 10 times the lowest point on the tube. Under convective conditions, as the angle around the tube increases, the heat transfer coefficient decreases due to the reduction in film agitation, and thermal boundary layer growth. Several authors observed the heat transfer coefficient continuously decreasing to the bottom of the tube (Parken and Fletcher, 1982; Parken *et al.*, 1990; Tan *et al.*, 1990). However, other investigators noted that a local maxima was observed at the bottom of the tube (Mitrovic, 1986; Parken and Fletcher, 1982; Parken *et al.*, 1990; Putilin *et al.*, 1996; Rifert *et al.*, 1989; Rifert *et al.*, 1992), and Rogers and Goindi (1989) observed a second local maxima at approximately 90 degrees around the tube. Parken and Fletcher (1982) and Parken *et al.* (1990) studied two tube diameters, and observed that with 25.4 mm diameter tubes, the heat transfer coefficient decreased with angle, while with 50.8 mm

diameter tubes, the second local maxima was observed at the bottom of the tube. This second local maxima, where present, is typically attributed to the fluid behavior near the breakaway region of the film. Under some conditions, this appears to enhance the heat transfer coefficient of the region, while in other studies it has a minimal effect. In addition, Tan *et al.* (1990) included a study of two enhanced tube designs with porous surfaces, and observed that they exhibited a local maxima at the bottom of the tube, although they did not see this behavior with smooth tubes. Under boiling conditions, the heat transfer coefficient decreases until approximately 45 degrees, after which it is relatively uniform with random fluctuations (Parken *et al.*, 1990). Most of these measurements are taken using a single tube instrumented with multiple thermocouples at various angles around the tube. Alternatively, fewer measurement sites have also been used with the tube rotated at each test condition (Mitrovic, 1986).

2.4.7   **Tube Diameter**

Under convective evaporation conditions, the heat transfer coefficient increases as tube diameter decreases (Liu and Zhu, 2005; Parken, 1975; Parken and Fletcher, 1982; Parken *et al.*, 1990). The highest local heat transfer coefficients are located at the top of the tube, as described in Section 2.4.6, and decrease as the distance from this point increases. As tube diameter increases, these locally high heat transfer coefficients apply to a smaller percentage of the total tube area. However, Liu *et al.* (2002) did not observe this trend in their experiments. They suggested that increased splashing losses at lower tube diameters offset the expected increase in heat transfer coefficient, resulting in a minimal net effect.

Under boiling conditions, the heat transfer coefficient has been observed to either increase or decrease as tube diameter increases. Parken *et al.* (1975; 1990) found that the heat transfer coefficient increases as tube diameter increases. They suggested that this was due to the percentage of surface area with superheated fluid appropriate for bubble nucleation. Superheating the fluid to an appropriate level will take a given flow length, so larger tubes have a larger portion of the tube surface area with bubble nucleation and higher local heat transfer coefficients. Meanwhile, several studies (Fletcher *et al.*, 1974; Moeykens, 1994; Moeykens and Pate, 1994) have observed a contrary trend, with the heat transfer coefficient decreasing as diameter increases. Ribatski and Jacobi (2005) suggested that the contrary observations noted above were due to the relative values of the local heat transfer coefficients in the boiling region compared to the other regions of the tube. In situations where the boiling heat transfer coefficients are lower, better heat transfer performance would be observed at smaller tube diameters.

2.4.8   Vapor Flow

Vapor flow can be directed either co-current, counter-current, or in cross-flow with respect to the liquid film. With each situation, it has the potential to either increase or decrease the heat transfer coefficient. The heat transfer coefficient could be increased by enhanced film waviness or reduced film thickness, but could be reduced by thicker films, liquid entrainment or deflection, or detrimental impacts of dryout (Garcia *et al.*, 1992; Ribatski and Jacobi, 2005). Under evaporation conditions, Liu (1975) found that the heat transfer coefficient would increase with co-current vapor flow, but would decrease with a countercurrent flow due to an increased film thickness. However, the heat transfer coefficient enhancement was relatively minimal. Parken (1975) also observed an

increase in heat transfer coefficient for boiling conditions with co-current vapor flow, despite reduced visible bubble nucleation, which was attributed to reduced film thickness. Yung *et al.* (1980) examined two potential negative impacts of vapor cross-flow, droplet and column deflection and liquid entrainment, and developed guidelines to avoid significant deflection in component designs. They found that the conditions necessary to prevent significant droplet and column deflection were also sufficient to prevent liquid entrainment. In addition, tests with subcooled falling films have found that increasing air velocities has a substantial impact on the flow mode (Ruan *et al.*, 2009; Wei and Jacobi, 2002). Increasing air velocity decreases the hysteresis between flow modes, and eventually results in unsteadiness.

2.4.9 <u>Tube Surface Enhancement</u>

A wide variety of enhanced tube surfaces have been used to increase heat transfer coefficients in the evaporation and boiling regimes. In the convective regime, surface enhancements have several potential mechanisms for increasing heat transfer: increasing surface area, increasing fluid coverage of the tube, reducing film thickness, impacting boundary layer development or other characteristics of the flow velocity profile, and enhancing film waviness or turbulence. This has been achieved with longitudinal fins or grooves, circumferential fins, helical fins, corrugated surfaces, knurling, and other methods. In the boiling regime, the primary goal is typically to provide a large number of nucleation sites for boiling, although the flow may also benefit from the same mechanisms that enhance convective heat transfer listed above. This is often achieved with porous coatings or other arrangements that provide surface cavities.

Under convective evaporation conditions, tubes with structured surfaces have demonstrated heat transfer coefficient enhancement of up to six times that of flow on plain tubes. Sabin and Poppendiek (1978) found that nickel-plated surfaces and Linde Hi-Flux tubes improved heat transfer by up to two times the performance of a smooth tube, partially due to improved surface wetting. Meanwhile, Rifert *et al.* (1989; 1992) and Putilin *et al.* (1996) found that longitudinal grooves and fins with rectangular, triangular, and circular cross-sections can increase heat transfer coefficients by a factor of 1.3 to 1.9. Local temperature measurements suggested that this was due to their impact on boundary layer development, but did not trip turbulence. Liu and Yi (2001, 2002) observed similar enhancement of 1.5 times with finned tubes, while roll-worked tubes offered up to three times enhancement over smooth tubes. They attributed the finned tube enhancement to increased surface area and surface tension effects at the solid-liquid interface. Roll-worked tubes induced limited bubble nucleation at low heat fluxes, which they suggested would interrupt the boundary layer, leading to the additional enhancement. Li *et al.* (2011b) suggested that the enhancement for finned tubes is highest at low Reynolds numbers, where the enhanced tubes help spread the film. When fully wet, the enhanced features are fully covered by film and are less advantageous. They observed enhancement of up to six times on finned tubes, while helically finned tubes offered enhancements of up to 2.5, and corrugated copper tubes offered enhancements of up to 1.7. Lee *et al.* (2012) also observed the highest enhancement at low flow rates due to the wetting characteristics, suggesting that it was aided by capillary action. Studies have also investigated brass or copper meshes wrapped around a finned tube, finding enhancement of up to four times (Chien and Chen, 2012; Chien and Tsai, 2011). However, not all

surface structures improve the heat transfer performance of the tube. Sabin and Poppendiek (1978) observed that knurled surfaces improve surface wetting, but do not increase the heat transfer coefficient due to an increased film thickness, and turned and burnished surfaces have poor performance due to trapped vapor. Meanwhile, other tubes with fin and groove structures can result in pockets of stagnant fluid, which have a detrimental effect on heat transfer (Putilin *et al.*, 1996).

Under boiling conditions, tubes with structured surfaces have demonstrated heat transfer coefficients of over 10 times those for flow over plain tubes. Bukin *et al.* (1982) tested nine types of porous tubes and three types of glass and stainless steel cloth wrappings with R12 and R22, with the goal of providing nucleation sites. They observed maximum heat transfer coefficient enhancement of three to five times compared to smooth tubes, and found that there is an optimal thickness for each type of porous coating, which appears to be related to new liquid being prevented from reaching the inner layers. Chyu *et al.* (1982) and Chyu and Bergles (1989) observed enhancement of up to eight times with Gewa-T tubes, which have a deformed low-fin surface, and five times enhancement with Thermoexcel-E tubes, which have a tunnel-pore surface. Lower levels of enhancement were observed for High Flux tubes, with a porous metallic matrix, but they noted that the matrix was not sized correctly for the working fluid. In addition, they noted two concerns for enhanced tube designs: that modifying heat flux quickly can reduce the number of active nucleation sites, and that fouling degrades the performance of structured surfaces over time, and it may be challenging to clean many of the porous structures. Further studies with porous tubes have observed enhancement of up to seven times compared to plain tubes (Tan *et al.*, 1990), while low-finned tubes with spray

feeding have shown enhancement of less than three times plain tubes (Zeng *et al.*, 1998). Moeykens *et al.* (1995a) compared the performance of enhanced condensation and boiling tubes, finding that the enhanced condensation tubes actually offered better enhancement, up to four times that of plain tubes, compared to three times for the boiling tube designs. In addition, mixing a lubricant with the fluid further enhanced heat transfer by up to 1.8 times, although it was visually observed that this led to foaming. However, tests with R-134a and R-236fa found that enhanced boiling tube designs outperform enhanced condensation tubes, with enhancement of up to over 10 times compared to plain tubes (Christians and Thome, 2012a; Habert and Thome, 2010a; Roques and Thome, 2007a). Generally, the highest enhancement was observed for low heat fluxes, which may be because the heat transfer coefficients for enhanced tube designs have a weaker dependence on heat flux. Comparisons were also made to pool boiling heat transfer coefficients for several tube designs, indicating that falling-film evaporation outperformed pool boiling by up to 2.5 times (Christians and Thome, 2012a). High levels of enhancement have also been observed with meshes wrapped around finned surfaces, generating enhancement of three to eight times over plain tubes (Chien and Chen, 2012; Chien and Tsai, 2011).

2.4.10 **Tube Bundles**

Most of the studies discussed above were conducted with a single heat transfer tube or a single column of tubes. However, in practical applications, a tube bundle is commonly used. A number of studies have examined the performance of tube bundles using plain and enhanced tubes in square and triangular pitch arrangements, generally

finding that bundle effects reduce heat transfer performance. A summary of these configurations is provided in Table 2.4.

Under conditions with complete wetting, several studies have observed minimal differences between single tube and bundle heat transfer coefficients for both convective evaporation and boiling conditions (Christians and Thome, 2012a; Lorenz and Yung, 1982; Roques and Thome, 2007a). However, others studies have observed lower heat transfer performance in tube bundles. This is attributed to the distribution method and film-flow characteristics, with film breakdown often being the dominant influence.

Film breakdown refers to poor tube wetting caused by a low flow rate, high heat flux, poor liquid distribution, or other phenomena. This substantially reduces the heat transfer coefficients in tube bundles (Chang and Chiou, 1999; Fujita and Tsutsui, 1998; Habert and Thome, 2010a; Lorenz and Yung, 1982; Moeykens and Pate, 1995; Zeng *et al.*, 1997). Film breakdown on one tube leads to adverse fluid flow on the tube below, causing bundle depth to increase the degree of dryout. For instance, Fujita and Tsutsui (1998) observed that, with full wetting on the top tube of a five tube array, wetting was reduced to ~90% on the second tube, and was progressively reduced on subsequent tubes to below 50% wetting on the fifth tube. Due to this effect, as well as possible tube misalignments and the impact of vapor flow, Lorenz and Yung (1982) found that a large array with 3000 tubes reached the film breakdown region at substantially higher Reynolds numbers than single tube tests. Alternatively, they suggested that this could be due to measurement methodologies. Single tube tests often rely on thermocouple measurements at a single point along the length of the tube, and thus would not capture the onset of film breakdown accurately if the thermocouples are located in a wetted

region of the tube. Habert and Thome (2010a) observed that film breakdown could also occur at high film Reynolds numbers. They observed that R-134a and R-236fa heat transfer coefficients first increased with Reynolds number, reached a maximum, and then decreased. This was attributed to a significant portion of the liquid traveling without contacting the surface, which may be due to splashing, transfer between tubes, or nucleate boiling causing the flow to travel as a two-phase bubbly layer. Moeykens and Pate (1995) found that triangular-pitch tube arrangements may have poor wetting characteristics compared to square-pitch bundles due to the liquid leaving a tube not impacting the center of the tube below. This leads to better wetting, and thus heat transfer performance, on tubes that are vertically in-line with the top row of tubes. However, in a subsequent study, Moeykens *et al.* (1995b) found that triangular-pitch arrangements are only more susceptible to dryout due to flow rate variation, but have better performance than square-pitch designs at high heat fluxes.

The liquid distribution method influences the impact characteristics of the fluid on the top tube and determines the fluid distribution characteristics on the bundle. Spray distributors generate high local heat transfer coefficients on the top tube (Chang and Chiou, 1999; Moeykens, 1994; Moeykens and Pate, 1995; Zeng *et al.*, 2001a, 2001b; Zeng *et al.*, 1997), but may lead to a portion of the inlet fluid not impacting the test tubes. Moeykens and Pate (1995) found that for a single flow rate, 54 to 77% of the liquid leaving the nozzle impacted the test tubes, with the variation depending on nozzle design. Increasing spray nozzle height or distributing over wider angles reduces this impact effect and may also result in worse overall flow distribution in the bundle (Zeng *et al.*, 2001a, 2001b). In addition, tubes in the top row not directly below the spray tube often have

lower heat transfer coefficients (Zeng *et al.*, 1997), which can be attributed to both the smaller impact area and lower degree of liquid coverage. Experiments with three low-momentum distributor designs, including a porous tube, tube with small holes, and plate with small holes, found that the distributor can also lead to heat transfer coefficients approximately 10 to 20% lower than subsequent tubes (Fujita and Tsutsui, 1998). Spray distributors have also been interspersed in the tube bundle to increase heat transfer performance. Tatara and Payvar (2001) found that including two spray distributors in a bundle of 36 triangular-pitch tubes, with the top row fed by tubes with an array of holes, can improve heat transfer performance. Under some conditions, the lower tube rows actually have higher heat transfer performance, with the performance of the overall tube bundle depending on the vapor mass flux. Chang *et al.* (2011; 2009) examined configurations with internal spray distributors using one spray tube per three heated tubes and one spray tube for each heated tube, and observed substantially reduced levels of dryout with both arrangements relative to a distribution system with no internal spray tubes.

Enhanced tube surfaces can reduce the heat transfer performance penalty of tube bundles by increasing film spreading, which reduces film thickness and leads to lower levels of film breakdown. In tests with R-134a, Moeykens *et al.* (1995b) found that a Turbo-B enhanced boiling tube had improved heat transfer relative to plain tubes, and a Turbo-CII enhanced condensation surface further improved performance, and actually delivered higher heat transfer coefficients on the second tube row, rather than the top row. However, this relationship was reversed with R-123, with the Turbo-B surface outperforming the Turbo-CII tube (Moeykens *et al.*, 1996). Thome (1999) suggested that

this was due to the different mechanisms each tube relies on to promote film coverage, which would be impacted by the increased surface tension of R-123. Meanwhile, finned tubes prevent longitudinal film spread and can lead to higher levels of film breakdown (Moeykens *et al.*, 1995b). Habert and Thome (2010a) and Christians and Thome (2012a) also observed that enhanced boiling tubes may aid in preventing film breakdown at high Reynolds numbers. Tests with R-134a and R-236fa found decreased heat transfer performance at high Reynolds numbers for plain tubes and an enhanced condensation tube (Gewa-C+LW), while enhanced boiling tubes (Gewa-B4, Gewa-B5, and Turbo-B5) did not encounter a similar decrease.

Studies have also proposed improving the wetting characteristics of tube bundles using oil additives and liquid collectors beneath the tubes. Moeykens and Pate (1996) found that adding a mass fraction of 1 to 2.5% of polyol-ester oil to R-134a or alkyl-benzene oil to R-22 increased the bundle heat transfer performance. A similar improvement was noted for enhanced tube surfaces, with the exception of enhanced boiling tubes at high heat fluxes, which actually had lower heat transfer performance. Tests with R-123 and mineral oil found similar trends (Moeykens *et al.*, 1996). This was attributed to the oil additives causing foaming and increasing film tube coverage, although improvement was also noted in situations without foaming. Thome (1999) suggested that the degradation of heat transfer coefficient at high heat fluxes may be attributed to the mass transfer resistance introduced by the oil additive. Chang and Chiou (1999) found that film wetting could also be improved by liquid collectors, which are small curved plates placed slightly below the bottom half of each tube. They are intended to ensure wetting on the bottom half of each tube and redistribute the flow in triangular-

pitch bundles. Further experiments considered additional liquid collector spacings (Chang and Chiou, 2005) and demonstrated improved performance with finned tubes (Chang, 2006).

Table 2.4. Summary of tube bundle configurations

Study	Fluid	Tube Surface	Bundle Design (rows × columns)
Danilova *et al.* (1976)	R-12, R-22, R-113	Plain	5 × 1, 5 × 3, and up to 40 rows of triangular pitch tubes with 2 columns
Semiat *et al.* (1978)	Water	Plain and Enhanced	5 × 3, square pitch
Lorenz and Yung (1982)	Ammonia	Plain	30 × 100, triangular pitch
Moeykens (1994)	R-134a	Plain and Enhanced	4 × 5, triangular pitch, 1 column adiabatic
Moeykens and Pate (1995)	R-134a	Enhanced	4 × 5, triangular pitch, 1 column adiabatic
Moeykens *et al.* (1995b)	R-134a	Plain and Enhanced	4 × 5, triangular and square pitch, 1 column adiabatic
Moeykens *et al.* (1996)	R-123 with oil additive	Plain and Enhanced	4 × 5, triangular and square pitch, 1 column adiabatic
Moeykens and Pate (1996)	R-134a and R-22 with oil additive	Plain and Enhanced	4 × 5, triangular pitch, 1 column adiabatic
Zeng *et al.* (1997)	Ammonia	Plain	3 × 3, square pitch
Fujita and Tsutsui (1998)	R-11	Plain	5 × 1, square pitch
Chang and Chiou (1999)	R-141b	Enhanced	3-2 triangular pitch
Tatara and Payvar (2001)	R-11	Enhanced	5 × 8, triangular pitch with 2 spray tubes in bundle
Zeng *et al.* (2001a, 2001b)	Ammonia	Plain	3-2-3 triangular pitch
Chang and Chiou (2005)	R-141b	Enhanced	2-3-2 triangular pitch
Chang (2006)	R-141b	Enhanced	3-2 triangular pitch
Roques and Thome (2007a)	R-134a	Plain and Enhanced	6 × 1 to 10 × 1 square pitch
Chang *et al.* (2009)	R-141b	Plain	3-4-5-4-3 triangular pitch, 6 heated tubes with 7 spray tubes
Habert and Thome (2010a)	R-134a, R-236fa	Plain and Enhanced	10 × 1 square pitch, 10 × 3 triangular pitch
Chang *et al.* (2011)	R-141b	Plain	2 × 2 square pitch of heated tubes with 3 × 3 square pitch of spray tubes
Christians and Thome (2012a)	R-134a, R-236fa	Enhanced	10 × 1 square pitch, 10 × 3 triangular pitch

Table 2.5 Summary of experimental heat transfer studies

Author	Fluid	Tube Material	d [mm]	H [mm]	s [mm]	$\Gamma \times 10^3$ [kg m^{-1} s^{-1}]	T [°C]	q'' [kW m^{-2}]	Surface
Water Studies									
Fletcher *et al.* (1974; 1975)	Water, Sea Water	Copper-Nickel	25.4, 50.8	-	-	0–314	49–127	0–63	Plain, Enhanced
Liu (1975)	Water	Stainless Steel	25.4, 50.8	8–54	-	144–377	55–100	19–76	Plain
Parken (1975), Parken and Fletcher (1982)	Water	Brass	25.4, 50.8	3.2	-	133–373	45–127	16–79	Plain
Danilova *et al.* (1976)	R-12, R-22, R-113	Stainless Steel	18	1.8–21.6	1.8–21.6	7-167	-40–50	0.5–25	Plain
Semiat *et al.* (1978)	Water	Aluminum	19	-	-	61–364	70	-	Plain
Ganić and Roppo (1980)	Water	Copper	25.4	25.4, 50.8	-	4–40	27, 50	0–83	Plain
Chyu *et al.* (1982), Chyu (1984), Chyu and Bergles (1985)	Water	Copper	5.4	3–63.5	-	14–156	99	1–208	Plain, Enhanced
Ganić and Gatechew (1986)	Water, Ethyl Alcohol	Copper	25.4	25.4, 50.8	-	3–50	57	0–80	Enhanced
Mitrovic (1986)	Water, Isopropyl Alcohol	Copper	18	4.5–87	-	38–130	22, 25	9, 18	Plain
Chyu and Bergles (1987; 1989)	Water	Copper	25.4	3–63.5	-	21–156	99	2–208	Plain, Enhanced
Rifert *et al.* (1989)	Water	-	38	-	-	40–400	40–100	15–75	Enhanced
Rogers and Goindi (1989)	Water	Aluminum	132	-	-	-	17–50	71–158	Plain
Parken *et al.* (1990)	Water	Brass	25.4, 50.8	6.3	-	135–366	49–127	30–80	Plain
Rifert *et al.* (1992)	Water	Constantan	38	-	10–20	80–400	100	10	Enhanced

Table 2.5. Summary of experimental heat transfer studies (continued)

Author	Fluid	Tube Material	d [mm]	H [mm]	s [mm]	$\Gamma \times 10^3$ [kg m^{-1} s^{-1}]	T [°C]	q" [kW m^{-2}]	Surface
Armbruster and Mitrovic (1995, 1998)	Water, Isopropyl Alcohol	Copper	19.5	2–49	-	5–150	9–50	0–150	Plain
Hu (1995), Hu and Jacobi (1996b)	Water, Ethylene Glycol, Glycol/Water, Glycol/Water/ Ethyl Alcohol	Brass	9.5–22.2	0–100	-	0–360	25–40	0–115	Plain
Putilin *et al.* (1996)	Water	Constantan Foil	38	10–20	-	40–400	42–100	15–75	Enhanced
Liu and Yi (2001, 2002)	Water, Water/Salt, R-11	Copper	18	6	3–18	15–354	24, 99	2–500	Enhanced
Liu *et al*. (2002)	Water	Copper	13–30	6	10, 13	32–353	99	40–60	Plain
Liu and Zhu (2005)	Water	Stainless Steel	13–30	5	-	32–353	20–90	40	Plain
Yang and Shen (2008)	Water	Aluminum-Brass	14	5–13	7	13–62	50	15–55	Plain
Wang *et al.* (2011)	Water	Aluminum	3.2 × 25.4	2	9.6, 14.5	0–145	18	10–18	Plain
Li *et al.* (2010)	Water	Copper	15.9	25.4	9.5	4–39	7	0–25	Plain, Enhanced
He *et al.* (2011)	Water	Brass	25.4	2	31.8	10–60	58, 61	10–50	Plain
Lee *et al.* (2012)	Water	Copper	15.9	19.7	19.7	5–26	71	-	Plain, Enhanced
Ammonia Studies									
Conti (1978)	Ammonia	Stainless Steel	50.8	-	-	4–202	22	5–16	Enhanced

Table 2.5. Summary of experimental heat transfer studies (continued)

Author	Fluid	Tube Material	d [mm]	H [mm]	s [mm]	$\Gamma \times 10^3$ [kg m^{-1} s^{-1}]	T [°C]	q'' [kW m^{-2}]	Surface
Sabin and Poppendiek (1978)	Ammonia	Steel	25.4	25.4	-	4–37	13–24	3–25	Enhanced
Owens (1978)	Ammonia	Stainless Steel	50.8	50.8	-	4–350	22	5–16	Plain
Lorenz and Yung (1982)	Ammonia	Titanium	25.4	-	6.4	2–68	22.2	-	Plain
Zeng *et al.* (1995; 1998)	Ammonia	Stainless Steel	19.1	51, 102	-	7–39	-23–10	8–80	Plain, Enhanced
Zeng *et al.* (2001a, 2001b; 1997)	Ammonia	Stainless Steel	19.1	0–150	4.8	35–380	-23–10	3–35	Plain
Synthetic Refrigerant Studies									
Bukin *et al.* (1982)	R-12, R-22	Stainless Steel, Copper	20	-	22–44	19–184	-40–0	–25	Enhanced
Kuwahara *et al.* (1990)	R-11	Copper	18	20	-	8–91	24	1–43	Enhanced
Tan *et al.* (1990)	R-113	Copper	22	-	-	32–96	47	7–73	Enhanced
Moeykens (1994), Moeykens and Pate (1994)	R-134a	Copper	12.7, 19.1	-	-	5–6	-14, 2	5–40	Plain, Enhanced
Fujita and Tsutsui (1995b, 1996, 1998)	R-11	Copper	25	25	25	1–180	45	1–3	Plain
Fujita and Tsutsui (1998)	R-11	Copper	25	25	25	1–180	44.6	0.5–15	Plain
Chang and Chiou (2005; 1999), Chang (2006), Chang *et al.* (2011; 2009)	R-141b	Copper	19.1	-	5.2–20.9	45–60	20–28	10–200	Plain, Enhanced
Tatara and Payvar (2001)	R-11	Copper	19.1	0.2	0.2	-	4.4	5–28	Enhanced

Table 2.5. Summary of experimental heat transfer studies (continued)

Author	Fluid	Tube Material	d [mm]	H [mm]	s [mm]	$\Gamma \times 10^3$ [kg m^{-1} s^{-1}]	T [°C]	q'' [kW m^{-2}]	Surface
Roques (2004), Roques and Thome (2007a)	R-134a	Copper	19.1	-	3.4–6.6	0–187	5	20–60	Enhanced
Habert (2009), Habert and Thome (2010a)	R-134a, R-236fa	Copper	19.1	3.25	3.25	0–278	5	20–60	Plain, Enhanced
Christians (2010), Christians and Thome (2012a)	R-134a, R-236fa	Copper	19.1	3.2	3.2	20–300	5	20–60	Enhanced
Chien and Tsai (2011)	R-245fa	Copper	19	5	-	12–40	5, 20	3–49	Plain, Enhanced
Chien and Chen (2012)	R-134a	Copper	19	9.5	-	8–36	0, 26.7	5–49	Plain, Enhanced
Studies on Fluids with Additives									
Moeykens *et al.* (1995a)	R-134a / Polyol-ester	Copper	19.1	-	-	13	2	5–40	Enhanced
Moeykens *et al.* (1996)	R-123 with oil	Copper	18.9	44.3	0.2	-	2	19-40	Plain, Enhanced
Moeykens and Pate (1996)	R-134a and R-22 with oil	Copper	18.9	66.7	0.2	-	2	19-40	Plain, Enhanced
Ruan and Jacobi (2011)	Water with Nanoparticles	Copper	19.1	1	10	10–185	20–40	0–29	Enhanced
Ruan and Jacobi (2012)	Water and Ethylene Glycol with Nanotubes	Copper	19.1	-	-	10–150	20	-	Plain

2.5   Heat Transfer Models

This section reviews the empirical, analytical, and semi-analytical approaches used to predict falling-film evaporation heat transfer coefficients in prior studies. Some discussion of relevant studies on sensible heat transfer with subcooled fluid is also included.

2.5.1   Empirical Approaches

Empirical correlations have demonstrated good performance for a variety of fluids, tube surfaces, and test conditions. Generally, these approaches identify the dominant parameters influencing heat transfer and use those to select appropriate nondimensional parameters, or use a simplified analytical approach to develop a scaling relationship. They typically offer simple implementation, but each correlation is based on the collected data and may have poor performance outside of the conditions for which it was developed. This section focuses on empirical correlations used to predict falling-film evaporation heat transfer performance, although some subcooled single-phase falling-film heat transfer correlations are also included. These correlations and the corresponding source data are shown in Table 2.6.

The most widely used dimensionless parameters in empirical correlations are the Reynolds number (*Re*) and Prandtl number (*Pr*), and in the boiling regime, a nondimensionalized heat flux. Some studies have also achieved good agreement with data using the tube spacing, tube diameter, pressure or temperature, Archimedes number (*Ar*), Bond number (*Bo*), modified Galileo number (*Ga*), parameters unique to the tube surface characteristics, and several unique combinations accounting for fluid property effects, often incorporating surface tension or the latent heat of vaporization.

The formulation of an empirical correlation is often divided based on the dominant mechanisms influencing heat transfer. These divisions may require different empirical coefficients or nondimensional parameters. Almost all empirical correlations are subdivided based on the transition from the convective evaporation regime to the boiling regime (Danilova *et al.*, 1976; Owens, 1978; Parken *et al.*, 1990), although several recent studies have recommended approaches to combine correlations for each regime using superposition (Chien and Chen, 2012; Chien and Cheng, 2006; Chien and Tsai, 2011). Similarly, enhanced tube surfaces typically require unique empirical coefficients (Christians and Thome, 2012b; Habert and Thome, 2010b; Li *et al.*, 2011b; Li *et al.*, 2010; Putilin *et al.*, 1996; Rifert *et al.*, 1992; Roques and Thome, 2007b; Zeng *et al.*, 1998), which in some cases are structured to provide a ratio of enhanced to smooth tube performance (Li *et al.*, 2011b; Li *et al.*, 2010; Putilin *et al.*, 1996; Rifert *et al.*, 1992). Although many of these correlations require a unique equation for each tube surface, Christians and Thome (2012b) recently demonstrated good performance with an approach that only requires a single tube-specific parameter, which was provided for eight enhanced tubes. Finally, the heat transfer performance of tube bundles is typically correlated separately from that of single tubes (Fujita and Tsutsui, 1998; Habert and Thome, 2010b; Zeng *et al.*, 1997), and square-pitch bundles require separate coefficients than triangular-pitch bundles (Zeng *et al.*, 2001b; Zeng *et al.*, 1997).

In addition to these divisions, investigators have recommended additional subdivisions based on the tube or flow characteristics. In a widely used correlation based on vertical tubes, Chun and Seban (1971, 1972) recommended an empirical correlation split into the laminar, wavy-laminar, and turbulent regimes. Owens (1978) found good

performance using a similar approach, which split the flow into laminar and turbulent regimes, with horizontal tube data. Sernas (1979) provided correlations unique to each tube diameter with subcooled fluid, and Parken (1990) found good performance using a similar approach for both evaporative and boiling data. Using fits to numerical results, Chen and Kocamustafaogullari (1989) provided separate correlations based on the wall boundary condition having a constant heat flux or constant temperature. In tests with subcooled water, it has been demonstrated that local heat transfer coefficients can be empirically correlated separately for the developing thermal boundary layer and the developed region (Rogers and Goindi, 1989), or alternatively by providing separate correlations for the droplet, jet, and sheet modes (Hu and Jacobi, 1996b).

Empirical correlations have also captured the influence of partial dryout under evaporation and boiling conditions. These correlations must first predict the Reynolds number at which the onset of dryout occurs, and then the reduction in heat transfer performance due to dryout. Under evaporation conditions, Li *et al.* (2011a; 2011b) found that the onset of dryout occurs at a constant Reynolds number unique to each tube surface condition, while under boiling conditions, the onset of dryout appears to be a function of heat flux, fluid properties, and the tube surface condition (Christians and Thome, 2012b; Habert and Thome, 2010b; Ribatski and Thome, 2007; Roques and Thome, 2007b). With partial dryout present, several studies have found that the heat transfer coefficient decreases linearly with Reynolds number (Habert and Thome, 2010b; Roques and Thome, 2007b). Alternatively, good performance has been found correlating the heat transfer coefficient or Nusselt number with the Reynolds number raised to an empirical

exponent (Li *et al.*, 2011b; Ribatski and Thome, 2007), and Li *et al*. (2011a) developed separate equations for regions with complete wetting and separate dryout.

Table 2.6. Summary of empirical modeling studies

Study	Eqn.	Correlation	Notes
Chun and Seban (1971, 1972)	(2.18) (2.19) (2.20)	Laminar: $Nu = 1.101 Re^{-1/3}$ Wavy-laminar: $Nu = 0.822 Re^{-0.22}$ Turbulent: $Nu = 0.00381 Pr^{0.65} Re^{0.4}$	• Data: Water, Vertical Tube, Evaporative • Laminar: $Re < 2.44 Ga^{1/11}$ • Turbulent: $Re \geq 5800 Pr^{-1.06}$
Danilova *et al.* (1976)	(2.21) (2.22)	Evaporative: $Nu = 0.03 Re^{0.22} Pr^{0.32} (s/d)^{0.48} \left(\dfrac{q''}{i_{fg} \rho_v \nu} \left(\dfrac{\nu^2}{g} \right)^{1/3} \right)^{0.04}$ Boiling: $h = 0.00132 \, k \, Pr^{0.48} \left(\dfrac{q''}{i_{fg} \rho_v \nu} \left(\dfrac{\nu^2}{g} \right)^{1/3} \right)^{0.63} \left(\dfrac{P_{sat}}{\sigma} \right)^{0.72} \left(\dfrac{\sigma}{g(\rho - \rho_v)} \right)^{-0.14}$	• Data: R-12, R-22, R-113
Owens (1978)	(2.23) (2.24) (2.25)	Evaporative, Laminar: $Nu = 2.2(s/d)^{0.1} Re^{-1/3}$ Evaporative, Turbulent: $Nu = 0.185(s/d)^{0.1} Pr^{0.5}$ Boiling, Turbulent: $Nu = 0.0175 \, (s/d)^{0.1} q''^{0.25} Pr^{0.5}$	• Data: Ammonia and Water • Laminar: $Re < 1680 Pr^{-1.5}$
Sernas (1979)	(2.26) (2.27)	25 mm Diameter: $Nu = 0.01925 Re^{0.24} Pr^{0.66}$ 50 mm Diameter: $Nu = 0.01729 Re^{0.24} Pr^{0.66}$	• Data: Subcooled Water
Slesarenko (1979)	(2.28)	$Nu = 0.092 \left(\dfrac{q''}{i_{fg} \rho_v \nu} \left(\dfrac{\nu^2}{g} \right)^{1/3} \right)^{0.45} \left(\dfrac{s}{d} \right)^{0.2} Pr^{-0.1}$	• Data: Sea Water, Boiling
Mitrovic (1986)	(2.29)	$Nu = \dfrac{0.0137 Re^{0.349} Pr^{0.5} (s/d)^{0.158}}{1 + \exp(-0.0032 Re^{1.32})}$	• Data: Subcooled Water

Table 2.6. Summary of empirical modeling studies (continued)

Study	Eqn.	Correlation	Notes
Parken (1990)	(2.30)	Evaporative, 25.4 mm Diameter: $Nu = 0.042 Re^{0.15} Pr^{0.53}$	• Data: Water • Units: q'' in W m^{-2}
	(2.31)	Evaporative, 50.8 mm Diameter: $Nu = 0.038 Re^{0.15} Pr^{0.53}$	
	(2.32)	Boiling, 25.4 mm Diameter: $Nu = 0.00082 Re^{0.10} Pr^{0.65} q''^{\,0.4}$	
	(2.33)	Boiling, 50.8 mm Diameter: $Nu = 0.00094 Re^{0.10} Pr^{0.65} q''^{\,0.4}$	
Rifert *et al.* (1992), Putilin *et al.* (1996)	(2.34)	$h = 0.295\, k\, d^{-1} Re^{0.63} Pr^{0.36}$	• Data: Water, Evaporative • Correlations adjust result for fin or groove dimensions and spacing
	(2.35)	$h_{pr,0} = h \cdot 0.53 Re^{0.11} \left(f_w/f_d \right) \exp\left[-0.23 \left(f_w/f_d \right) \right]$	
	(2.36)	$h_{pr} = h_{pr,0} \cdot 1.33 \left(f_s/f_{s,0} \right)^{0.45} \exp\left[-0.31 \left(f_s/f_{s,0} \right) \right]$	
Chen and Kocamustafaogullari (1989)	(2.37)	Constant Heat Flux: $Nu = 0.143 Pr^{0.46} Re^{0.15} \left(\dfrac{d}{v^2/g} \right)^{-0.2} \left(\dfrac{2s}{v^2/g} \right)^{0.08}$	• Data: Water, Ammonia • Empirical fits to numerical approach, then compared to data
	(2.38)	Constant Wall Temperature: $Nu = 0.127 Pr^{0.46} Re^{0.15} \left(\dfrac{d}{v^2/g} \right)^{-0.2} \left(\dfrac{2s}{v^2/g} \right)^{0.08}$	
Rogers and Goindi (1989)	(2.39)	Developing Thermal B-L: $Nu = 0.063 Re^{0.466} Ar^{2/9} Pr^{1/3} \left(\sin\theta / P(\theta) \right)^{1/3}$	• Data: Subcooled Water • Developing region: $P(\theta_d) < 0.0606\, Re^{4/3} Ar^{-1/3} Pr$
	(2.40)	$P(\theta) = \int_0^\theta \left(\sin\theta \right)^{1/3} d\theta$	
	(2.41)	Developed Thermal B-L: $Nu = 4.55 Re^{-0.467} Ar^{1/3} \left(\sin\theta \right)^{1/3}$	
Rogers *et al.* (1995)	(2.42)	$Nu = 0.2071\, Re^{0.24} Pr^{0.66} Ar^{-0.111}$	• Data: Subcooled Water
Hu and Jacobi (1996b)	(2.43)	Droplet Mode: $Nu = 0.113\, Re^{0.85} Pr^{0.85} Ar^{-0.27} \left(s/d \right)^{0.04}$	• Data: Subcooled Water, Ethylene Glycol, and Mixtures
	(2.44)	Jet Mode: $Nu = 1.378\, Re^{0.42} Pr^{0.26} Ar^{-0.23} \left(s/d \right)^{0.08}$	
	(2.45)	Sheet Mode: $Nu = 2.194\, Re^{0.28} Pr^{0.14} Ar^{-0.20} \left(s/d \right)^{0.07}$	

Table 2.6. Summary of empirical modeling studies (continued)

Study	Eqn.	Correlation	Notes
Fujita and Tsutsui (1998)	(2.46)	Top Tube: $Nu = \left(Re^{-2/3} + 0.008 Re^{0.3} Pr^{0.25} \right)^{0.5}$	• Data: R-11, Evaporative • Bundle: 5 Tube Array
	(2.47)	Lower Tubes: $Nu = \left(Re^{-2/3} + 0.010 Re^{0.3} Pr^{0.25} \right)^{0.5}$	
Zeng *et al.* (1997)	(2.48)	Single Tube: $Nu = 0.0518\, Re^{0.039} Pr^{0.278} P_r^{0.385} \left(\dfrac{q'' d}{(T_{\text{crit}} - T)k} \right)^{0.753}$	• Data: Ammonia, Boiling • Bundle: 3×3 Square Pitch
	(2.49)	Tube bundle: $Nu = 0.0495\, Re^{-0.00399} Pr^{0.209} P_r^{0.261} \left(\dfrac{q'' d}{(T_{\text{crit}} - T)k} \right)^{0.722}$	
Zeng *et al.* (1998)	(2.50)	$Nu = 0.0568\, Re^{-0.0058} Pr^{0.193} P_r^{0.323} \left(\dfrac{q'' D}{(T_{\text{crit}} - T)k} \right)^{1.034}$	• Data: Ammonia, Boiling, Finned Tube
Zeng *et al.* (2001b)	(2.51)	$Nu = 0.0678\, Re^{0.049} Pr^{0.296} P_r^{0.456} \left(\dfrac{q'' D}{(T_{\text{crit}} - T)k} \right)^{0.704}$	• Data: Ammonia, Boiling • Bundle: 3-2-3 Triangular Pitch
Chien and Cheng (2006)	(2.52)	$h = \left[0.185 + 56.2 \dfrac{\left(\dot{m}^2 d\, A^{-2} \rho^{-1} \sigma^{-1} \right)^{0.453}}{\left(q'' A\, i_{fg}^{-1} \dot{m}^{-1} \right)^{0.687} Re^{1.308}} \right] h_{\text{nb}} + h_{\text{cv}}$	• Data: R-11, R-123, R-134a, R-22, R-141b (other studies) • Combines convective and boiling correlations with superposition
Chien and Tsai (2011)	(2.53)	$Nu_{\text{cv}} = 0.0386\, Re^{0.09} Pr^{0.986}$	• Data: R-245fa • Combines convective and boiling correlations with superposition
	(2.54)	$h = \left[0.0152 \dfrac{\left(\dot{m}^2 d\, A^{-2} \rho^{-1} \sigma^{-1} \right)^{0.283}}{\left(q'' A\, i_{fg}^{-1} \dot{m}^{-1} \right)^{-1.179} Re^{-1.254}} \right] h_{\text{nb}} + h_{\text{cv}}$	

Table 2.6. Summary of empirical modeling studies (continued)

Study	Eqn.	Correlation	Notes
Chien and Chen (2012)	(2.55)	$h = \left[56.13 \dfrac{\left(\dot{m}^2 d \ A^{-2} \rho^{-1} \sigma^{-1} \right)^{0.588}}{\left(q'' A \ i_{fg}^{-1} \dot{m}^{-1} \right)^{0.180} Re^{-0.246}} \right] h_{nb} + h_{cv}$	• Data: R-134a • Combines convective and boiling correlations with superposition
Roques and Thome (2007b)	(2.56) (2.57) (2.58) (2.59)	$K_{ff} = h / h_{pb}$ $K_{ff} = \left(1 - 0.335 \dfrac{p}{p_{min}} \right) \left(2.059 + 2.370 \dfrac{q''}{q_{crit}} - 7.793 \left(\dfrac{q''}{q_{crit}} \right)^2 \right)$ Partial Dryout: $K_{ff,dry} = \left(K_{ff} / Re_{trans} \right) Re$ Transition to Dryout: $Re_{trans} = 0.00678 \ q'' + 165$	• Data: R-134a, Boiling • Provides ratio to pool boiling heat transfer coefficient • Coefficients unique to tube surface, provided for plain and 3 enhanced tubes
Ribatski and Thome (2007)	(2.60) (2.61) (2.62) (2.63)	$h = h_{wet} F + h_{dry} \left(1 - F \right)$ $h_{wet} = 376 \ P_r^{0.22} q''^{0.38}$ Partial Dryout: $F = A_{wet} / A = 0.0024 \ Re^{0.91}$ Transition to Dryout: $Re_{trans} = 6.93 \times 10^5 \left(q'' \left(\rho_l - \rho_v \right)^{-1} i_{fg}^{-3/2} \right)^{0.47}$	• Data: R-134a, Boiling • Above Re_{trans}, $F = 1$
Habert and Thome (2010b)	(2.64) (2.65) (2.66) (2.67)	$h_{wet} = 1.695 \ h_{pb} \left(q''/q''_{crit} \right)^{-0.324}$ Partial Dryout: $F = A_{wet} / A = Re / Re_{trans}$ Transition to Dryout: $Re_{trans} = 65.8 \left(q'' \ d \ \mu^{-1} \ i_{fg}^{-1} \right)^{0.63}$ Bundle Adjustment: $h_{bundle} = \left[1 + 0.6 \exp\left(-9 \times 10^{-7} \left(Re - 800 \right)^2 \right) \right] h$	• Data: R-134a, R-236fa, Boiling • Coefficients unique to tube surface, provided for plain and 3 enhanced tubes • Bundle: 3×10 triangular pitch • Bundle coefficients unique to fluid, heat flux, tube surface • Above Re_{trans}, $F = 1$

Table 2.6. Summary of empirical modeling studies (continued)

Study	Eqn.	Correlation	Notes
Christians and Thome (2012b)	(2.68)	$h_{\text{wet}} = 9.623 \times 10^4 \left(\dfrac{k}{d} \right) \left(\dfrac{q''^2 d}{i_{\text{fg}}^{5/2} \mu (\rho_1 - \rho_v)} \right)^{0.0328} G_{\text{t-s}}^{1.25}$	• Data: R-134a, R-236fa, Boiling • Only one tube-specific parameter, $G_{\text{t-s}}$, provided for 8 enhanced tubes
	(2.69)	Transition to Dryout: $Re_{\text{onset}} = 20.7 \left(q'' \, d \, \mu^{-1} \, i_{\text{fg}}^{-1} \right)^{1.04} G_{\text{t-s}}^{0.175}$	
Li *et al.* (2010)	(2.70)	$\dfrac{h_{\text{en}}}{h} = 2.7733 Ga^{0.357} \left(\dfrac{\sigma}{\rho g f_{\text{d}} f_{\text{s}}} \right)^{-2.67} \left(\dfrac{L_{\text{c}}}{2L} \right)^{10.33}$	• Data: Water, Evaporative • Ratio of enhanced to smooth tube performance • L_{h}: heated length
Li *et al.* (2011b)	(2.71)	$Nu_{\text{wet}} = 182.1 \, Re^{-1.56}$	• Data: Water, Evaporative • Ratio of enhanced to smooth tube performance • Transition from wet to partial dryout at $Re_{\text{trans}} = 54$
	(2.72)	$Nu_{\text{dry}} = Nu_{\text{wet}} \left(Re / Re_{\text{trans}} \right)^{2.67}$	
	(2.73)	$\dfrac{h_{\text{en}}}{h} = 5.635 \, Re^{-0.426} \left(\dfrac{\sigma}{\rho g f_{\text{d}} f_{\text{s}}} \right)^{0.164} \left(\dfrac{L_{\text{c}}}{2L} \right)^{0.732}$	
Li *et al.* (2011a)	(2.74)	$h_{\text{wet}} = 7.426 (k/L) \, Re^{-0.679} Bo^{-0.235}$	• Data: Water, Evaporative • Transition from wet to partial dryout at constant Re, unique to each tube
	(2.75)	$h_{\text{dry}} = 4.86 \times 10^{-3} (k/L) \, Re^{1.071} Bo^{-0.659}$	

2.5.2   Analytical Approaches

Analytically based models often divide the flow into several regions. These typically include the thermally developing and fully developed regions, although free fall, stagnation, and jet impingement regions have also been used. Within each region, the local heat transfer coefficients can be calculated with an empirical, analytical, or numerical approach, and are then averaged across the surface to find the total heat transfer coefficient. A summary of analytical modeling studies is provided in Table 2.7.

The basis of many analytical models is the classic Nusselt (1916) film analysis, originally conducted for *condensation* on an isothermal vertical surface. It applies the continuity, momentum, and energy equations to an idealized film flow. The analysis assumes a steady, laminar film flow with constant properties and a smooth liquid-vapor interface. Heat transfer in the film is assumed to be by conduction only, and inertial effects are assumed to be negligible relative to gravitational and viscous forces in the
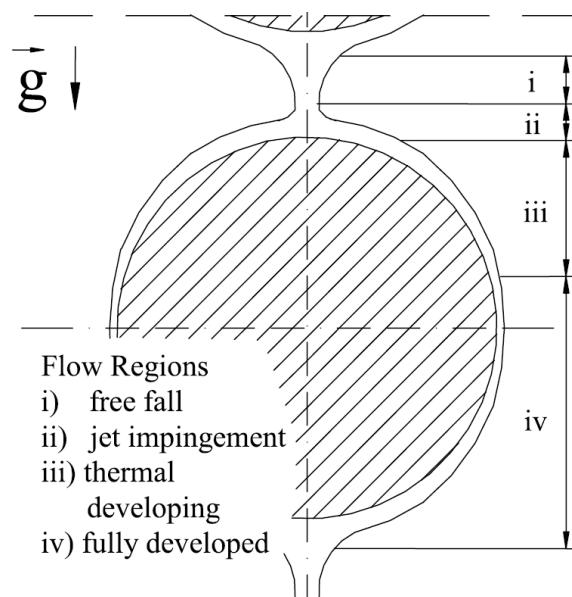

Figure 2.3. Division of falling-film flow into several regions (Ribatski and Jacobi, 2005)

momentum balance. The vapor is considered to be stationary, with negligible drag at the liquid-vapor interface. This analysis can be easily adjusted to inclined surfaces by modifying the gravitational term in each equation.

Lorenz and Yung (1978) proposed a model using superposition of convective and boiling contributions, treating the tube as an unwrapped vertical surface. The convective heat transfer coefficient was predicted by dividing the flow into the developing and developed regions. The developing region uses an analytical approach based on the Nusselt analysis, while the developed region is calculated with the Chun and Seban (1972) correlation. Meanwhile, they predicted the boiling performance with the Rohsenhow (1951) correlation, which they considered to be a conservative approach. They found good agreement between this model and data reported by Fletcher *et al.* (1974; 1975).

Sabin and Poppendiek (1978) modified the Nusselt analysis for evaporation, and accounted for the influence of angle around the tube. They found good agreement with data taken with ammonia, but the model predicted that the heat transfer coefficient would decrease as flow rate increased, which was not observed in the data. They suggested that this may be because the local wall temperature measurements are not representative of the average tube wall temperature. Semiat *et al.* (1978) also extended the Nusselt analysis by accounting for the influence of turbulence. They selected the eddy diffusivity models of Deissler near the wall and Von-Karman elsewhere (Sideman and Pinczewski, 1975). Good agreement was found between this model and data taken with water for Reynolds numbers from 100 to 2000. Interestingly, this agreement was better than what was achieved with a laminar flow model accounting for waviness even at low Reynolds

numbers. Later, Barba and Di Felice (1984) used a similar approach but accounted for turbulence using the method of Dukler (1960). They found that this compares well with data taken by several investigators (Fletcher *et al.*, 1974; Fletcher *et al.*, 1975; Liu, 1975), and had improved performance compared to the Lorenz and Yung (1978) correlation at high Reynolds numbers.

Rogers (1981) proposed a laminar film analysis that divided the flow into the developing and developed regions. The Nusselt film analysis was modified to account for waviness using an empirical correlation by Kutateladze and Gogonin (1979). Rogers and Goindi (1989) simplified this model to allow a closed-form solution, and found that it compared well with data taken with subcooled water on large diameter tubes.

Parken and Fletcher (1982) conducted a modified laminar-film analysis using a third-order polynomial for the velocity profiles, solved iteratively with the Runge-Kutta method. This compared well with data taken with water, with the largest disagreement with local heat transfer data taken at the bottom and top of the tube. Bourouni *et al.* (2001) modified Parken and Fletcher's model by including a stagnation region at the top of the tube, which reduces the local heat transfer coefficients in this region relative to Parken and Fletcher's model, although they are still the highest local heat transfer coefficients. This improved agreement of the local heat transfer coefficients at the top of the tube, and they found overall improved agreement with data taken with water.

Chyu and Bergles (1985, 1987) developed a model splitting the flow into the jet impingement, thermal developing, and thermally developed regions. The jet impingement heat transfer coefficients were predicted using the Miyasaka and Inada (1980) correlation for the 2D impingement of a jet on a flat plate. The thermal developing region was

analyzed using an analytical approach. Two approaches were used for the thermally developed region: a laminar analytical film analysis, and the Chun and Seban (1972) correlation. The model was compared with data taken with water, and better agreement was found using the Chun and Seban correlation for the developed region. However, both correlations underpredicted the heat transfer coefficient in the droplet and jet modes.

Fujita and Tsutsui (1995a) also recommended a three-zone model using the developing, transitional, and developed regions. Analytical models were used in the developing and developed regions, with the developing region using a third-order polynomial for the temperature profile, and a linear profile in the developed region. The transition region provided a smooth transition between these approaches. The developed region assumed turbulent flow, with the eddy conductivity equal to the eddy viscosity. They found good agreement with data taken with R-11 (Fujita and Tsutsui, 1995b).

Ruan and Jacobi (2012) used the Nusselt analysis to predict heat transfer variation with property changes. This was used to account for the bulk property changes introduced by adding carbon nanotube suspensions of 0 to 0.24% by volume to water and ethylene glycol. Although relatively low levels of enhancement were observed, the analytical scaling relationship was found to predict it well.

Most of the proposed analytical correlations capture the high local heat transfer coefficient at the top of each tube, but have larger deviations from data towards the bottom of the tube (Ribatski and Jacobi, 2005). They have demonstrated good performance with a number of fluids, but have several limitations. First, the available models have only been developed for the sheet mode, although Fujita and Tsutsui (1995a) have suggested that time-averaged droplets and columns can be modeled as

sheets. In addition, film waviness and boiling, both significant factors impacting falling-film heat transfer performance, have only been incorporated through empirical adjustments. The available analytical models are only applicable to situations with full wetting, which is often not observed at low flow rates or high heat fluxes, and Ribatski and Jacobi (2005) noted that Marangoni effects are not included.

Table 2.7. Summary of analytical modeling studies

Study	Approach	Comments
Nusselt (1916)	• Analytical approach for idealized film flow condensation on a vertical surface • Assumptions: steady, laminar flow, constant properties, smooth liquid-vapor interface, inertial effects minimal, no convection in film, no vapor shear at interface	• Widely adapted for falling-film evaporation and forms the basis of many correlations • Poor agreement with most falling-film evaporation data due to developing region, turbulence, dryout, boiling, and other factors
Lorenz and Yung (1978)	• Superposition of boiling and convective contributions • Convective divided into thermal developing and developed regions • Developing region uses simplified analytical approach • Developed region uses Chun and Seban (1972) • Boiling predicted with pool boiling correlations	• Targeting ocean thermal energy conversion (OTEC) applications • Compares well to data by Fletcher *et al.* (1974; 1975) • Treat tube as a vertical surface
Semiat *et al.* (1978)	• Combined turbulent falling-films with internal condensation • Analytical approach similar to Nusselt formulation with turbulence • Eddy diffusivity model of Deissler near wall and Von-Karman elsewhere (Sideman and Pinczewski, 1975)	• Compares well with data taken with water • Better performance than laminar approach throughout entire data range
Sabin and Poppendiek (1978)	• Used Nusselt formulation modified for evaporation, accounting for angle around the tube	• Predictions are relatively close to data with ammonia, but model predicts flow rate trend not observed in the data

Table 2.7. Summary of analytical modeling studies (continued)

Study	Approach	Comments
Rogers (1981)	• Laminar film split into developing and developed regions • Analytical film analysis in both regions with empirical enhancement for waviness (Kutateladze and Gogonin, 1979)	• Targeting nuclear reactor cooling applications with sensible cooling • Suggested film breakdown could be caused by reducing flow rate, Marangoni instabilities, or nucleate boiling
Parken and Fletcher (1982)	• Analytical laminar film analysis • Velocity profile considered to be a third order polynomial, found iteratively using Runge-Kutta method	• Compares well to data taken with water • Largest disagreement with data at bottom and top of tube
Barba and Di Felice (1984)	• Analytical approach assuming velocity profile is constant, giving a constant film thickness • Accounted for turbulence using method of Dukler (1960)	• Treat tube as a vertical surface • Compares well with data from several studies (Fletcher *et al.*, 1974; Fletcher *et al.*, 1975; Liu, 1975) • Better performance than Lorenz and Yung (1978) correlation at high Reynolds numbers
Chyu and Bergles (1985, 1987)	• Three regions: jet impingement, thermal developing, and thermally developed • Jet impingement: correlation for 2D jet on flat plate (Miyasaka and Inada, 1980) • Thermal developing: analytical analysis • Thermally developed compared two approaches: analytical laminar analysis and Chun and Seban (1972) correlation	• Better agreement with data taken with water when Chun and Seban (1972) correlation is used • The analytical approach based on Nusselt's analysis underpredicts heat transfer coefficients • Both correlations underpredict in the droplet and jet modes
Rogers and Goindi (1989)	• Simplified earlier approach of Rogers (1981) to allow a closed-form solution	• Compare to data with subcooled water on large diameter tubes, find relatively good agreement with model overpredicting data by about 20%

Table 2.7. Summary of analytical modeling studies (continued)

Study	Approach	Comments
Fujita and Tsutsui (1995a)	• Laminar flow analysis splitting flow into developing, transitional, and developed region • Assumes third-order polynomial temperature profile in developing region, linear profile in developed, smooth transition • Separate correlation for turbulent flow, assumes universal velocity profile and eddy conductivity equal to eddy viscosity	• Suggest that time-averaged droplets and columns can be modeled as sheets • Compared with data for R-11 (Fujita and Tsutsui, 1995b), relatively good agreement but underpredicts by approximately 20%
Bourouni *et al.* (2001)	• Built on model of Parken and Fletcher (1982) by including stagnation region at the top of the tube	• Reduces the overprediction of heat transfer coefficient at the top of the tube • Compares well to data taken with water
Ruan and Jacobi (2012)	• Analytical relationship to predict heat transfer variation with property changes • Laminar film assumptions following Nusselt analysis	• Predicting enhancement of falling-film heat transfer with addition of carbon nanotube suspensions • Compares well to data taken with water and ethylene-glycol based nanofluids

2.6   Specific Research Needs

Falling-film evaporation over horizontal round tubes has been the subject of significant study. However, there is limited information available on horizontal rectangular tubes and tube banks, representative of the external profile of microchannel extrusions, which has been proposed as a promising alternative geometry. The few studies that are available suggest that round-tube heat transfer coefficient correlations and flow characteristic data are not applicable to this geometry (Wang *et al.*, 2010, 2011). Furthermore, the limited rectangular tube data were taken with subcooled fluid at atmospheric pressure, and are not sufficient to predict the performance of evaporating falling films at sub-atmospheric pressures. Thus, there is a need for an experimental study

examining the flow characteristics and heat transfer coefficients for flow with this geometry, allowing a heat transfer model to be developed.

Falling-film evaporation studies over both horizontal round and rectangular tubes require a liquid distributor to establish an even fluid flow along the length of the tube. They can directly impact heat transfer performance by modifying the fluid impact region, local film thicknesses, wetted tube area, and other enhancement mechanisms such as the film waviness. Although this influence on heat transfer performance has been noted, most studies only qualitatively assess their performance. Thus, there is a need to quantitatively assess the performance of these liquid distributors.

2.7   Objectives of the Present Study

The objective of this study is to gain a fundamental and quantitative understanding of falling-film evaporation over rectangular tubes using water at sub-atmospheric pressures as the working fluid. This includes an evaluation of flow distributor performance, flow visualization of the falling films with quantification of key characteristics, heat transfer coefficient measurements, and development of a heat transfer model. The specific tasks are as follows:

- Quantitatively compare the performance of eight flow distributors with water at atmospheric pressure.

- Conduct a high-speed flow visualization study of falling-film evaporation of water over horizontal rectangular tube banks with a cross-section of 27.4 mm × 1.42 mm over Reynolds numbers ranging from 25 to 125.

- Analyze the flow visualization data to determine droplet dimensions, droplet impact frequency, and wave dimensions.

- Measure heat transfer coefficients during falling-film evaporation of water over horizontal rectangular tubes with a cross-section of 27.4 mm × 1.42 mm over saturation temperatures of 10 to 30°C, heat fluxes of 10 to 20 kW m^{-2}, Reynolds numbers of 50 to 550, and tube spacings of 5 to 15 mm.

- Develop a heat transfer model based on the collected data using insights obtained from the flow visualization results.

CHAPTER 3: EXPERIMENTAL METHODS

A test facility was constructed for this study to conduct falling-film evaporation heat transfer and flow visualization experiments, as well as to assess the performance of liquid distributor designs. The test facility is designed to allow variation of the flow rate, saturation pressure, tube spacing, and heat flux during falling-film evaporation experiments at subatmospheric pressures. In addition, the facility was run at atmospheric pressure for the liquid distributor experiments. Water was used as the refrigerant for all of the experiments. This chapter describes the test facility, experimental procedures, and test matrix.

3.1 Experimental Setup

This section describes the facility used for the heat transfer, flow visualization, and liquid distributor experiments. It also describes the instrumentation, heat transfer test sections, flow visualization setup, and liquid distributors.

3.1.1 <u>Test Facility</u>

A photograph of the test facility is shown in Figure 3.1, and a schematic in Figure 3.2. The primary test chamber is a cubic anodized aluminum vacuum chamber with internal dimensions of $0.61 \times 0.61 \times 0.61$ m (Abbess Instruments, Model 24" Cube AL, S/N 50332). The front surface of the chamber is made of 48.3 mm thick transparent acrylic, allowing full, undistorted visual access to the test section. In addition, there is a 0.33 m square acrylic window on the back of the test chamber, enabling the provision of lighting for high-speed video. The primary flow loop is constructed of 316 stainless steel

tubing with an outer diameter of 12.7 mm and a wall thickness of 0.89 mm. The secondary loops providing cooling fluid to the subcooler and condenser are constructed of copper pipe with an outer diameter of 15.88 mm, an inner diameter of 14.45 mm, and a wall thickness of 0.71 mm. Connections in the primary loop were made using Swagelok compression fittings and NPT threaded fittings, while the secondary loop used soldered and NPT threaded connections.

In the main refrigerant flow loop, referring to Figure 3.2, saturated liquid exits the test chamber at state point [1] and flows down to two magnetic gear pumps which set the
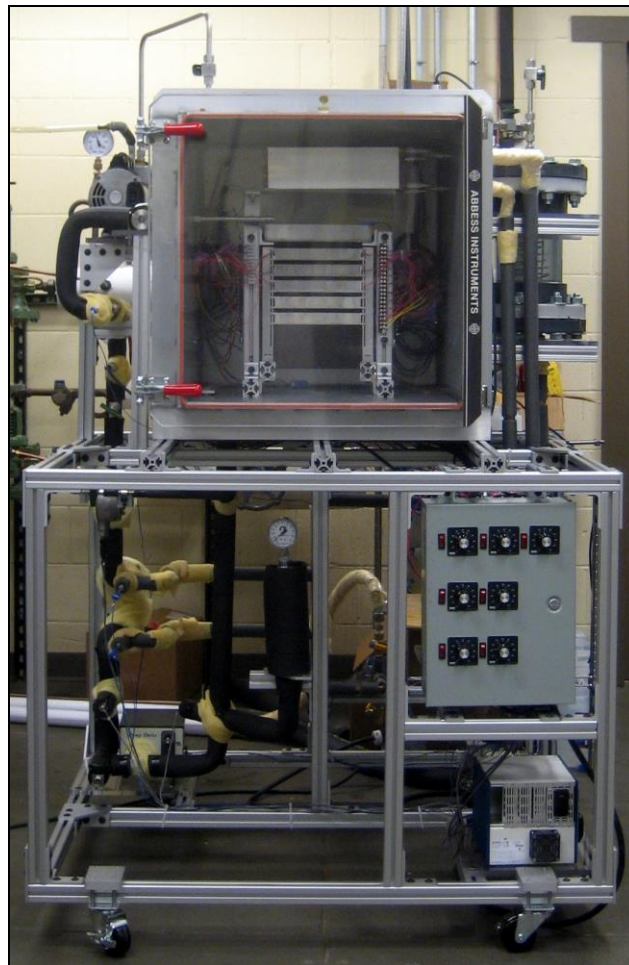

Figure 3.1. Photograph of experimental facility

flow rate of the refrigerant (Micropump Model 201-000-000, Serial Number 884821, with Gear Drive Model 83433, and Micropump Model GB-P23.PVS.A, Serial Number 1537500 with Gear Drive Model 75225-12). At low flow rates only a single gear pump was used, while at higher flow rates both gear pumps were run in parallel. The refrigerant then flows through a heat exchanger (FlatPlate Model 131002572, Serial H014DC19009051) coupled to the secondary cooling loop, bringing the liquid to a subcooled condition at state point [2]. The flow rate is read with a positive displacement flow meter (AW Flow Meters Model JVS-01UF-25-NPT) or rotameter (Omega Model FL4302), with the rotameter only being used when the flow exceeded the range of the positive displacement flow meter. Then, an electric immersion heater (McMaster-Carr, Model# 4654T13) brings the flow to saturated conditions before entering the test chamber at state point [4]. A sight glass is used to confirm that the flow is liquid when entering the test chamber. Within the chamber, the fluid enters the liquid distributor, which spreads the liquid over the test section. The test section evaporates some of the test fluid. The evaporated test fluid is condensed by two cold plates (Lytron, Model 07440670) at the top of the test chamber, allowing a constant pressure to be maintained in the test chamber. The condensed liquid from these cold plates, as well as fluid that does not evaporate while flowing over the heated tubes, flows to the bottom of the chamber, where a constant liquid level is maintained to supply a constant gravitational head on the pump. The entire system was insulated to minimize heat gains from the ambient. The primary test chamber was insulated with 50 mm thick rigid fiberglass insulation (~0.03 W m^{-1} K^{-1}), except the door and window for visualization, and the flow loops were insulated with 25 mm thick fiberglass wrap (~0.03 W m^{-1} K^{-1}). In addition to the

instrumentation locations shown in Figure 3.2, it should be noted that there are 5 thermocouples located in the test chamber. Two thermocouples are placed in the liquid distributor, two thermocouples read the temperature of the test chamber vapor, and one thermocouple reads the temperature of the liquid pool. The liquid pool temperature was measured at the bottom of the chamber, 25 mm above the fluid exit.

The coolant is a 50/50 mixture of ethylene glycol and water. The cooling temperature is set by a Thermo Scientific recirculating chiller (NESLAB Merlin M150 series, Serial Number 111010064) with a temperature range of -15°C to 35°C, temperature stability of ±0.15°C, and a cooling capacity of 4.8 kW. This chiller supplies cooling fluid to both the condenser in the test chamber and the subcooler. The condenser in the test chamber consists of two 6-pass cold plates (Lytron model CP15G05) with the cooling fluid passing in parallel through them. Each cold plate contains copper pipes with an outer diameter of 6.4 mm making 6 passes through an aluminum plate with a length of
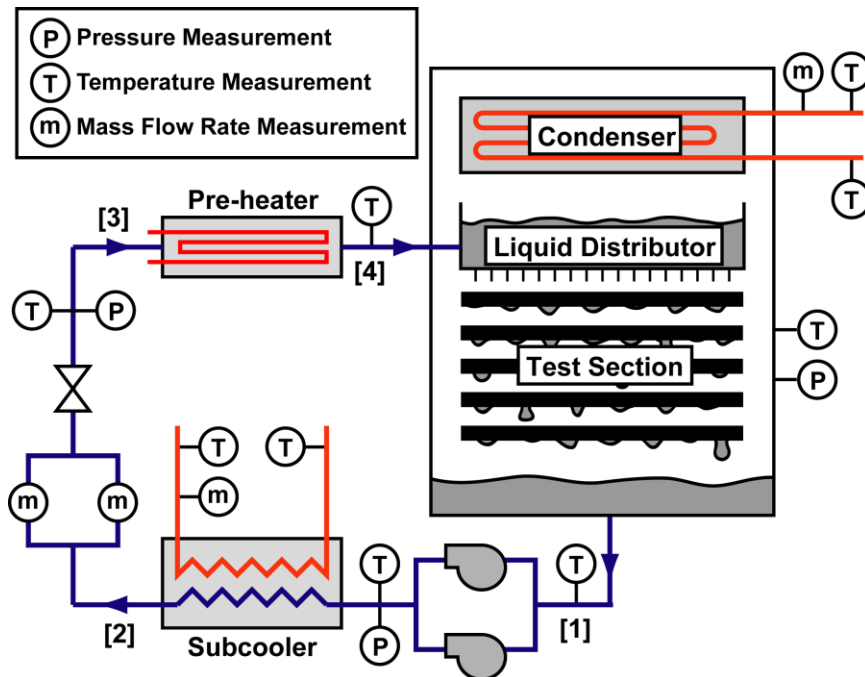
Figure 3.2. Experimental facility schematic

305 mm and a height of 95 mm. The subcooler is a flat plate heat exchanger (FlatPlate Model 131002572, Serial H014DC19009051) with 14 plates and nominal dimensions of 76 mm × 203 mm. The two heat exchangers are arranged in parallel, with metering valves controlling the flow rates in each unit.

For the liquid distributor experiments, which were conducted at atmospheric pressure, the test chamber door remained open and a 100 mm tall acrylic retaining wall was installed inside the chamber door to allow the liquid level to be maintained. In addition, the test section array was replaced with a liquid collection box, which measured the local flow rate variation along the length of the distributor. It measures the uniformity of the distribution with ten segments that are each 25.4 mm wide, 64.0 mm deep, and 196.9 mm tall. Eight of the segments are directly below the intended distribution length, with an additional segment on either end to capture liquid leaving this area. During measurements, the liquid collection box was centered with respect to the depth of the distributor, providing 32 mm of collection area on either side of the intended distribution area. A linear scale was placed on the side of each liquid collection segment to allow the liquid depth to be measured.
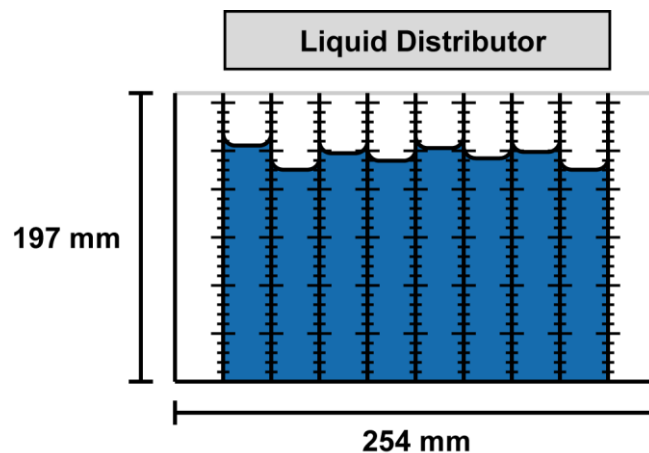
Figure 3.3. Collection box below a liquid distributor

3.1.1.1 *Facility Instrumentation*

All measurements were taken with a National Instruments data acquisition system, with specifications shown in Table 3.1, and recorded and analyzed using National Instruments LabView software.

Table 3.1. Data acquisition system specifications

Instrument	Manufacturer	Model Number	Serial Number
DAQ Chassis	National Instruments	SCXI-1000	14726B1
USB Data Acquisition Module	National Instruments	SCXI-1600	1489084
32 Channel Signal Conditioning Module	National Instruments	SCXI-1102	146A684
			146A685
32 Channel Isothermal Terminal Block	National Instruments	SCXI-1303	1482073
			1482096

All temperature measurements were made using type-T thermocouples. The thermocouples in the flow loop are prefabricated thermocouple probes (Omega Engineering Model# TMQSS-125U-6), while the test section thermocouples were fabricated from 40 gauge type-T thermocouple wire (Omega Engineering Model# TT-T-40-SLE-500) with a thermocouple welder (DCC Corporation Hotspot II Model). Each thermocouple was calibrated in the applicable range with a temperature controlled calibration bath (Hart Scientific Model# 7340, Serial# A57096) using silicone oil (Hart Scientific Model# 5012) and a high precision, NIST-traceable RTD (Hart Scientific Model# 5612, Serial# 748503) with an accuracy of $\pm0.012°C$. The maximum uncertainty of the thermocouples after this calibration was found to be $\pm0.30°C$, which was conservatively applied to all thermocouple measurements.

The flow rate in the primary loop was read using a positive displacement flow meter (AW Flow Meters, Model# JVS-01UF-25-NPT) at flow rates below 0.9 L min^{-1}, and a rotameter at higher flow rates (Omega Engineering Inc., Model# FL4302). The secondary fluid flow rates were read using rotameters (Omega Engineering Inc., Model# FL4302). The pressures within the test chamber and at state point [3] were read by high accuracy pressure transducers (OMEGA Engineering Inc., Model PX409-005AI), while

Table 3.2. Instrumentation specifications

Location	Manufacturer and Model Number	Serial Number	Range	Uncertainty
Pressure Transducers				
Test Chamber	Omega, PX409-005AI	411572	0-34.5 kPa absolute	±0.08% FS (±28 Pa)
Test Chamber Inlet	Omega, PX409-005AI	411570	0-34.5 kPa absolute	±0.08% FS (±28 Pa)
Main Flow Loop	Omega, PX209-030AI	85387	0-206.8 kPa absolute	±0.25% FS (±517 Pa)
Flow Meters				
Main Loop	AW Flow Meters, Positive Displacement JVS-01UF-25-NPT	15311219	0.002-0.95 L min^{-1}	±2% Reading
Main Loop	Omega, Rotameter FL4302	797709000002	0.76-7.6 L min^{-1}	±2% FS (±0.15 L min^{-1})
Secondary Loop, Subcooler Line	Omega, Rotameter FL4302	027803000001	0.76-7.6 L min^{-1}	±2% FS (±0.15 L min^{-1})
Secondary Loop, Condenser Line	Omega, Rotameter FL4302	815109000001	0.76-7.6 L min^{-1}	±2% FS (±0.15 L min^{-1})
Thermocouples				
Flow Loops	Omega, Type-T TMQSS-125U-6	–	Max 220°C	±0.30°C
Test Sections	Omega, Type-T TT-T-40-SLE-500	–	Max 150°C	±0.30°C
Watt Transducers				
Test Sections and Preheater	Ohio Semitronics, PC5-010EY25	09120609 09120610 09120611 09120613 09120614	0-1 kW	±0.5% FS (±5 W)

the pressure downstream of the pumps was read using a pressure transducer with a wider range (OMEGA Engineering Inc., Model PX209-030AI). The power delivered to the pre-heater and test sections was controlled using variable voltage controls (Payne Engineering, Model# 18TBP-1-10), and measured with watt transducers (Ohio Semitronics, Model# PC5-010EY25).

3.1.2   Heat Transfer Test Section

The heat transfer test section was designed to mimic the external profile of commercially available rectangular multi-port extruded aluminum tubes, but utilized internal electric heaters to simplify the experimental design and reduce measurement uncertainty. Shown in Figure 3.4, each test section is constructed of aluminum with external dimensions of $203 \times 1.42 \times 27.4$ mm (length $\times$ width $\times$ height) and rounded edges lengthwise. Internally, it contains a polyimide film electric heater with a maximum capacity of 1.3 kW at 115 V (Omega Engineering Inc., Model# KHLV-104/10) and eight 40 gauge type-T thermocouples located along two diagonal lines across the tube, offset at the midpoint from one another. The test section is connected to a mounting stand with four small extensions with a height of 3.9 mm each to limit heat transfer due to conduction and prevent film flow to the supports.
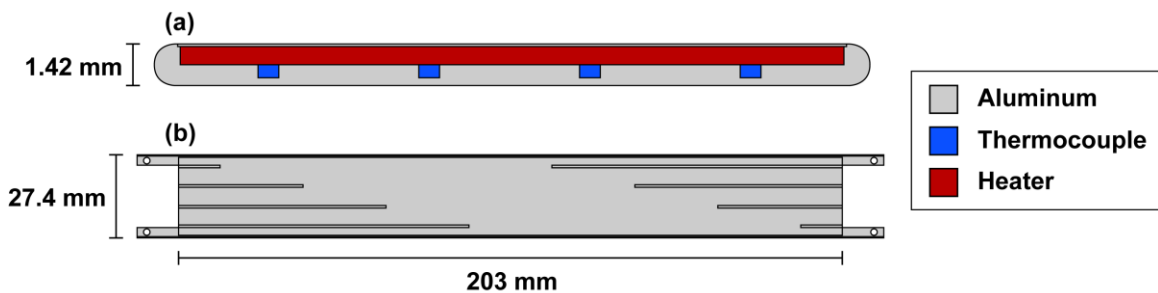
Figure 3.4. Electrically heated test section: (a) zoomed and rotated side view of assembled tube, and (b) front view of machined aluminum piece

89

The steps in the fabrication of a test section are shown in Figure 3.5. First, a plate of aluminum is machined to the correct external profile, with cutouts for the thermocouples, heater, and aluminum shim. The wide, shallow groove for the electric heater and aluminum shim is 0.71 mm deep, allowing room for both components and two thin layers of bonding cement. The thermocouple grooves are each 0.66 mm wide and 0.46 mm deep, and space the thermocouples 25.4 mm apart axially and 5.7 mm apart vertically. This results in the aforementioned even thermocouple spacing across the tube in two diagonal lines. Then, 40 gauge type-T thermocouples are soldered in place to minimize thermal contact resistance. To provide the internal heating to the test section, two polyimide film electric heaters (Omega Engineering Inc., Model# KHLV-104/10), each 25.4×101.6 mm are installed in the test section using high thermal conductivity
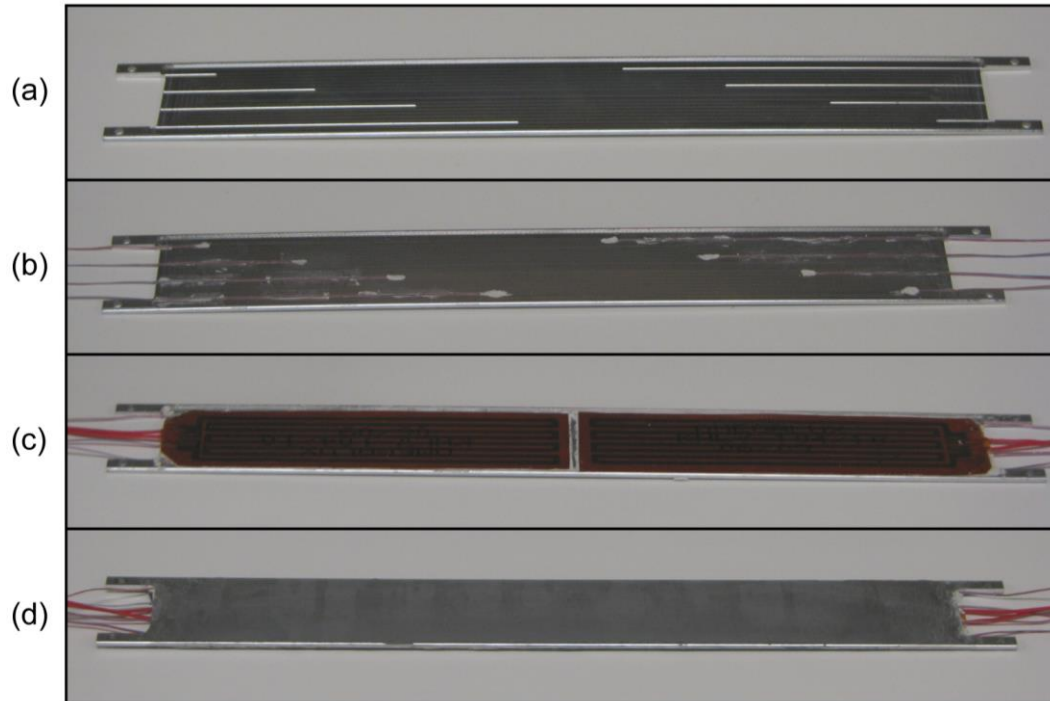
Figure 3.5. Steps in test section fabrication: (a) machine aluminum plate; (b) solder in 40-gauge thermocouples; (c) attach electric heaters; (d) attach aluminum shim and apply surface finish

cement (Omega Engineering Inc., Model# CC High Temp). The heaters are then covered with a 0.25 mm thick aluminum shim with the same bonding agent in order to maintain a uniform external aluminum profile. Finally, the surface was polished with emery cloth 320/P400 to provide a uniform surface finish.

The test section assembly includes a liquid distributor, an adiabatic tube, and up to three heated test sections, as shown in Figure 3.6. The liquid distributor used for heat transfer testing is described in Section 3.1.4. The adiabatic tube is a machined aluminum tube with the same external profile as the test sections, but with no internal components, and was included to aid in the establishment of the flow distribution. Finally, during testing, an array of between one and three test sections was used. Test section 1 is the top test section, followed by test sections 2 and 3. During the experimental study, three test sections were not always used when local temperatures reached levels that could potentially damage the test section. This primarily occurred when the heat flux was increased or the flow rate was decreased, which potentially led to dryout, where no liquid is flowing over an area of the test section.
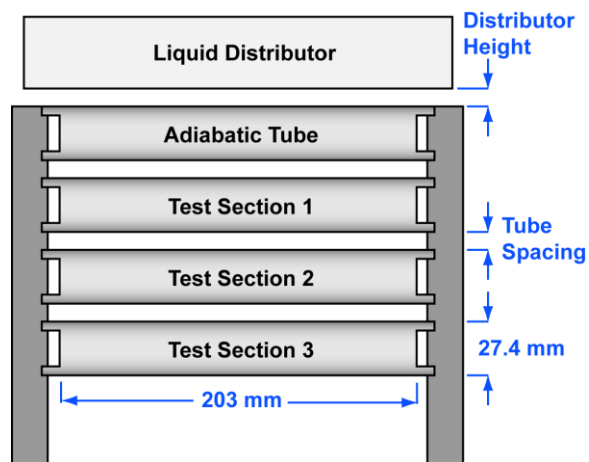
Figure 3.6. Array of test sections

3.1.3 Flow Visualization Setup

The flow visualization tests were conducted using a high-speed camera (Photron FASTCAM – Ultima 1024, Model 161CC, Serial Number 31705025) with a Nikon camera lens (Model Micro-Nikkor 105 mm). The camera provides a resolution of 1024×1024 at 500 frames per second and enough internal memory to store 1 s of video. Video was recorded using Photron FASTCAM viewer software (version 2.4.5.1), which controlled the shutter speed, frame rate, and resolution. To provide sufficient lighting for the high frame rates used, lighting was provided by three Lowell Omni sources with 500 W tungsten/halogen bulbs. Two lights provided lighting through the front door of the chamber in order to observe the films on the flat front surfaces of the test sections, with one light providing back lighting in order to view films traveling between the test section rows. The back light was projected onto a light diffusion screen to provide even lighting with an appropriate intensity. The field of view was set to include the full width of test sections. This allowed the variation of the film flow across the test section to be observed while still providing sufficient resolution to observe local film behavior.

Figure 3.7. Top view of high speed camera and lighting setup

3.1.4 <u>Liquid Distributors</u>

Eight flow distributors were fabricated in order to quantitatively compare the performance of different types of designs. Each distributor is based on a design used in previous studies, and was selected to represent a range of common designs. In each case, the geometry and key features were designed to be as similar to the previous design as possible with a uniform distribution length of 203 mm. However, gi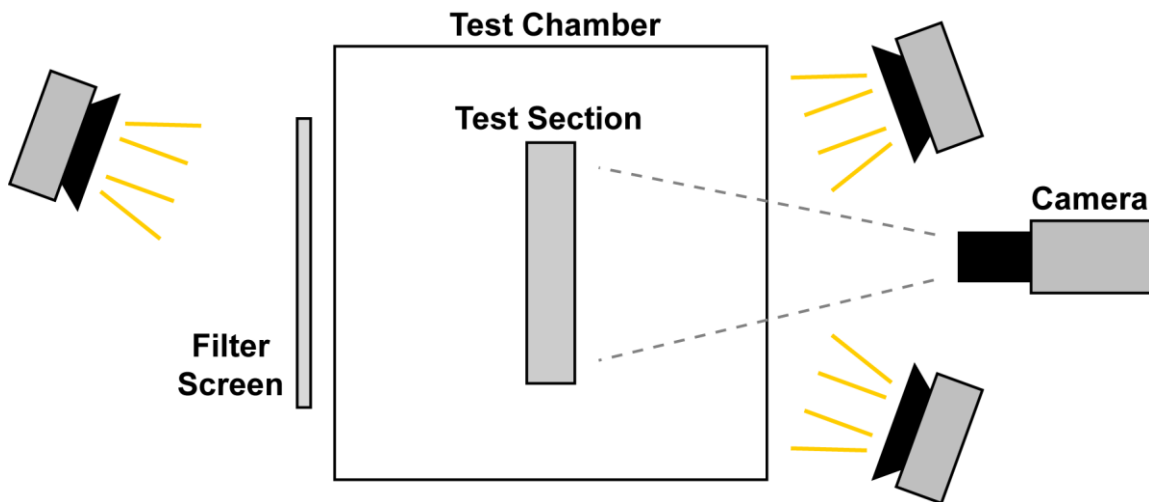ven that each distributor was originally designed for a specific fluid, operating condition, and distribution length, the results of this study should not be used to evaluate their performance under the original operating conditions. A brief description of each design is provided in Table 3.3. Two of these liquid distributors were used for the flow visualization and heat transfer testing. The box-based distributor using an array of small, vertical exit tubes was developed for the flow visualization study to deliver good performance at low flow rates, and the box-based distributor with an array of holes on the bottom and a feeder tube, based on Wang *et al*. (2010), was selected for the heat transfer study based on its performance over a wider flow rate range.

Table 3.3. Brief description of each liquid distributor

Type	Description	Based on
Box	Array of holes on bottom, feeder tube	Wang *et al*. (2010)
	Holes, feeder tube, and 2 foam layers	Roques and Thome (2003)
	Array of small vertical tubes on bottom	Bustamante and Garimella (2012)
	Slot on bottom, fluid enters into a curved plate	Liu and Zhu (2005)
Tube	Array of holes on bottom	Yang and Shen (2008)
	Holes on bottom, stabilizing tube below	Hu and Jacobi (1996a)
	Concentric tubes: inner has an array of holes on top, outer is half a tube over the inner tube	Killion and Garimella (2004a)
	Concentric tubes: inner has an array of holes on top, outer has slot on bottom	Honda *et al*. (1991)

3.1.4.1 *Box-type Distributor Designs*

The first box-type design (Figure 3.8a), based on the design by Wang *et al.* (2010), is an aluminum and Plexiglas rectangular box with dimensions of $241 \times 64 \times 194$ mm (length $\times$ width $\times$ height). The liquid enters into both sides of a feeder tube 204 mm above the bottom of the box. The feeder tube is a 20 mm inner diameter, 26.7 mm mm outer diameter, PVC tube with 41 holes that are 3 mm in diameter and a 5 mm center-to-center distance along the bottom. This tube provides an initial distribution along the length of the box below. The fluid in the box then exits through an array of holes in the bottom plate, made of aluminum with a thickness of 3.1 mm. This plate has 41 holes with
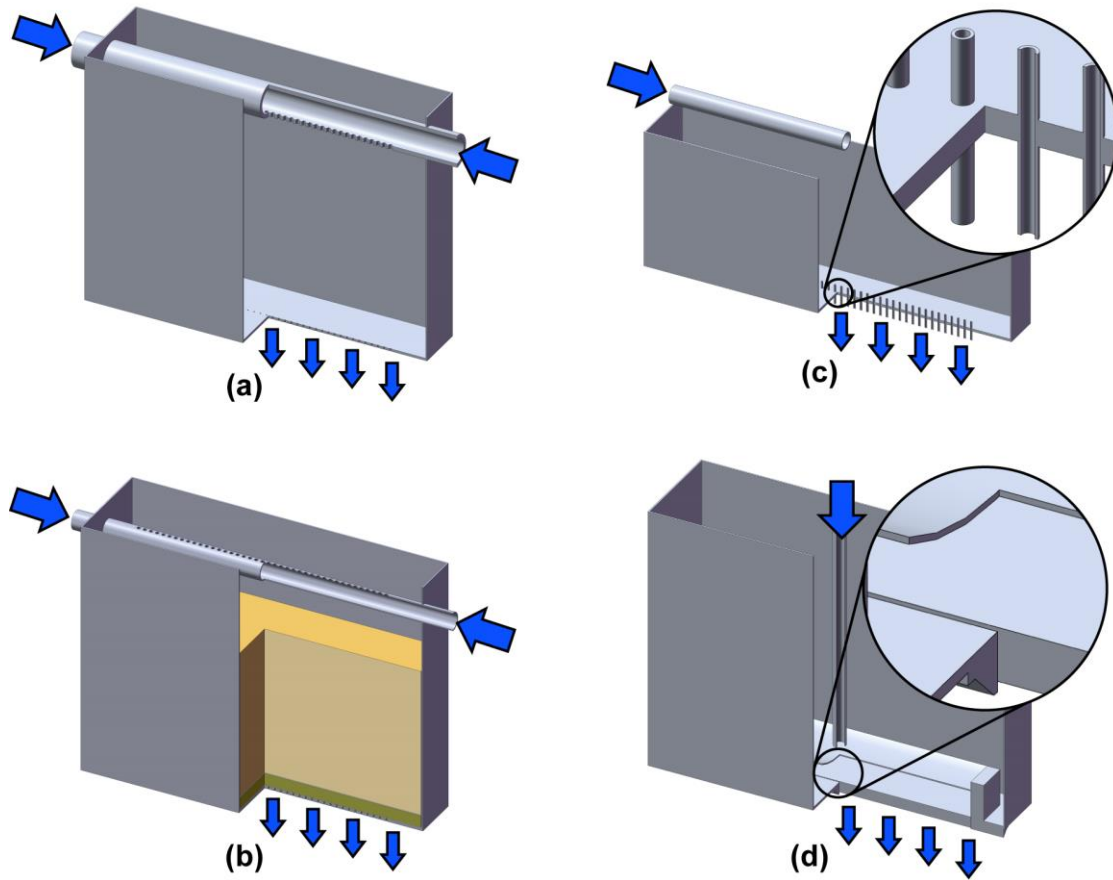

Figure 3.8. Box-type distributor designs: (a) holes and feeder tube, (b) holes, feeder tube, and foam, (c) vertical tubes, (d) slot and curved plate

a 1 mm diameter and a 5 mm center-to-center distance.

The second box-type design (Figure 3.8b), based on the design by Roques and Thome (2003), is an aluminum and Plexiglas rectangular box with dimensions of 241 $\times$ 64 $\times$ 194 mm (length $\times$ width $\times$ height). The liquid enters into both sides of a feeder tube above the main box. The feeder tube is a 14.3 mm inner diameter, 15.9 mm outer diameter, copper pipe with 41 holes that are 3 mm in diameter and a 5 mm center-to-center distance along the top. The flow then passes through two layers of open cell, polyurethane foam, with a density of 44.9 kg m^{-3}. The first layer is 150 mm thick and has a 25% deflection firmness rating of 2.1 kPa, while the second layer is 10 mm thick and has a 25% deflection firmness rating of 4.8 kPa. The second layer of foam has a smaller pore diameter, increasing pressure drop to assist in the distribution of the fluid. After the fluid passes through the foam, it exits the box through an array of holes in the bottom plate, made of aluminum with a thickness of 3.1 mm. There are 102 holes with a 1.5 mm diameter and a 2 mm center-to-center distance.

The third box-type design (Figure 3.8c), developed for the present study and reported by Bustamante and Garimella (2012), is a stainless steel and Plexiglas rectangular box with dimensions of 254 $\times$ 31 $\times$ 83 mm (length $\times$ width $\times$ height). The liquid enters from a tube above the center of the distributor, offset to one side from the exit tube array, and exits through an array of small vertical stainless steel tubes centered on the bottom plate of the distributor, made of stainless steel with a thickness of 1.5 mm. Each vertical tube has an inner diameter of 0.83 mm, an outer diameter of 1.27 mm, and a height of 16 mm, evenly distributed above and below the bottom plate of the distributor. The tubes have a center-to-center distance of 4.75 mm, with a total liquid distribution

length of 203 mm. The small vertical tubes help ensure good lateral distribution of the test fluid by providing evenly spaced sites with an even pressure head for the liquid pool.

The fourth box-type design (Figure 3.8d), based on the design by Liu and Zhu (2005), is an aluminum and Plexiglas rectangular box with dimensions of $241 \times 64 \times 194$ mm (length $\times$ width $\times$ height). The liquid enters from a tube centered 6 mm above a curved plate that provides an initial distribution. The curved plate is constructed of 0.5 mm thick plastic, is 15 mm above the bottom of the box, has a width of 50 mm, a length of 197 mm, and an internal radius of 53.3 mm. After collecting in the curved plate the liquid overflows into the bottom of the box, where it exits out of a slot. The slot is located in a rectangular cutout in the bottom of the box that is 6.2 mm deep, 11.5 mm wide, and 227 mm long. The slot has a width of 1.0 mm, a length of 191 mm, and a depth of 6.4 mm. The exit of the slot on the bottom of the box is a triangular prism 3.5 mm tall and 7 mm wide with 45 degree angles.

3.1.4.2 *Tube-type Distributor Designs*

The first tube-type design (Figure 3.9a), based on a design by Yang and Shen (2008), is a brass tube with an inner diameter of 11.0 mm, an outer diameter of 14.3 mm, and a length of 302 mm. The liquid enters through a vertical tube centered on the top of the distributor, with both ends of the distributor being capped. The liquid exits through an array of 9 holes, each with a 2 mm diameter and a 25 mm center-to-center spacing.

The second tube-type design (Figure 3.9b), based on a design by Hu and Jacobi (1996a), is a brass tube with an inner diameter of 15.9 mm, an outer diameter of 22.2 mm, and a length of 302 mm. The liquid enters from both ends of the brass tube, and exits through an array of 135 holes with a 1.5 mm diameter and a 1.5 mm center-to-center

spacing on the bottom of the tube. An adiabatic tube with the same diameter is placed 1.4 mm below the distributor tube to aid in developing an even distribution.

The third tube-type design (Figure 3.9c), based on a design by Killion and Garimella (2004a), has two concentric copper tubes. The inner tube has an inner diameter of 14.3 mm, an outer diameter of 15.9 mm, and a length of 303 mm. It has an array of 7 holes facing upwards, each with a 1.4 mm diameter and a 31.8 mm center-to-center distance. The outer tube has an inner diameter of 17.7 mm, an outer diameter of 19.0 mm, a length of 236 mm, and is split in half. Only the top half of the outer tube is used. Liquid enters from one side of the inner tube and exits through the holes on the top of the inner
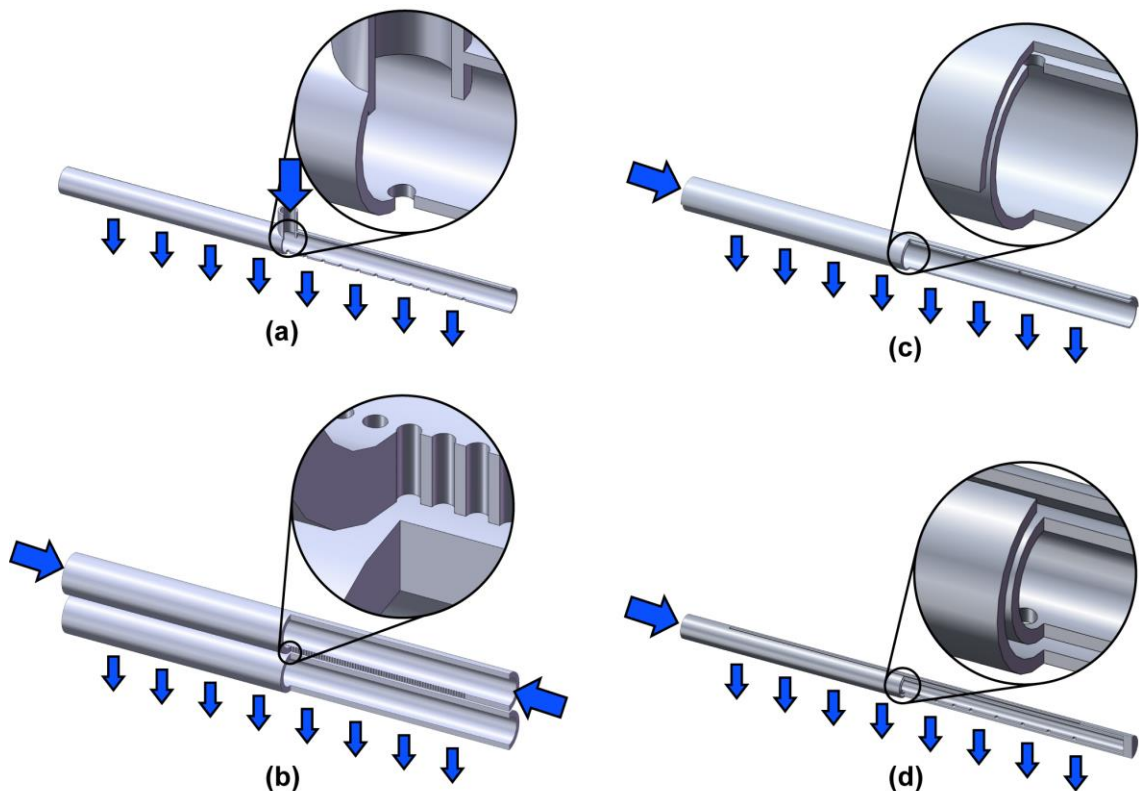

Figure 3.9. Tube-based distributor designs: (a) holes, (b) holes and stabilizing tube, (c) concentric tubes with holes and half-tube, (d) concentric tubes with holes and slot

tube, passing into the annulus between the tubes, and then exiting the annulus as it flows towards the bottom of the tube.

The fourth tube-type design (Figure 3.9d), based on a design by Honda *et al.* (1991), has two concentric copper tubes. The inner tube has an inner diameter of 7.8 mm, an outer diameter of 9.6 mm, and a length of 304 mm. It has an array of 26 holes facing upwards, each with a 1.4 mm diameter and a 5 to 15 mm center-to-center distance. The hole spacing is larger near the liquid entrance and decreases towards the far end of the tube. The initial 5 holes are spaced 15 mm apart, the next 7 holes are 10 mm apart, and the final 14 holes have a spacing of 5 mm. The outer tube has an inner diameter of 11.3 mm, an outer diameter of 12.7 mm, a length of 256 mm, and has a 2 mm wide, 203 mm long slot along the bottom. Liquid enters from one end of the inner tube, exits through the array of holes in the top of the tube into the annulus, and then exits the annulus through the slot along the bottom of the outer tube.

3.2   Experimental Procedures

The experimental procedures used to conduct the heat transfer, flow visualization, and flow distributor studies are described in this section. This includes of discussion of leak testing the system, charging the system, system startup and shutdown, and the methods used to take data points in each study.

3.2.1   Leak testing

After completing assembly of the test facility, leaks in the system were located and removed to limit air ingression into the system under the vacuum test conditions. The presence of air in the system would limit the performance of the condenser plates, lead to

98

an inaccurate calculation of the saturation temperature based on the chamber pressure, and at sufficient levels interfere with the falling-film evaporation heat transfer process.

The leaks were initially located by isolating the primary flow loop from the test chamber. This allowed the primary flow loop to be pressurized with nitrogen. Large leaks were then located using soapy water mixture, which bubbles near leaks. After fixing these leaks, the primary flow loop was pressurized with R-134a and leaks were identified using a refrigerant leak detector (Yellow Jacket AccuProbe Leak Detector, Model# 686800-49365). After removing these smaller leaks, the test chamber and primary flow loop were reconnected, and the total air ingression rate into the chamber was measured by bringing the system to vacuum (~3 Pa) and measuring the pressure rise over 24 hours. Leak rates of under 2 Pa hr^{-1} were achieved using these techniques, with the major part of this air ingression being through the O-ring seals on the test chamber door and rear window.

After the system had been charged with water, the measured pressure rise in the system after being pulled to vacuum was substantially higher due to water desorption from the test chamber surfaces. The measured pressure rise in these situations was approximately 10 to 20 Pa hr^{-1}. This results in a discrepancy between the measured pressure increase in the system and the actual degree of air ingression into the system. This influence could be removed by "baking" the system at vacuum, which requires heating the test facility surfaces while at vacuum pressures to slowly remove water from the surfaces, but doing so required 1 to 2 weeks and was not considered practical during the testing period. Instead, the actual air ingression rate was measured after charging the system with distilled water by comparing the agreement of the measured saturation

pressure and temperature of the system before and after the test period, after giving the system time to come to equilibrium. Heat transfer tests were only conducted when the measured leak rate using this technique was under 5 Pa hr^{-1}, with the majority of tests being conducted with air ingression rates of 3 to 5 Pa hr^{-1}. This corresponds to a measured saturation temperature change of 0.01 to 0.06 °C hr^{-1}. A separate test was conducted comparing these values over 160 hours to ensure that this method successfully captured the air ingression rate.

3.2.2   Charging and discharging the system

To charge the system, the test configuration was first installed in the test chamber, ensuring that the test sections are level with a standard bubble level, and the system was sealed. The system was then evacuated to the lowest reading that could be measured with the installed pressure transducers (0 ± 28 Pa) using a 2-stage direct drive pump rated to 15 microns (JB Industries Platinum Model DV-142N, Serial# 0312), and the system was evacuated for an additional hour to ensure vacuum conditions had been reached. A water tank was attached to an input valve on the system, and the charging line was also evacuated. Afterwards, distilled water was slowly charged into the system using a connection from the bottom of the external tank, ensuring that no air entered the system. Sufficient water was charged into the system to maintain a water level approximately 50 mm deep in the main test chamber, which was necessary to maintain a liquid head on the pumps throughout the experiments.

To discharge the system, a filtered valve in the test chamber was opened to the atmosphere to slowly allow air into the system. When the system reached atmospheric pressure, a valve at the bottom of the primary flow loop was opened and the liquid was

pumped out. Any remaining liquid was removed from the test chamber and primary flow loop using compressed air or nitrogen. Some tests also used heating tape (Omega Engineering Inc., Model# HTWAT051-010) to aid in removing remaining liquid, but gas flow was found to be more effective at removing the bulk liquid. After water was removed with this method, the vacuum pump removed the remaining fluid by evacuating the system.

3.2.3   System startup and shutdown

When starting the system, the fluid and test chamber are at the temperature of the surrounding room, approximately 21°C, corresponding to a saturation pressure of 2.5 kPa. From this state, the pump was first turned on and set to the flow rate of the highest targeted data point in that test run, which begins wetting the test sections. After running at this condition for two hours, the recirculating chiller is used to begin bringing the system to the targeted saturation temperature. The system is kept at this temperature for a period of two hours before beginning any testing, ensuring that the thermal mass of the system has reached steady-state. Then, the preheater and test section electric heaters are powered at the appropriate level, with a corresponding decrease in the chiller temperature to offset the additional heat input. In addition, the flow of the recirculating chiller was redistributed to direct the major part of the flow through the condenser plates.

3.2.4   Heat transfer coefficient measurement

In a single experimental run, heat transfer coefficient measurements were taken for a fixed saturation temperature, heat flux, and tube spacing for a range of mass flow rates. The flow rate was initially set at the highest desired point, and decreased throughout the experimental run. Before taking the first measurement at a high flow rate,

the system was first run for a period of four to five hours to ensure that the tubes were fully wetted, as was described in the system startup procedure. During the first experiments with a newly fabricated test section, this time was increased to eight hours to ensure that the surface finish of the test section would not be modified by the fluid flow, changing the surface roughness and therefore wetting characteristics. After this initial data point, the flow rate was decreased to the next nominal condition. If necessary, the preheater input and recirculating chiller conditions were also adjusted to maintain the correct saturation conditions both at the inlet to the test chamber and the test chamber saturation pressure. The system was kept at steady-state for 15 minutes before taking the next data point. Due to the possible impact of air ingression into the system on the measured heat transfer coefficients and test facility performance, measurements were only taken over a two-day period before discharging and recharging the system. Although methods were tested to remove air from the system, this was found to be more consistent, and only required minimal system discharges in addition to those that would be required due to test section configuration modifications.

The heat transfer coefficient measurements were taken with the LabView interface, with the instrument measurements being captured three times per second for three minutes, a total of 540 measurements with each instrument. These measurements were averaged for the data analysis. In addition, the flow mode at each measurement was recorded. If it was not visually apparent which flow mode was present, high-speed video was used to distinguish between modes. High-speed videos were also taken at some heat transfer data points to allow examination of the flow characteristics.

3.2.5 <u>Flow visualization procedure</u>

The procedure for taking a flow visualization data point was very similar to that used when taking heat transfer data. The same initial startup requirements were maintained, and again the experiments began at the highest targeted flow rate. As above, the system was kept at steady-state for 15 minutes before capturing video. When capturing video, good quality was first confirmed using live feed in the FASTCAM Viewer software. The lights were adjusted as necessary to ensure good visual contrast of the flow features, with a particular focus on droplet and wave boundaries. However, the lights were only turned on during the time a video was being captured due to their high operating temperature and the additional heat input to the test chamber. Video was recorded at a 1024×1024 pixel resolution at 500 fps for the maximum duration allowed by the memory, 512 frames or 1.02 s. The video was saved in AVI format with no reduction in image quality. Each video was then opened and verified to be of good quality before proceeding with additional data points.

3.2.6 <u>Liquid distributor maldistribution measurement</u>

Before taking liquid distributor maldistribution measurements, the flow was first given time to come to equilibrium at the correct temperature and flow rate. This was considered to be two hours for the first data point in a series, and 30 minutes for all subsequent data points. As in the cases above, data were first taken at the highest possible flow rate, and decreased throughout the experimental range. The impact of reversing the progression of flow rates, to account for hysteresis, was examined briefly and found to have a minimal effect. However, this influence was not investigated throughout the full experimental range.

The axial flow rate variation, referred to as the flow maldistribution, of each liquid distributor was measured using the liquid collection box. The liquid collection box was placed under the distributor and liquid was collected until a segment of the box reached 95% of its maximum volume. Then, the box was removed from the flow and a high-speed video was taken for analysis of the resulting droplets and columns. The liquid depth in each collection box segment was measured based on the bottom of the liquid meniscus in each segment, and the liquid was emptied back into the liquid reservoir.

3.3   Test Matrix

Experiments were conducted separately for the heat transfer, flow visualization, and flow distributor studies. Heat transfer coefficient measurements were taken for a range of saturation temperatures, tube spacings, heat fluxes, and flow rates. The nominal conditions of the experiments included saturation temperatures of 10, 15, 20, and 30°C, corresponding to saturation pressures of 1230 to 4250 Pa, tube spacings of 5, 10, and 15

Table 3.4. Heat transfer test matrix

Test Section Spacing [mm]	Nominal Temperature [°C]	Heat Flux [kW m^{-2}]	Mass Flow Rate per Unit Width, $\Gamma \times 10^3$ [kg m^{-1} s^{-1}]								
			16	23	31	37	47	62	78	93	109
5, 10, 15	10	10	×	×	×	×	×	×	×	×	×
		15	×	×	×	×	×	×	×	×	×
		20	×	×	×	×	×	×	×	×	×
	15	10	×	×	×	×	×	×	×	×	×
		15	×	×	×	×	×	×	×	×	×
		20	×	×	×	×	×	×	×	×	×
	20	10	×	×	×	×	×	×	×	×	×
		15	×	×	×	×	×	×	×	×	×
		20	×	×	×	×	×	×	×	×	×
	30	10	×	×	×	×	×	×	×	×	×
		15	×	×	×	×	×	×	×	×	×
		20	×	×	×	×	×	×	×	×	×

mm, heat fluxes of 10, 15, and 20 kW m^{-2}, and flow rates of 0.38, 0.57, 0.76, 0.95, 1.14, 1.51, 1.89, 2.27, and 2.65 L min^{-1}, corresponding to a Reynolds number range of 48 to 544. This resulted in heat transfer coefficient measurements taken at a total of 324 conditions.

The flow visualization experiments were run for a more limited experimental range. High-speed video was taken at a saturation temperature of 17°C, corresponding to a saturation pressure of 1940 Pa, a tube spacing of 10 mm, and a heat flux of 10.8 kW m^{-2}. Videos were taken at linear mass fluxes of 0.0062, 0.0155, 0.0248, and 0.0341 kg m^{-1} s^{-1}, corresponding to a Reynolds number range of 20 to 125. Four videos were taken at each condition during separate experimental runs to account for possible variation in the development of the film-flow characteristics. Wave characteristics were evaluated based on the videos taken at a Reynolds number of 92. The flow visualization study was limited to a lower flow rate range than the heat transfer study because the image analysis techniques were only applicable to droplet flow. Meanwhile, the waves were selected in order in order to examine wave development on smooth film without interaction with other waves. At lower flow rates, waves frequently interacted with dryout regions, while at higher flow rates, waves typically overlapped with other waves.

Table 3.5. Flow visualization test matrix

Video Number	Test Section Spacing [mm]	Temperature [°C]	Heat Flux [kW m^{-2}]	Mass Flow Rate per Unit Width, $\Gamma \times 10^3$ [kg m^{-1} s^{-1}]			
				6.2	15.5	24.8	34.1
1				×	×	×	×
2	10	17	10.8	×	×	×	×
3				×	×	×	×
4				×	×	×	×

The flow distributor experiments were conducted at a temperature of 20°C, atmospheric pressure, and Reynolds numbers ranging from 12 to 495. With each distributor, the experimental range was limited at low flow rates by the capabilities of the pumps, and also by extremely poor distributor performance. Distributor performance was considered to be too low for testing if the flow exited the distributor at a single location and was not providing a distribution, or was missing the collection box entirely due to slinging or other phenomena. Experiments were limited at high flow rates by the capabilities of the pumps, overflow of box-based designs, or poor performance as described above. Many of the distributors could be easily adapted to other flow rate ranges by increasing or decreasing the cross-sectional area of exit features or allowing for increased gravitational head with taller box walls, but these possibilities were not examined in this study.

Table 3.6. Flow distributor test matrix

Type	Based on	Mass Flow Rate per Unit Width, $\Gamma \times 10^3$ [kg m^{-1} s^{-1}]																
		5	8	16	23	31	39	47	54	62	70	78	85	93	101	109	116	124
Box	Wang *et al.* (2010)	×	×	×	×	×	×	×	×	×	×	×	×	×	×	×	×	
	Roques and Thome (2003)			×	×	×	×	×	×	×	×	×	×	×	×	×	×	×
	Bustamante and Garimella (2012)	×	×	×	×	×	×											
	Liu and Zhu (2005)			×	×	×	×	×	×	×	×	×	×	×	×	×	×	×
Tube	Yang and Shen (2008)	×	×	×	×	×	×	×	×	×	×	×	×	×	×	×	×	×
	Hu and Jacobi (1996a)	×	×	×	×	×	×	×	×	×	×	×	×	×	×	×	×	
	Killion and Garimella (2004a)	×	×	×	×	×												
	Honda *et al.* (1991)			×	×	×	×	×	×	×	×	×	×	×	×	×	×	×

CHAPTER 4: DATA ANALYSIS AND RESULTS

This chapter presents the data analysis techniques and results for the flow visualization, heat transfer, and liquid distributor portions of the present study. Each section first describes the approach used to analyze the collected data, followed by the results and a discussion of trends.

4.1   Flow Visualization

The flow visualization study investigated falling films under evaporation conditions. This included qualitative observations of the falling-film flow, as well as quantification of key parameters using a custom image analysis program developed in MATLAB (2010). This image analysis program was used to measure droplet and wave parameters, including the droplet frequency, droplet width, droplet surface area, droplet volume, droplet velocity, wave width, wave velocity, and wave surface area.

4.1.1   <u>Flow visualization analysis</u>

The collected high-speed videos were analyzed mathematically to extract quantitative information on key droplet and wave characteristics. The selected image analysis method is based on the techniques developed by Killion and Garimella (2004a) to examine evolving droplets on horizontal tube banks for absorption systems. Using a semi-automated process, this method identifies the edges of the droplets and waves and fits them with splines. These splines, with appropriate geometric assumptions, are then used to determine the desired droplet and wave parameters.

The image analysis method is semi-autonomous, and begins with the user manually identifying the droplet or wave to be analyzed. Then, the edge of the droplet or wave is detected and fit with a spline. This spline allows the quantities of interest to be determined. A brief description of each of these steps is provided here and shown in Figure 4.2. A more detailed explanation can be found in the work by Killion (2003) and Killion and Garimella (2004a). The entire process is carried out using a program written in the commercial software program MATLAB (2010), with a graphical user interface (GUI) that allows the analysis to be performed efficiently on a large number of video frames. A screenshot of the GUI is shown in Figure 4.1.
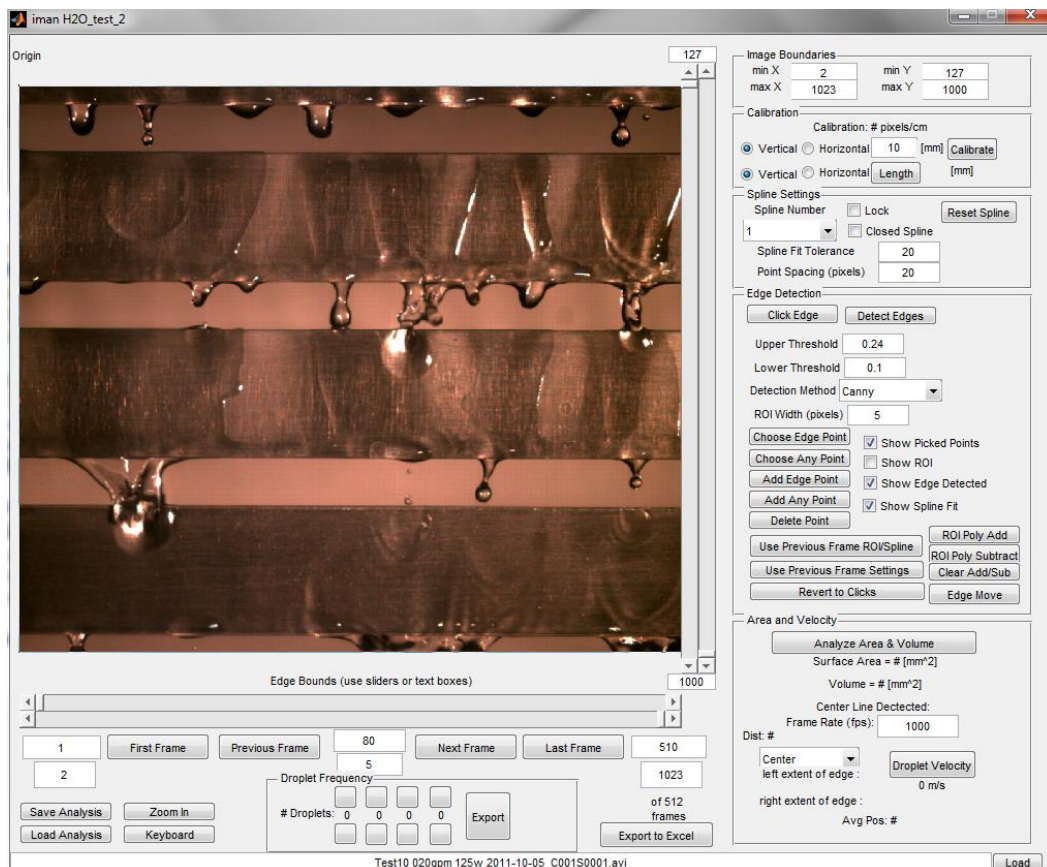

Figure 4.1. Screenshot of image analysis program interface

The first step in the method is the manual identification of the location and approximate shape of the droplet or wave to be analyzed (Figure 4.2a). This step is performed manually due to the difficulty of autonomously identifying the relevant edges among all of those typically present in each video frame. These initial selections are used to define a region of interest (Figure 4.2b), within which an appropriate edge-detection algorithm identifies the edges of the droplet or wave. In this case, the Canny edge-detection algorithm (1986) was selected with appropriate thresholds. For situations where the entire interface was not correctly identified with this algorithm, the edge points could be manually moved as needed. This was required most frequently when analyzing waves, which do not maintain a consistent light gradient along the entire edge of the wave,
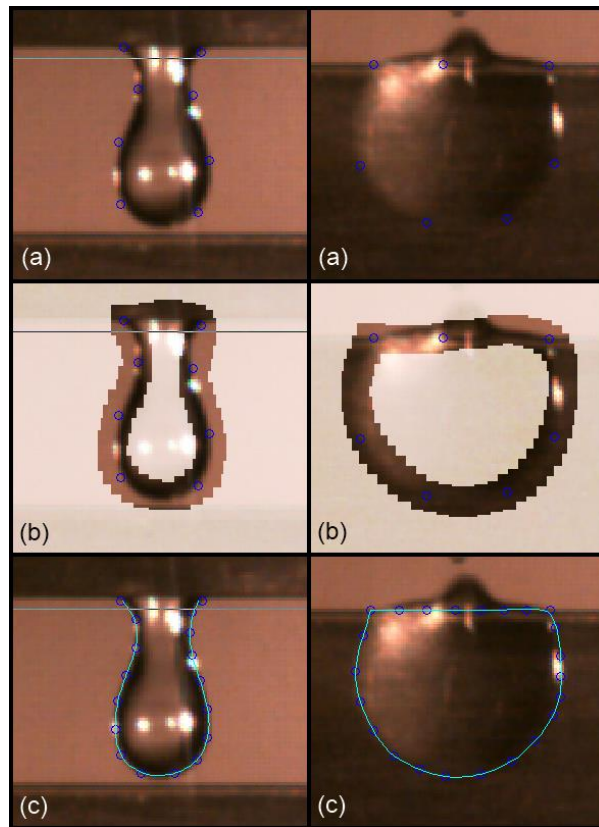

Figure 4.2. Steps of image analysis: (a) manual selection of interface location, (b) region of interest defined, and (c) edge detected and spline fit

making it difficult to identify the entire wave edge with a single set of light intensity thresholds.

The second step in the image analysis process is fitting a spline to the previously determined edges (Figure 4.2c). Splines are piecewise polynomial functions that blend smoothly, allowing the identified edges to be combined into a single curve. The spline algorithms in the MATLAB Spline Toolbox, based on the work of de Boor (1978), were used in this analysis. Splines minimize the strain energy for a function passing through a set of data points, creating a smooth interpolation. This makes them well suited for fitting the surface of a liquid-vapor interface, where surface tension leads to equilibrium states that minimize surface energy or surface area (Killion and Garimella, 2004a).

The final step in the process is using the splines to determine the desired quantities. The width of the waves and droplets is directly calculated based on measured dimensions, and the velocity is determined based on the relative location of the leading edge of the spline across two frames. To determine the surface area and volume of the droplets, it is necessary to assume a cross-sectional profile. Pendant droplet profiles are approximately axisymmetric about their vertical axis; therefore, the vertical axis was used as an axis of revolution to create a three-dimensional shape. The average of the two edges was used as the axis of revolution, and each edge was revolved separately. Each profile was integrated numerically using an adaptive Simpson quadrature method to calculate the surface area and volume. Then, the average surface area and volume from these two revolved edges is recorded. The wave surface was also calculated numerically with an assumed flat profile. In other words, the surface area of the wave spline was calculated without accounting for three-dimensional characteristics. To convert the measured values

from image pixels to metric units, the image was calibrated using the height of a test section. Finally, the droplet frequency was tracked independently using a simple marking system with manual inputs. When tracking the droplet impacts, only the primary droplets were considered, and satellite droplets or other phenomena were not noted.

For both the surface area and volume measurements, the portion of the droplet within 0.5 mm of the top tube is not included. This cutoff is seen as a horizontal line in Figure 4.2 and removes the portion of the droplet that is stretched in the axial tube direction. Because this portion of the droplet is not axisymmetric about the vertical axis, the corresponding surface area and volume would be overestimated by the image analysis program.

To account for possible variation in the development of the film flow characteristics, the image analysis was conducted on videos from four independent tests at each flow rate. Each video was taken during a separate testing period, and the system was discharged and recharged between tests. The droplet measurements were taken on 15 independent droplets taken from these videos. Meanwhile, the wave measurements were taken for three separate waves at 2 ms increments throughout the duration of the wave.

4.1.2 **Flow visualization results**

Flow visualization experiments were run at a saturation temperature of 17°C, corresponding to a saturation pressure of 1940 Pa, a tube spacing of 10 mm, and a heat flux of 10.8 kW m^{-2} over a film Reynolds number range of $23 < Re < 126$. This flow rate range represents the droplet flow regime, bounded by substantial dryout at the low end and the transition to column flow at the high end. Within this range, videos were analyzed at Reynolds numbers of 23, 57, 92, and 126. Wave characteristics were

evaluated based on the videos taken at a Reynolds number of 92. The waves to be analyzed were selected in order to examine wave development on smooth films. At lower flow rates, waves frequently interacted with dryout regions, while at higher flow rates, they typically overlapped with other waves. The following sections describe the qualitative observations of the film flow, followed by the quantitative results of the image analysis. In all figures, Test Section 1 refers to the top test section, Test Section 2 refers to the middle test section, and Test Section 3 refers to the bottom test section.

4.1.2.1 *Progression of the Interface*

The flow patterns over rectangular horizontal tubes are similar to those over horizontal round tubes, which were described in detail by Killion and Garimella (2003). A brief description of the development of a droplet on a horizontal rectangular tube is presented here. Figure 4.3 shows a typical droplet formation, droplet impact, and wave formation from an undisturbed portion of the film. The initial disturbance in the film is
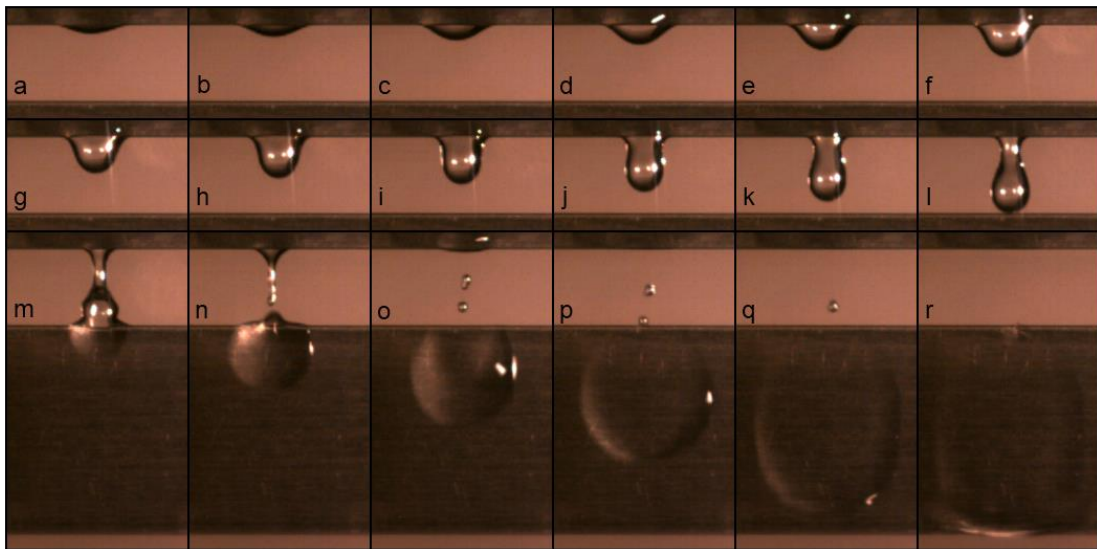

Figure 4.3. Progression of a pendant drop and wave (a-g: 20 ms between frames, g-r: 10 ms between frames)

caused by film instabilities and is stretched in the axial tube direction. A droplet then begins to form as more fluid arrives (Figure 4.3, frames a-e), a process that is often significantly accelerated by the arrival of a wave. As the droplet grows, it elongates downward due to gravitational forces and develops a spherical cap (Figure 4.3, frames f-h). The droplet continues to stretch further and a narrow liquid neck is formed between the droplet and the tube (Figure 4.3, frames i-l). For the geometry under consideration, this liquid neck usually still connects the droplet to the tube when the droplet impacts the next tube. As the droplet forms a wave and begins flowing over the next tube, this liquid bridge between the two tubes breaks up. During breakup, the liquid inventory in this bridge is split into three parts: a portion that joins the droplet and flows over the tube below, the volume that is retracted into the film of the originating tube, and the liquid that forms small satellite droplets between the tubes (Figure 4.3, frames n-q). Each impacting droplet initiates a wave on the tube below. This wave assumes the saddle shape characteristic of flow over round tubes, and is elongated down the tube (Figure 4.3, frames m-r). These waves travel down the tube in the form of roll waves. A thin film is maintained both upstream and downstream of the wave except in areas of dryout, which can cover a significant portion of the tube at low flow rates.

This droplet and wave development pattern is relatively consistent when it is not disturbed by other phenomena, but in many cases, interactions between droplets, waves, and dryout impact the structure and patterns of each phenomenon. This results in many droplets not having a pendant shape, and waves not assuming a saddle profile. In addition, these interactions change the velocity and size of the droplet or wave. For instance, wave arrival during droplet formation can significantly accelerate droplet

113

formation. Such interactions are frequent occurrences, particularly at high flow rates. The possible behaviors resulting from these interactions are similar to those in flow over round tubes, which were documented by Killion and Garimella (2003), and are not discussed in detail here.

Visually, this droplet development process is very similar to that observed for flow over horizontal round tubes, but three notable differences relative to flow over horizontal round tubes were observed. First, the droplet generation process is frequently initiated by the arrival of a wave, whereas on round tubes the initial film disturbance leading to droplet formation is typically attributed to film instabilities. Secondly, due to the longer vertical travel and minimal circumferential travel of the waves on rectangular tubes, the shape they assume is stretched vertically relative to that encountered on round tubes, whereas the wave progresses in a "saddle shape" over round tubes. Finally, due to the narrower thickness of the rectangular tubes and the resulting smaller radius at the bottom of the tubes, the portion of the droplet connected to the tube appears to be stretched more in the axial direction than it would be on a round tube.

4.1.2.2 *Quantitative Droplet and Wave Characteristics*

The droplet impact frequency and the time between droplet impacts are shown in Figure 4.4. In both data sets, only primary droplets are considered. There is no differentiation based on droplet size or formation of temporary liquid bridges, and satellite droplets are not included. Combining the results of the four videos, a total of between 110 and 440 droplet impacts were recorded at each flow rate. As is seen in Figure 4.4, the droplet frequency increases as flow rate increases. This trend is approximately linear for the top two test sections, but there is a noticeably lower impact

frequency for the lowest test section. This suggests that a greater volume of fluid is carried by each droplet flowing between Test Sections 2 and 3. This can take the form of either larger droplets or more fluid movement through the temporary bridges created by droplets. The volume of the droplets does not increase significantly with flow rate, suggesting that fluid movement through temporary bridges is the dominant influence responsible for this trend. In addition, the time between droplet impacts is shown in Figure 4.4. The droplet impact distribution appears to be stochastic at all flow rates. This is different from the typical assumptions regarding fluid flow between tubes in falling film models, which often assume either continuous sheet flow or regularly spaced droplets. This droplet impact behavior will in turn affect the heat transfer coefficient of each tube. The timing and number of the droplet impacts will determine the level of waviness and mixing on each tube, and the changing amount of fluid transport through temporary liquid bridges could be a significant factor influencing heat transfer in tube banks.

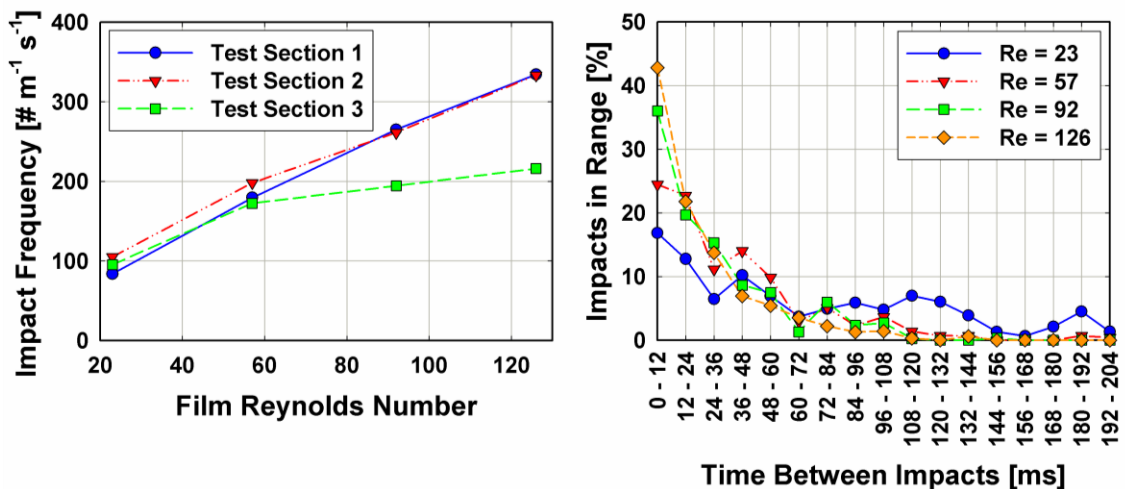The droplet width, surface area, volume, and velocity at time of impact are shown

Figure 4.4. Droplet impact frequency and time between droplet impacts

in Figure 4.5. Droplets experience a continuous increase in size and velocity up to the moment of impact; this point represents the maximum of these values during the development of a given droplet. In addition, this moment is most relevant to models of heat transfer on the tube surface because the droplet development has a minimal influence on the heat transfer relative to the influence of the droplet impact and resulting phenomena, and thus was selected as the focus of this portion of the study. Only pendant droplets were included in the analysis due to the limitations of the information that could be extracted from the video frames. Because the video was taken only from one side of the test section and not also from the orthogonal axis, features that are not axisymmetric can only be analyzed in a limited fashion. Many irregular droplet shapes were created by interacting phenomena, but are not axisymmetric about the vertical axis and thus would
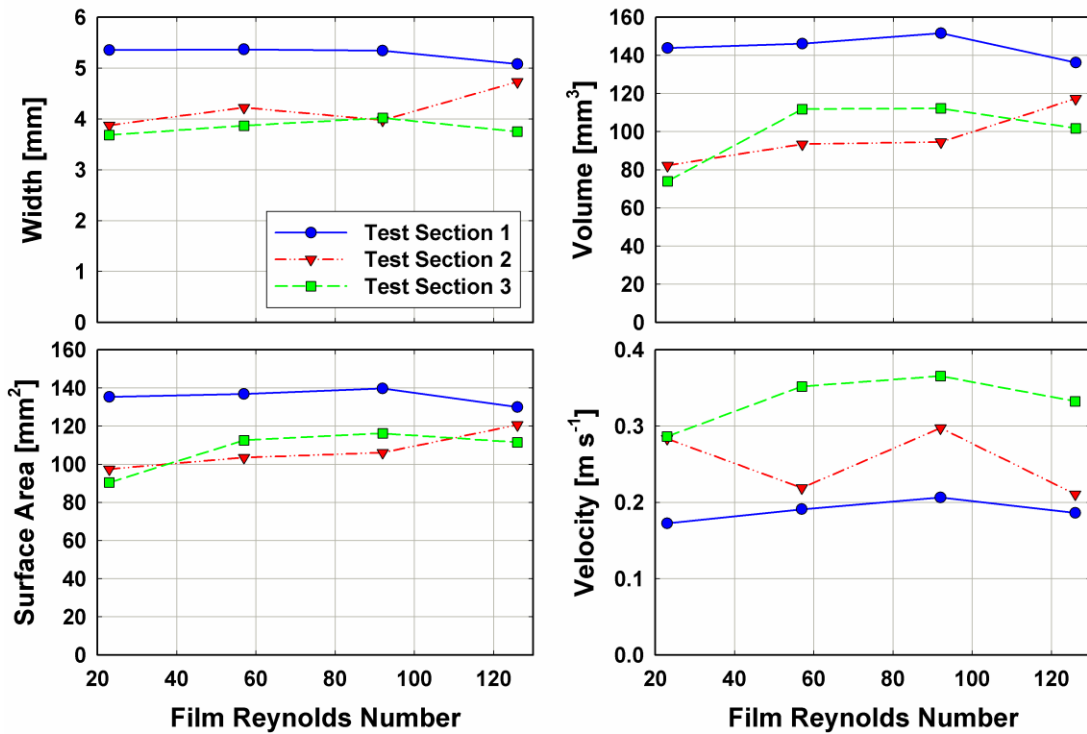

Figure 4.5. Droplet width, surface area, volume, and velocity. Each data point is the average of 15 measurements from four videos.

not be accurately represented by the assumptions of the image analysis method used here. The velocity of the droplets is measured from the leading edge of the droplet, which is the lowest point in the droplet, and may not be representative of the average velocity of the total droplet. As is seen in Figure 4.5, the droplet width, surface area, and volume are not significantly influenced by film Reynolds number. Test Sections 2 and 3 have similar droplet sizes, but droplets for Test Section 1 are substantially larger. This can be attributed to the influence of the liquid distributor. The droplet velocity increases as the test section number increases, but again, the film Reynolds number has a negligible influence on this parameter. This increasing velocity is different from the observed behavior on round tubes, where it is typically assumed that the fluid stagnates at the bottom of each tube, and thus would have the same velocity passing between each tube row. In tube banks consisting of several tube rows, this increasing velocity and the resulting fluid inventory carried could lead to higher levels of dryout on lower tubes and limit heat transfer performance.

The wave width, surface area, and velocity are shown in Figure 4.7, and Figure
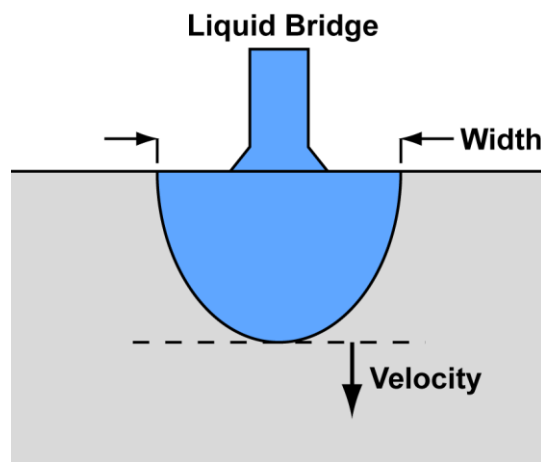
Figure 4.6. Wave and liquid bridge on a test section, with the location of the wave width and velocity measurements

4.6 demonstrates the maximum wave width and velocity measurements. The wave measurements were taken on each video frame, and in this figure, each data point is an average over 10 ms, or 5 frames. In contrast to the previous data sets, which showed averages of single points across several videos, Figure 4.7 displays the development of a single wave over time. This is considered more relevant to heat transfer models, as film waviness can significantly enhance heat transfer, and thus the entire wave residence time is important. The wave development is shown from the time of droplet impact to when
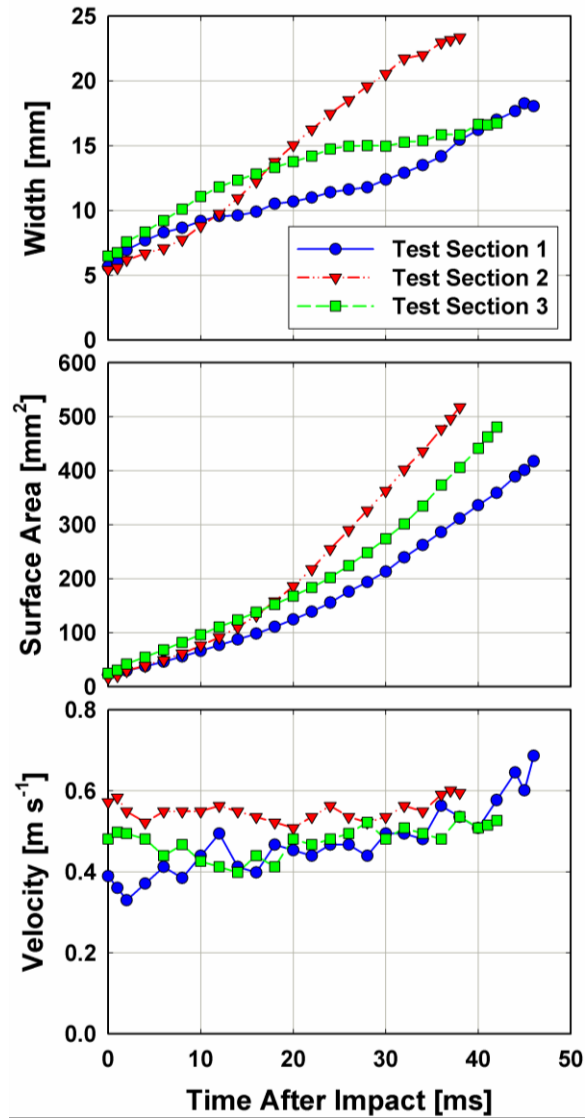

Figure 4.7. Wave width, surface area, and velocity

the wave reaches the bottom of the tube, after which it becomes less distinct and either flows to the bottom of the tube or is absorbed into the film. Three wave developments are shown, all taken at a single flow rate corresponding to $Re = 92$. The width is measured as the maximum width of the wave, and the velocity is again taken from the leading edge of the wave, which is the lowest edge of the wave. The surface area is only that of one side of the tube, and is half of the total surface area resulting from a single droplet if even flow distribution on each side of the tube is assumed. Visually, the waves resulting from droplet impact appeared to be roll waves, which are dominated by gravitational and inertial forces, rather than surface tension. The maximum wave width increases with time after impact, but the width of each wave exhibits a unique trend throughout its development. This may indicate that different amounts of fluid are being supplied by the droplet and liquid bridge providing the liquid for the wave. Despite this, the surface area coverage by each wave exhibits a similar trend, with the surface area increasing throughout the development of the wave. Given that the wave surface area continues to increase after further fluid is no longer being delivered by the droplet and liquid bridge, the average wave thickness must be decreasing, reducing the conductive heat transfer resistance as the wave spreads into a thin film. Meanwhile, the velocity remains approximately constant throughout the wave development, with only a slight increase observed in one wave. This is consistent with the expected performance of roll waves, which maintain a relatively constant velocity as they travel down a wall (Patnaik and Perez-Blanco, 1996). Roll waves are characterized by a relatively steep wave front and then smoother slope back to the film thickness after the wave crest. The velocity of the wave will result in a lower convective heat transfer resistance during its passage. In

119

addition, it will mix the fluid from the droplet with the fluid on the tube, replenishing the thin film that is being evaporated by heat transfer from the tube. This aids in avoiding dry spots on the tube, which have a substantially lower heat transfer coefficient.

Some of the results described above can be directly compared with data available for falling films on horizontal round tubes. Yung *et al.* (1980) reported that the droplet diameter could be predicted by Equation (4.1), where a_0 is an empirical constant found to be 3.0 in their study using ethyl alcohol and water at 20°C and tubes with a 38 mm diameter.

$$d = a_0 \sqrt{\frac{\sigma}{\rho g}} \tag{4.1}$$

This correlation predicts a droplet diameter of 8.2 mm for the present conditions, whereas diameters in the range of 3.5 − 5.5 mm were observed in the present study. This deviation can be attributed to the much larger diameter of the tubes examined in their study. Killion and Garimella (2004a) examined pendant droplets over tubes with a 15.9 mm diameter and a tube-to-tube spacing of 15.9 mm using aqueous lithium-bromide, and measured a maximum droplet surface area of 180 mm^2, and a droplet volume of 200 mm^3. The present study measured droplet surface areas and volumes ranging from 90 to 140 mm^2, and 70 to 150 mm^3, respectively. As in the case of droplet diameter, the present study observed smaller droplets. Yung *et al.* (1980) found that the wavelength corresponding to droplet spacing can be predicted by Equation (4.2), where the constant a_0 has a value of 2 if the film is relatively thin.

$$\lambda = 2\pi \sqrt{\frac{a_0 \sigma}{\rho g}} \tag{4.2}$$

This correlation predicts a droplet spacing of 24.3 mm for the conditions of the present study. The droplet frequency data collected here are not sufficient to directly calculate the droplet spacing for comparison. To enable this, the time between droplet impacts was manually measured for 5 sets of droplet impacts at a film Reynolds number of 34, corresponding to the droplet development shown in Figure 4.3. The average time between impacts for this condition was 0.31 s. Combining this information with the measured droplet frequency data suggests that the average droplet spacing ranged from 23.8 to 28.1 mm. Thus, good agreement is seen between the droplet spacing predicted by the Yung *et al.* (1980) correlation and those observed in the present study.

These results can provide valuable guidance for the development of accurate, phenomena-based heat transfer models of falling-film evaporation over horizontal rectangular tube banks. For instance, the portion of tubes wetted by the film has a significant influence on the overall heat transfer coefficient. This effect is more significant at low flow rates, where dryout is expected to be greatest. To accurately model the heat transfer performance of this situation, an accompanying hydrodynamic model that predicts this wetting behavior is necessary. The development of such a model for the present study is described in Chapter 5. The results from the present study can guide and confirm the droplet and wave characteristics predicted by this hydrodynamic model. Meanwhile, modeling the film heat transfer enhancement due to waves requires assumptions regarding the development of these waves. The present work can again guide and validate these assumptions using the collected values for width, surface area, and velocity over time.

4.2   Heat Transfer

This section presents the analysis and results for the experimental heat transfer coefficient measurements. Calculations were conducted on the Engineering Equation Solver (EES) platform (Klein, 2013), which also provided necessary the fluid properties. The uncertainty analysis was carried out using the EES uncertainty propagation feature, and is described with a sample calculation in Appendix C. For clarity, this section presents the analysis of a representative data point for the case of water at a pressure of 4247 Pa, flow rate of 0.0927 kg m^{-1} s^{-1}, tube spacing of 10 mm, and heat flux of 13.9 kW m^{-2}. A sample calculation is shown in Appendix A.

4.2.1   <u>Heat transfer analysis</u>

Before taking each heat transfer data point, the flow regime was manually noted. In cases where the regime was not apparent from a visual observation through the acrylic door of the test chamber, a short video was taken. The flow regime definitions were based on the transition criteria of Roques *et al.* (2002), who divided the flow into the droplet, droplet-jet, jet, jet-sheet, and sheet modes. These transition definitions are applied to the flow between the stabilizing tube and the top test section. The droplet mode existed when only droplets traveled between the stabilizing tube and test section, and there is not a continuous liquid link between the two. The flow is in droplet-jet mode when at least one stable liquid column or jet connects the stabilizing tube to the test section. The jet mode is observed when there are only stable liquid columns or jets connecting the stabilizing tube and test section. The transition to jet-sheet mode is considered to occur when at least one liquid sheet is formed, typically by merging two or more liquid jets. Finally, the flow is in sheet mode when only one continuous sheet exists.

For all of the above transitions, the droplet, jet, or other flow feature closest to each end of the tube was not considered due to possible edge effects.

The average heat transfer coefficient for each test condition was calculated by first finding the local heat transfer coefficient corresponding to each test section wall temperature measurement, and then averaging these across the surface. The local heat transfer coefficients are found using the heat duty, saturation temperature, wall temperature, and tube area.

$$\frac{Q_{\text{TS}}}{8} = h_{\text{TS},i}\left(\frac{A_{\text{TS}}}{8}\right)\left(T_{\text{wall},i} - T_{\text{sat}}\right) \tag{4.3}$$

$$A_{\text{TS}} = 2L_{\text{TS}}\left(H_{\text{TS}} - 2R_{\text{TS}}\right) + 2\pi R_{\text{TS}} L_{\text{TS}} \tag{4.4}$$

$$h_{\text{avg}} = \frac{1}{8}\sum_{i=1}^{8} h_{\text{TS},i} \tag{4.5}$$

Heat input to the test section is directly measured with the watt transducer attached to the internal electric heater. In general, the measured heat input to a test section should be adjusted to account for the conductive losses to the mounting frame, as well as the radiation heat transfer to or from the surroundings. However, in this case, the conduction losses are minimal due to the small temperature difference between the test section and frame, as well as the small contact area, and were neglected. A conservative calculation of the radiation heat transfer to or from the test section found it to have a minimal effect as well (<0.1% of heat duty), and it was also neglected. The details of this radiation calculation are provided in Appendix B. The measured heat input, as well as the surface area known from the fabricated geometry, are divided by eight so that only the heat duty and surface area corresponding to a single wall thermocouple measurement are considered. For the sample data point, the heat input, Q_{TS}, is 159 ± 5 W, and the surface

123

area, A_{TS}, is 0.0115 ± 0.00003 m^2. A measurement uncertainty of ± 0.05 mm was assigned to the test section length, width, and corner radius to determine the uncertainty of this area.

The local wall temperatures are measured using eight thermocouples located in each test section. However, these measurements are taken at a point inside each test section, and must be adjusted to calculate the external wall surface temperature, T_{wall}, used to calculate the local heat transfer coefficients. This difference is due to conduction and contact resistance. Both of these influences were estimated using a 2D model in COMSOL (2013). The details of this model, and all of the calculations described below, are shown in Appendix B. This model estimated that both influences are relatively minimal. Conduction through the wall results in a maximum difference of 0.07°C between the thermocouple measurement and either wall temperature reading. Rather than incorporating this minimal difference into each heat transfer coefficient calculation, the maximum predicted temperature difference (± 0.07°C) was added to the uncertainty of the wall temperature measurement. The COMSOL model also predicted that thermal contact resistance would only lead to an additional 0.002°C difference between the thermocouple reading and the wall temperature measurement, and was neglected. In addition, this model was used to estimate the influence of fabrication errors associated with the solder fill in each thermocouple groove. These were also found to be minimal, with a maximum influence of 0.10°C, even with conservative assumptions. In addition, a test section was disassembled and such fabrication problems were not in evidence. Thus, it is not expected to have an influence on the heat transfer coefficient measurements. The wall temperatures for the sample data point range from 32.6 to 39.9°C, as seen in Table 4.1.

The saturation temperature is calculated based on the pressure inside the test chamber. This saturation temperature was used, rather than the measurements of the thermocouples in the test chamber, because it is more uniform and generally results in lower uncertainty. However, over time air slowly leaks into the test chamber, causing a difference between the measured chamber pressure and the saturation pressure of the fluid. The level of air ingression was measured by comparing the agreement of the measured chamber pressure with the saturation pressure calculated from the three thermocouples in the test chamber. This air ingression rate was measured before each system discharge, after allowing the test chamber to come to equilibrium. In the uncertainty calculations, a conservative 25% uncertainty was assigned to this air ingression rate. Tests were only conducted with air ingression rates under 5 Pa hr^{-1}. For the sample data point, the leak rate was measured to be 3.5 Pa hr^{-1}. The data point was taken 23 hours after sealing the chamber, resulting in a total pressure leak of 80.5 ± 20.1 Pa. This is subtracted from the measured chamber pressure, 4247 ± 28 Pa, to find the saturation pressure of 4167 ± 35 Pa. This results in a saturation temperature of 29.7 ± 0.14°C. This method was verified with a 160 hr test, as shown in Figure 4.8. In the figure, the black line represents the temperature measured by the thermocouples in the test chamber, while the blue line is the saturation temperature at the measured pressure. Air ingression caused the difference between the measured temperature and the saturation temperature calculated from chamber pressure to drift by ~4°C over this test period, as shown with the dashed blue line. However, adjusting the saturation temperature with the measured leak rate (5.3 Pa hr^{-1} for this test) gives much closer agreement, shown with the

red line. This resulted in a maximum temperature difference of 0.18°C, the dashed red line in the figure, and was well within the measurement uncertainty of the thermocouples.

After determining the saturation temperature, the temperature difference between each wall temperature measurement and the saturation temperature was calculated. For the sample data point, this difference ranged from 2.9 to 10.2°C, as seen in Table 4.1. Any thermocouple readings with a ΔT of under 1.0°C were not used in the average heat transfer coefficient calculation. The uncertainty of the temperature measurements was the largest contribution to heat transfer coefficient uncertainty, and ΔTs under this level resulted in an uncertainty over ~50% in the local heat transfer coefficient. This was generally only a concern at the lowest heat flux (10 kW m^{-2}) tested, and occurred in just 2.2% of the local temperature measurements (58 of 2,592).
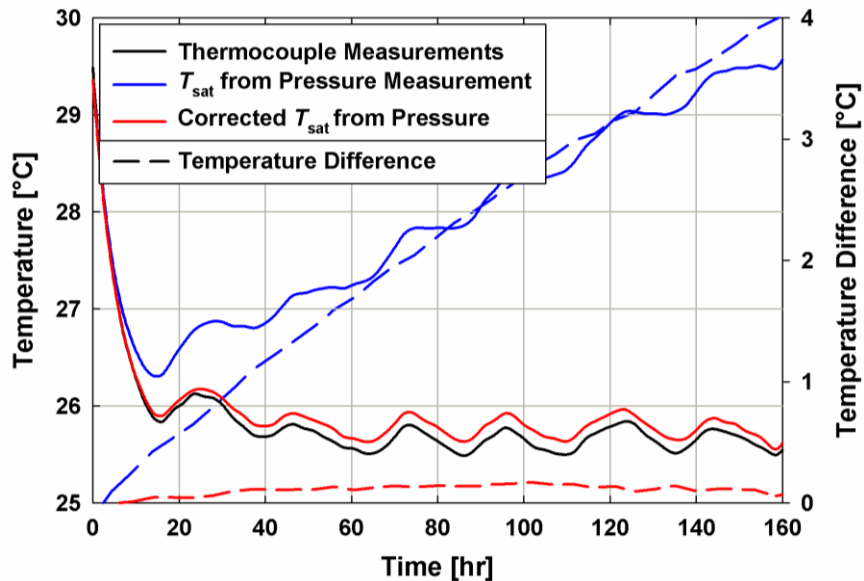

Figure 4.8. Difference between measured temperature and temperature calculated based on chamber pressure before and after correction for air ingression
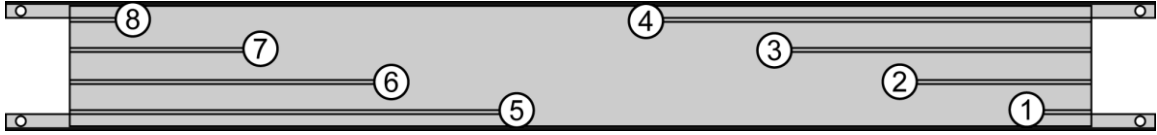
Figure 4.9. Location of local thermocouple measurements.

After these quantities have been calculated, the local heat transfer coefficients can be found using Equation (4.3). The local heat transfer coefficients for the sample data point varied from 1354 to 4740 W m^{-2} K^{-1}, as seen in Table 4.1. These values can vary significantly due to the different liquid flow patterns and levels of wetting present on or near each thermocouple. Averaging these values, the sample data point has an average heat transfer coefficient of 2871 $\pm$ 170 W m^{-2} K^{-1}.

The average heat transfer coefficient is non-dimensionalized using the Nusselt number, shown in Equation (4.6), and the film Reynolds number at the given condition is calculated using Equation (4.7).

$$Nu = \frac{h}{k}\left(\frac{\mu^2}{\rho^2 g}\right)^{1/3} \tag{4.6}$$

$$Re = \frac{4\Gamma}{\mu} \tag{4.7}$$

Table 4.1. Heat transfer coefficient

Thermocouple Number	T_{wall} [°C]	T_{sat} [°C]	ΔT [°C]	$h_{TS,i}$ [W m^{-2} K^{-1}]	h_{avg} [W m^{-2} K^{-1}]
1	34.2±0.37		4.5±0.40	3049±282	
2	33.9±0.37		4.2±0.40	3261±321	
3	39.9±0.37		10.2±0.40	1358±68	
4	39.9±0.37	29.7±0.14	10.2±0.40	1354±67	2871±170
5	34.0±0.37		4.4±0.40	3179±306	
6	35.4±0.37		5.8±0.40	2407±182	
7	33.5±0.37		3.8±0.40	3618±391	
8	32.6±0.37		2.9±0.40	4740±659	

4.2.2 Heat transfer results

This section presents the flow regime observations and heat transfer coefficient data. The observed flow regimes are shown in Figure 4.10. In the test matrix considered in the present study, there were a total of 57 data points in the droplet mode, 112 data points in the droplet-jet mode, 21 data points in the jet mode, and 134 data points in the jet-sheet mode. These data are plotted against test section spacing, temperature, heat flux, and flow rate in Figure 4.11. As expected, it can be seen that there is a clear relationship between the mass flow rate and the flow regime. At low flow rates, the droplet mode is observed, and as flow rate increases, the mode transitions to the droplet-jet, jet, and then jet-sheet mode. If the flow rate were increased even further, a transition to full sheet mode would be expected, although no sheet mode flow was observed in this study. In addition, there appears to be a relationship between the flow regime and tube spacing.
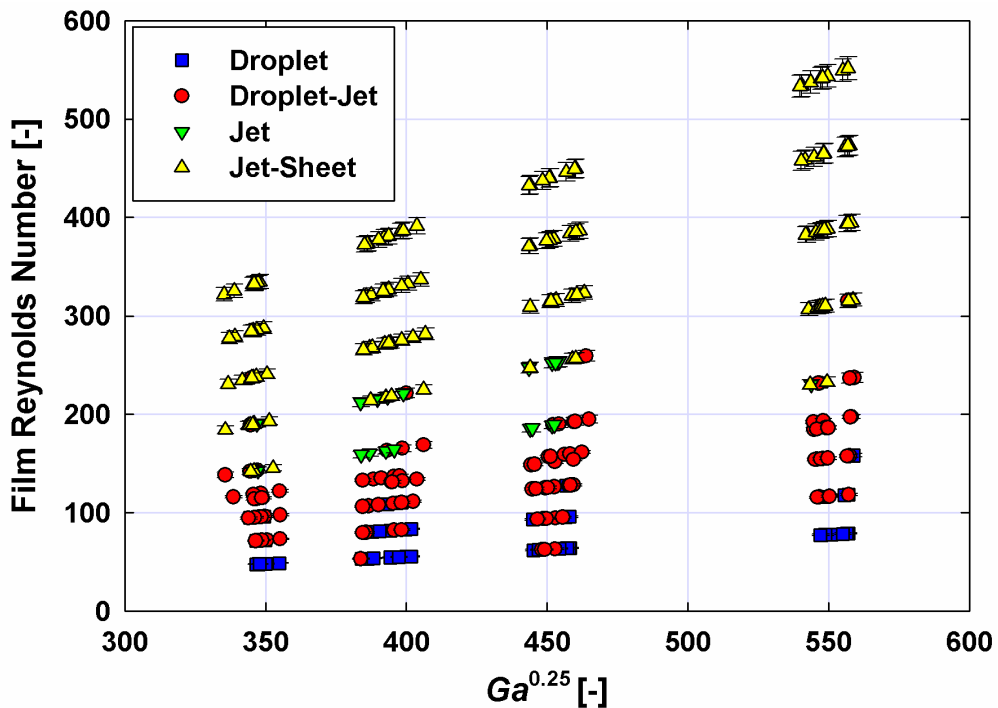

Figure 4.10. Flow regime observations

Increasing the test section spacing appears to result in all of the flow mode transitions occurring at higher flow rates. For instance, at a mass flow rate per unit width, Γ, of 0.047 kg m^{-1} s^{-1} with a 5 mm test section spacing, 33% of the data points are in the droplet-jet regime, but with a 15 mm test section spacing, 92% of the data points are in the droplet-jet regime. Physically, this trend is expected, as a larger intertube distance allows more height for jets to break up into droplets, or sheets to break apart into jets. As this height is increased, the speed of a falling jet increases, decreasing the jet's diameter, and ultimately leading to breakup into droplets. This breakup is driven by a combination of surface tension and inertial forces. Small instabilities in the jet are amplified, causing a
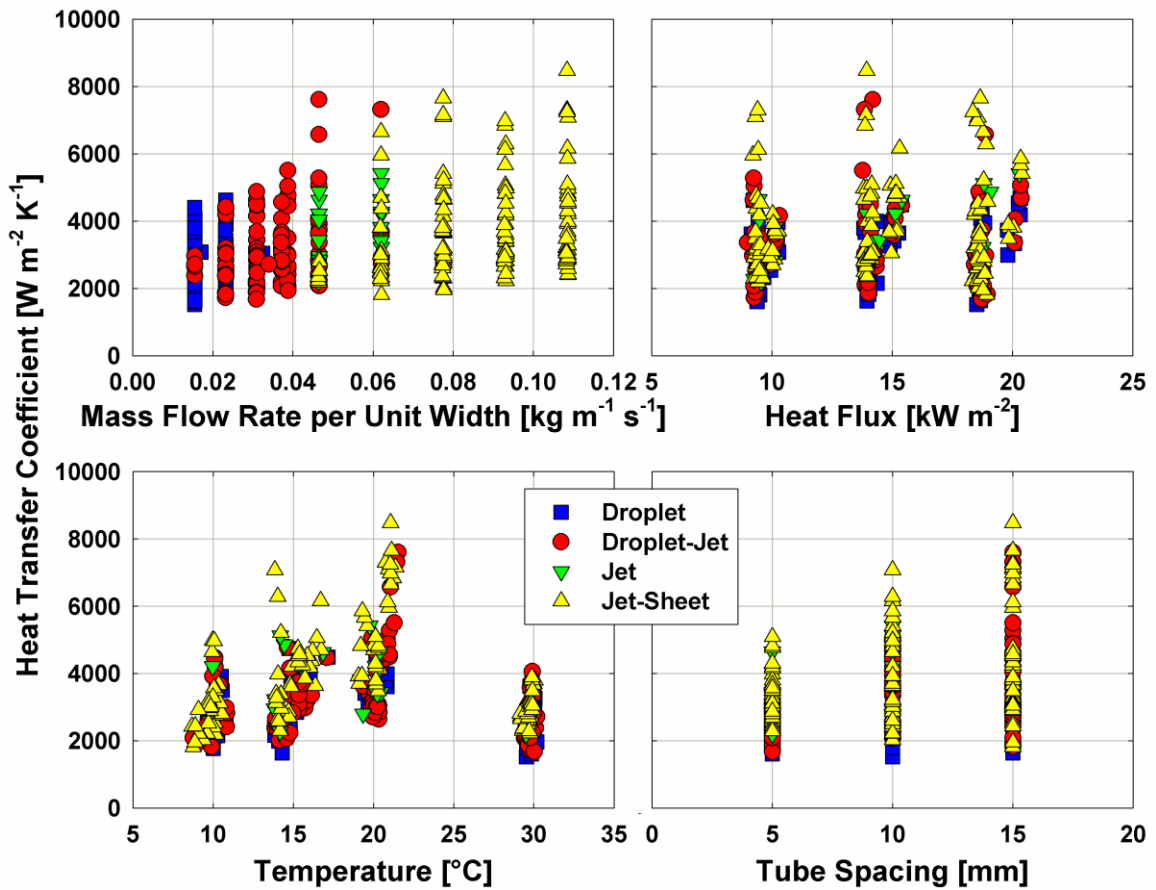

Figure 4.11. Experimental heat transfer coefficient versus mass flow rate, heat flux, temperature, and tube spacing

129

breakup into droplets (Carey, 2008). A similar trend would be expected with the breakup of sheets into jets. Finally, there is expected to be a relationship between the flow rate at which mode transitions occur and temperature due to the change in fluid properties. As discussed in Chapter 2, the transitional Reynolds number is expected to increase as surface tension or liquid density increases, and decrease as viscosity increases. Surface tension and inertial forces directly contribute to the breakup of jets into droplets and sheets into jets by promoting the growth of instabilities. Thus, increases in either surface tension or density allow droplets and jets to persist at higher mass flow rates. This shifts the transition out of the droplet mode into the jet mode, and out of the jet mode into the sheet mode, to higher mass flow rates. Viscosity has a minimal influence on transitional mass flow rate, and only impacts transitional Reynolds number due to the viscosity term in the film Reynolds number definition. At high viscosities, shear stress reduces the velocity of the fluid on the test section, but generally, the fluid stagnates at the bottom of the tube due to surface tension forces, and thus, the viscosity does not significantly influence the flow pattern below. In the intertube region, viscosity also has a minimal influence because the shear stress between the liquid and vapor is negligible relative to gravitational and surface tension forces, particularly for the low vapor pressures and test section spacings examined in the present study. In the present data set, the surface tension and density of the liquid only change by 4.2% and 0.2%, respectively, while the viscosity changes by 64%. There are not substantial enough changes in surface tension or density of the fluid to observe their expected influences on transitional flow rate. Thus, no clear relationship is observed between the transitional mass flow rate and temperature, and the transitional Reynolds number decreases as viscosity increases.

Figure 4.11 also demonstrates the general relationship between the measured heat transfer coefficients and each parameter that was varied in the test matrix. Heat transfer coefficient increased as mass flow rate or tube spacing was increased, first increased and then decreased as temperature was increased, and there was no significant relationship between heat transfer coefficient and heat flux. These relationships are discussed further after an overview of the uncertainty present in the experimental measurements is discussed.

The primary contribution to the heat transfer coefficient uncertainty is the uncertainty of the wall temperature and saturation temperature measurements. A lower temperature difference between these values results in a high overall uncertainty. Figure 4.12 plots this temperature difference for all 2,592 local heat transfer coefficient measurements. Two measurements are over the y-axis scale maximum of 40°C and do
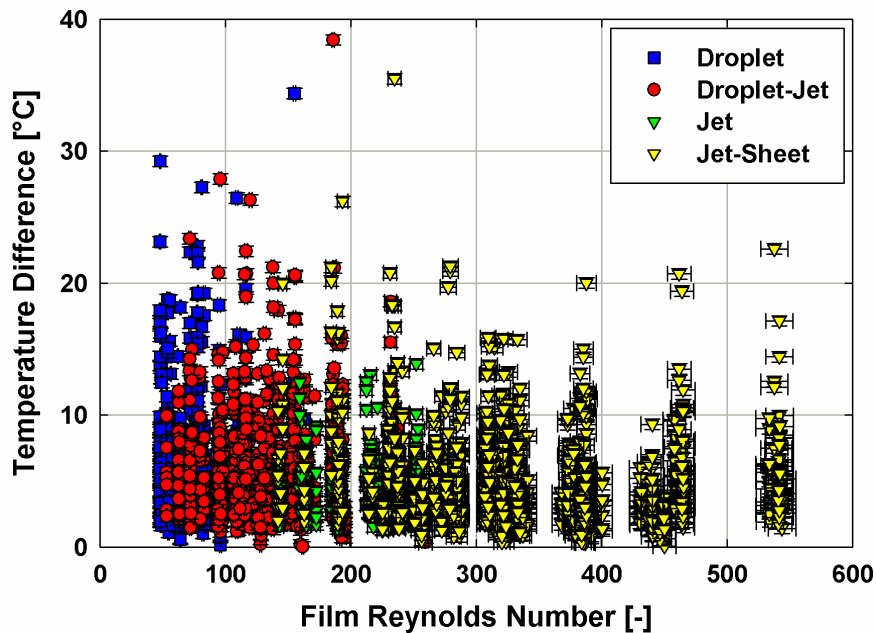

Figure 4.12. Difference between local wall temperature and saturation temperature

not appear in the figure. A maximum temperature difference of 50.8°C was observed with an average value of 5.7°C. Under most conditions, this large of a temperature difference would cause boiling in the flow, but there was no boiling in the present study because these high temperature differences only occurred in areas with dryout. For instance, Carey (2008) finds that the minimum superheat for bubble growth beyond the mouth of wall cavities in pool boiling is given by Equation (4.8), where R is the smallest active cavity radius.

$$T_{\mathrm{w}} - T_{\mathrm{sat}} = \frac{2\sigma T_{\mathrm{sat}}}{\rho_{\mathrm{v}} h_{\mathrm{lv}} R} \qquad (4.8)$$

For the conditions of the present study, this model predicts that, even with cavities that are only 0.01 mm in diameter, boiling would begin with a superheat of $11.6 - 12.7$ K. However, this analysis considers quiescent fluid. For comparison, in falling-film evaporation tests with water over round tubes, Parken *et al.* (1990) found that boiling began near a heat flux of 30 kW m^{-2}, and with low pressure (1000 Pa) water Li *et al.* (2011a) observed no boiling up to heat fluxes of 27 kW m^{-2}, while heat fluxes of up to 20 kW m^{-2} were investigated in the present study. In addition, no boiling was visually observed during the present study, although it was easily observed at heat fluxes above those in the test matrix, even without high-speed visualization. Thus, these high local temperature differences must be in regions without fluid and can be attributed to dryout.

Fifty-eight measurements, or 2.24% of measurements, had a local temperature difference below 1°C, which was used as a cutoff to exclude data points with unacceptably high uncertainty. This temperature difference was influenced by heat flux and the local heat transfer coefficient. The temperature difference increased as heat flux increased, and decreased as the local heat transfer coefficient increased. However, in

these experiments, increasing heat flux further to lower uncertainty was often not an option, as it would cause boiling in the flow, substantially changing the overall fluid flow and heat transfer behavior. In addition, at high heat fluxes, local overheating of the test sections could occur in areas with dryout, damaging the internal electric heaters.

The local temperature differences and heat transfer coefficients are shown versus location along the test section in Figure 4.13. In this figure, the location is measured as the length from the left side of the test section using the front view shown in Figure 4.9; i.e., thermocouple number 8 is located at a position of 12.7 mm. This plot includes all 2,592 local temperature differences and heat transfer coefficients—324 at each location along the tube. There is a wide variation in local heat transfer coefficients at each location along the tube. This variation is due to the wide variety of local flow conditions, and is strongly influenced by the presence of dryout either on or near the thermocouple location. In addition, the local heat transfer coefficient is influenced by the vertical location of the thermocouple on the tube. In the presence of a liquid film, the highest heat transfer coefficients are found at the top of the tube (at positions 12.7 mm and 114.3 mm in
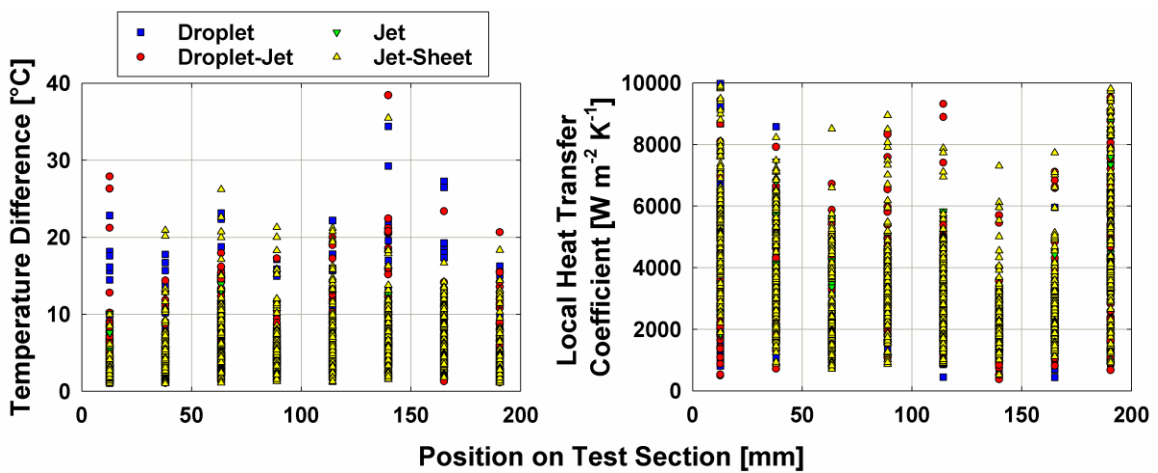

Figure 4.13. Local temperature difference between the saturation temperature and wall temperature and the local heat transfer coefficient versus position along the test section

133

Figure 4.13) and bottom of the tube (at positions 88.9 mm and 190.5 mm in Figure 4.13), as was discussed in Section 2.4.6, due to the influence of the fluid impact, boundary layer development, and the fluid exit point. In addition, edge effects can result in higher or lower local heat transfer coefficients at both ends of the tubes (positions 12.7 mm and 190.5 mm in Figure 4.13), resulting in a larger variation of heat transfer coefficients at these points. Despite the possible influence of edge effects, these data were included in the analysis to fully capture the lateral and vertical variation of the local heat transfer coefficients, which are generally more significant than edge effects. However, removing these data points from the analysis did not significantly affect the trends or absolute values of the average heat transfer coefficients. In addition, it should be noted that there is significant variation in the local heat transfer coefficients for each flow regime.

To facilitate discussion of the variation in local heat transfer coefficients at a single operating condition, the local heat transfer coefficients of the sample data point are shown in Figure 4.14. There is a direct relationship between the temperature difference and local heat transfer coefficient; therefore, areas with large temperature differences have low local heat transfer coefficients, and vice versa. It is apparent that there is a large variation in the local heat transfer coefficients at a single flow condition, in this case ranging from 1354 to 4740 W m^{-2} K^{-1}. The highest local temperature differences, which correspond to the lowest local heat transfer coefficients, occur in areas with dryout on or near the thermocouple wall temperature measurement. This occurs at 114 and 140 mm in the sample data point. Meanwhile, the locations with the highest local heat transfer coefficients (13 and 38 mm in the sample data point) have good fluid coverage and flow conditions that enhance heat transfer, such as waviness, boundary layer development, or

134

other phenomena. These areas with high and low local heat transfer coefficients are not consistent between data points. Recurring patterns in the location of these areas could indicate poor test section leveling or alignment, distributor effects, or a nonuniform surface finish. The relationship between local heat transfer coefficients and fluid wetting conditions was confirmed with visual observations of the test section during experiments. The high-speed camera was not able to fully capture this relationship because it only viewed one side of each test section, and the fluid wetting conditions may not be uniform on both sides of each test section.

The uncertainty in the average test section heat transfer coefficients is shown in Figure 4.15. The average uncertainty in the heat transfer measurements was 11.1%. The minimum uncertainty was 3.2%, and the maximum was 57.5%. Generally, the uncertainty in the heat transfer coefficient measurement is lower as heat transfer
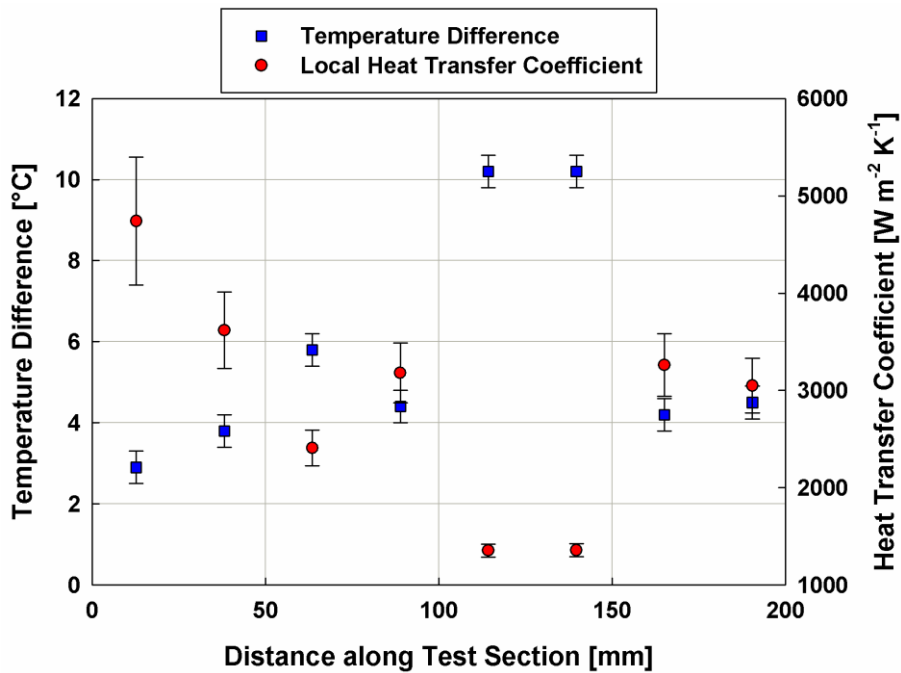

Figure 4.14. Local temperature difference and heat transfer coefficient at the sample data point

coefficient decreases. This is due to the dependence of heat transfer coefficient on the temperature difference described above. However, there is still substantial spread in the uncertainty at a single average heat transfer coefficient due to the variety of test conditions and local temperature measurements that can contribute to the same average heat transfer coefficient measurement. These contributing factors will each have a range of uncertainties that contribute to the overall uncertainty.

Influence of Temperature

Figure 4.16 plots the heat transfer coefficient versus mass flow rate, and Nusselt number versus film Reynolds number for the four temperatures considered in this study. It can be seen that the heat transfer coefficient increases as temperature increases from 10 to 20°C, but then decreases when temperature increases further from 20 to 30°C. The spread in the data at each mass flow rate is due to the different heat flux and tube spacing
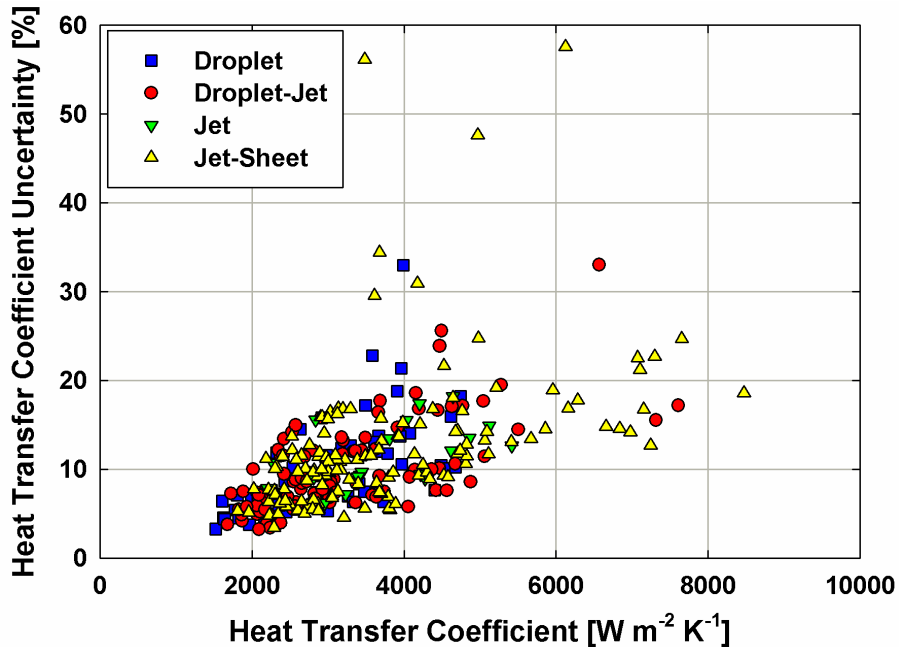

Figure 4.15. Uncertainty in experimental heat transfer data

of each test condition. To determine the cause of these heat transfer trends with temperature, it is necessary to first examine the fluid properties at each temperature, shown in Table 4.2. Although there are minimal changes in the density, conductivity, and surface tension of the liquid, the most significant change is in the liquid viscosity, which increases by 64% from 30°C to 10°C. This substantial viscosity change is expected to be the dominant property impacting the heat transfer trends. There is also a significant change in the density of the vapor, but the large volume of the quiescent test chamber makes this factor unlikely to contribute significantly to the heat transfer coefficient.

Table 4.2. Liquid water properties at 10 and 30°C

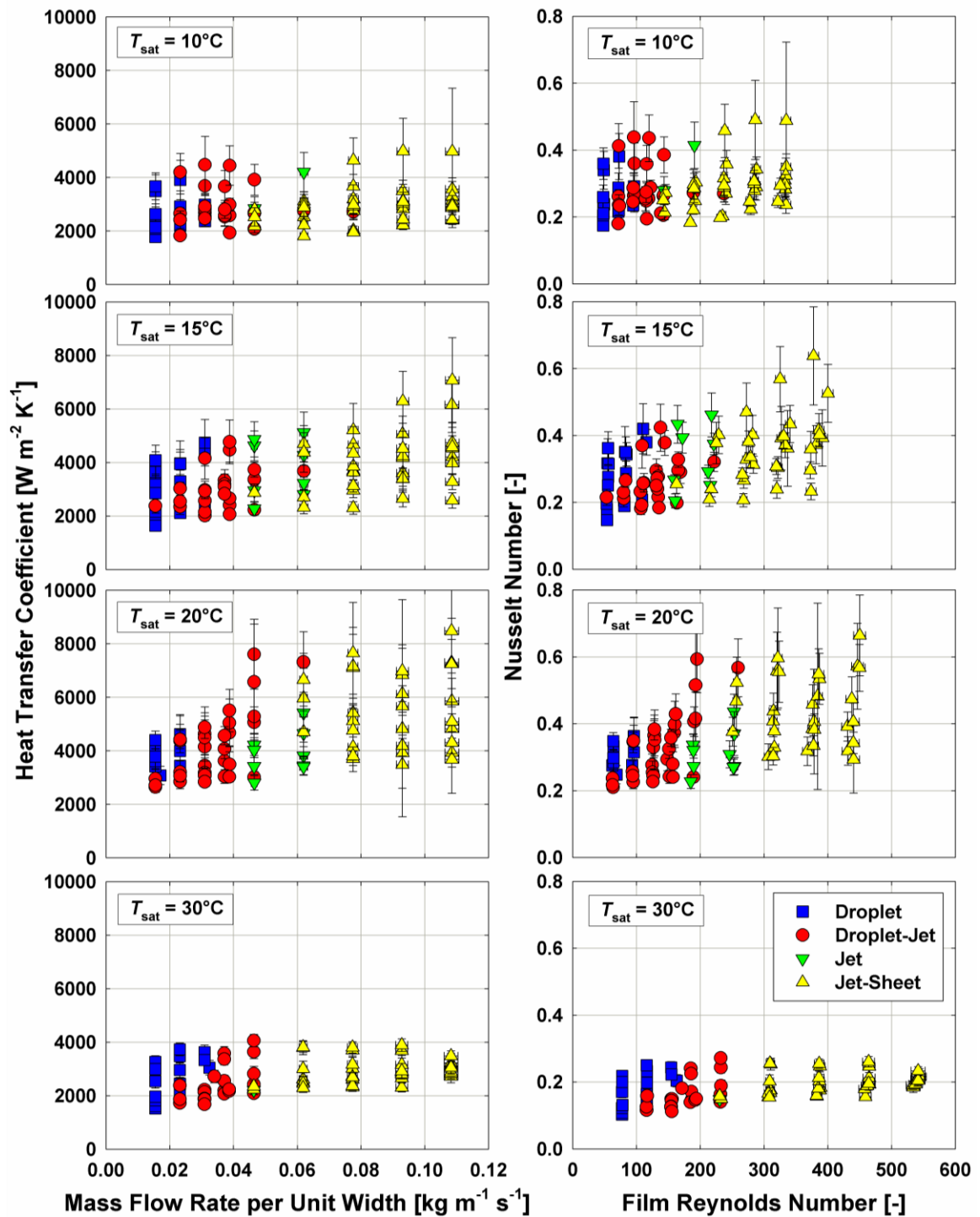| Temperature	10°C	30°C	Change [%]
Density [kg m^{-3}]	998	996	0.2
Conductivity [W m^{-1} K^{-1}]	0.57	0.60	5.3
Surface Tension [N m^{-1}]	0.074	0.071	4.2
Viscosity $\times$ 10^3 [kg m^{-1} s^{-1}]	1.31	0.80	64
Specific Heat [kJ kg^{-1} K^{-1}]	4.19	4.18	0.2
Latent Heat of Vaporization [kJ kg^{-1}]	2477	2430	1.9

Figure 4.16. Experimental heat transfer coefficient versus mass flow rate per unit width and Nusselt number versus film Reynolds number for increasing temperature

138

The initial increase in heat transfer coefficient as temperature increases is consistent with trends observed in the literature, as described in Section 2.4.4. This is generally attributed to the liquid viscosity decreasing with increasing temperature. This decreases the thickness of the film, leading to a lower heat transfer resistance and higher heat transfer coefficients. However, under evaporation conditions, only Li *et al*. (2011a; 2010) observed a decrease in heat transfer coefficient with an increase in temperature in tests with horizontal round tubes using water at low Reynolds number. They suggested that this trend was due to either sensible heating of the fluid, or a decreased temperature difference between the fluid and heating source, increasing the thickness of the film. It is unlikely that either of these options is responsible for the trend observed in the present study. The test facility and test procedure were designed to provide fluid at saturation conditions, minimizing the impact of sensible heating on the measured heat transfer coefficients. In addition, there is no correlation between the measured heat transfer coefficients and heat flux, which would be expected if sensible heating were responsible for a large change in the heat transfer coefficient measurements. A decreased temperature difference between the fluid and heating source should not be responsible for this change because the same heat flux conditions were provided for each test condition, and again there was no observed relationship between heat flux and heat transfer coefficient. Finally, it should be noted that this temperature transition is independent of flow rate and heat flux.

Given that the explanations in previous studies do not satisfactorily explain this inflection point in heat transfer coefficient as temperature increases, it is proposed that this trend is due to film breakdown. More specifically, that it occurs when the momentum

139

and gravitational forces are greater than the surface tension forces at the bottom of the test section, which would normally cause the film to stagnate at the bottom of the tube. As temperature is increased and viscosity decreases, the thickness of the film decreases, but this increases the velocity of the film, increasing the momentum of the film. Meanwhile, increasing temperature decreases the surface tension of the film, although by a lesser degree. As temperature is increased, this leads to a point where the momentum and gravitational forces are greater than the surface tension force, causing the film to exit the test section without first stagnating, as has been generally observed for round tubes. When this point is reached, it will lead to high fluid exit velocities, causing slinging and film breakdown on the tube below, increasing dryout and decreasing the heat transfer coefficient. This was confirmed by visual observations, which qualitatively showed substantial film breakdown at the high temperature (30°C nominal) conditions.

To quantify this transition point, the magnitudes of the momentum, gravitational, and surface tension forces were estimated using a control volume around film at the bottom of the test section, as shown in Figure 4.17. The momentum force was estimated
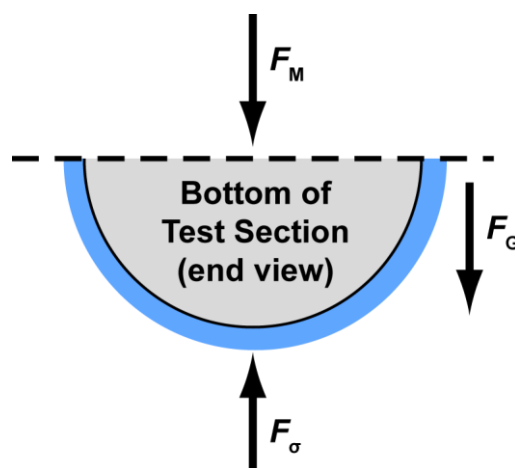

Figure 4.17. A force balance on the liquid film at the bottom of the test section, including the momentum, gravitational, and surface tension forces

using the velocity profile developed in the classic Nusselt film analysis (Nusselt, 1916) and integrated across the thickness of the film, as seen in Equation (4.9), with the velocity given by Equation (4.10). The multiple of two in Equation (4.9) accounts for the flow on each side of the test section, and W is a unit width along the length of the test section. The highest momentum force is expected when a wave enters the control volume. This wave thickness is accounted for by replacing the film thickness, δ, with a wave thickness, δ_{wv}, that is considered to be the film thickness multiplied by a constant. The following analysis finds the wave thickness necessary for the momentum force to overcome surface tension forces, demonstrating that it is a reasonable value, and thus, that this explanation is plausible. This modeling approach would benefit from further support by film and wave thickness measurements; however, such measurements were not taken in the present study. These dimensions are shown in Figure 4.18.

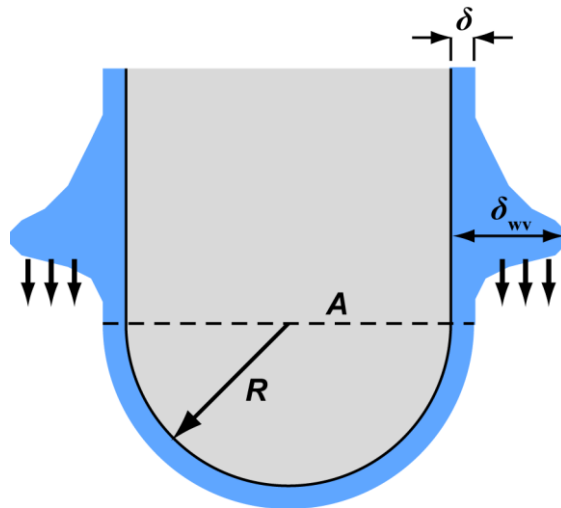$$F_{\mathrm{M}} = 2W\rho_{\mathrm{l}}\int_{0}^{\delta_{wv}} U^{2}dy \qquad (4.9)$$

Figure 4.18. Schematic of dimensions used to quantify the transition point. Unit width W is into the page, and the projected area A extends into the page

$$U = \frac{(\rho_1 - \rho_v)g}{\mu_1}\left(y\delta_{wv} - \frac{y^2}{2} \right) \tag{4.10}$$

$$F_M = \frac{2W\rho_1(\rho_1 - \rho_v)^2 g^2}{\mu_1^2}\left(\frac{2}{15}\delta_w^5 \right) \tag{4.11}$$

The gravitational force is found based on the volume of the fluid, assuming that a uniform film thickness is present around the bottom of the test section, as seen in Equations (4.12) and (4.13).

$$F_G = \rho g V \tag{4.12}$$

$$V = W\pi(R+\delta)^2 - W\pi R^2 \tag{4.13}$$

$$F_G = \rho g W \pi (2\delta R + \delta^2) \tag{4.14}$$

Finally, the surface tension force is found with the Young-Laplace equation, using the projected area of the film in the vertical direction and an assumed smooth film.

$$F_\sigma = A \cdot \Delta P = W(2\delta + 2R)\left(\frac{2\sigma}{\delta + R} \right) \tag{4.15}$$

$$F_\sigma = 4W\sigma \tag{4.16}$$

To calculate each of these forces, the film thickness of the wetted region must be known, which requires an estimation of the wetted tube area. Given that a correlation is not currently available to predict the wetting area of the fluid flow, this theory will be explored using the wetting ratio correlation developed in Chapter 5, shown in Equation (4.17), which finds the wetting ratio, *WR*, as a function of the Reynolds number, modified Galileo number, tube spacing, and capillary length.

$$WR = A \cdot Re \cdot Ga^{-0.27}(s/\xi)^{-0.52} \tag{4.17}$$

Using this wetting ratio, it is found that the film thickness of the sample data point is $\delta = $ 0.36 mm. With waves that are 5.3 times taller than this film thickness, or $\delta_{wv} = 1.9$ mm, the momentum and gravitational forces would be greater than the surface tension forces at a temperature of approximately 22°C, as seen in Figure 4.19, which is consistent with the location of the transition in the heat transfer data.

The location of this transition point is proportional to the ratio of the momentum and gravitational forces to the surface tension force, as seen in Equation (4.18).

$$\frac{F_{\mathrm{M}}+F_{\mathrm{G}}}{F_{\sigma}} \sim \frac{\rho^3 g^2 \delta_{\mathrm{w}}^5}{\mu^2 \sigma} + \frac{\pi \rho g}{\sigma}\left(2 \delta R + \delta^2\right) \qquad (4.18)$$

If the coefficients of the wetting ratio correlation, Equation (4.17), are rounded to an even square and fourth root, as seen in Equation (4.19), this equation can be further simplified to a relationship between the modified Galileo number, thickness of the tube, and capillary length, as seen in Equation (4.20).
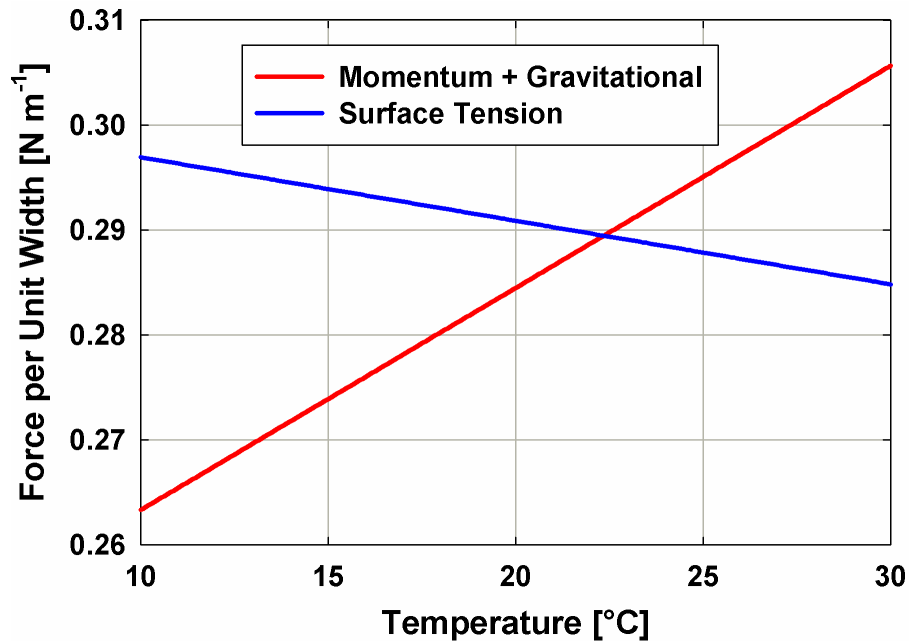

Figure 4.19. The surface tension, momentum, and gravitational forces at the bottom of a test section

143

$$WR = A \cdot Re \cdot Ga^{-0.25} \left(s/\xi \right)^{-0.50} \tag{4.19}$$

$$\frac{F_{\mathrm{M}} + F_{\mathrm{G}}}{F_{\sigma}} \sim Ga^{0.5} + R\xi^{-1} + 1 \tag{4.20}$$

Recognizing that, under the conditions of interest, the first term in Equation (4.20), $Ga^{0.5}$, is several orders of magnitude larger than the sum of the other two terms, this equation can be further simplified to Equation (4.21).

$$\frac{F_{\mathrm{M}}}{F_{\sigma}} \sim Ga^{0.5} \tag{4.21}$$

The relationship between the Nusselt number data and the proposed transition point, $Ga^{0.5}$, is shown in Figure 4.20. It can be seen that this transition criterion effectively captures the temperature transition point in the data.
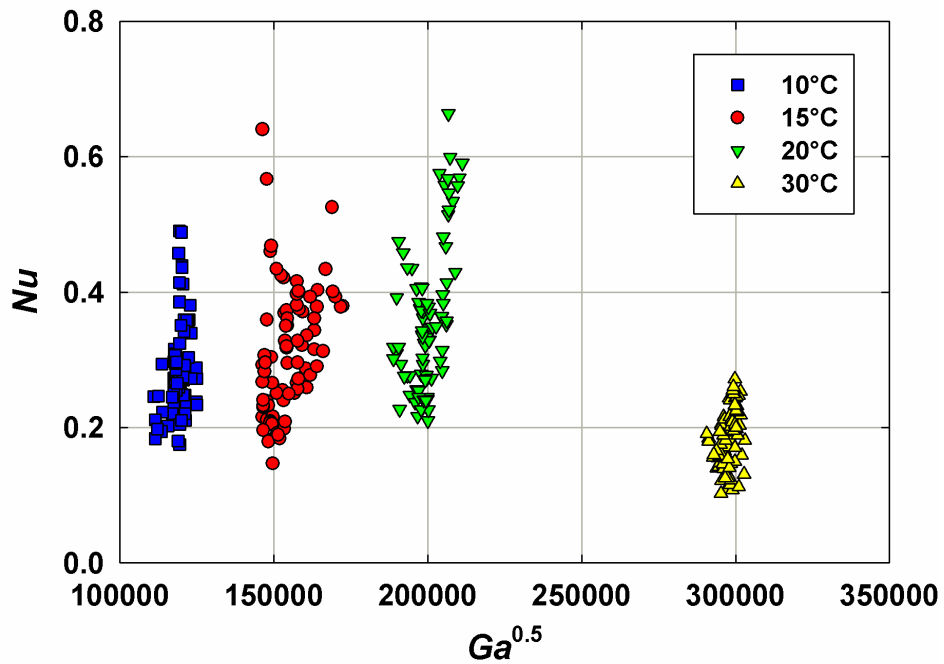

Figure 4.20. Experimental Nusselt number versus the square root of modified Galileo number for each nominal temperature

144

Influence of Mass Flow Rate

Figure 4.21 plots the experimental heat transfer coefficient data versus the mass flow rate per unit width for each temperature and test section spacing. It can be seen that the heat transfer coefficient increases as mass flow rate increases. However, in some cases, such as a saturation temperature of 30°C and 15 mm test section spacing, the heat transfer coefficients did not increase with mass flow rate. In previous studies, it was observed that the heat transfer coefficient increased, decreased, and then increased again as mass flow rate was increased, as described in Section 2.4.1. The initial increase is attributed to increased wetting area. When full wetting is reached, the heat transfer coefficient decreases as the film thickness increases. Finally, the heat transfer coefficient begins increasing again due to turbulence or boundary layer development. In the present
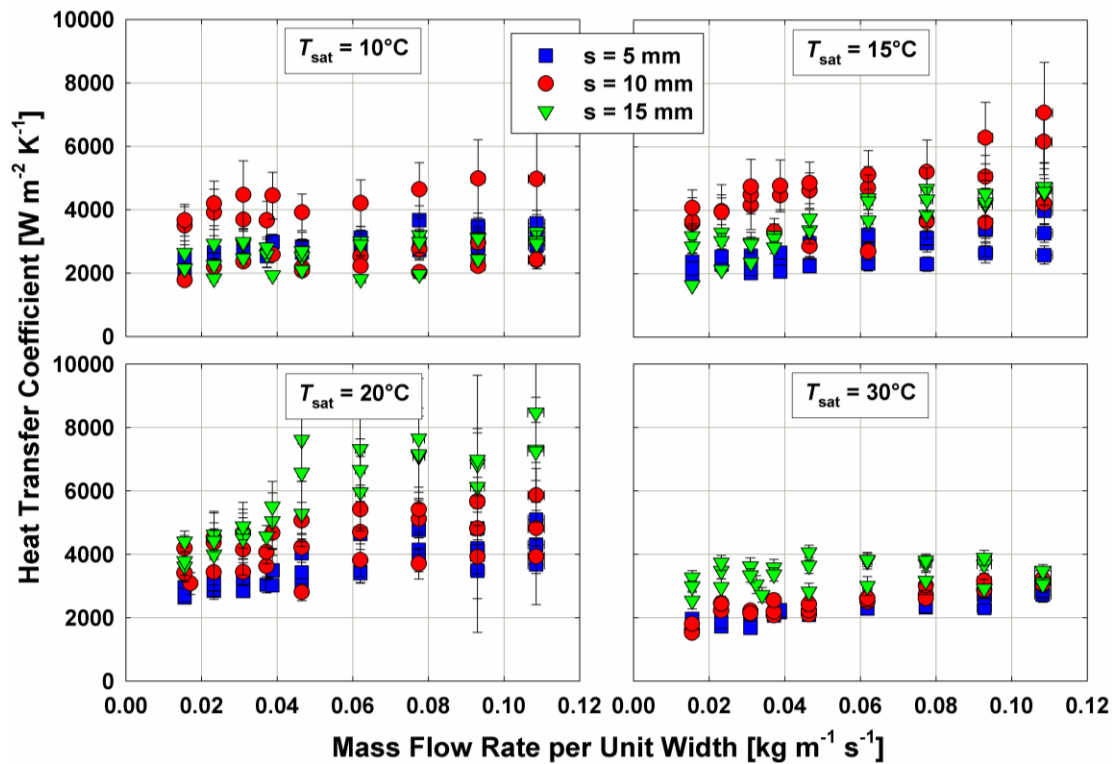

Figure 4.21. Experimental heat transfer coefficient versus mass flow rate per unit width for increasing test section spacings

study, the tube was only partially wetted. Thus, the observed trend is consistent with that found in previous studies, and can be attributed to the increased liquid coverage area as flow rate increases. In the cases where heat transfer coefficient did not increase with mass flow rate, which occurred at high test section spacings, slinging and other detrimental phenomena probably resulted in higher mass flow rates not substantially increasing the wetted tube area.

Influence of Test Section Spacing

The influence of test section spacing on heat transfer coefficient is shown in Figure 4.21. As the test section spacing is increased, the heat transfer coefficient generally increases. This can be attributed to an increase in the local heat transfer coefficient at the top of the tube due to the increased fluid impact velocity. In addition, the increased fluid velocity increases the boundary layer development length, again increasing heat transfer coefficient. However, in some cases, the largest test section spacing has lower heat transfer coefficients than the intermediate test section spacing. In these cases, the increased fluid velocity leads to film breakdown, which decreases the film tube coverage and decreases the average heat transfer coefficient. This is often due to slinging, where fluid exiting the stabilizing tube or test section does not contact the tube below. This was observed visually during tests with high test section spacing. Both of these observations are consistent with those observed in the literature, as described in Section 2.4.5.

Influence of Test Section Row

Figure 4.22 shows the reduction of experimental heat transfer coefficient with test section row relative to the measurements with the top test section row. In this study, 90

measurements were taken with the second test section row, and 40 measurements were taken with the third test section row. These were limited in some cases due to excessive dryout. Increased film breakdown on lower test section rows leads to low local heat transfer coefficients and high local wall temperatures, which would damage the electric heaters in the test section. In all cases, the heat transfer coefficient decreased with increasing test section row. The average reduction in heat transfer coefficient was 31% for row 2 and 49% for row 3. This can be attributed to decreased wetting on the lower test section rows due to film breakdown. This is consistent with the trends observed in the literature in investigations of tube bundles, as discussed in Section 2.4.10, in situations where full wetting is not present. This substantial reduction in heat transfer performance in tube bundles would be a significant barrier to implementation of these microchannel geometries in practical applications, suggesting that steps must be taken to increase the wetting behavior under these conditions.
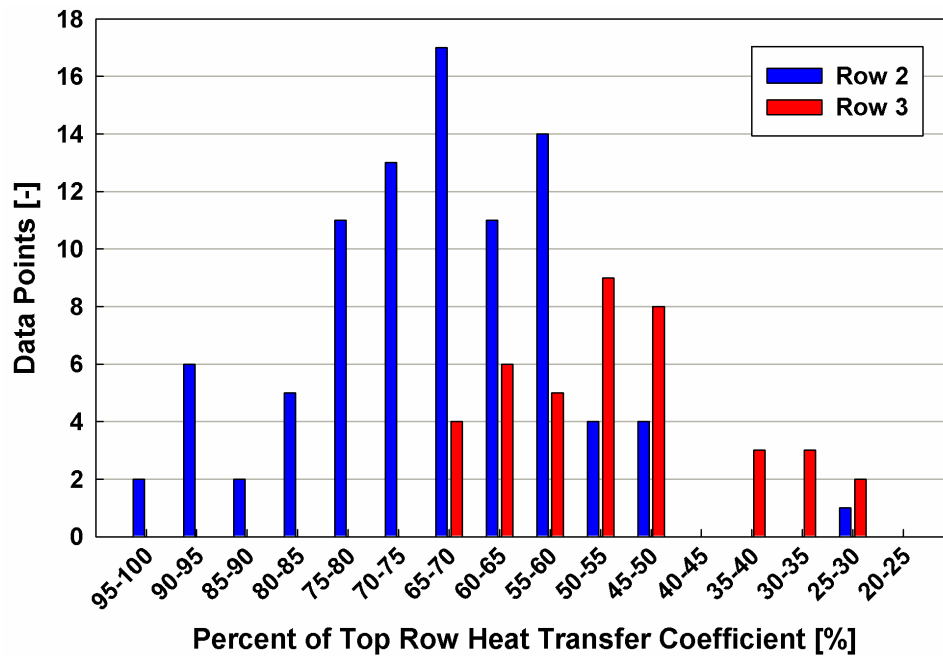
Figure 4.22. Experimental heat transfer coefficients of test section rows two and three relative to those of the top test section

147

4.3   Flow Distributors

The flow visualization study investigated the performance of eight flow distributors with water at atmospheric pressure. The distribution characteristics of each distributor were measured, and high-speed videos were taken at each data point. These videos were used to quantify the generated droplet and jet sizes using the image analysis program developed for the flow visualization study. For clarity, the maldistribution calculation of a representative data point is presented here. This point was taken with the box-based distributor based on the Wang *et al.* (2010) design using an array of holes on the bottom and a feeder tube. The test was conducted at a temperature of 20°C, atmospheric pressure, and a Reynolds number of 217.

4.3.1   <u>Flow distributor analysis</u>

Each liquid distributor was evaluated at a given flow rate by measuring the flow regime, distribution of the flow, and droplet or jet characteristics. The flow regime of each distributor was considered to be in the droplet, droplet-jet, jet, jet-sheet, or sheet modes. This regime may vary for a given distributor based on the distance and size of the tube bank below the distributor. Without a tube array below the distributor, the flow regime naturally varies with distance from the distributor, and was measured based on a uniform distance of 20 mm below the distributor. The flow regime definitions were based on the transition definitions of Roques *et al.* (2002), as was the case in the heat transfer study. The droplet mode existed when only droplets existed at the measurement point, with no continuous liquid link to the distributor above. The flow is in droplet-jet mode when at least one stable liquid column or jet connects the measurement point to the distributor above. The jet mode is observed when there are only stable liquid columns or

jets connecting the measurement point to the distributor. The transition to jet-sheet mode is considered to occur when at least one liquid sheet is formed, typically by merging two or more liquid jets. Finally, the flow is in sheet mode when only one continuous sheet exists at the measurement point.

The distribution of the flow was measured using the liquid collection box. During tests, the flow was first given time to come to equilibrium, considered to be 2 hours at steady-state for the first data point in a series, and 30 minutes for all subsequent points. Then, the liquid collection box was placed under the distributor and liquid was collected until a segment was almost full. The liquid depth in each segment was measured to determine the volume in each segment, and the percent maldistribution across the segments was calculated by taking the percent difference between the depth in a given segment and the average depth across all segments.

$$V_{avg} = \frac{1}{N}\sum_{i=1}^{N}V_i \qquad (4.22)$$

$$M = \frac{V - V_{avg}}{V_{avg}} \times 100 \qquad (4.23)$$
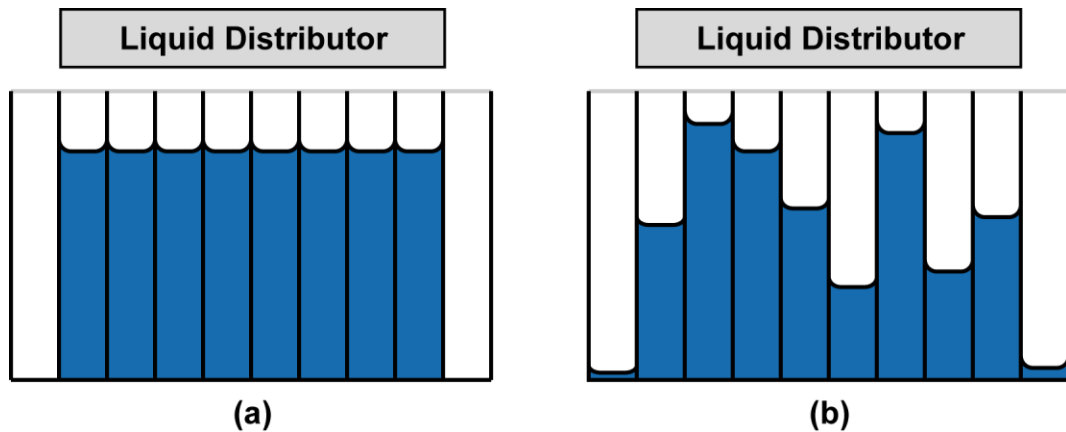

Figure 4.23. Collection box with (a) even flow distribution, and (b) substantial maldistribution

These calculations only included the segments directly below the liquid distributor, although the end segments were also measured to ensure that a minimal amount of liquid left the intended distribution region. For the sample data point, 0.6% of the total flow was collected in the two end segments.

The average maldistribution was found by averaging the maldistribution of these segments. These values were calculated for segments with a width of 25.4 mm, 50.8 mm, and 76.2 mm to minimize the impact of the collection box design on the results. The depth measurements and resulting maldistribution calculations for the sample data point are shown in Table 4.3. A maldistribution of 10.0% was measured with 25.4 mm segments. This decreased to 5.7% with 50.8 mm segments, and 4.9% with 76.2 mm segments.

Table 4.3. Maldistribution calculation for sample data point

Segment Size: 25.4 mm									
Segment	1	2	3	4	5	6	7	8	Average
Depth [mm]	151	122	118	133	135	136	172	113	135
Volume $\times 10^{-3}$ [mm^3]	245	198	192	216	219	221	280	184	219
Maldistribution [%]	11.9	9.6	12.6	1.5	0.0	0.7	27.4	16.3	**10.0**
Segment Size: 50.8 mm (averaging two segments)									
Segment	1-2	2-3	3-4	4-5	5-6	6-7	7-8		Average
Depth [mm]	137	120	126	134	136	154	143		135
Volume $\times 10^{-3}$ [mm^3]	222	195	204	218	220	250	232		220
Maldistribution [%]	0.8	11.4	7.3	1.1	0.1	13.7	5.2		**5.7**
Segment Size: 76.2 mm (averaging three segments)									
Segment	1-3	2-4	3-5	4-6	5-7	6-8			Average
Depth [mm]	130	124	129	135	148	140			134
Volume $\times 10^{-3}$ [mm^3]	212	202	209	219	240	228			218
Maldistribution [%]	3.0	7.4	4.2	0.2	9.9	4.5			**4.9**

The droplet surface areas and volumes, and jet diameters generated by each distributor were measured with image analysis of high-speed videos. The semi-autonomous image analysis program developed in MATLAB (2010) for the flow visualization study, described in Section 4.1.1, was also used in this portion of the study. In each video, the primary droplet sizes were measured after separation from the liquid neck connecting them to the distributor. Meanwhile, the jet diameters were measured at a distance of 20 mm below the distributor, which was also the distance used to determine the flow regime. A video was taken at each flow distribution measurement point, but the total number of videos varied depending on the range of operation of each distributor. A minimum of seven videos were taken for the distributors with the narrowest flow rate range, increasing to 17 videos for the distributors with the highest flow rate range. The length calibration, establishing the relative number of pixels per metric unit, was based on a known dimension of each distributor. Ten droplet or jet measurements were taken from each high-speed video if possible, although in some cases, a smaller number of jets was present. Finally, the mean of these ten measurements was taken to find an average droplet or jet size at a given Reynolds number.

4.3.2   <u>**Flow distributor results**</u>

Experiments were conducted over a film Reynolds number range of 12 to 495 at a temperature of 20°C and atmospheric pressure. Experiments were limited at low flow rates by the capabilities of the pumps or by extremely poor distributor performance. Distributor performance was considered to be too low for testing if the flow exited the distributor at a single location and was not providing a distribution, or was missing the collection box entirely due to slinging or other phenomena. Experiments were limited at
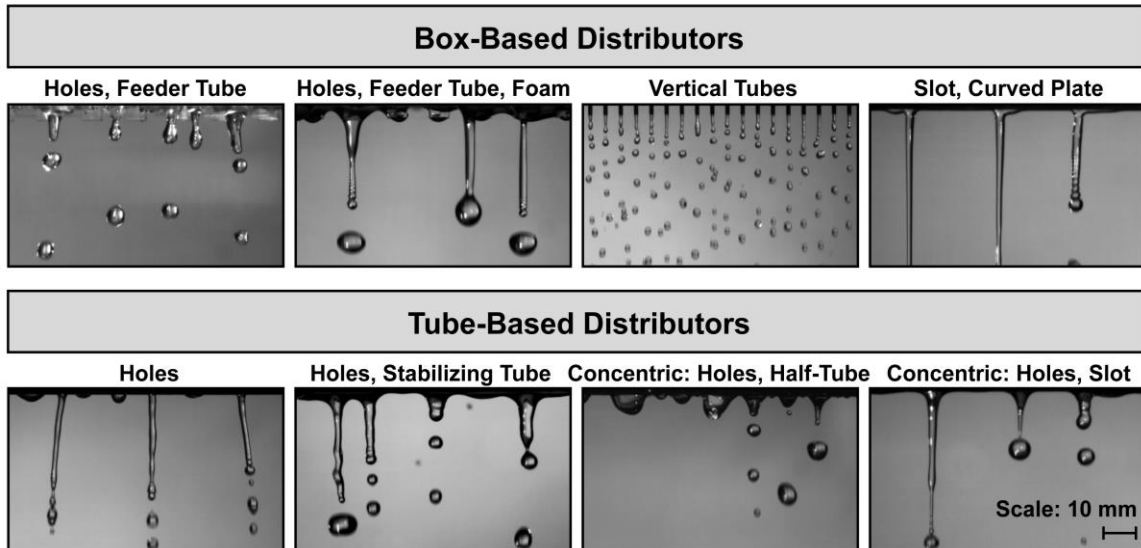
Figure 4.24. Image of flow from each distributor at *Re* = 124 with a uniform scale

high flow rates by the capabilities of the pumps, overflow of box-based designs, or poor performance as described above. Many of these distributors could be easily adapted to other flow rate ranges by increasing or decreasing the cross-sectional area of exit features or allowing for increased gravitational head with taller box walls.

As is seen in Figure 4.24, qualitatively the distributors generate substantially different liquid flow patterns. At the same Reynolds number, distributors provided flow in the droplet, droplet-jet, and jet flow regimes, and droplet sizes varied substantially based on the distributor geometry. In addition, in some cases, such as the box-based vertical tube design, the geometry of the distributor provides uniformly spaced droplet generation sites.

The flow regime generated with each distributor is shown in Figure 4.25. There was substantial variation between distributor designs, with some designs limited to only droplet mode flow, while other designs varied from the droplet-jet mode to sheet mode. Generally, distributors that provided an initial distribution with a feeder tube, or had other
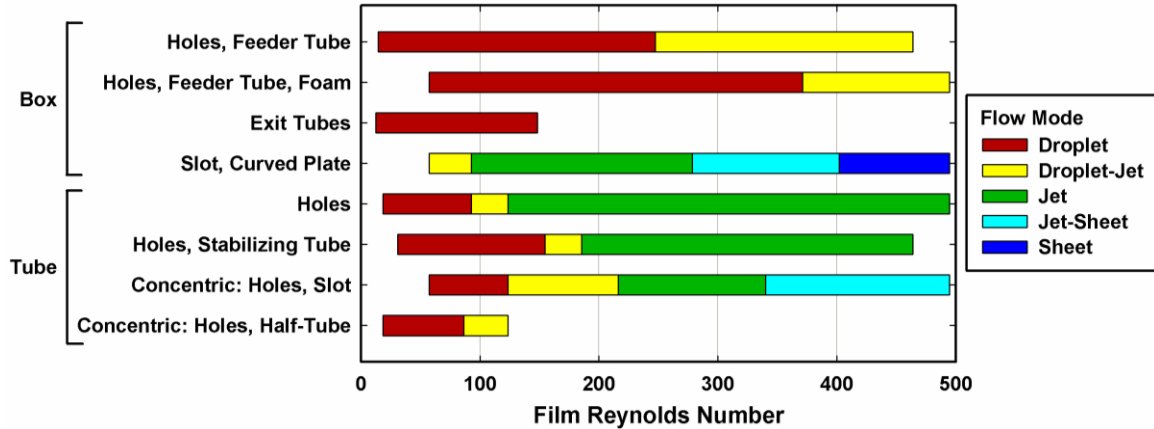
Figure 4.25. Flow regimes observed for each distributor as a function of film Reynolds number

features designed to increase pressure drop or otherwise encourage lateral distribution, appeared to delay the transition out of droplet mode. Meanwhile, distributors with arrays of holes as the final exit point appear to elongate the jet regime, and slotted exits lead to a transition to sheet mode at lower Reynolds numbers. However, it should be noted that this study is not sufficient to determine whether these flow regime variations persist throughout a tube bank.

The maldistribution of each distributor with 25.4 mm wide segments in the collection box is shown in Figure 4.26. The majority of the distributors exhibited poor performance under these conditions, with all of the distributors resulting in maldistribution greater than 50% throughout at least a portion of the range. Most of the distributors had worse performance at low Reynolds numbers due to the poor lateral distribution with limited droplet generation sites. In addition, some distributors, particularly those with tube-based designs, had worse performance at high Reynolds numbers that appeared to be due to higher exit velocities. This caused two distributors to reach their best performance at intermediate Reynolds numbers in the range they
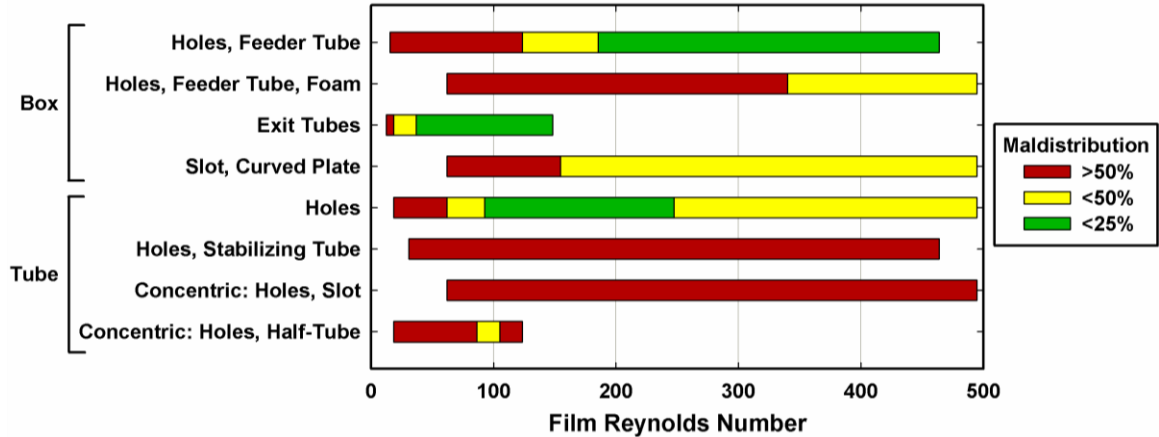
Figure 4.26. Maldistribution of distributors with 25.4 mm wide segments (eight segments total) in the collection box

performed. With this segment size, generally the box-based designs had better performance than tube-based designs, and the best performance was observed for the box-based design with exit tubes, but its operation is limited to a relatively small Reynolds number range.

Larger segment sizes in the collection box were examined to determine whether the maldistribution was localized in certain areas of the distributor, or if the maldistribution was across more distant segments. Increasing the segment size to a width
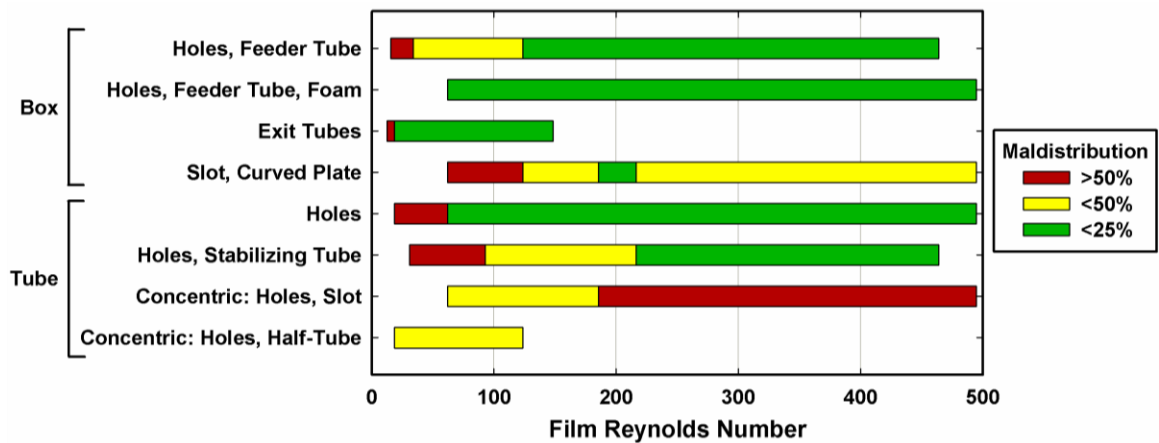

Figure 4.27. Maldistribution of distributors with 50.8 mm wide segments (seven segments total) in the collection box

of 50.8 mm resulted in lower degrees of maldistribution, as is shown in Figure 4.27. This is most evident in the box-based design with an array of holes, a feeder tube, and 2 foam layers. With the larger segment size, maldistribution was under 25% for the entire Reynolds number range, a substantial improvement compared to its performance with 25.4 mm segments. Overall, box-based designs continued to outperform tube-based designs, with the concentric tube designs resulting in the highest levels of maldistribution.

Increasing the collection box segment width to 76.2 mm lowered the degree of maldistribution observed further, as seen in Figure 4.28. Generally, the tube-based designs continued to have higher levels of maldistribution compared to box-based designs. The box-based distributor designs with an array of exit holes and a feeder tube demonstrated the best performance over a wide operating range. Relatively good performance was also found for tube designs with arrays of exit holes, but they had poor distribution at low flow rates, suggesting that an initial distribution step may be beneficial. Both slot-based designs had relatively poor performance, but this may be
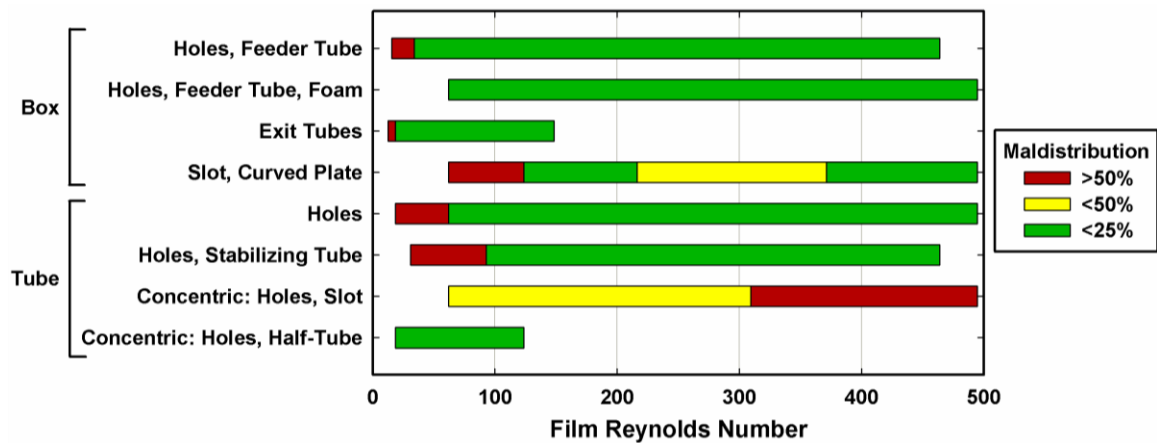

Figure 4.28. Maldistribution of distributors with 76.2 mm wide segments (six segments total) in the collection box

attributed to the relatively low Reynolds numbers tested.

The surface areas and volumes of the droplets generated by each distributor, which were measured with the image analysis program, are shown in Figure 4.29. As was observed visually, the distributors generate a wide range of droplet sizes. The box-based distributor with exit tubes generated droplets with volumes under 20 mm^3, while the box-based design with an array of holes, a feeder tube, and foam generated droplets averaging over 500 mm^3. The size of the droplets generated were determined by the exit features and overall distribution provided by each distributor. Although significant variation was measured for both the box-based and tube-based distributors, the box-based distributors had a wider range of droplet sizes. In addition, it should be noted that the narrow range of droplet sizes observed for the box-based design with a slot was due to the narrow range
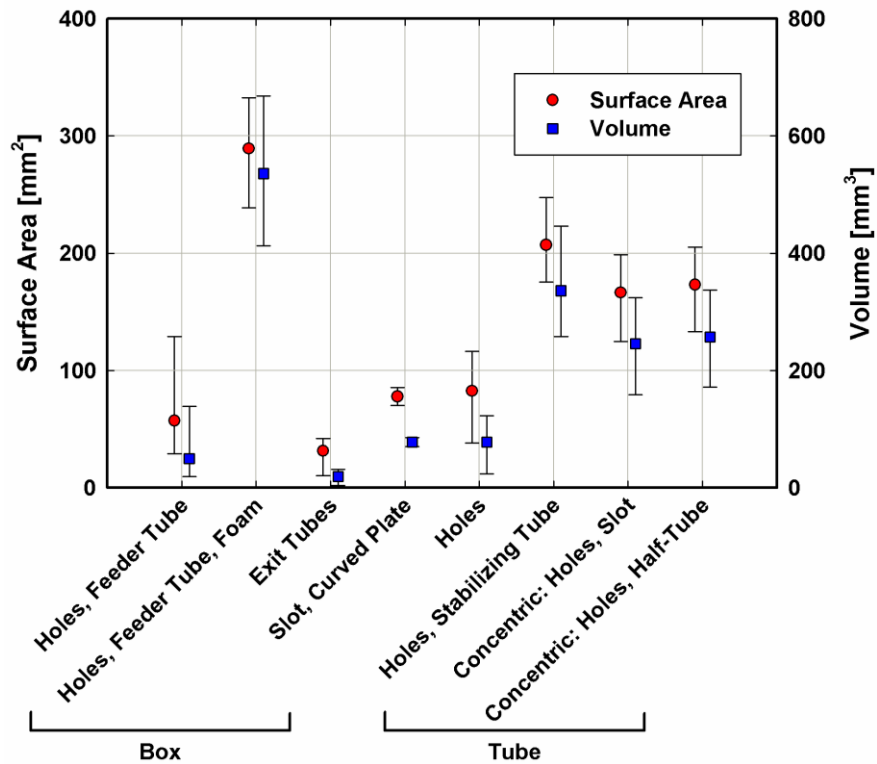

Figure 4.29. Droplet surface areas and volumes generated by distributors. Bars indicate range of values observed across *Re* range with data point at average

156

of Reynolds numbers for which droplets were present.

The jet diameters generated by each distributor are shown in Figure 4.30. As above, the narrow range of jet diameters observed for two distributors is due to the small number of jets measured, and one distributor design did not generate jet flow. The minimum jet diameter observed was approximately 1.2 mm with the box-based design using an array of exit holes and a feeder tube, while the maximum jet diameters measured were over 4 mm. The jet diameter and spacing varied based on the exit features of the distributors. With sufficient exit surface area, the fluid would generally collect at the bottom of a distributor and then leave at regularly spaced sites, the spacing of which has been attributed to Taylor instabilities (Hu and Jacobi, 1998). However, in some cases, such as the tube-based design with an array of exit holes, the relatively low cross-
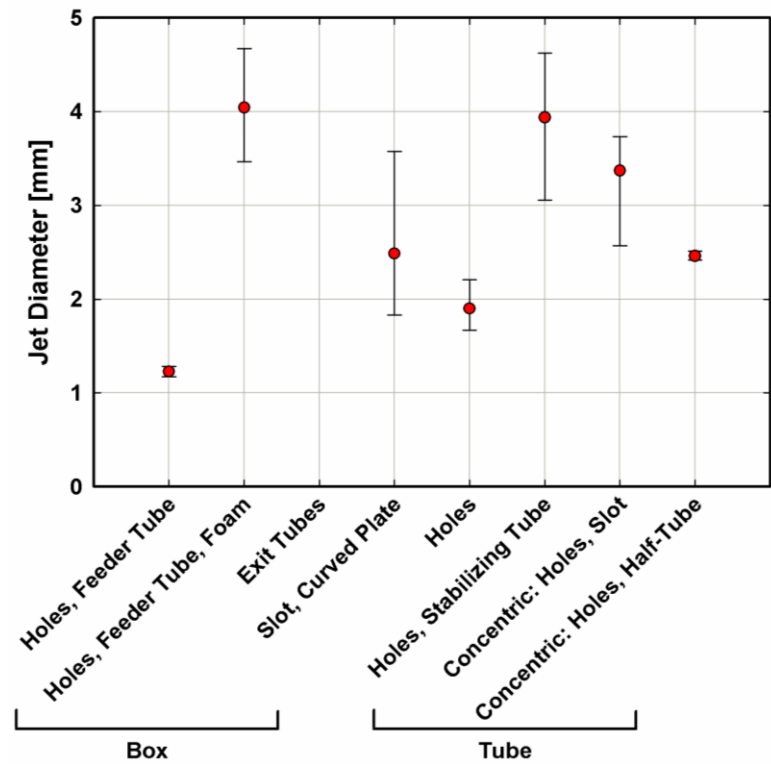

Figure 4.30. Jet diameters generated by distributors. Bars indicate range of values with data point at average

157

sectional area of the exit holes resulted in higher internal pressure and liquid jets dominated by inertial forces. The largest jet diameters could be generated by such exit features, or be the result of significant maldistribution, with a large portion of the flow exiting the distributor at fewer locations.

These results may be used to guide distributor selection for falling-film test facilities and components. Generally the goal of the distributor is to establish an even fluid flow along the length of the horizontal tube, and to imitate the performance of liquid entering from a tube above the tube bank. Fujita and Tsutsui (1995b, 1996) observed that the maldistribution of flow exiting their distributors was dampened after passing over approximately three tubes, suggesting that an even fluid distribution also achieves the goal of imitating the performance of additional tubes. If the droplet or jet characteristics of falling-film flow over a given tube geometry are known, the distributor can be selected to generate flow with similar characteristics. For instance, the flow visualization portion of this study reported droplet volumes ranging from 80 to 150 mm^3 for flow over a horizontal rectangular tube bank, suggesting that the box-based distributor design with holes and a feeder tube, which generated droplets ranging from 20 to 140 mm^3 with low levels of maldistribution, may be the most appropriate design among those considered here. In cases where the characteristics of the flow over the tube bank are unknown, distributor selection can target an even flow distribution throughout the range of fluid properties and flow rates being targeted. This study measured substantial levels of maldistribution from several common distributor designs, suggesting that further investigation may be warranted. However, it must be recognized that this study was

limited to a single fluid and distribution length, and distributor performance may vary as the flow conditions are altered.

CHAPTER 5: DISCUSSION AND MODEL DEVELOPMENT

This chapter compares the experimental data of the present study with predictions of correlations from the literature and presents the development of new flow regime and heat transfer coefficient models. The flow regime model is based on a thermodynamic analysis proposed by Wang and Jacobi . The heat transfer coefficient model first predicts the wetted tube area based on a hydrodynamic analysis supported by the flow visualization study, and then models the heat transfer coefficient based on the classic Nusselt film heat transfer theory (Nusselt, 1916).

5.1   Flow Regime Model

The flow regime model divides the flow into five possible flow regimes: droplet, droplet-jet, jet, jet-sheet, and sheet modes. The definitions of these flow modes can be found in Section 4.2.1. This section first evaluates the performance of the Wang *et al.* (2012) correlation, which is currently the only correlation available for horizontal rectangular geometries. Then, a new correlation is developed to predict flow mode transitions for the geometry investigated in the present study.

5.1.1   <u>Comparison to the Literature</u>

Currently, the only available flow regime model for horizontal rectangular tubes, as were used in the present study, was developed by Wang *et al.* (2012). They observed the flow mode transitions over adiabatic tubes with dimensions of $400 \times 25.4 \times 3.18$ mm (length $\times$ height $\times$ width) and a corner radius of 0.76 mm. The tube spacing was varied from 4.8 to 24.9 mm, with Reynolds numbers up to 575 using seven liquids: hydraulic

Table 5.1. Empirical coefficients in Wang *et al.* (2012) flow mode correlation

Transition	Decreasing Flow Rate				Increasing Flow Rate			
	a_0	a_1	a_2	a_3	a_0	a_1	a_2	a_3
Droplet to Droplet-Jet	-0.143	0.071	0.210	0.314	-0.149	0.084	0.211	0.310
Droplet-Jet to Jet	-0.589	0.202	0.201	0.284	-0.627	0.241	0.175	0.280
Jet to Jet-Sheet	-1.369	0.733	0.146	0.249	-2.355	1.062	0.134	0.235
Jet-Sheet to Sheet	6.835	0.565	0.176	0.264	-4.201	1.697	0.132	0.220

oil, ethylene glycol, water, and four mixtures of ethylene glycol and water. The flow mode was divided into the droplet, droplet-jet, jet, jet-sheet, and sheet regimes. The sheet mode was further split into the torn sheet and whole sheet modes, but will be considered as a single sheet mode here, consistent with the flow mode definitions used in the present study.

On the basis of these observations, they developed an empirical correlation relating the transitional film Reynolds number to the modified Galileo number and the tube spacing non-dimensionalized with the capillary length, as seen in Equation (5.1).

$$Re = a_0 + a_1 \left(s/\xi \right)^{a_2} Ga^{a_3} \tag{5.1}$$

The coefficients and exponents a_0, a_1, a_2, and a_3 were determined empirically for each flow regime transition, and separate coefficients were defined for increasing and

Table 5.2. Agreement of Wang *et al.* (2012) correlation with data from present study

Flow Regime	Number of Data Points		Percentage	
	Experimental	Predicted	Correct Prediction	False Positive
Droplet	57	168	100%	195%
Droplet-Jet	112	36	6%	26%
Jet	21	72	24%	319%
Jet-Sheet	134	36	27%	0%
Sheet	0	12	-	-
Total	324	324	32%	-

decreasing flow rates, accounting for transition hysteresis. The coefficients for each mode transition are shown in Table 5.1.

Figure 5.1 plots the flow regimes observed in the present study and the Wang *et al.* (2012) correlation predictions. The film Reynolds number is plotted versus fourth root of the modified Galileo number for each experimental test section spacing. Table 5.2 presents the agreement between the Wang *et al.* (2012) correlation and the data from the present study. With a decreasing flow rate, as was used in the present study, 32% of the data points are predicted correctly. The correlation predicts a much larger droplet regime than was observed in the present study. Thus, 100% of the droplet mode observations are predicted correctly, but agreement is poor in the other regimes. This is also reflected in Figure 5.1. It is apparent that the transition out of the droplet regime occurred at much lower film Reynolds numbers in the present study. In addition, the droplet-jet and jet-sheet regimes in the present study occurred over a wider range of film Reynolds numbers. These observations can be attributed to several differences between the studies. First, the larger tube width used in their study—3.18 mm, compared to 1.42 mm in the present study—would result in less axial stretching of the droplet and jet formation sites at the bottom of the tube, contributing to earlier breakup. In addition, it is possible that the unique distributors used in each study contributed to these differences. In particular, the Wang *et al.* (2012) study used a round stabilizing tube below the distributor, while the present study used a rectangular stabilizing tube with the same external dimensions as the test sections. Finally, the Wang *et al.* (2012) study used adiabatic tubes, which may allow full film wetting at lower Reynolds numbers. Higher degrees of film wetting would spread out the film, resulting in lower local mass flow rates and delayed mode transitions.

There is a minimal difference between the Wang *et al.* (2012) correlations provided for increasing and decreasing flow rates under the present conditions. An
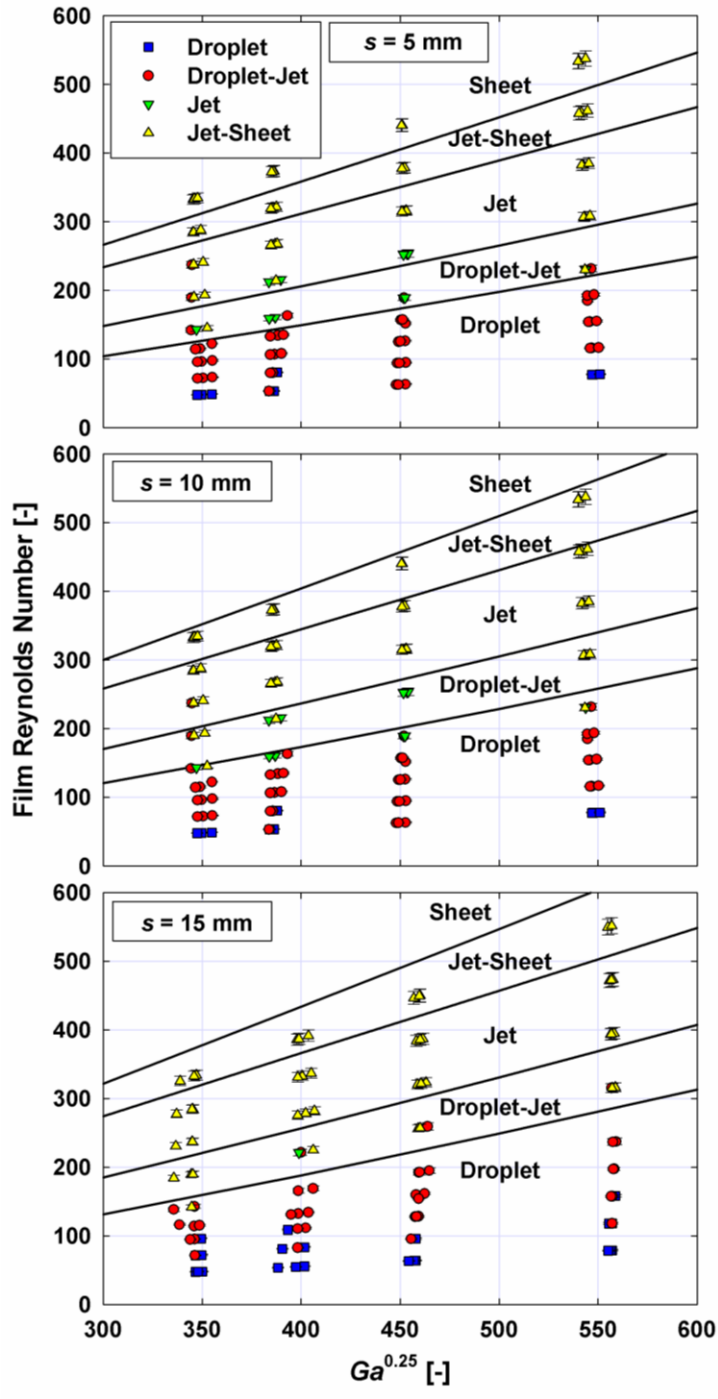

Figure 5.1. Comparison of Wang *et al.* (2012) correlation with experimental data from the present study

average difference of just 1.5% in the transitional film Reynolds number is predicted, with an absolute average deviation of 4.6%. Generally, this hysteresis effect results in each transition occurring at higher Reynolds numbers. Thus, the number of correctly predicted data points decreases slightly to 29% using the coefficients corresponding to an increasing flow rate.

5.1.2   Flow Regime Model Development

A new model was developed to predict flow regime transitions for the geometry in the present study. This model uses the thermodynamic analysis proposed by Wang and Jacobi (2014), with empirical constants fit to the present data, to predict the point of thermodynamic equilibrium between two neighboring modes, at which point both modes are available and a transition can occur. To determine this point, a control volume is drawn around a single tube in the droplet, jet, and sheet modes. The point of thermodynamic equilibrium occurs when the Helmholtz potentials of the control volumes with two neighboring modes are equal.

First, consider a control volume around the jet and sheet modes with idealized flow. Figure 5.2 demonstrates this situation with round tubes, and the same analysis applies to the horizontal rectangular test sections under consideration in the present study. These two control volumes both have fluid at the same conditions and flow rate. In addition, for this analysis, an adiabatic system with no heat or work is considered. Thus, the Helmholz potentials in the sheet and jet control volumes can be expressed by Equation (5.2):

$$m_{\mathrm{S}}\left(e - T_0 S\right)_{\mathrm{S}} = m_{\mathrm{J}}\left(e - T_0 S\right)_{\mathrm{J}} \tag{5.2}$$

Note that S represents the intensive entropy to avoid confusion with the test section spacing variable. However, given that the mass flow rates of each control volume are equal, this can be simplified to find that the intensive total energy in each control volume must be equal:

$$e_S = e_J \tag{5.3}$$

The intensive energy within the control volume includes the internal, kinetic, potential, and interfacial energy:

$$e = \frac{1}{m}\left(\int \rho\left(u + U^2/2 + g\left(z - z_0\right)\right)d\forall + A_{lv}\sigma\right) \tag{5.4}$$

It is assumed that the jet and sheet modes have a thin film with equal thicknesses on the tube and operate with free-fall between the tubes. In addition, both systems have the same fluid properties. Thus, the internal, kinetic, and potential energies of both control volumes will be equal. Removing these terms, this equation simplifies to only include the interfacial energy of the jet and sheet modes, suggesting that the liquid-vapor interfacial area of each mode will be equal at the transition point:
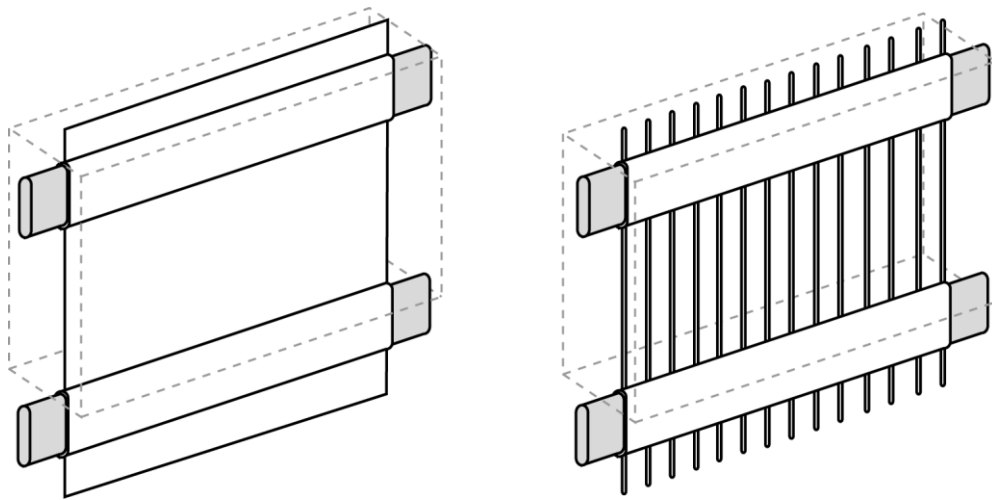

Figure 5.2. Control volume around a single test section in the jet and sheet flow regimes

$$A_{\mathrm{lv,S}} = A_{\mathrm{lv,J}} \tag{5.5}$$

Again noting that the jet and sheet modes have thin films with the same thickness on the tube, this portion of the area is equal in both flow modes, and this equation only includes the interfacial area between two tubes. Idealizing each flow mode, this area includes a single sheet the width of the tube in sheet mode, and a number of equally spaced columns in the jet mode:

$$A_{\mathrm{lv,S}} = 2Ls + A_{\mathrm{f,T}} \tag{5.6}$$

$$A_{\mathrm{lv,J}} = N_{\mathrm{J}} \pi d_{\mathrm{J}} s + A_{\mathrm{f,T}} \tag{5.7}$$

The number of jets, N_{J}, can be determined using a Taylor instability analysis, as discussed in Section 2.3. Using the Bellman and Pennington (1954) model for the jet spacing, the number of jets can be represented as:

$$N_{\mathrm{J}} = \frac{L}{2\pi} \sqrt{\frac{\rho g}{3\sigma}} \tag{5.8}$$

Then, the diameter of the jets is determined using the conservation of mass, where again the velocity is determined assuming free-fall between the tubes. This gives the jet interfacial area:

$$A_{\mathrm{lv,J}} = 2.21 \sqrt{\frac{2\Gamma L^2 s^{1.5}}{\rho^{0.5}\sigma^{0.5}}} + A_{\mathrm{f,T}} \tag{5.9}$$

Setting Equations (5.6) and (5.9) equal to one another with appropriate simplifications yields a scaling relationship for the flow mode transition:

$$\Gamma \sim \sqrt{\sigma \rho s} \tag{5.10}$$

166

Non-dimensionalizing this relationship, we find that the transitional film Reynolds number is a function of the fourth root of the modified Galileo number and the square root of the tube spacing non-dimensionalized by the capillary length.

$$Re \sim Ga^{0.25} \left(s/\xi \right)^{0.5} \tag{5.11}$$

A similar analysis can then be conducted examining the transition from droplet to jet mode, as seen in Figure 5.3. As in the case of the jet-to-sheet transition, the point of thermodynamic equilibrium can be found by considering the Helmholtz potential of each system, and this simplifies to the interfacial area of the two modes:

$$A_{lv,D} = A_{lv,J} \tag{5.12}$$

The interfacial area of the jet mode is given by Equation (5.9), while the interfacial area of the droplets can be found using Equation (5.13), which assumes an equal droplet spacing and timing with uniform volumes.

$$A_{lv,J} = N_J N_D \pi d_D^2 + A_{f,T} \tag{5.13}$$

The number of droplets, N_D, is found using the Yung *et al.* (1980) correlation for droplet
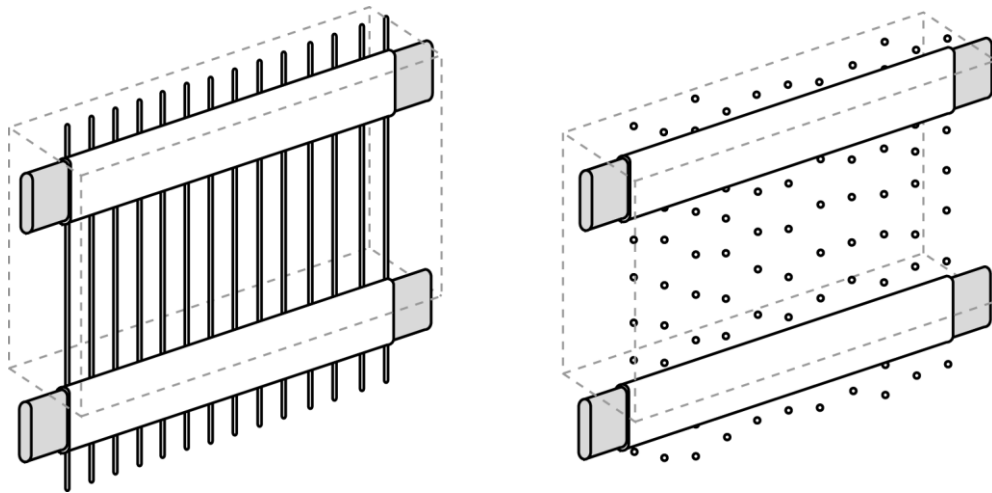

Figure 5.3. Control volume around a single test section in the jet and droplet flow regimes

diameter, conservation of mass, and free-fall between tubes:

$$N_{\mathrm{D}} = \frac{24\Gamma}{g d_{\mathrm{D}}^3} \sqrt{\frac{6s\sigma}{\rho^3}} \tag{5.14}$$

This allows the interfacial area to be found:

$$A_{\mathrm{lv,D}} = \frac{12L\Gamma}{\rho d_{\mathrm{D}}} \sqrt{\frac{2s}{g}} + A_{\mathrm{f,T}} \tag{5.15}$$

Setting Equations (5.9) and (5.15) equal to one another with appropriate simplifications yields a scaling relationship for the flow mode transition:

$$\Gamma \sim \sqrt{\sigma \rho s} \tag{5.16}$$

Interestingly, this yields the same scaling relationship that predicted the transition from the jet to sheet mode. Again, nondimensionalizing this relationship, we find that the transitional film Reynolds number is a function of the fourth root of the modified Galileo number and the square root of the tube spacing nondimensionalized by the capillary length.

$$Re \sim Ga^{0.25} \left(s/\xi \right)^{0.5} \tag{5.17}$$

On the basis of this scaling relationship, the form of Equation (5.18) was used to model each flow mode transition, where the constants a_0 and a_1 were determined from a regression analysis of the experimental data. The coefficients for each of the three observed mode transitions are shown in Table 5.3.

$$Re = a_0 + a_1 Ga^{0.25} \left(s/\xi \right)^{0.5} \tag{5.18}$$

Table 5.4. Empirical coefficients for flow mode transition model

Transition	a_0	a_1
Droplet to Droplet-Jet	31.7	0.0847
Droplet-Jet to Jet	46.8	0.183
Jet to Jet-Sheet	95.8	0.157

The agreement of the new flow regime transition model with the experimental data is shown in Table 5.4 and Figure 5.4. The new model predicts 82% of the flow regimes correctly. Agreement is highest in the droplet and jet-sheet regimes, where 89% and 91% of the flow modes, respectively, are correctly predicted. Meanwhile, agreement is lowest in the jet mode. This is due to the small range of film Reynolds numbers where the jet mode was observed in the present study (only 21 data points in the jet regime were observed in the present study). Figure 5.4 plots the experimental data and new model using the transitional film Reynolds number versus the scaling term in the model. In general, it can be seen that the flow mode transitions are expected to occur at higher Reynolds numbers as the tube spacing or modified Galileo number increases, and lower Reynolds numbers as the capillary length increases. The modified Galileo number and capillary length are functions of the fluid properties.

Table 5.3. Agreement of flow regime model with data from present study

Flow Regime	Number of Data Points		Percentage	
	Experimental	Predicted	Correct Prediction	False Positive
Droplet	57	65	89%	25%
Droplet-Jet	112	112	77%	15%
Jet	21	21	33%	67%
Jet-Sheet	134	135	91%	10%
Sheet	0	0	100%	0%
Total	324	324	82%	-

$$Ga = \sigma^3 \rho g^{-1} \mu^{-4} \qquad\qquad\qquad (5.19)$$

$$\xi = \sigma^{0.5} \rho^{-0.5} g^{-0.5} \qquad\qquad\qquad (5.20)$$

Combining these effects, we find that the transitional Reynolds number increases as the surface tension or liquid density increases, but decreases as the liquid viscosity increases. As described in Section 4.2.2, this is expected because surface tension and inertial forces directly contribute to the breakup of jets into droplets and sheets into jets by promoting the growth of instabilities. This shifts the transition out of the droplet mode into the jet mode, and out of the jet mode into the sheet mode, to higher mass flow rates. Viscosity has a minimal influence on transitional mass flow rate, but impacts transitional Reynolds number due to the viscosity term in the film Reynolds number definition. At high viscosities, shear stress reduces the velocity of the fluid on the test section, but generally,
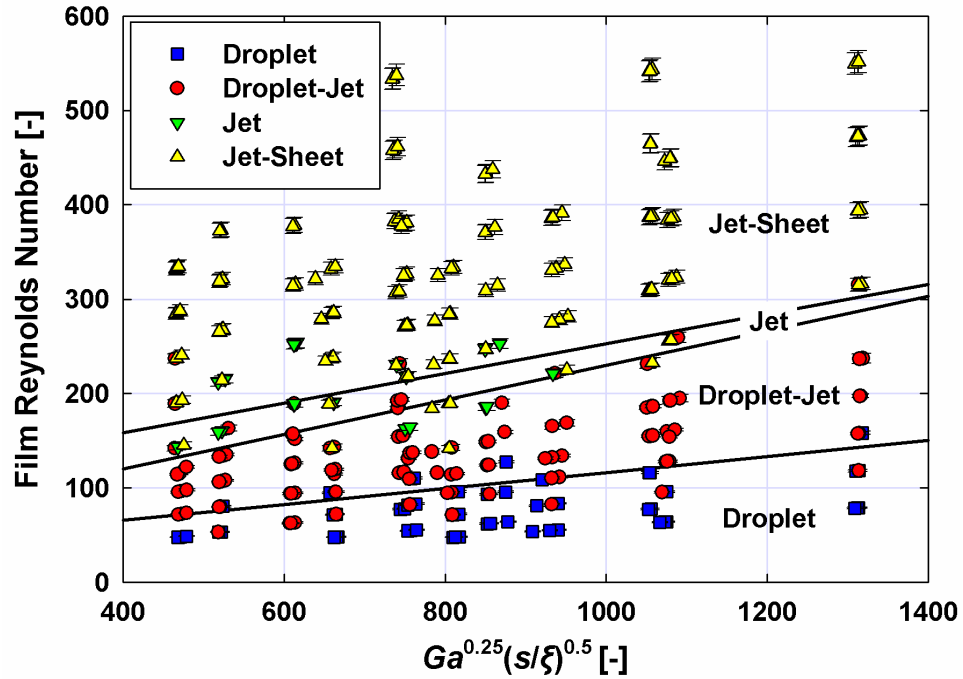

Figure 5.4. Comparison of flow regime model with data from the present study

the fluid stagnates at the bottom of the tube due to surface tension forces, and thus the viscosity does not significantly influence the flow pattern below. In the intertube region, viscosity also has a minimal influence because the shear stress between the liquid and vapor is negligible relative to gravitational and surface tension forces, particularly for the low vapor pressures and test section spacings investigated in the present study.

5.2   Heat Transfer Model

The heat transfer model predicts the average heat transfer coefficient of the test section. This section first evaluates the performance of nine models from the literature, and then develops a new model to predict the heat transfer coefficients measured in the present study.

5.2.1   <u>Comparisons with the Literature</u>

There are currently no heat transfer models available in the literature for evaporating falling films over the horizontal rectangular tubes investigated in the present study. This section compares the experimental data to predictions made by nine round tube models. These include one vertical tube model, three subcooled falling-film models, and five round tube falling-film evaporation models. The section first discusses the agreement of each individual model, and then summarizes the relative performance of the models. The model predictions are compared with the data from the present study on the basis of average deviation (AD) and absolute average deviation (AAD):

$$\text{AD} = \frac{h_{\text{pred}} - h_{\text{exp}}}{h_{\text{exp}}} \times 100 \tag{5.21}$$

$$\text{AAD} = \frac{\left| h_{\text{pred}} - h_{\text{exp}} \right|}{h_{\text{exp}}} \times 100 \tag{5.22}$$

The agreement of the Chun and Seban (1972) correlation with the present data is shown in Figure 5.5. It predicts the data with an average deviation (AD) of 9% and an absolute average deviation (AAD) of 35%, with 48% of the data predicted within 25%, and 78% of the data predicted within 50%. This correlation is based on data taken with water over a large diameter vertical round tube. In the Reynolds number range considered

in their study, it predicts a decreasing heat transfer coefficient with increasing Reynolds number, while the opposite trend was observed in the present study. Thus, the correlation overpredicts the heat transfer coefficient at low Reynolds numbers, and underpredicts the heat transfer coefficient at high Reynolds numbers. This can be attributed to the range of conditions in their experimental study, which was limited to situations with full tube wetting, while the present study examined situations with partial wetting and rivulets. The correlation captures the correct magnitude of the resulting heat transfer coefficients, but does not capture the data trends with mass flow rate, temperature, or tube spacing.

The Danilova *et al.* (1976) correlation consistently underpredicts the present data, as shown in Figure 5.5, with an AD of -43%. The overall agreement of the correlation is relatively low, with an AAD of 44%, 19% of the data predicted within 25%, and 52% of the data predicted within 50%. However, it was based on data for R-12, R-22, and R-113; therefore, extrapolation to falling films of water may not be appropriate. The correlation
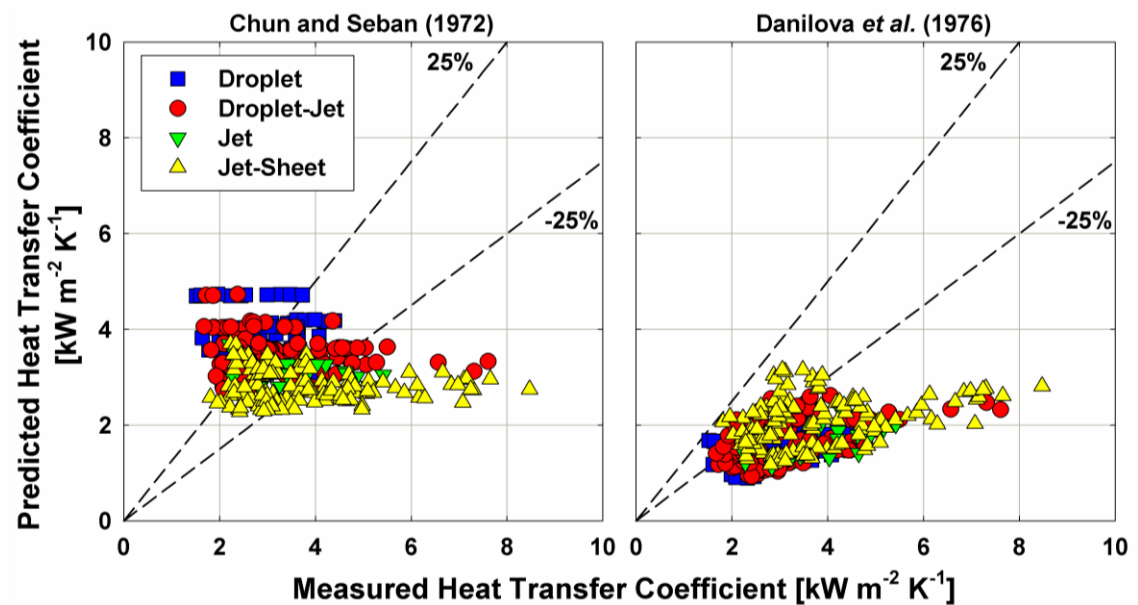

Figure 5.5. Comparison of the Chun and Seban (1972) and Danilova *et al.* (1976) correlations with the present data

exhibits the same general trends as the experimental data with Reynolds number and tube spacing, as well as capturing the initial influence of increasing temperature via Prandtl number. It also predicts a tube diameter and heat flux influence. The heat flux influence was not observed in the present study, and only a single test section geometry was considered, precluding an examination of the influence of modifying the test section dimensions. Given that the Danilova *et al.* (1976) include the round tube diameter in their correlation, an equivalent diameter was used for comparison. This is found by taking the diameter of a round tube with the surface area of the rectangular test section, as shown in Equation (5.23).

$$A_{TS} = \pi D_{eq} L \qquad (5.23)$$

The agreement of the Owens (1978) correlation with the present data is shown in Figure 5.6. It predicts the experimental data with an AD of 54% and AAD of 64%, with 32% of the data predicted within 25%, and 54% of the data predicted within 50%. In
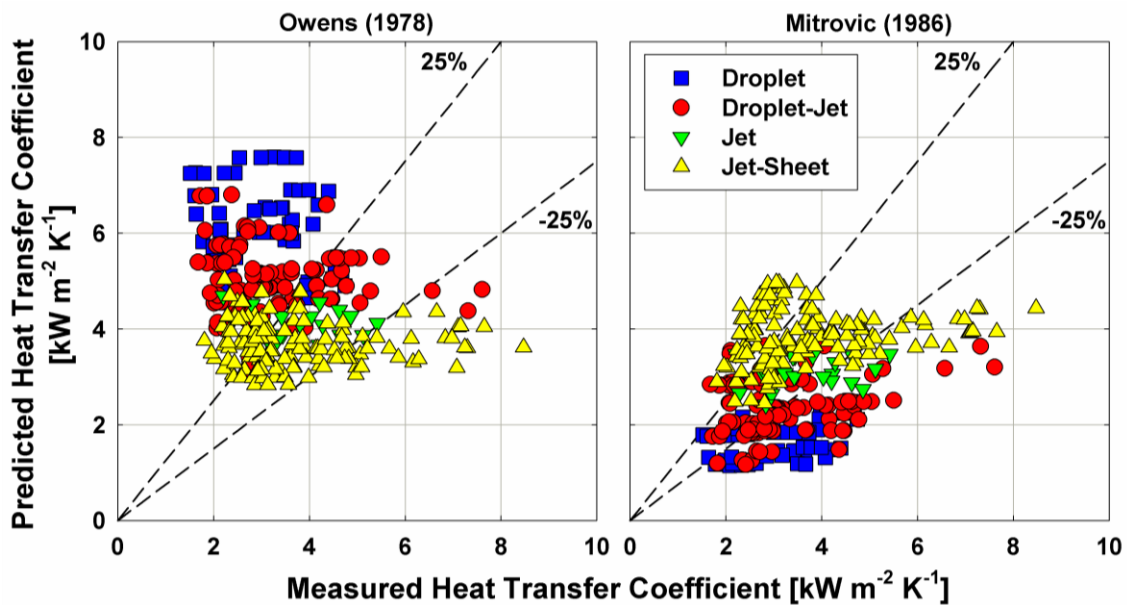

Figure 5.6. Comparison of the Owens (1978) and Mitrovic (1986) correlations with the present data

general, it substantially overpredicts the heat transfer coefficient at low film Reynolds numbers in the droplet mode, but improved agreement is observed at higher film Reynolds numbers in the jet-sheet mode. The Owens (1978) correlation predicts a decreasing heat transfer coefficient as Reynolds number increases, while the opposite trend is observed in the present study. However, it predicts the tube spacing trend observed in the present study. These differences can be attributed to the experimental range of their data. The correlation is based on ammonia and water data taken with large diameter round tubes and focused on higher Reynolds number flow, where better agreement was observed. As above, this correlation includes a function of tube diameter, and an equivalent tube diameter based on Equation (5.23) was used.

The Mitrovic (1986) correlation underpredicts the present data with an AD of -8% and an AAD of 32%, with 40% of the data predicted within 25%, and 78% of the data predicted within 50%. The underprediction is largest in the droplet and droplet-jet mode, with better agreement in the jet and jet-sheet mode. The correlation is based on data taken with subcooled water, and finds the heat transfer coefficient as a function of film Reynolds number, Prandtl number, tube spacing, and tube diameter. As above, an equivalent tube diameter, shown in Equation (5.23), was used for the tube diameter. The correlation predicts similar trends with Reynolds number and tube spacing to those observed in the present data, but does not fully capture the observed heat transfer coefficient trends with temperature. However, the correlation is based on data taken at a single temperature; therefore, the inability to capture this trend is expected.

175

Parken *et al.* (1990) provided separate correlations for tubes with a diameter of 25.4 and 50.8 mm with falling-film evaporation of water. The agreement of the present data with their 25.4 mm tube correlation is shown in Figure 5.7. It predicts the present data with an AD of 4% and an AAD of 26%, with 52% of the data predicted within 25%, and 89% of the data predicted within 50%. This is the best agreement among the considered correlations. The Parken *et al.* (1990) correlation is a function of film Reynolds number and Prandtl number. Although it correctly captures the influence of mass flow rate and the initial change in heat transfer coefficient with temperature, it does not capture the influence of tube spacing or the inflection point in the temperature trend that was observed in the present study. Overall, the correlation predicts relatively uniform heat transfer coefficients throughout the range of conditions investigated in the present study. Thus, it overpredicts low heat transfer coefficient measurements, and underpredicts high heat transfer coefficient measurements. These differences can be
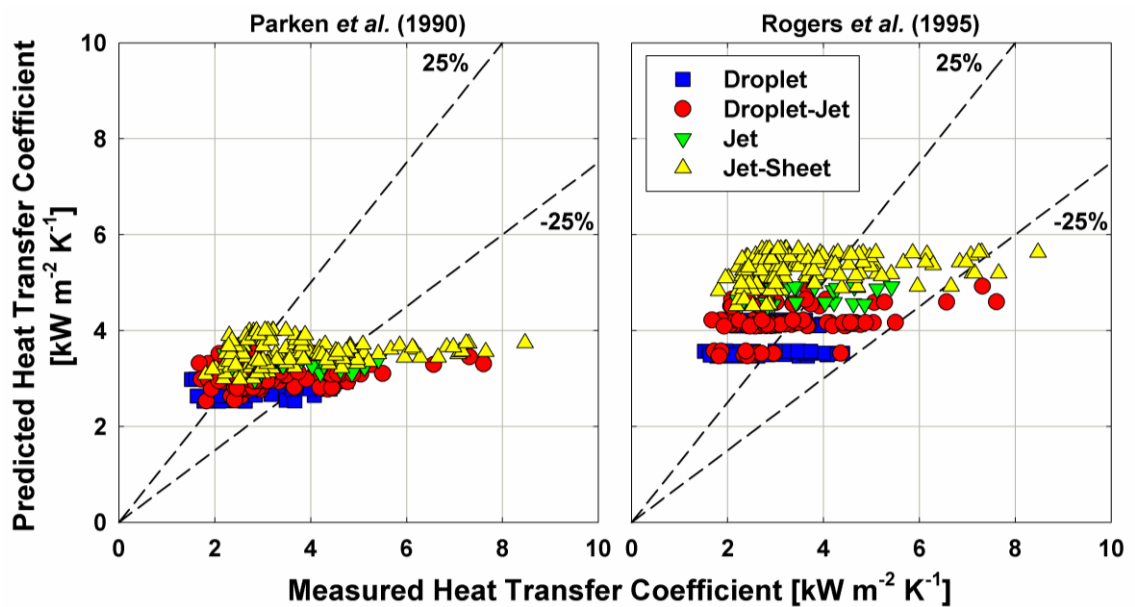

Figure 5.7. Comparison of the Parken *et al.* (1990) and Rogers *et al.* (1995) correlations with the present data

attributed to the influence of the additional trends noted above.

The agreement of the Rogers *et al.* (1995) correlation with the present data is shown in Figure 5.7 Their correlation, based on single-phase heat transfer data taken with subcooled water, overpredicts most of the present data with an AD of 48% and an AAD of 52%, predicting 31% of the data within 25% and 54% of the data within 50%. It relates the Nusselt number to a function of the Reynolds number, Prandtl number, and Archimedes number. Although the correlation captures the heat transfer coefficient trend with increasing Reynolds number, it does not capture the inflection point in the trend with temperature, and does not account for tube spacing.

The Hu and Jacobi (1996b) model provides separate correlations for the droplet, jet, and sheet modes based on single-phase heat transfer data taken with subcooled water, ethylene glycol, and water-glycol mixtures. Using the new flow regime model developed in Section 5.1.2, their model predicts the present heat transfer data with an AD of 23%
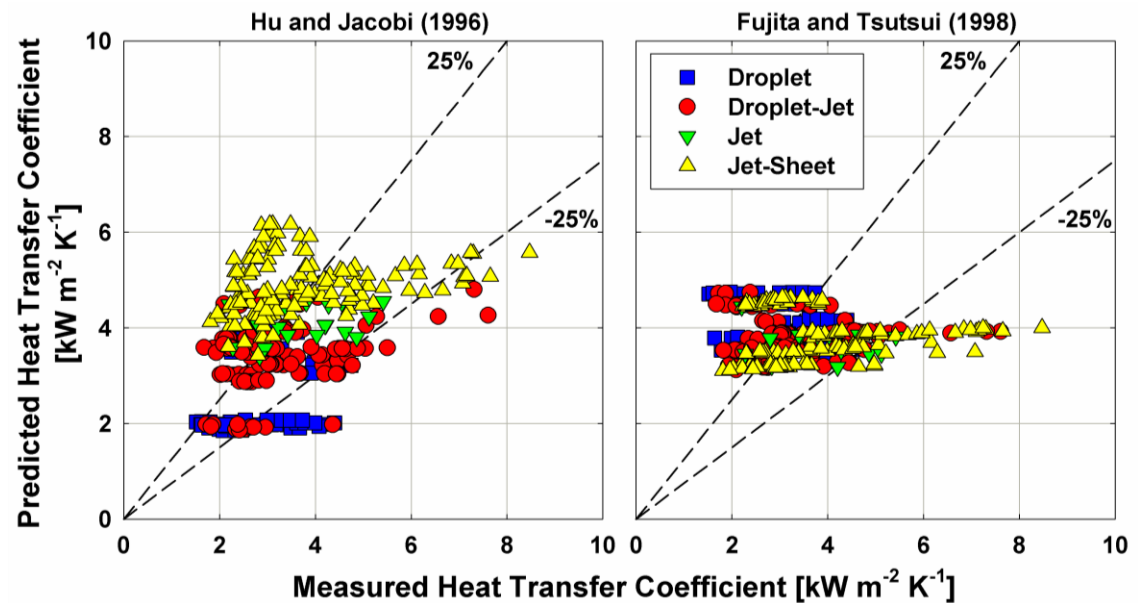

Figure 5.8. Comparison of the Hu and Jacobi (1996) and Fujita and Tsutsui (1998) correlations with the present data

and an AAD of 39%, with 44% of the data predicted within 25%, and 74% of the data predicted within 50%. Agreement only decreased slightly using the Hu and Jacobi (1996b) flow regime model developed for round tubes. Their correlations relate the Nusselt number to a function of the Reynolds number, Prandtl number, Archimedes number, and tube spacing nondimensionalized with the tube diameter. As above, an equivalent tube diameter, shown in Equation (5.23), was used for the tube diameter for this comparison. The correlation underpredicts a portion of the data at low film Reynolds numbers in the droplet regime, which can be attributed to observing a weaker tube spacing influence than was seen in the present study. Meanwhile, it overpredicts a portion of the data at high film Reynolds numbers, due to not exhibiting an inflection point in the heat transfer coefficient trend with increasing temperature.

The comparison with the Fujita and Tsutsui (1998) correlation is shown in Figure 5.8. Based on data taken with R-11, it predicts the data with an AD of 26% and an AAD of 39%, with 46% of the data predicted within 25%, and 73% of the data predicted within 50%. Their correlation relates the Nusselt number to a function of film Reynolds number and Prandtl number. However, it generally finds that the heat transfer coefficient decreases with increasing film Reynolds number, while the opposite trend is present in the current data. In addition, it predicts a fairly narrow range of heat transfer coefficients near 4 kW m^{-2} K^{-1}. These differences can be attributed to the structure of their correlation not extrapolating well to the conditions of the present study.

The Li et $al.$ (2011b) correlation substantially underpredicts the majority of the present data with an AD of -59% and an AAD of 72%. Only 7% of the data are predicted within 25%, and 20% of the data are predicted within 50%. Agreement is highest in the

droplet regime, with worse agreement observed at higher Reynolds numbers. Their correlation was developed based on data taken with water at subatmospheric pressures, similar to that of the present study. However, they examined low Reynolds number (22–108) flow on round tubes. Thus, the correlation performs relatively well in the low Reynolds number range examined, but cannot be extrapolated to the higher Reynolds (50–550) examined in the present study. In addition, Li *et al.* (2011b) observed full wetting at a film Reynolds number of 54, much lower than was observed in the present study, contributing to the overprediction of a portion of the experimental data from the present study.

The average and absolute average deviation of each model are shown in Figure 5.10. The best predictions were observed with the Parken *et al.* (1990) correlation, which was developed based on falling-film evaporation data taken with water on 25.4 mm diameter round tubes. It predicts the present data with an AD of 4% and an AAD of 26%.
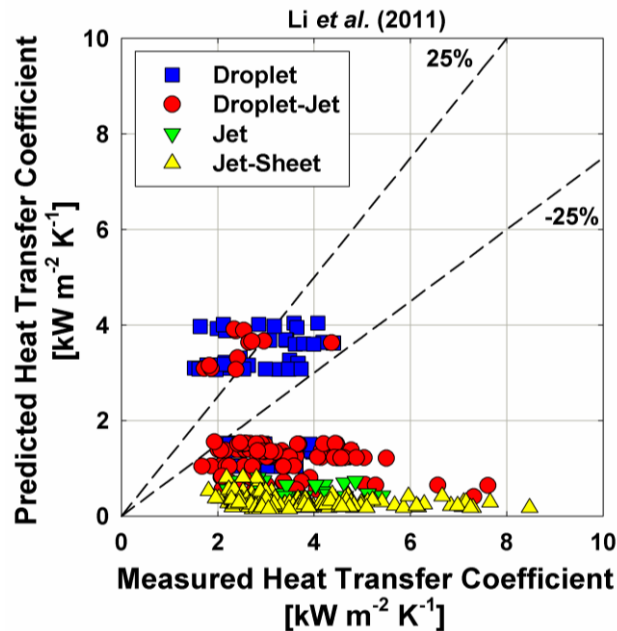

Figure 5.9. Comparison of the Li *et al.* (1978) correlation with the present data

However, it does not accurately capture the heat transfer coefficient trends in the present data as the fluid properties or test section spacing are modified. All of these models are based on round tube data, which limits their applicability to the data in the present study with rectangular geometries. In addition, the data sets forming the basis of these models often do not capture the experimental range of the present study, and thus may not extrapolate accurately to these conditions. Thus, their inadequate prediction of the data
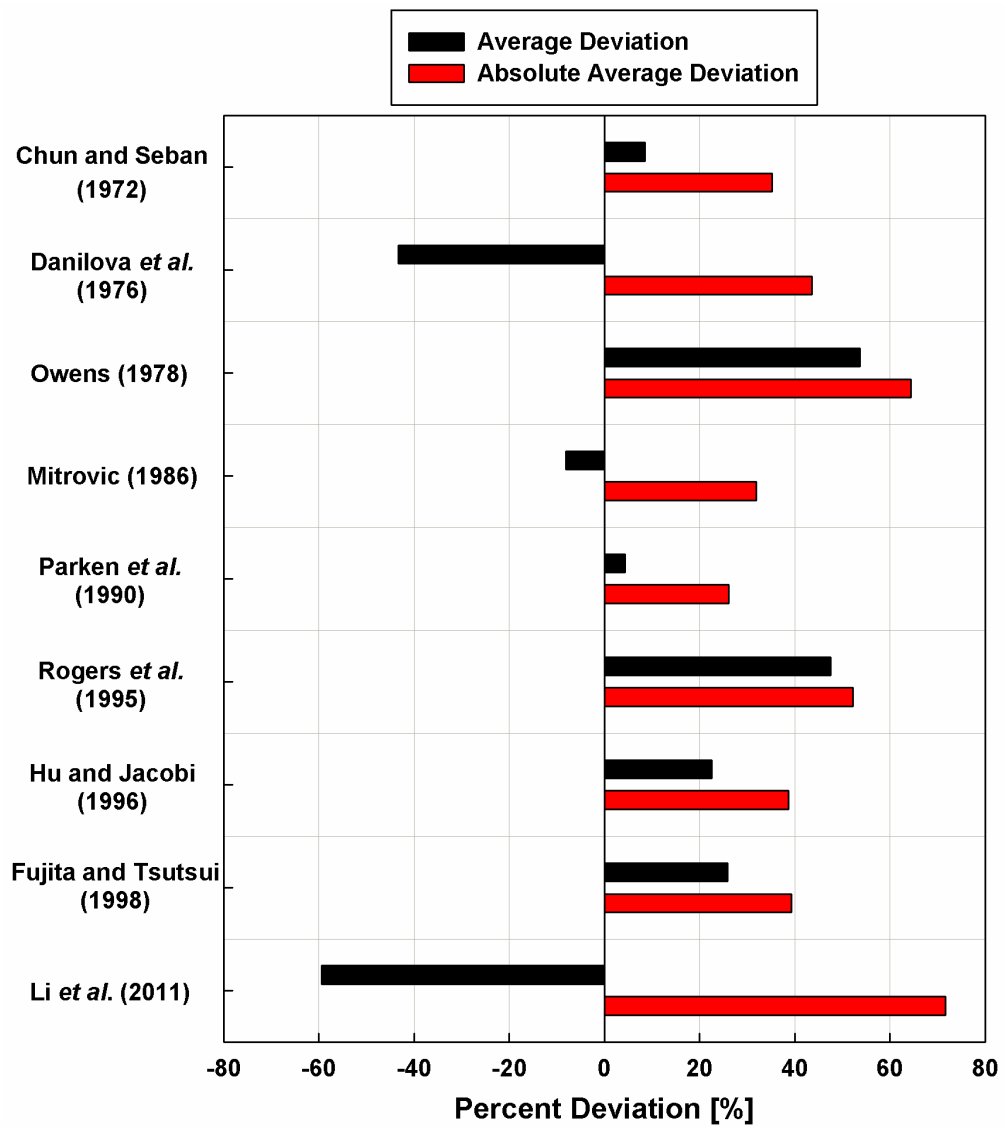

Figure 5.10. The average and absolute deviation of nine models relative to the experimental data in the present study

from the present study is expected. Several correlations, such as the Li *et al.* (2011b) model, exhibit stronger performance for limited portions of the data taken with conditions similar to their intended usage.

The percent of the experimental data predicted within 25 and 50 percent tolerance ranges is shown in Figure 5.11. Again, the best predictions were observed with the Parken *et al.* (1990) model, which predicted 52% of the data within 25% and 89% of the data within 50%. Good prediction was also observed with the Chun and Seban (1972)
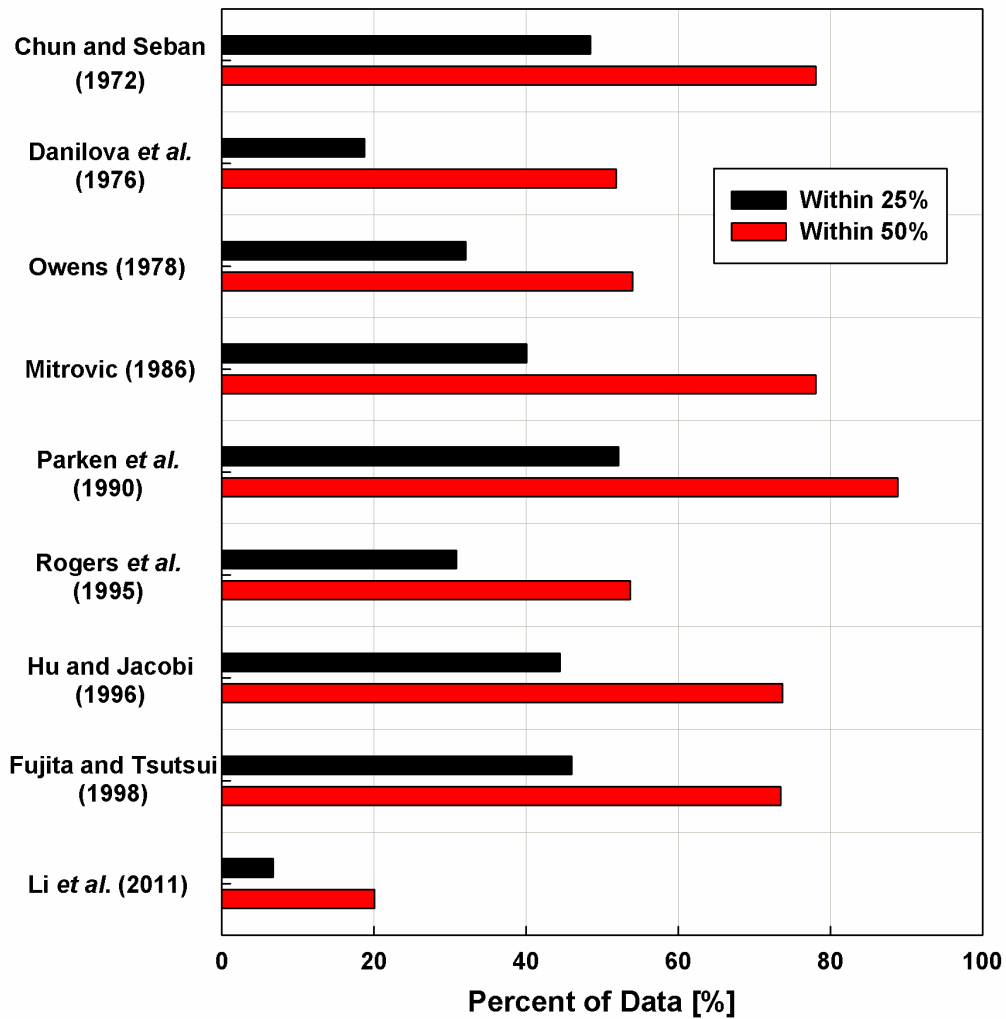

Figure 5.11. The percent of the experimental data in the present study predicted within two tolerance ranges by nine models

correlation, which predicts 48% of the data within 25% and 78% of the data within 50%. This correlation, based on data taken for falling-film evaporation of water on vertical round tubes, also does not accurately capture the trends in the present study, but is able to accurately capture the correct magnitude of the resulting heat transfer coefficients. From these comparisons, it is apparent that previous models are not able to accurately predict the experimental data from the present study, and a new model was developed to fully capture these trends.

5.2.2   Heat Transfer Model Development

This section details the development of a heat transfer coefficient model based on the experiments conducted in the present study. This model first uses a hydrodynamic model to predict the wetted tube area. This analysis is supported by the flow visualization data. Then, the hydrodynamic model is used as the basis for a heat transfer model, which is guided and validated by the data from the heat transfer experiments.

Hydrodynamics Model

The primary goal of the hydrodynamic model is to predict the wetting ratio, or the portion of the tube area that is wetted for the range of conditions in the present study. In order to do so, an idealized model of the flow is developed to estimate the wave coverage of the tube over time. This transient wave model is then integrated over time to determine a single average wetting ratio at each condition. Where possible, this analysis uses analytical or the theoretical approaches. In areas where this is not practical, it draws on the experimental data from the flow visualization study.

The analysis begins by idealizing each wave shape as an ellipse. These ellipses begin with their vertical centerpoint at the top of the test section. Then, when the wave

reaches a specified height, it detaches and travels down the test section. This provides an accurate approximation of the wave shape over time, as can be seen in Figure 5.12, which shows the development of a wave from the flow visualization study and the corresponding idealized wave.

The area of an ellipse can be determined by Equation (5.24), where the constants 'a' and 'b' are one half of the length and width of the ellipse, respectively.

$$A_{ellipse} = \pi ab \tag{5.24}$$

$$A_{partial,ellipse} = \frac{\pi ab}{2} + ab\ \sin\left(\frac{x}{a}\right) + \frac{bx}{a}\sqrt{a^2 - x^2} \tag{5.25}$$

The area of an ellipse up to a line parallel to the minor axis, as shown in Figure 5.13, is given by Equation (5.25). This equation is used when only a portion of the ellipse, representative of the wave, is on the test section.

The wave was initially taken to be an ellipse with the minor axis located at the top of the test section (Figure 5.14a). This location was maintained until one half of the
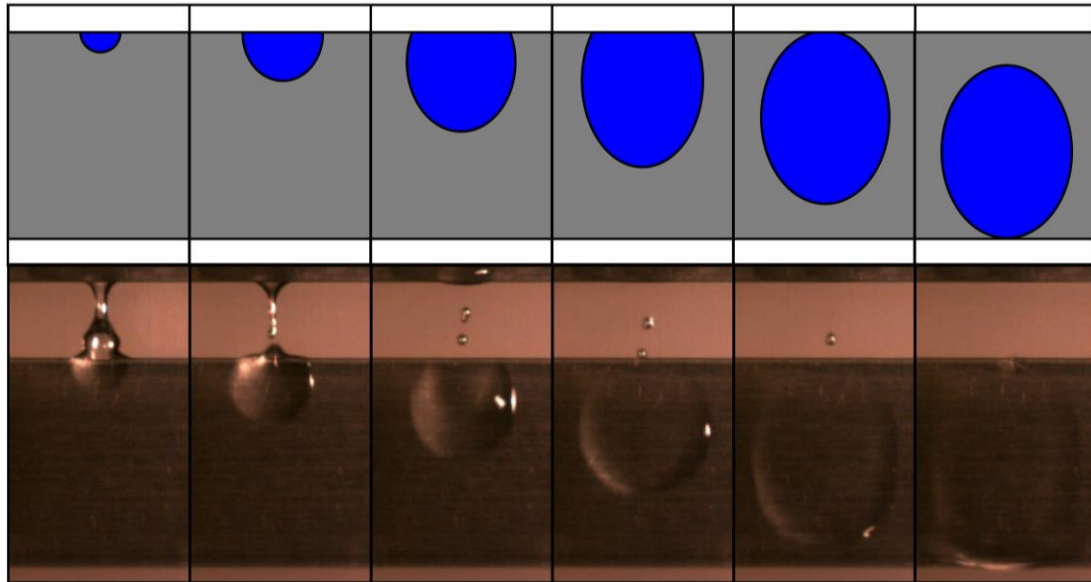

Figure 5.12. Idealized wave flow compared to experimental wave observation

183
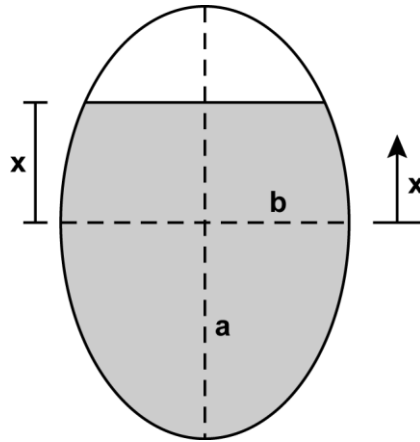
Figure 5.13. Shaded area demonstrates area of a partial ellipse up to line x

maximum wave height was reached. At this point, the minor axis of the ellipse also traveled at the same velocity as the leading edge of the ellipse (Figure 5.14b). In other words, the wave travelled down the test section. As the wave progressed, it detached from the top of the test section (Figure 5.14c) and eventually reached the bottom edge of the test section. As the wave reaches the bottom of the test section, it is assumed to continue traveling and leave the test section (Figure 5.14d).

Each wave is considered to begin with a width equal to the diameter of the impacting droplet. The droplet diameter was taken from the droplet volume data in the flow visualization study, assuming a spherical droplet shape. This average droplet

Figure 5.14. Stages of the idealized wave flow

184

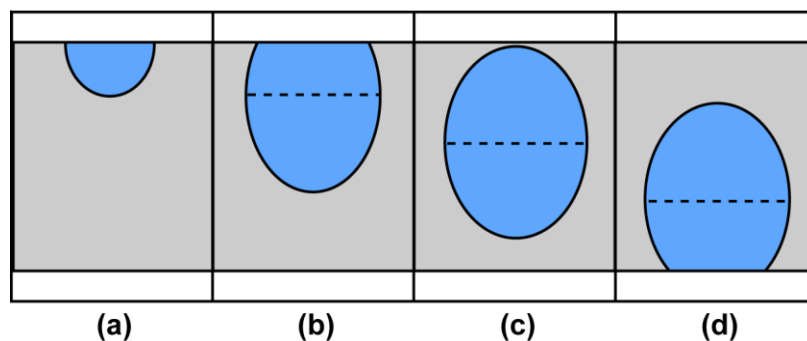diameter was 6.51 mm. Although the flow visualization study was taken at a single fluid property condition, Yung *et al*. (1980) found that the droplet diameter is a function of the surface tension, liquid density, and gravity. All of these values change minimally in the present study, and thus, this uniform droplet diameter is considered to be an acceptable approximation.

At the time the droplet contacts the test section, the wave is taken to have no height, but then grow at a uniform rate. This velocity is taken to be the velocity of the fluid at the time of the droplet impact, assuming free fall between each test section. Although this velocity is that of the droplet, and the wave velocity would be lower due to the additional influence of viscous drag due to the tube surface, as well as due to the different flow area compared to that of the impinging drops, in the absence of other reliable ways to predict wave velocity from the measurements taken in this study, it is viewed as an adequate approximation based on the following considerations. The droplet diameters in the flow visualization study were found to range from approximately 4 to 5 mm, while the test section is only 1.4 mm thick, and the top portion of the test section is rounded. Thus, the test section is not wide enough to fully stagnate the droplet or redirect the fluid flow, as would be the case with large diameter round tubes. Also, the wave velocities measured in the flow visualization study show excellent agreement with the impact velocity calculated using free fall, as shown in Figure 5.16. And finally, the flow visualization study found that the wave velocity is approximately constant throughout its residence time on the test section. The impact velocity determines the initial velocity of the wave, and given that the wave velocity is almost constant, it can also be assumed to determine the wave velocity throughout its residence time on the test section. With this

185

assumption, the impact velocity is a function of the gravity and the test section spacing, as seen in Equation (5.26), and the wave travels with this impact velocity over the test section.

$$V_{wave} = \sqrt{2gs} \tag{5.26}$$

The maximum wave height, determining the location of the trailing edge of the wave, was taken to be 3.5 times the droplet width. This is consistent with the flow visualization observations, and results in good agreement with surface area data taken in the flow visualization study. Meanwhile, the growth of the wave width was also taken to be a constant rate, using the average wave width growth rate in the experimental data from the flow visualization study. This resulted in a wave width growth rate of 0.308 m s^{-1}. A comparison between these wave width and height predictions and a sample wave is shown in Figure 5.15.

Using these assumptions, the transient growth of a wave throughout time was calculated. The wave behavior predicted by this model is compared to the results of the flow visualization study in Figure 5.16. Good agreement is observed in terms of the wave width, surface area, and velocity. Although the wave width predictions have a strong
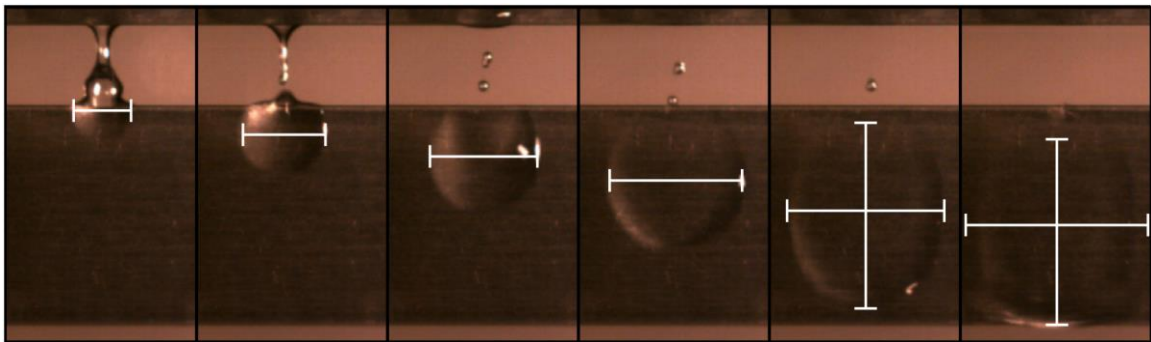
Figure 5.15. Wave height and width predicted by model overlaid on sample wave development

186

empirical basis, the wave velocity predicted by the model has a theoretical basis and is independent of the measured values, and the wave surface area predictions are only partially based on empirical data. The change in the trend of the surface area predictions by the model corresponds to the location when the wave reaches its maximum height. The trailing edge of the wave was difficult to capture in the flow visualization analysis,
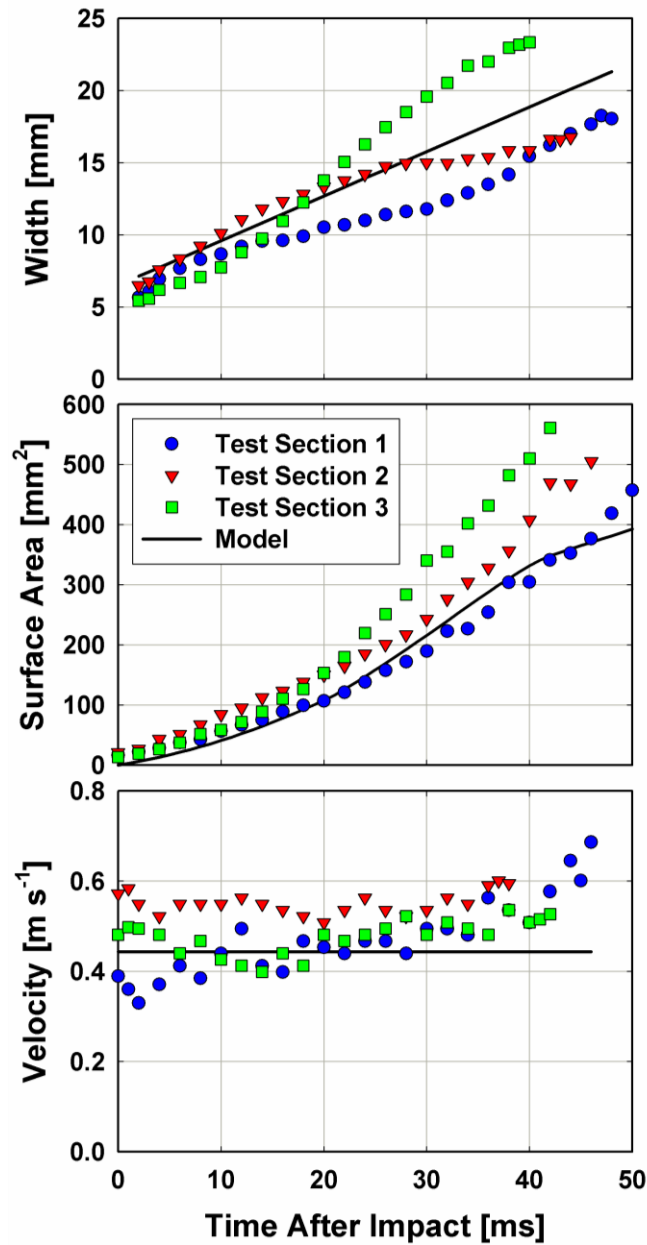
Figure 5.16. Comparison of model to flow visualization wave data

which may account for this discrepancy in the time period with the largest wave heights. However, the model still shows good agreement with the range of surface areas values observed in this region.

Flow visualization data were only taken during the growth of each wave, from the point of impact until it reached the bottom of the test section. This limitation was due to the reduced light gradients present at the trailing edge of the wave. Past this point, the wave is much smoother and cannot be measured with the techniques used in the present study. The predicted surface area development of a full wave is shown in Figure 5.17. The initial increase in surface area, from 0 to 20 ms, takes place when the wave is still located at the top of the test section, with the minor axis of the ellipse at the top surface of the test section. Then, from 21 to 41 ms, the wave has begun traveling down the test section, with the minor axis of the ellipse leaving the top of the test section. At 42 ms the wave no longer contacts the top of the test section and is entirely on the tube. From 51 to 92 ms, this wave is contacting the bottom of the test section, and is partially off the test
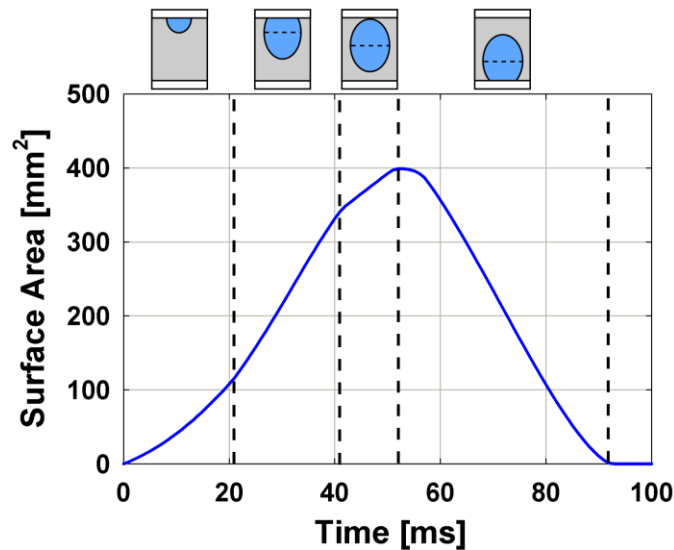

Figure 5.17. Development in the surface area of a single wave

188

section. Finally, at 93 ms, the wave exits the test section.

In order to find the average wetting of the test section over time, two additional pieces of information are needed: the spacing between adjacent waves, and the time between each wave. The spacing between each wave was found using Yung *et al*. (1980) correlation for droplet or jet spacing based on a Taylor instability analysis, as shown in Equation (4.2). The flow visualization experiments found good agreement between these predictions and the present data, as described in Section 4.1.2.

$$\lambda = 2\pi \sqrt{\frac{2\sigma}{\rho g}} \tag{5.27}$$

After this wave spacing is found, the timing between waves can be found using a mass balance. The mass flow rate can be set equal to the droplet mass delivered over a given time, as shown in Equation (5.28), where τ_D is the time between droplet impacts (Wang and Jacobi, 2014).

$$\Gamma \lambda = \frac{\pi \rho d_D^3}{12 \tau_D} \tag{5.28}$$

This information allows the average wetting ratio to be found, where the wetting ratio is the percentage of tube area that is wetted.

$$WR = \frac{A_{\text{wet}}}{A_{\text{TS}}} \tag{5.29}$$

To determine the average wetting ratio, the wetting ratio was calculated using 1 ms time steps. In areas where no wave is present, the wetting ratio is simply 0. Then, these wetting ratios were averaged to find a single average wetting ratio for each condition. These calculations were carried out in the droplet mode for the conditions of the experimental data, as shown in Figure 5.18a, as well as throughout the full experimental

data range, as shown in Figure 5.18b. Although the present study was not able to directly measure wetting ratio, these predictions are consistent with experimental observations. The wetting ratio generally increases with film Reynolds number. Partial dryout was observed for all of the experimental conditions, which is consistent with the results of the model, which predicts wetting ratios ranging from 7% to 89%.

The film thicknesses predicted by this model are compared in Figure 5.19 with those by Lel *et al.* (2005), an experimental correlation based on silicone fluids (Polydimethylsiloxane, CAS No.: 63148-62-9, DMS-T01.5, T05, and T12) with a similar viscosity range, as well as the classic theoretical Nusselt approach (Nusselt, 1916). There is excellent agreement between the average film thickness predicted by the Lel *et al.* (2005) correlation and the present model, but the Nusselt (1916) approach predicts significantly lower values. However, it is a theoretical approach based on the assumption of full tube wetting. If the mass flow rate in the Nusselt approach is adjusted using the
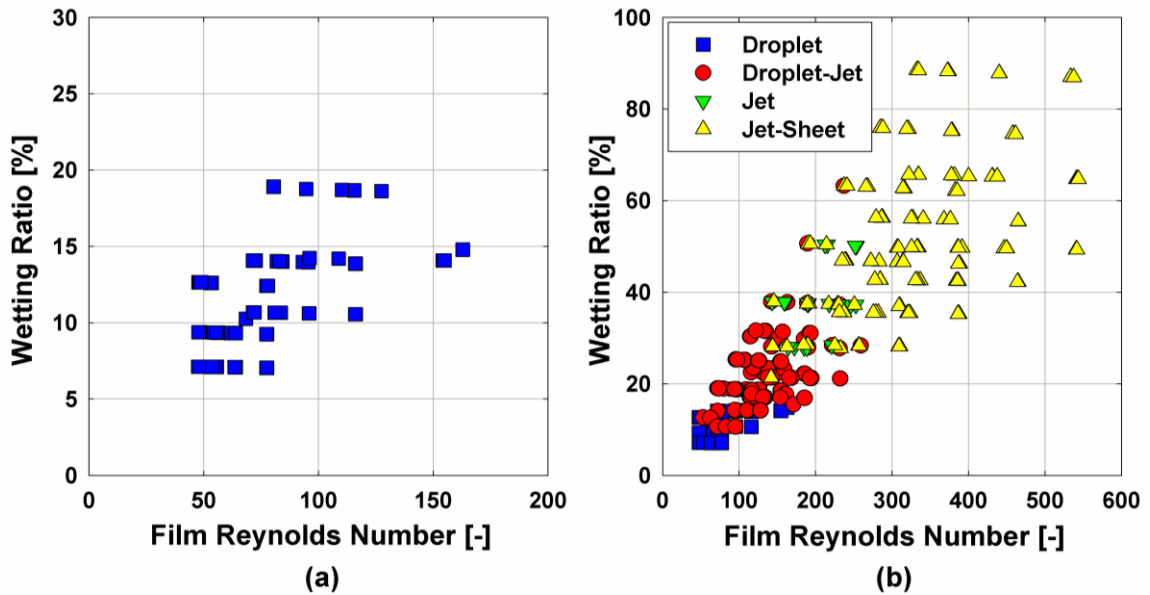
Figure 5.18. Model wetting predictions in (a) the droplet mode, and (b) for all of the flow regimes

wetting ratio predictions developed in the present study, these adjusted Nusselt values, also shown in Figure 5.19, also show good agreement with the present model.

During application of this model, it is impractical to predict the transient wave behavior at each condition to find the wetting ratio. Thus, a wetting ratio correlation was developed on the basis of this wetting model. It was found that the wetting is well predicted as a function of the film Reynolds number, modified Galileo number, and test section spacing nondimensionalized by the capillary length. These are the same parameters used in the flow regime model. The wetting ratio cannot exceed 100%. Thus, if Equation (5.30) predicts a wetting ratio over this value, a wetting ratio of 100% should be used.

$$WR = 1.95 \; Re \; Ga^{-0.269} \left(s/\xi \right)^{-0.519} \tag{5.30}$$

$$Ga = \sigma^3 \rho_1 g^{-1} \mu_1^{-4} \tag{5.31}$$

$$\xi = \sqrt{\sigma \rho_1^{-1} g^{-1}} \tag{5.32}$$

The coefficients in Equation (5.30) were determined based on a regression
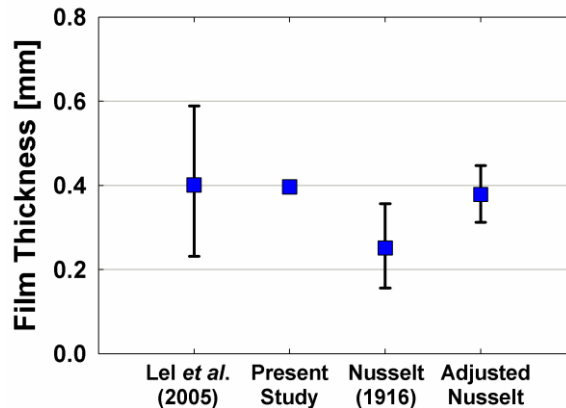
Figure 5.19. Film thickness predictions of the present study compared to several correlations. The data point indicates the average, with the black bars representing the range of values

analysis of the wetting model predictions. Interestingly, the exponent corresponding to the film Reynolds number was found to have a value of 1. This is consistent with the observations of Roques and Thome (2007b) and Habert and Thome (2010b); both studies found that wetting ratio is linearly proportional to Reynolds number.

The performance of the wetting correlation relative to the wetting model is shown in Figure 5.20. In the droplet regime, the wetting correlation predicted the results of the wetting model with an AD of -2.24% and an AAD of 2.55%, with a maximum deviation of 6.20%.

Although the assumptions in the wetting model are only completely applicable in the droplet regime, similar wetting behavior is expected throughout the full range of the experimental study. For instance, the linear relationship between wetting ratio and Reynolds number observed by Roques and Thome (2007b) and Habert and Thome (2010b) was not limited to a single flow mode. The extrapolation of the model to other
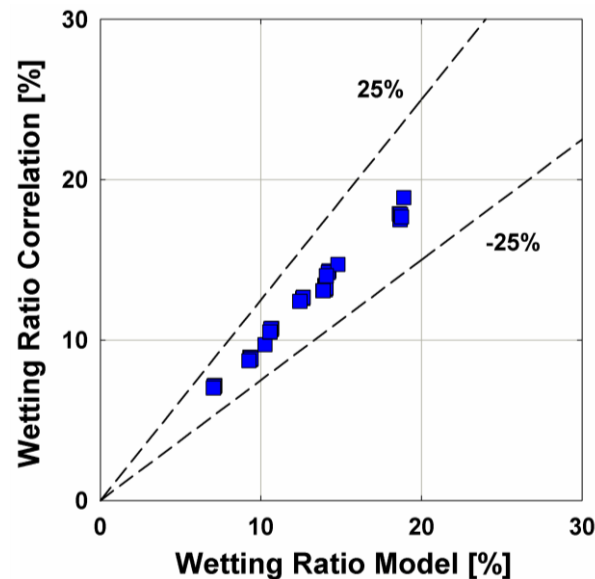
Figure 5.20. Comparison of the wetting correlation and wetting model in the droplet mode

Table 5.5. Agreement of the wetting correlation and wetting model

Data Conditions	AD	AAD	Maximum Deviation
Droplet Data	-2.24%	2.55%	6.20%
All Data	-1.66%	2.10%	6.22%

flow modes was approached in two ways. First, the wetting model was directly applied at these conditions, as shown in Figure 5.21a. Second, the correlation developed based on droplet mode data was simply extrapolated to these conditions, as shown in Figure 5.21b. The predictions using either approach are very similar. Using the wetting model predictions for all of the data conditions, it was found that the correlation predicts the model with an AD of -1.66% and an AAD of 2.10%, with a maximum deviation of 6.22%.

The wetting ratio trends of the new hydrodynamic model are shown in Figure
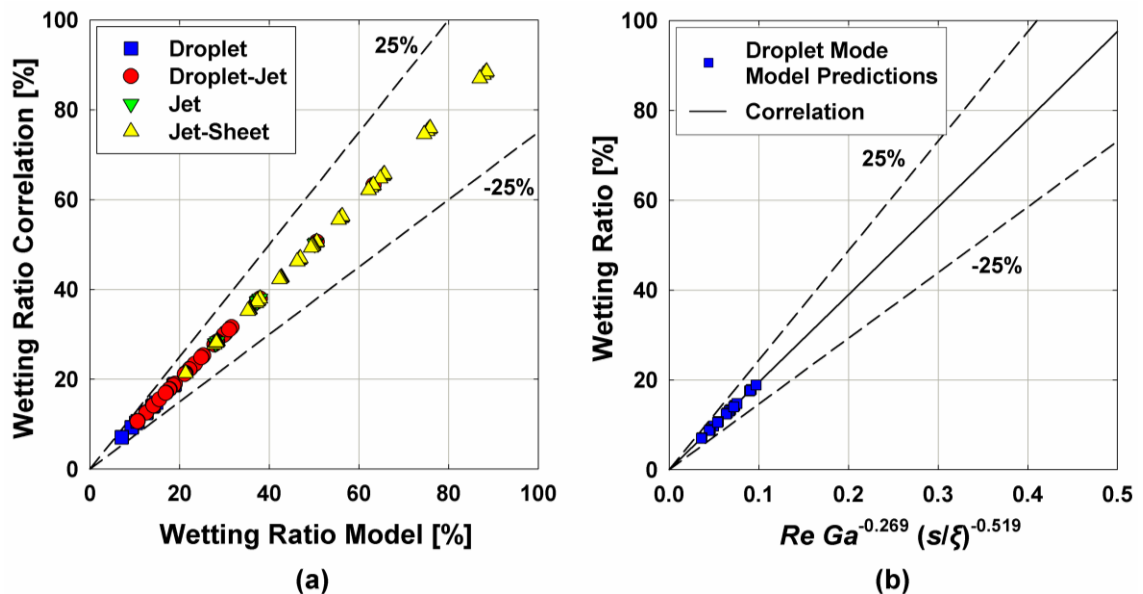
Figure 5.21. Wetting ratio predictions for (a) the wetting model applied to all of the flow modes, and (b) extrapolating the wetting correlation developed based on the droplet mode

5.22. The wetting ratio is plotted versus film Reynolds number for three test section spacings and three saturation temperatures. The wetting ratio increases linearly as film Reynolds number increases, and decreases as tube spacing increases. At a set film Reynolds number, the wetting ratio will decrease as saturation temperature increases. This is due to the viscosity term in the film Reynolds number definition. The wetting ratio changes minimally as saturation temperature increases for a set mass flow rate and test section spacing. This performance matches the wetting ratio trends observed during the experimental study. Increasing the mass flow rate provides additional fluid to wet the tube and increases the wetting ratio. As the mass flow rate decreases, the wetting ratio also decreases, reaching a point with zero wetting when there is no fluid flow. Increasing the test section spacing decreases the wetting ratio due to the higher impact velocities and potential for fluid loss due to splashing or slinging, although this influence is weaker than that of mass flow rate in the experimental range under consideration in the present study.
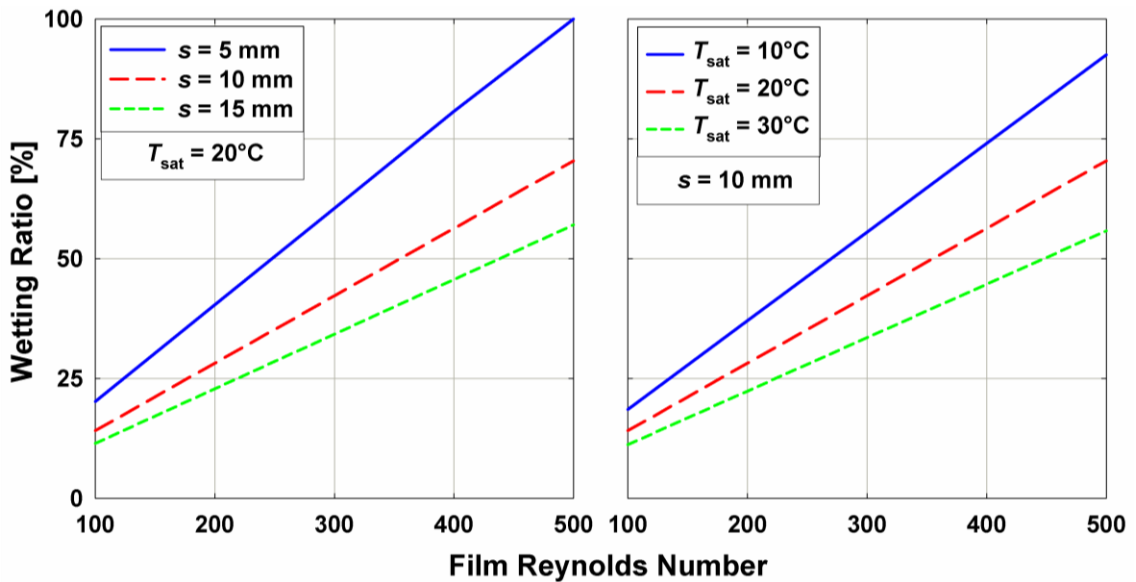
Figure 5.22. Wetting correlation trends with tube spacing, temperature, and Reynolds number

Finally, modifying the fluid properties by changing the saturation temperature has a minimal influence within the experimental range, but the model predicts that fluid properties will influence wetting ratio if they are changed substantially, as would be expected.

This hydrodynamic model represents a new approach to predicting wetting behavior in falling-film evaporation models. This is an important aspect of determining overall falling-film heat transfer behavior. Although it incorporates a number of significant flow idealizations, it shows good agreement with the flow visualization data, qualitative observations, and trends in the literature. It serves as an input to the heat transfer model discussed next.

Heat Transfer Coefficient Model

The hydrodynamics model developed in the present study, as well as the experimental heat transfer data, were used to develop a new model for predicting falling-film evaporation heat transfer coefficients. The model follows an approach similar to that proposed by Roques and Thome (2007b) for falling-film heat transfer with nucleate boiling on round tubes. They observed similarities between the dominant mechanisms in falling-film heat transfer with nucleate boiling and pool boiling heat transfer, and proposed an empirical falling-film factor K_{ff}, which is the ratio of the falling-film heat transfer coefficient to the pool boiling heat transfer coefficient:

$$K_{ff} = \frac{h_{ff}}{h_{pb}} \tag{5.33}$$

The present model proposes a similar relationship between falling-film evaporation heat transfer without boiling and the classic Nusselt film heat transfer theory (Nusselt, 1916), which was originally developed for condensation heat transfer. A heat transfer coefficient is calculated with Nusselt film theory, and then an empirical falling-film factor is used to account for enhancement due to boundary layer development, the impact region, and film waviness or other disturbances.

$$K_{ff} = \frac{h_{ff}}{h_{NF}} \tag{5.34}$$

The Nusselt analysis considers film flow down an isothermal vertical or inclined surface. It assumes a steady, laminar film flow with constant properties and a smooth liquid-vapor interface. Heat transfer is considered to be by conduction only in the film, and inertial effects are assumed to be negligible relative to gravitational and viscous

forces in the momentum balance. The vapor is considered to be stationary, with negligible drag at the liquid-vapor interface. As shown in Equation (5.35), this results in a relationship between average Nusselt number and film Reynolds number.

$$Nu = 1.468 Re^{-1/3} \tag{5.35}$$

However, this approach assumes uniform film coverage over the tube surface. In the present study, dryout restricts the film to more limited areas of the tube surface, as has been captured in the wetting ratio of the hydrodynamic model. Thus, the Reynolds number is adjusted by the wetting ratio so that the different film thickness in the wetted region is addressed.

$$Nu_{\mathrm{NF}} = 1.468 \left(\frac{Re}{WR} \right)^{-1/3} \tag{5.36}$$

This calculated Nusselt number is adjusted by a falling-film factor K_{ff}. As discussed above, this factor accounts for heat transfer enhancement due to boundary layer development, the impact region, and film waviness or other disturbances. Each of these phenomena is expected to be a function of flow rate, fluid properties, and the tube spacing, which affects the impact velocity. These influences were captured with three nondimensional parameters. The flow rate was accounted for with Reynolds number (Re), the tube spacing was nondimensionalized with the capillary length (s/ξ), and the modified Galileo number (Ga) accounted for the effect of fluid properties.

As was discussed in Section 4.2.2, a transition point was observed in the data as temperature was increased. A force balance suggested that this corresponds to the point when momentum forces are greater than surface tension forces at the bottom of the tube. The ratio of momentum to surface tension forces, which determines this transition point, is equal to $Ga^{0.5}$. Thus, this model includes a transition point based on the modified

Galileo number. Based on the transition observed in the data, this transition occurs at $Ga_\text{T}^{0.5} = 2 \times 10^5$, or $Ga_\text{T} = 4 \times 10^{10}$. Thus, the falling-film factor takes the form shown in Equation (5.37).

$$K_\text{ff} = b_1 Re^{b_2} \left(s/\xi\right)^{b_3} \left(Ga/Ga_\text{T}\right)^{b_4} \tag{5.37}$$

A regression analysis of the data below the transitional modified Galileo number yields b_1, b_2, b_3, and b_4 values of 114, -0.75, 1, and 2/3, respectively. A regression analysis of the data above the transitional modified Galileo number yields b_1, b_2, b_3, and b_4 values of 114, -0.75, 1, and -0.5, respectively. As expected, the exponents relating to both the Reynolds number and nondimensionalized tube spacing remain constant across this transition. The exponent on the modified Galileo number term varies significantly across this transition point, with a value of 2/3 for $Ga < Ga_\text{T}$ and -0.5 for $Ga > Ga_\text{T}$. This reflects the significant transition point observed in the experimental heat transfer coefficient data with increasing temperature. For $Ga < Ga_\text{T}$, , increasing temperature reduces the viscosity of the film, decreasing the film thickness and increasing the heat transfer coefficient. This results in the positive exponent on the modified Galileo number term. At the transition point, film breakdown begins having a significant detrimental impact on heat transfer coefficient, as was discussed in Chapter 4. Thus, increasing temperature further reduces the average heat transfer coefficient, which is reflected in the shift to a negative exponent.

$$Ga_\text{T} = 4.0 \times 10^{10}$$

$$Ga < Ga_\text{T}: \ K_\text{ff} = 114 Re^{-0.75} \left(s/\xi\right) \left(Ga/Ga_\text{T}\right)^{2/3} \tag{5.38}$$

$$Ga > Ga_\text{T}: \ K_\text{ff} = 114 Re^{-0.75} \left(s/\xi\right) \left(Ga/Ga_\text{T}\right)^{-0.5} \tag{5.39}$$

The heat transfer coefficient in the wetted area is found by multiplying the Nusselt number from the initial laminar film analysis by the falling-film enhancement factor.

$$Nu_{wet} = Nu_{NF}K_{ff} \qquad (5.40)$$

$$Nu_{wet} = \frac{h_{wet}}{k}\left(\frac{\mu^2}{\rho^2 g}\right)^{1/3} \qquad (5.41)$$

Finally, the average heat transfer coefficient across the tube surface is calculated by multiplying the heat transfer coefficient in the wetted region by the wetting ratio.

$$h_{avg} = h_{wet} \cdot WR \qquad (5.42)$$

Note that this does not account for the influence of natural convection on the unwetted areas of the tube. This can be incorporated into the model by doing a surface-area-weighted average between the natural convection and falling-film heat transfer contributions using the wetting ratio. However, under the conditions of the present study, natural convection has a negligible influence on the average heat transfer coefficient, and thus was not included for simplicity.

Model Performance

The agreement of the heat transfer model with the data in the present study is shown in Figure 5.23. The model predicted the data with an AD of -2.9% and an AAD of 16.3%, with 75.3% of the data predicted within 25% and 98.5% of the data predicted within 50%. Agreement is similar in each flow regime. The model underpredicts the highest heat transfer coefficients, but generally follows the trends observed in the data.

The agreement of the heat transfer model with the data across the modified Galileo number transition is shown in Figure 5.24. A total of 208 data points were taken below this transition, and 116 data points above the transition point. At modified Galileo

199
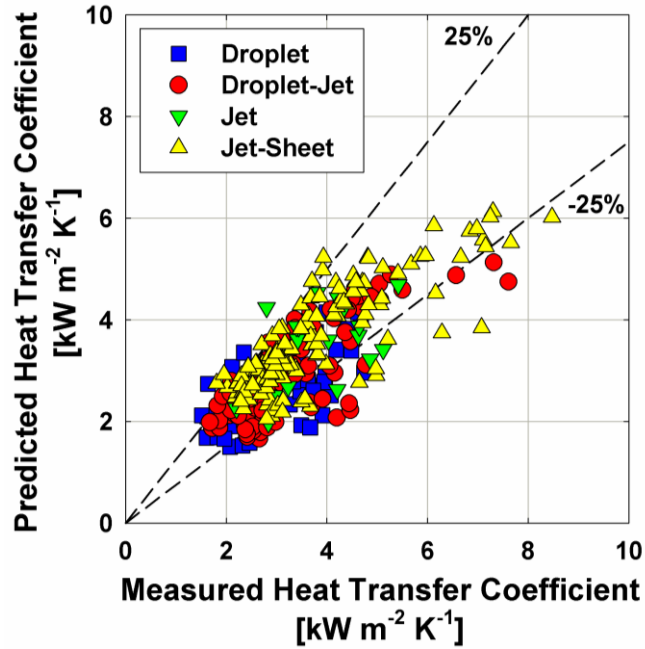
Figure 5.24. Agreement of heat transfer model with data

numbers below the transition criteria, the model predicted the data with an AD of -5.0% and an AAD of 18.1%. At modified Galileo numbers greater than the transition criteria,
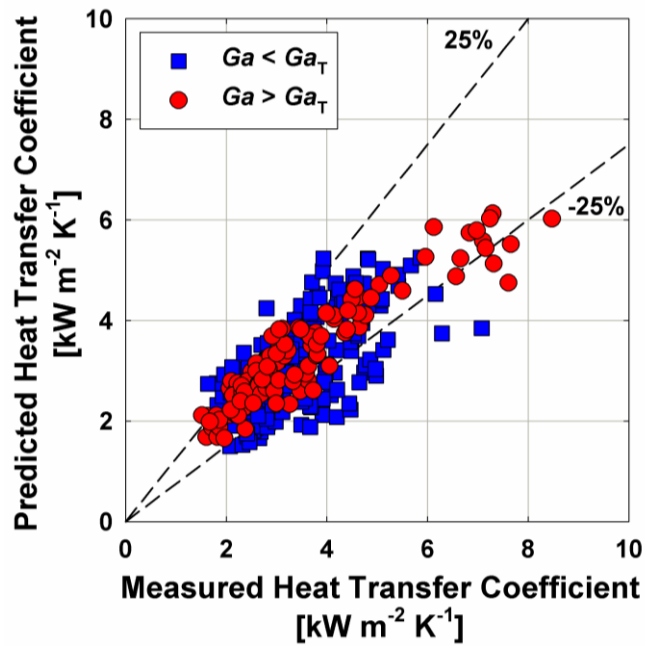
Figure 5.23. Agreement of heat transfer model with data across modified Galileo number transition

the model predicted the data with an AD of 0.8% and an AAD of 13.2%.

The average and absolute average deviations of the present model are compared to those with models in the literature in Figure 5.25. The new model shows improved agreement with the data over the models available in the literature on the basis of both AD and AAD. However, as was noted in Section 5.2.1, none of these models were
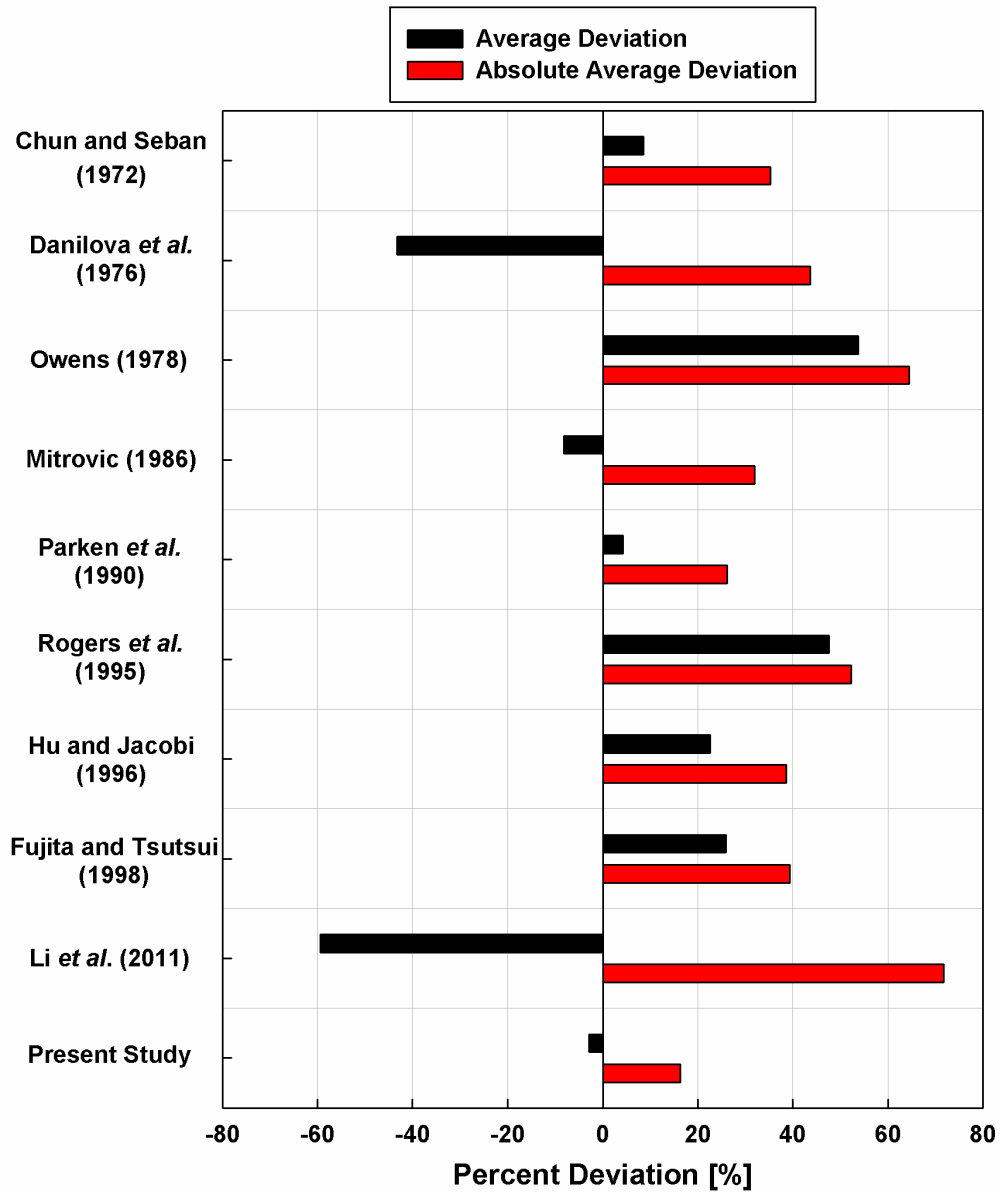
Figure 5.25. The AD and AAD of the present model compared to nine models in the literature using the data taken in the present study

developed for the geometry investigated in the present study. In addition, these models were based on experimental data that were either outside the range of conditions of the present study, or did not capture the influence of each relevant parameter. Thus, an increased level of disagreement is expected.

The percent of the experimental data predicted within 25% and 50% tolerance
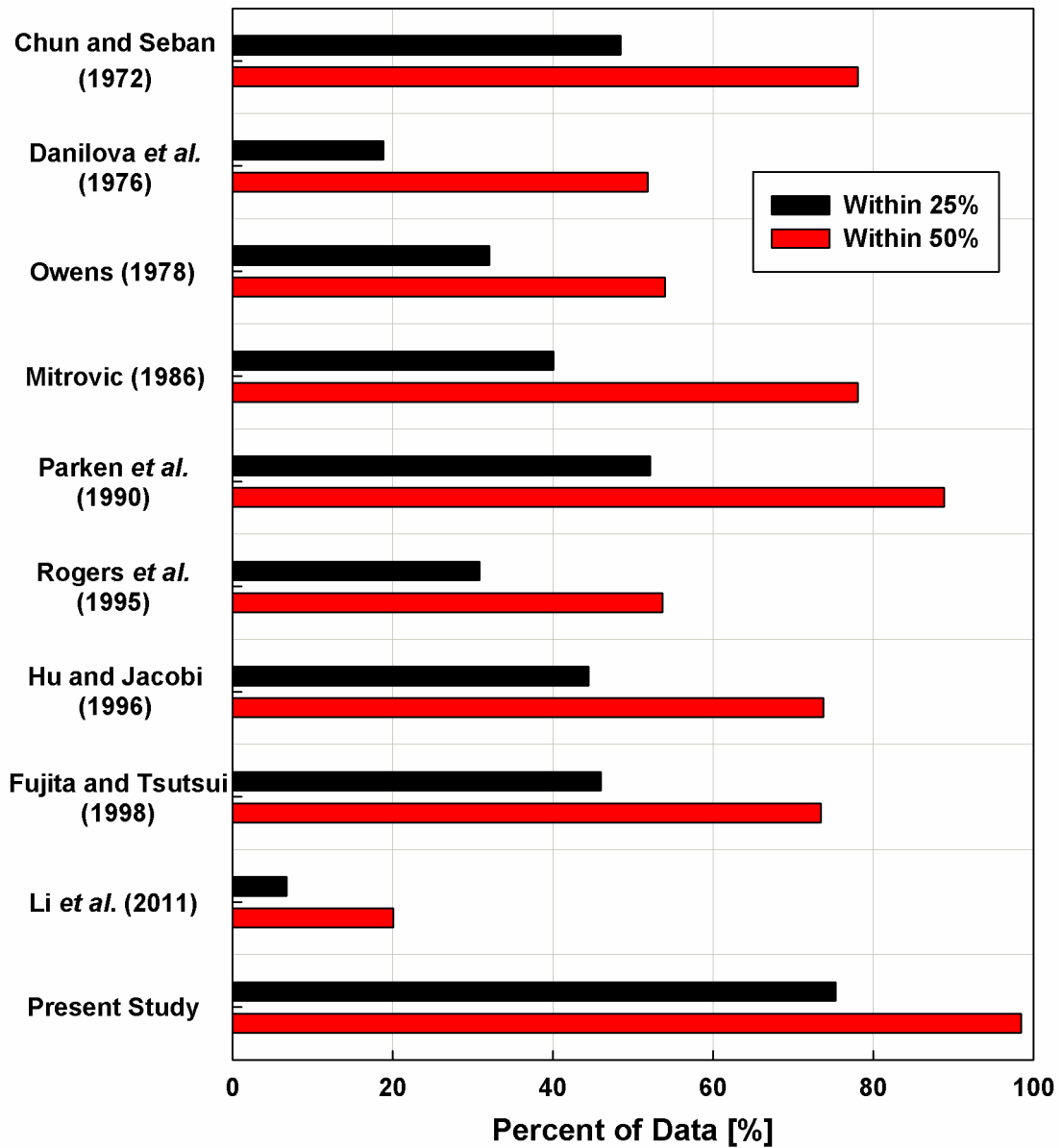
Figure 5.26. The percent of the experimental data predicted within two tolerance ranges by nine models in the literature and the present model

ranges by the present model and nine models from the literature is shown in Figure 5.26. The present model shows increased agreement relative to the models previously available with tolerance ranges of 25 and 50 percent. As above, this can be attributed to the geometry unique to this study, as well as the experimental range examined.

Representative data points from this study are compared with the corresponding model predictions in Figure 5.27. Although the model captures the overall trends in the data, there is still substantial scatter. This can be attributed to the instability of the film and the unique flow patterns and wetted tube area resulting from the film development. The model shows good agreement with the heat transfer coefficient trends observed in the data with respect to mass flow rate, temperature, and test section spacing. The heat transfer coefficient increases as the mass flow rate or test section spacing increases, and
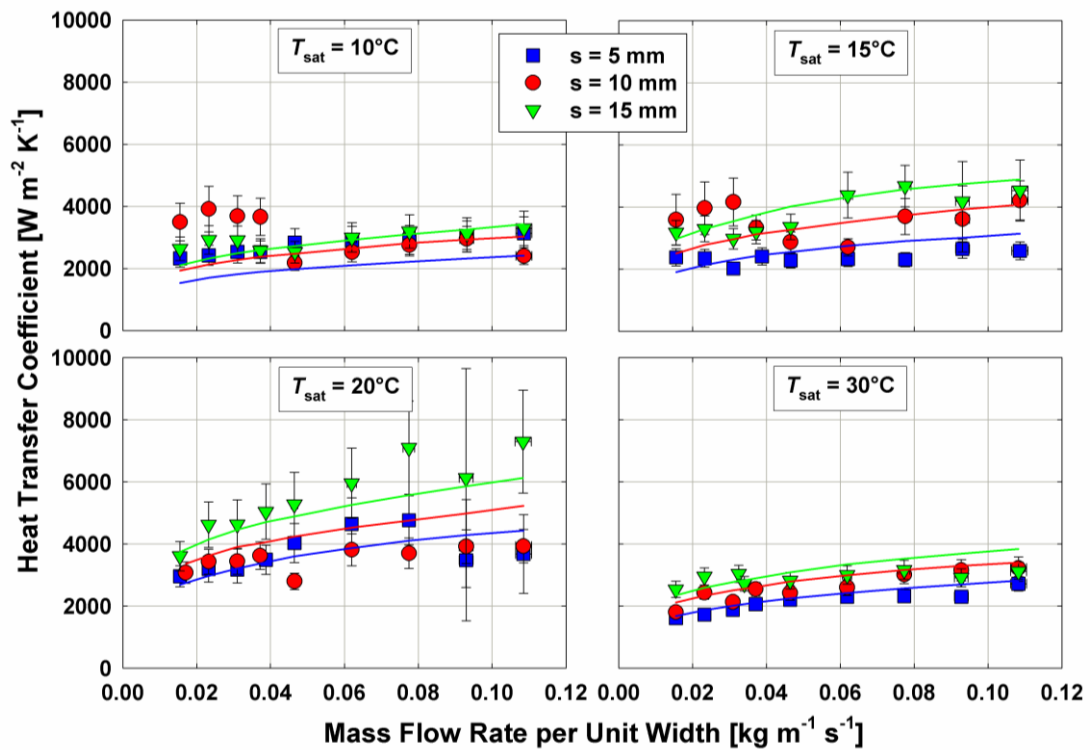
Figure 5.27. Experimental heat transfer data with model predictions overlay at a heat flux of 10 kW m^{-2}

exhibits the temperature transition observed in the data. As temperature is increased, the heat transfer coefficient first increases, but then decreases again after the transition point is reached.

The heat transfer coefficient predictions with varying film Reynolds number, test section spacing, and saturation temperature are shown in Figure 5.28. The heat transfer model follows the observed trends with increases in each of these parameters. In addition to the trends noted above, Figure 5.28 demonstrates that both heat transfer coefficient equations predict the same heat transfer coefficient at the modified Galileo number transition point. The influence of reaching a condition with full wetting can also be observed, resulting in the slight decrease in heat transfer coefficient at a test section
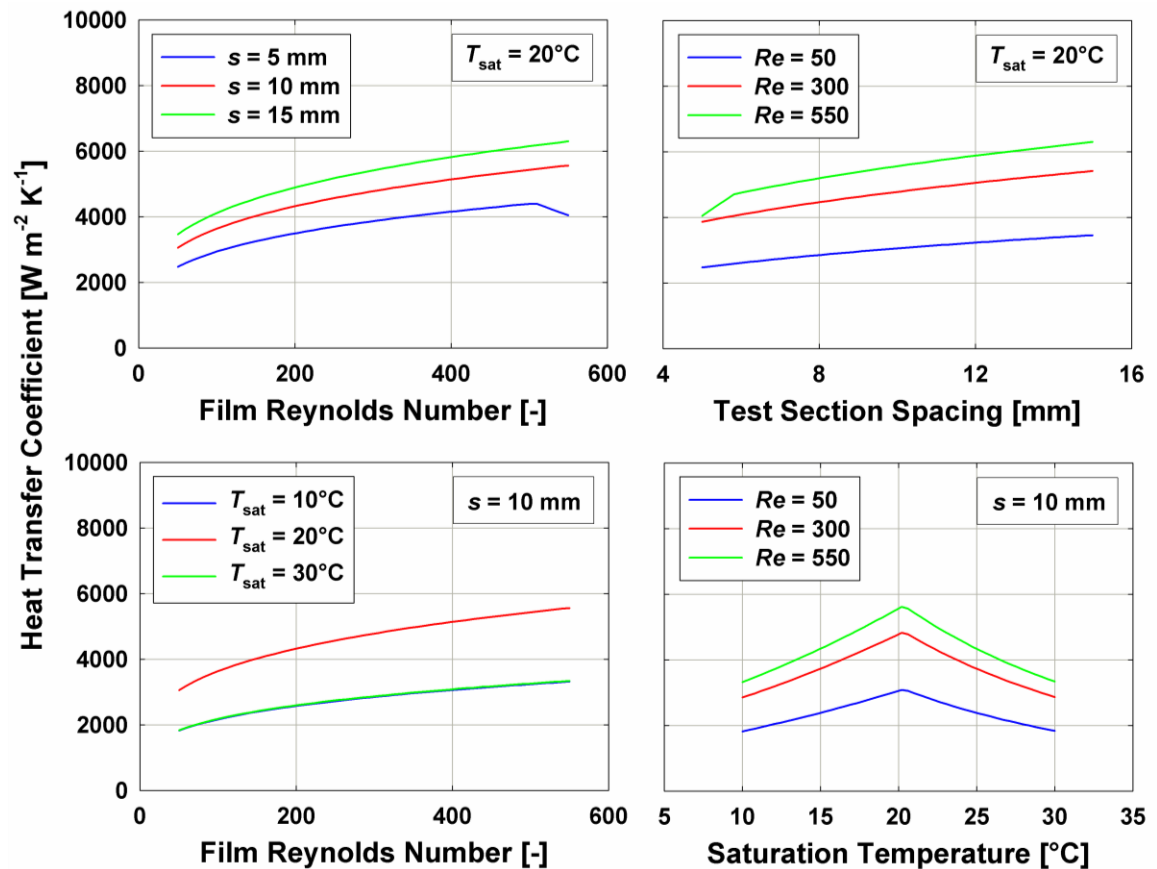
Figure 5.28. Heat transfer model prediction trends

spacing of 5 mm and a film Reynolds number of 550. This mimics the observed trend in the literature, where the laminar falling-film heat transfer coefficient decreases with increasing film Reynolds number after full wetting is achieved, even though this point was not observed in the present study.

5.3   Model Application

This section summarizes the usage of this model to predict flow regime, wetting ratio, and heat transfer coefficient. Each of these models first requires calculation of the film Reynolds number, modified Galileo number, and capillary length.

$$\Gamma = \frac{\dot{m}}{2L} \tag{5.43}$$

$$Re = 4\Gamma/\mu \tag{5.44}$$

$$Ga = \sigma^3 \rho_1 g^{-1} \mu_1^{-4} \tag{5.45}$$

$$\xi = \sqrt{\sigma \rho_1^{-1} g^{-1}} \tag{5.46}$$

Flow Regime

The flow regime model provides the transitional film Reynolds number as a function of modified Galileo number, tube spacing, and capillary length for the transitions between the droplet, droplet-jet, jet, and jet-sheet flow regimes.

$$\text{Droplet to Droplet-Jet: } Re = 31.7 + 0.0847 \, Ga^{0.25} \left(s/\xi\right)^{0.5} \tag{5.47}$$

$$\text{Droplet-Jet to Jet: } Re = 46.8 + 0.183 \, Ga^{0.25} \left(s/\xi\right)^{0.5} \tag{5.48}$$

$$\text{Jet to Jet-Sheet: } Re = 95.8 + 0.157 \, Ga^{0.25} \left(s/\xi\right)^{0.5} \tag{5.49}$$

Hydrodynamic Model

The hydrodynamic model predicts the wetting ratio, or the percentage of wetted tube area in the partial dryout region, as a function of film Reynolds number, modified Galileo number, tube spacing, and capillary length. If Equation (5.50) finds a wetting ratio greater than 100%, the wetting ratio is taken as 100%.

$$WR = 1.95 \, Re \, Ga^{-0.269} \left(s/\xi \right)^{-0.519} \tag{5.50}$$

Heat Transfer Model

The heat transfer model predicts the average heat transfer coefficient using the above wetting ratio and the film Reynolds number, modified Galileo number, tube spacing, and capillary length. This model first finds the Nusselt number corresponding to the Nusselt film analysis.

$$Nu_{\mathrm{NF}} = 1.468 \left(\frac{Re}{WR} \right)^{-1/3} \tag{5.51}$$

Then, this Nusselt number is adjusted by an empirical falling-film factor K_{ff}. The K_{ff} correlation includes a transition point at a modified Galileo number, Ga_{T}, of 4.0×10^{10}.

$$Ga < Ga_{\mathrm{T}}: \; K_{\mathrm{ff}} = 114 Re^{-0.75} \left(s/\xi \right) \left(Ga/Ga_{\mathrm{T}} \right)^{2/3} \tag{5.52}$$

$$Ga > Ga_{\mathrm{T}}: \; K_{\mathrm{ff}} = 114 Re^{-0.75} \left(s/\xi \right) \left(Ga/Ga_{\mathrm{T}} \right)^{-0.5} \tag{5.53}$$

The Nusselt number from the Nusselt film analysis is multiplied by this falling-film factor to find the Nusselt number of the wetted tube area, which gives the wetted tube heat transfer coefficient.

$$Nu_{\mathrm{wet}} = Nu_{\mathrm{NF}} K_{\mathrm{ff}} \tag{5.54}$$

$$Nu_{\mathrm{wet}} = \frac{h_{\mathrm{wet}}}{k} \left(\frac{\mu^2}{\rho^2 g} \right)^{1/3} \tag{5.55}$$

The average tube heat transfer coefficient is then the wetted tube heat transfer coefficient multiplied by the wetting ratio.

$$h_{\mathrm{avg}} = h_{\mathrm{wet}} \cdot WR \tag{5.56}$$

CHAPTER 6 : CONCLUSIONS AND RECOMMENDATIONS

A comprehensive investigation of falling-film evaporation over horizontal rectangular tubes was conducted. This geometry is representative of the external surfaces of flat microchannel tubes, which can couple external falling-film evaporation with internal microchannel flow. This configuration provides high heat transfer coefficients, favorable pressure drop characteristics, and a low working fluid charge. Incorporating this geometry into shell-and-tube heat exchangers has the potential to provide compact, high performance heat exchangers for a wide range of applications. This work is the first study of falling-film evaporation over such a geometry. The scope of the present study included three experimental studies: an assessment of liquid distributors for falling-film systems, visualization of falling-film evaporation to quantify flow characteristics, and measurement of heat transfer coefficients for a range of conditions. The results were used to develop new flow regime and heat transfer models for falling-film evaporation on this geometry.

The liquid distributor experiments assessed the performance of eight distributor designs with water at 20°C and atmospheric pressure over film Reynolds numbers ranging from 12 to 495. The designs were selected to be representative of common distributor designs in the literature. For each distributor, the flow regime, extent of maldistribution, and droplet or jet characteristics were measured throughout the experimental range. Substantial flow maldistribution (>50%) was measured with all of the distributor designs for a portion of the experimental range, with the highest degrees of maldistribution typically occurring at low film Reynolds numbers. Box-based distributor

designs relying on gravity-driven flow generally outperformed tube-based designs. The droplet and jet characteristics of the fluid exiting the distributors varied considerably. For instance, droplets generated with box-based designs had average volumes ranging from under 20 mm^3 to over 500 mm^3. This study was not sufficient to determine whether these distribution and flow characteristics persist throughout a tube bank; however, these results provide guidance for the design of distributors to initialize an evenly distributed film and target the optimal droplet and jet sizes for a specific application.

Falling-film evaporation experiments were conducted to measure heat transfer coefficients and identify droplet and wave characteristics with flow visualization. In both the flow visualization and heat transfer experiments, test sections with external dimensions of 203 × 1.42 × 27.4 mm (length × width × height) were used with water as the refrigerant. Heat transfer coefficient measurements were taken for saturation temperatures from 10 to 30°C, test section spacings from 5 to 15 mm, heat fluxes from 10 to 20 kW m^{-2}, and film Reynolds numbers of 48 to 544. These experiments identified a previously unexplained transition point in the heat transfer coefficient trends with increasing temperature. This transition was attributed to film breakdown, a theory supported by a force balance analysis. The heat transfer experiments also identified degradation of the heat transfer coefficient at the lower rows in a tube bank, an issue that must be addressed in heat exchanger designs with features such as periodic distributors to improve performance in many applications. In addition to the heat transfer measurements, flow visualization experiments were conducted at a saturation temperature of 17°C with Reynolds numbers ranging from 20 to 125. The flow morphology under these conditions was qualitatively described and key droplet and wave characteristics

were quantified with a semi-autonomous image analysis program. These included the droplet frequency, droplet width, droplet surface area, droplet volume, droplet velocity, wave width, wave velocity, and wave surface area. Observations taken during these studies were used to develop a new flow regime model. Based on the Wang and Jacobi model, it determines the location of the flow mode transitions by finding the point of thermodynamic equilibrium between neighboring modes with a control volume analysis. The model demonstrated good agreement with the data, predicting 82% of the flow regimes correctly.

Using the results of the flow visualization study, a new hydrodynamic model was developed to predict the wetted tube area. Using idealized fluid flow assumptions, this model predicted the development of a single wave throughout its residence time on the tube. Combining this with wave spacing information, the overall wetted tube area was calculated. The model showed good agreement with the flow visualization data, as well as trends observed in the literature. A correlation based on this model predicted the wetting ratios with an average deviation of -1.66% and an absolute average deviation of 2.10%, allowing straightforward implementation of this approach without the need to implement the full hydrodynamic model for each design case.

The results from the hydrodynamic model were then used to develop a new heat transfer model. The model incorporates an empirical falling-film factor to establish the heat transfer enhancement of the falling-film flow relative to the classic Nusselt film analysis (Nusselt, 1916), using the hydrodynamic model to limit the Nusselt predictions to the wetted tube area. The falling-film factor accounts for the impact region, boundary layer development, and film waviness. This model demonstrated improved predictions

210

compared to models available in the literature, predicting the data with an average deviation of -2.9% and an absolute average deviation of 16.3%. It predicts the heat transfer coefficient trends observed in the experimental study with increasing flow rate, temperature, and test section spacing. The model has demonstrated good agreement with the data both above and below the heat transfer coefficient transition point observed with increasing temperature. In addition, it predicts the decrease in heat transfer coefficient with increasing mass flow rate after full wetting is reached, noted by many studies in the literature, even though this transition point is not captured in the experimental study.

The findings of the present study make a significant contribution to the understanding of falling-film evaporation. The performance of a promising geometry was explored throughout a range of operating conditions, and the developed models will allow for more accurate component designs utilizing falling-film flow with microchannel tubes. Ultimately, this will lead to improved shell-and-tube heat exchanger performance with compact, efficient designs.

6.1   Recommendations for future work

Although this study has led to an increased understanding of falling-film evaporation, there are still several areas that require additional investigation, which are summarized below.

- The present study identified the flow maldistribution delivered by several common liquid distributor designs, as well as quantifying the wide range of droplet and jet characteristics generated. However, it is unclear to what degree these parameters influence the heat transfer performance, and also whether these characteristics persist throughout a tube bank. In addition, guidelines must be developed to enable the

design of effective liquid distributors with minimal and predictable maldistribution. These investigations will increase the repeatability of falling-film experimental research, and improve the performance of components utilizing falling-film heat transfer.

- While the present work provided an initial investigation into falling-film evaporation on horizontal rectangular geometries, there are still a wide range of experimental conditions that remain unexplored. Most notably, these include experiments with addition fluids, additional test section dimensions, higher flow rates, enhanced tube surfaces, and bundle effects. All of these are of significant interest in practical applications. In addition, these experiments focused on average heat transfer behavior. A full understanding of this phenomenon would benefit from further examination of local heat transfer behavior.

- Although the new hydrodynamic model was supported by data collected in the flow visualization study, as well as correlations and trends in the literature, this approach would benefit from experimental wetting ratio measurements during heat transfer at different saturation conditions and heat fluxes. This would allow direct validation of the model, as well as further exploration of the underlying assumptions. In particular, the present hydrodynamic model does not account for presence of a substrate film, or fluid buildup at the bottom of the tube.

- The developed heat transfer model uses several empirical assumptions and idealizations. It would benefit from modifications to increase its theoretical foundation, moving towards a more mechanistic approach. In addition, there are

currently no external data sets available to assess the performance of the model under conditions outside the range of the present study.

- The present study examined the heat transfer behavior of microchannel geometries with internal electric heating. The measured performance should be validated using a microchannel tube with internal fluid flow. This approach would demonstrate the high overall heat transfer performance possible with components using this arrangement.

APPENDIX A: REPRESENTATIVE DATA POINT SAMPLE

CALCULATIONS

Table A.1. Measurements

Test Section	
H_{TS} (m)	0.0274
L_{TS} (m)	0.203
Q_{TS} (W)	159
R_{TS} (m)	0.000711
s (m)	0.010
$T_{TS,1}$ (°C)	34.2
$T_{TS,2}$ (°C)	33.9
$T_{TS,3}$ (°C)	39.9
$T_{TS,4}$ (°C)	39.9
$T_{TS,5}$ (°C)	34.0
$T_{TS,6}$ (°C)	35.4
$T_{TS,7}$ (°C)	33.5
$T_{TS,8}$ (°C)	32.6
Test Chamber	
P_{C} (Pa)	4247
LR (Pa hr^{-1})	3.5
t_{Test} (hr)	23
Primary Flow Loop	
$\dot{m}$ (kg s^{-1})	0.0377

Table A.2. Experimental data point reduction sample calculation

Heat Transfer Coefficient Sample Calculations: 6/19/2013		
Inputs	**Equations**	**Results**
Test Section Heat Transfer Coefficient		
$T_{TS,1} = 34.2°C$	$\Gamma = \dot{m}/(2L_{TS})$	$\Gamma = 0.0927$ kg m^{-1} s^{-1}
$T_{TS,2} = 33.9°C$	$A_{TS} = 2L_{TS}(H_{TS} - 2R_{TS}) + 2\pi R_{TS}L_{TS}$	$A_{TS} = 0.0115$ m^2
$T_{TS,3} = 39.9°C$	$q'' = Q_{TS}/A_{TS}$	$q'' = 13.8$ kW m^{-2}
$T_{TS,4} = 39.9°C$	$P_{leak} = LR \cdot t_{Test}$	$P_{leak} = 80.5$ Pa
$T_{TS,5} = 34.0°C$	$P_{sat} = P_C - P_{leak}$	$P_{sat} = 4167$ Pa
$T_{TS,6} = 35.4°C$	$T_{sat} = f(P_{sat})$	$T_{sat} = 29.7°C$
$T_{TS,7} = 33.5°C$	$\Delta T_{TS,1} = T_{TS,1} - T_{sat}$	$\Delta T_{TS,1} = 4.5°C$
$T_{TS,8} = 32.6°C$	$\Delta T_{TS,2} = T_{TS,2} - T_{sat}$	$\Delta T_{TS,2} = 4.2°C$
$\dot{m} = 0.0377$ kg s^{-1}	$\Delta T_{TS,3} = T_{TS,3} - T_{sat}$	$\Delta T_{TS,3} = 10.2°C$
$P_C = 4247$ Pa	$\Delta T_{TS,4} = T_{TS,4} - T_{sat}$	$\Delta T_{TS,4} = 10.2°C$
$LR = 3.5$ Pa hr^{-1}	$\Delta T_{TS,5} = T_{TS,5} - T_{sat}$	$\Delta T_{TS,5} = 4.4°C$
$t_{Test} = 23$ hr	$\Delta T_{TS,6} = T_{TS,6} - T_{sat}$	$\Delta T_{TS,6} = 5.8°C$
$Q_{TS} = 159$ W	$\Delta T_{TS,7} = T_{TS,7} - T_{sat}$	$\Delta T_{TS,7} = 3.8°C$
$H_{TS} = 0.0274$ m^2	$\Delta T_{TS,8} = T_{TS,8} - T_{sat}$	$\Delta T_{TS,8} = 2.9°C$
$L_{TS} = 0.0203$ m^2	$h_{TS,1} = (Q_{TS}/8)/[(A_{TS}/8)\cdot\Delta T_{TS,1}]$	$h_{TS,1} = 3049$ W m^{-2} K^{-1}
$R_{TS} = 0.000711$ m^2	$h_{TS,2} = (Q_{TS}/8)/[(A_{TS}/8)\cdot\Delta T_{TS,2}]$	$h_{TS,2} = 3261$ W m^{-2} K^{-1}
	$h_{TS,3} = (Q_{TS}/8)/[(A_{TS}/8)\cdot\Delta T_{TS,3}]$	$h_{TS,3} = 1358$ W m^{-2} K^{-1}
	$h_{TS,4} = (Q_{TS}/8)/[(A_{TS}/8)\cdot\Delta T_{TS,4}]$	$h_{TS,4} = 1354$ W m^{-2} K^{-1}
	$h_{TS,5} = (Q_{TS}/8)/[(A_{TS}/8)\cdot\Delta T_{TS,5}]$	$h_{TS,5} = 3179$ W m^{-2} K^{-1}
	$h_{TS,6} = (Q_{TS}/8)/[(A_{TS}/8)\cdot\Delta T_{TS,6}]$	$h_{TS,6} = 2407$ W m^{-2} K^{-1}
	$h_{TS,7} = (Q_{TS}/8)/[(A_{TS}/8)\cdot\Delta T_{TS,7}]$	$h_{TS,7} = 3618$ W m^{-2} K^{-1}
	$h_{TS,8} = (Q_{TS}/8)/[(A_{TS}/8)\cdot\Delta T_{TS,8}]$	$h_{TS,8} = 4740$ W m^{-2} K^{-1}
	$h_{TS} = \dfrac{1}{8}\sum_{i=1}^{8} h_{TS,i}$ (exclude local heat transfer coefficients with $\Delta T < 1°C$; none in this sample calculation)	$h_{TS} = 2871 \pm 170$ W m^{-2} K^{-1}

Table A.3. Modeling sample calculation – flow regime and wetting ratio

Model Sample Calculations: 6/19/2013		
Inputs	**Equations**	**Results**
Flow Regime Model		
$P_{sat} = 4167$ Pa $\Gamma = 0.0927$ kg m^{-1} s^{-1} $s = 0.010$ m $g = 9.81$ m s^{-2}	$\rho_1 = f\left(P_{sat}, x = 0\right)$ $\mu_1 = f\left(P_{sat}, x = 0\right)$ $\sigma = f\left(P_{sat}\right)$	$\rho_1 = 996$ kg m^{-3} $\mu_1 = 0.000803$ kg m^{-1} s^{-1} $\sigma = 0.0712$ N m^{-1}
	$Ga = \sigma^3 \rho_1 g^{-1} \mu_1^{-4}$	$Ga = 8.815 \times 10^{10}$
	$\xi = \left(\sigma \rho_1^{-1} g^{-1}\right)^{0.5}$	$\xi = 0.00270$ m
	$Re = 4\Gamma/\mu$	$Re = 462$
	$Re_{D\text{-}DJ} = 31.7 + 0.0847 Ga^{0.25} \left(s/\xi\right)^{0.5}$ $Re_{DJ\text{-}J} = 46.8 + 0.183 Ga^{0.25} \left(s/\xi\right)^{0.5}$ $Re_{J\text{-}JS} = 95.8 + 0.157 Ga^{0.25} \left(s/\xi\right)^{0.5}$	$Re_{D\text{-}DJ} = 121$ $Re_{DJ\text{-}J} = 239$ $Re_{J\text{-}JS} = 260$
	$Re > Re_{J\text{-}JS}$	Flow in Jet-Sheet Mode
Wetting Ratio Model		
$P_{sat} = 4167$ Pa $\Gamma = 0.0927$ kg m^{-1} s^{-1} $s = 0.010$ m $g = 9.81$ m s^{-2}	$\rho_1 = f\left(P_{sat}, x = 0\right)$ $\mu_1 = f\left(P_{sat}, x = 0\right)$ $\sigma = f\left(P_{sat}\right)$	$\rho_1 = 996$ kg m^{-3} $\mu_1 = 0.000803$ kg m^{-1} s^{-1} $\sigma = 0.0712$ N m^{-1}
	$Ga = \sigma^3 \rho_1 g^{-1} \mu_1^{-4}$	$Ga = 8.815 \times 10^{10}$
	$\xi = \left(\sigma \rho_1^{-1} g^{-1}\right)^{0.5}$	$\xi = 0.00270$ m
	$Re = 4\Gamma/\mu$	$Re = 462$
	$WR = 1.95 \cdot Re \cdot Ga^{-0.269} \left(s/\xi\right)^{-0.519}$	$WR = 52\%$

Table A.4. Modeling sample calculation – heat transfer coefficient

Model Sample Calculations: 6/19/2013		
Inputs	**Equations**	**Results**
Heat Transfer Model		
$P_{sat} = 4167$ Pa	$\rho_1 = f\left(P_{sat}, x = 0\right)$	$\rho_1 = 996$ kg m^{-3}
$\Gamma = 0.0927$ kg m^{-1} s^{-1}	$\mu_1 = f\left(P_{sat}, x = 0\right)$	$\mu_1 = 0.000803$ kg m^{-1} s^{-1}
$s = 0.010$ m	$\sigma = f\left(P_{sat}\right)$	$\sigma = 0.0712$ N m^{-1}
$g = 9.81$ m s^{-2}	$Ga = \sigma^3 \rho_1 g^{-1} \mu_1^{-4}$	$Ga = 8.815 \times 10^{10}$
$Ga_T = 4.0 \times 10^{10}$	$\xi = \left(\sigma \rho_1^{-1} g^{-1}\right)^{0.5}$	$\xi = 0.00270$ m
$WR = 52\%$	$Re = 4\Gamma / \mu$	$Re = 462$
	$Re_w = Re / WR$	$Re_w = 890$
	$Nu_{NF} = 1.468 \cdot Re_w^{-1/3}$	$Nu_{NF} = 0.153$
	for $Ga < Ga_T$ $K_{ff} = 114 Re^{-0.75}\left(s/\xi\right)\left(Ga/Ga_T\right)^{2/3}$ for $Ga > Ga_T$ $K_{ff} = 114 Re^{-0.75}\left(s/\xi\right)\left(Ga/Ga_T\right)^{-0.5}$	$Ga > Ga_T$ $K_{ff} = 2.86$
	$Nu_{wet} = Nu_{NF} \cdot K_{ff}$	$Nu = 0.436$
	$h_{wet} = Nu_{wet} \cdot k \left(\dfrac{\mu^2}{\rho^2 g}\right)^{-1/3}$	$h_{wet} = 6485$ W m^{-2} K^{-1}
	$h_{avg} = h_{wet} \cdot WR$	$h_{avg} = 3364$ W m^{-2} K^{-1}

APPENDIX B: MINOR ADJUSTMENTS TO HEAT TRANSFER

ANALYSIS

B.1 Radiation heat exchange between the test section and surroundings

In order to examine the effect of radiation on the heat input to the test section, a simplified calculation was carried out with very conservative assumptions. It was found that, even with these conservative assumptions, the radiation contribution was minimal, and thus was neglected in all calculations. These calculations assumed that the test section wall only has radiation heat exchange with the surrounding room. This is conservative because there is a significant view factor between the test section and the test chamber and other internal features that are close to the saturation temperature. In addition, the transmissivity of the acrylic door and windows was ignored, and the test section was treated as a gray surface with an emissivity of 0.1.

$$Q_{\mathrm{rad}} = A_{\mathrm{TS}} \varepsilon \sigma \left(T_{\mathrm{TS}}^4 - T_{\mathrm{sur}}^4 \right) \tag{B.1}$$

These assumptions allow Equation (B.1) to be used. Note that, contrary to other locations in this document, this equation requires temperatures to be expressed in Kelvin. This calculation was carried out with each wall temperature measurement, and the contributions were summed to find the total radiation heat transfer into or out of the test section. This resulted in heat transfer ranging from -0.17 to 0.05 W into the test section. The maximum contribution was 0.11% of the total test section heat duty from the electric heater, with an average contribution of 0.03%. Given the minimal influence even with these conservative assumptions, it was neglected in this study.

B.2   Conduction through test section wall

The impact of conduction through the test section wall was examined using a 2D model in COMSOL (2013). This was selected rather than a simple 1D analytical conduction calculation due to the possible impact of the thermocouple and solder on the wall temperature relative to the thermocouple measurement. These simulations were run for heat transfer coefficients ranging from 1000 to 8000 W m^{-2} K^{-1} with the highest experimental heat flux, 20 kW m^{-2}. The model examined the temperature distribution around a single thermocouple, accounting for the influence of the heater, thermocouple, solder, and aluminum test section. The calculations were conducted assuming a steady system with a free triangular mesh with 10,735 elements and a maximum element size of 6.35×10^{-5} m. This geometry, the mesh, and a sample temperature distribution are shown in Figure B.1. For the range considered, the maximum difference between the thermocouple measurement and either measured wall temperature was predicted to be 0.07°C. In addition, this model predicted excellent temperature uniformity between the two wall surfaces despite the nonsymmetrical test section, with a maximum difference of 0.04°C. Given that conduction has a minimal effect on the difference between the wall temperature and the thermocouple reading, the maximum predicted temperature difference (±0.07°C) was added to the uncertainty of the thermocouple measurement.
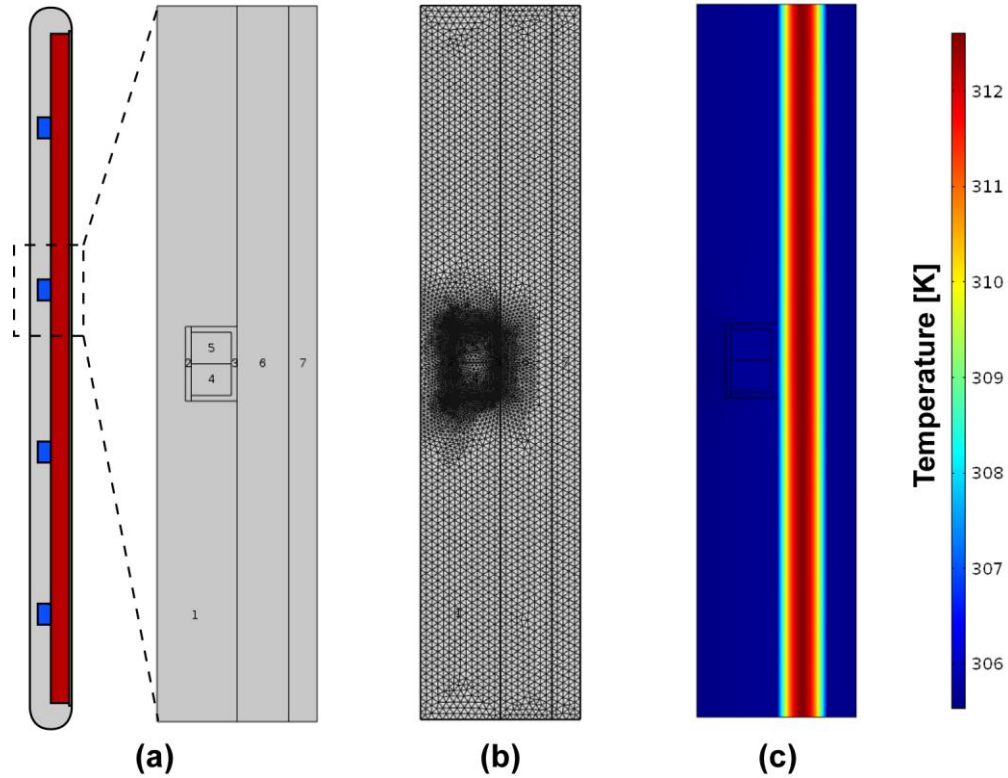
Figure B.1. COMSOL analysis of conduction in test section: (a) end view of test section with zoomed view of COMSOL control volume encompassing the test section wall with thermocouple and heater, (b) mesh, and (c) example temperature distribution with h = 4000 W m^{-2} K^{-1}

B.3   Contact resistance within test section

The COMSOL model used to examine the influence of conduction in the test section was also used to predict the influence of contact resistance between the electric heater and aluminum features. No direct information on the contact situation present in the current test sections was available, so three possible contact resistances were considered:

- Case 1: Aluminum/aluminum with Dow Corning 340 grease (7×10^{-6} m^2 K W^{-1}), from Incropera *et al.* (2007)

- Case 2: Aluminum/silicon with 0.02 mm epoxy ($2\text{-}9 \times 10^{-5}$ m^2 K W^{-1}), from Incropera *et al.* (2007)

- Case 3: a 0.025 mm thick layer of Omega CC High Temp thermal cement ($k = 1.2$ W/m-K)

These three contact resistances were considered to be representative of the test section fabrication technique. The COMSOL simulations predicted that the maximum impact on the difference between the measured and wall temperature, in addition to that present due to conduction, was only 0.002°C, and thus was neglected for simplicity.

B.4   Poor solder fill in thermocouple gap

Finally, the COMSOL model was used to examine the influence of a possible fabrication error, where the solder did not fill the thermocouple groove area behind the thermocouple, as seen in Figure B.2. Although such a gap was not expected to be present, this situation was examined to ensure that minor fabrication errors would not have a substantial impact on the measured heat transfer coefficients. Even with a gap spanning the full width of the thermocouple groove, the maximum difference between the thermocouple temperature and wall temperature was only 0.10°C.
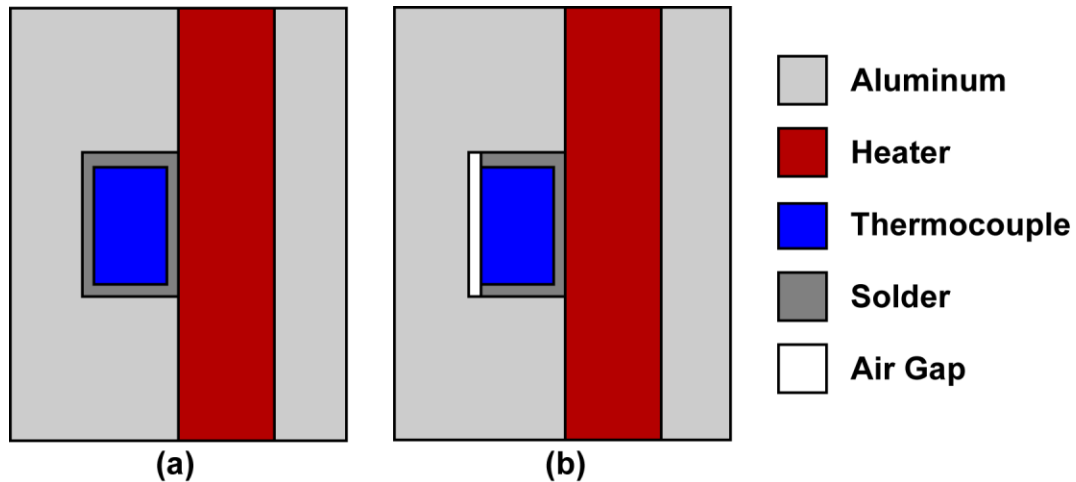
Figure B.2. Schematic of (a) desired fabrication arrangement and (b) possible poor solder fill during fabrication

This low temperature difference was primarily due to the high thermal conductivity of the aluminum pieces. In addition to examining the impact of this fabrication error using COMSOL, a damaged test section was also disassembled after testing and examined. No fabrication errors were visible in this disassembled test section.

APPENDIX C: UNCERTAINTY PROPAGATION

The uncertainty analysis was carried out using Engineering Equation Solver (EES) software (Klein, 2013). This section provides a sample uncertainty propagation calculation for the representative data point discussed in Chapter 4 and Appendix A. The data point was taken at a pressure of 4247 Pa, linear mass flux of 0.0927 kg m^{-1} s^{-1}, test section spacing of 10 mm, and heat input of 160 W.

First, the uncertainty in the saturation pressure is found as a function of the chamber pressure and air ingression. A conservative 25% uncertainty was assigned to this air ingression rate.

$$P_{\text{sat}} = P_{\text{C}} - P_{\text{leak}} \tag{C.1}$$

$$U_{P_{\text{sat}}} = \sqrt{\left(\frac{\partial P_{\text{sat}}}{\partial P_{\text{C}}}\right)^2 U_{P_{\text{C}}}^2 + \left(\frac{\partial P_{\text{sat}}}{\partial P_{\text{leak}}}\right)^2 U_{P_{\text{leak}}}^2} \tag{C.2}$$

$$U_{P_{\text{sat}}} = \sqrt{(1)^2 (28.0 \text{ Pa})^2 + (1)^2 (20.1 \text{ Pa})^2} = 34.5 \text{ Pa} \tag{C.3}$$

Then, the saturation temperature is found as a function of the saturation pressure. To determine the uncertainty, the differential was approximated using the upper and lower bounds of the pressure range.

$$U_{T_{\text{sat}}} = \sqrt{\left(\frac{\partial T_{\text{sat}}}{\partial P_{\text{sat}}}\right)^2 U_{P_{\text{sat}}}^2} \tag{C.4}$$

$$U_{T_{\text{sat}}} = \sqrt{\left(\frac{T_{\text{sat}}\left(P_{\text{sat}} + U_{P_{\text{sat}}}\right) - T_{\text{sat}}\left(P_{\text{sat}} - U_{P_{\text{sat}}}\right)}{2 \cdot U_{P_{\text{sat}}}}\right)^2 U_{P_{\text{sat}}}^2} \tag{C.5}$$

$$U_{T_{\text{sat}}} = \sqrt{\left(\frac{29.8°C - 29.5°C}{2 \cdot 34.5 \text{ Pa}}\right)^2 (34.5 \text{ Pa})^2} = 0.14°C \qquad \text{(C.6)}$$

The uncertainty of the test section surface area is determined based on the uncertainty of the height, length, and corner radius of the test section. Each of these dimensions was assigned an approximate uncertainty of ±0.05 mm, although they were machined to the designed dimensions.

$$A_{\text{TS}} = 2L_{\text{TS}}\left(H_{\text{TS}} - 2R_{\text{TS}}\right) + 2\pi R_{\text{TS}} L_{\text{TS}} \qquad \text{(C.7)}$$

$$U_{A_{\text{TS}}} = \sqrt{\left(\frac{\partial A_{\text{TS}}}{\partial L_{\text{TS}}}\right)^2 U_{L_{\text{TS}}}^2 + \left(\frac{\partial A_{\text{TS}}}{\partial H_{\text{TS}}}\right)^2 U_{H_{\text{TS}}}^2 + \left(\frac{\partial A_{\text{TS}}}{\partial R_{\text{TS}}}\right)^2 U_{R_{\text{TS}}}^2} \qquad \text{(C.8)}$$

$$U_{A_{\text{TS}}} = \sqrt{\left(2\left(H_{\text{TS}} - 2R_{\text{TS}}\right) + 2\pi R_{\text{TS}}\right)^2 U_{L_{\text{TS}}}^2 + \left(2L_{\text{TS}}\right)^2 U_{H_{\text{TS}}}^2 + \left(4L_{\text{TS}} + 2\pi L_{\text{TS}}\right)^2 U_{R_{\text{TS}}}^2} \qquad \text{(C.9)}$$

$$U_{A_{\text{TS}}} = \sqrt{\begin{array}{l}(0.051 \text{ m})^2 (0.00005 \text{ m})^2 + (0.406 \text{ m})^2 (0.00005 \text{ m})^2 \\ + (0.464 \text{ m})^2 (0.00005 \text{ m})^2\end{array}} \qquad \text{(C.10)}$$

$$U_{A_{\text{TS}}} = 0.0000309 \text{ m}^2 \qquad \text{(C.11)}$$

The uncertainty in the temperature difference could be found using the uncertainty of the wall temperature measurement and the uncertainty in the saturation temperature. The wall temperature measurement uncertainty includes a factor accounting for wall conduction, as discussed in Appendix B.

$$\Delta T_{\text{TS,1}} = T_{\text{TS,1}} - T_{\text{sat}} \qquad \text{(C.12)}$$

$$U_{\Delta T_{\text{TS,1}}} = \sqrt{\left(\frac{\partial \Delta T_{\text{TS,1}}}{\partial T_{\text{TS,1}}}\right)^2 U_{T_{\text{TS,1}}}^2 + \left(\frac{\partial \Delta T_{\text{TS,1}}}{\partial T_{\text{sat}}}\right)^2 U_{T_{\text{sat}}}^2} \qquad \text{(C.13)}$$

$$U_{\Delta T_{\text{TS,1}}} = \sqrt{(1)^2 (0.37°C)^2 + (1)^2 (0.14°C)^2} = 0.40°C \qquad \text{(C.14)}$$

The uncertainty of each local heat transfer coefficient can be calculated based on the known uncertainties of the heat input, test section area, and temperature difference. Note that the heat input and test section area are both divided by 8, but these factors cancel. Equations (C.15) to (C.19) demonstrate this calculation for a single local heat transfer coefficient measurement.

$$h_{\text{TS},1} = \frac{Q_{\text{TS}}}{A_{\text{TS}} \Delta T_{\text{TS},1}} \tag{C.15}$$

$$U_{h_{\text{TS},1}} = \sqrt{\left(\frac{\partial h_{\text{TS},1}}{\partial Q_{\text{TS}}}\right)^2 U_{Q_{\text{TS}}}^2 + \left(\frac{\partial h_{\text{TS},1}}{\partial A_{\text{TS}}}\right)^2 U_{A_{\text{TS}}}^2 + \left(\frac{\partial h_{\text{TS},1}}{\partial \Delta T_{\text{TS},1}}\right)^2 U_{\Delta T_{\text{TS},1}}^2} \tag{C.16}$$

$$U_{h_{\text{TS},1}} = \sqrt{\left(\frac{1}{A_{\text{TS}} \Delta T_{\text{TS},1}}\right)^2 U_{Q_{\text{TS}}}^2 + \left(-\frac{Q_{\text{TS}}}{A_{\text{TS}}^2 \Delta T_{\text{TS},1}}\right)^2 U_{A_{\text{TS}}}^2 + \left(-\frac{Q_{\text{TS}}}{A_{\text{TS}} \Delta T_{\text{TS},1}^2}\right)^2 U_{\Delta T_{\text{TS},1}}^2} \tag{C.17}$$

$$U_{h_{\text{TS},1}} = \sqrt{\begin{gathered}\left(\frac{1}{\left(0.0115\ \text{m}^2\right)\left(4.56°\text{C}\right)}\right)^2 \left(5\ \text{W}\right)^2 + \left(-\frac{\left(159.2\ \text{W}\right)}{\left(0.0115\ \text{m}^2\right)^2 \left(4.56°\text{C}\right)}\right)^2 \\ \times \left(0.0115\ \text{m}^2\right)^2 + \left(-\frac{\left(159.2\ \text{W}\right)}{\left(0.0115\ \text{m}^2\right)\left(4.56°\text{C}\right)^2}\right)^2 \left(0.40°\text{C}\right)^2\end{gathered}} \tag{C.18}$$

$$U_{h_{\text{TS},1}} = 281\ \text{W}\ \text{m}^{-2}\ \text{K}^{-1} \tag{C.19}$$

The uncertainty of the average heat transfer coefficient is determined from the input parameters, including the test section dimensions, saturation pressure, heat input, and wall temperatures. Note that this uncertainty cannot be directly determined from the local heat transfer coefficient uncertainties because they are not uncorrelated values. Thus, using the local heat transfer coefficient uncertainties would underestimate the average heat transfer coefficient uncertainty.

$$h_{\text{TS}} = f\left(L_{\text{TS}}, H_{\text{TS}}, R_{\text{TS}}, P_{\text{C}}, P_{\text{leak}}, Q_{TS}, T_{\text{TS},1}, T_{\text{TS},2}, T_{\text{TS},3}, T_{\text{TS},4}, T_{\text{TS},5}, T_{\text{TS},6}, T_{\text{TS},7}, T_{\text{TS},8}\right) \quad \text{(C.20)}$$

$$U_{h_{\text{TS}}} = \sqrt{\begin{array}{l} \left(\dfrac{\partial h_{\text{TS}}}{\partial L_{\text{TS}}}\right)^2 U_{L_{\text{TS}}}^2 + \left(\dfrac{\partial h_{\text{TS}}}{\partial H_{\text{TS}}}\right)^2 U_{H_{\text{TS}}}^2 + \left(\dfrac{\partial h_{\text{TS}}}{\partial R_{\text{TS}}}\right)^2 U_{R_{\text{TS}}}^2 + \left(\dfrac{\partial h_{\text{TS}}}{\partial P_{\text{C}}}\right)^2 U_{P_{\text{C}}}^2 \\[3mm] + \left(\dfrac{\partial h_{\text{TS}}}{\partial P_{\text{leak}}}\right)^2 U_{P_{\text{leak}}}^2 + \left(\dfrac{\partial h_{\text{TS}}}{\partial Q_{TS}}\right)^2 U_{Q_{TS}}^2 + \left(\dfrac{\partial h_{\text{TS}}}{\partial T_{\text{TS},1}}\right)^2 U_{T_{\text{TS},1}}^2 + \left(\dfrac{\partial h_{\text{TS}}}{\partial T_{\text{TS},2}}\right)^2 U_{T_{\text{TS},2}}^2 \\[3mm] + \left(\dfrac{\partial h_{\text{TS}}}{\partial T_{\text{TS},3}}\right)^2 U_{T_{\text{TS},3}}^2 + \left(\dfrac{\partial h_{\text{TS}}}{\partial T_{\text{TS},4}}\right)^2 U_{T_{\text{TS},4}}^2 + \left(\dfrac{\partial h_{\text{TS}}}{\partial T_{\text{TS},5}}\right)^2 U_{T_{\text{TS},5}}^2 + \left(\dfrac{\partial h_{\text{TS}}}{\partial T_{\text{TS},6}}\right)^2 U_{T_{\text{TS},6}}^2 \\[3mm] + \left(\dfrac{\partial h_{\text{TS}}}{\partial T_{\text{TS},7}}\right)^2 U_{T_{\text{TS},7}}^2 + \left(\dfrac{\partial h_{\text{TS}}}{\partial T_{\text{TS},8}}\right)^2 U_{T_{\text{TS},8}}^2 \end{array}} \quad \text{(C.21)}$$

Each of these differentials is approximated using the upper and lower bounds of the uncertainty, as in Equation (C.5).

$$U_{h_{\text{TS}}} = \sqrt{\begin{array}{l} \left(\dfrac{-2 \text{ W m}^{-2}\text{ K}^{-1}}{2\cdot 0.00005 \text{ m}}\right)^2 (0.00005 \text{ m})^2 + \left(\dfrac{-10 \text{ W m}^{-2}\text{ K}^{-1}}{2\cdot 0.00005 \text{ m}}\right)^2 (0.00005 \text{ m})^2 \\[4mm] + \left(\dfrac{-12 \text{ W m}^{-2}\text{ K}^{-1}}{2\cdot 0.00005 \text{ m}}\right)^2 (0.00005 \text{ m})^2 + \left(\dfrac{158 \text{ W m}^{-2}\text{ K}^{-1}}{2\cdot 28 \text{ Pa}}\right)^2 (28 \text{ Pa})^2 \\[4mm] + \left(\dfrac{-113 \text{ W m}^{-2}\text{ K}^{-1}}{2\cdot 20.1 \text{ Pa}}\right)^2 (20.1 \text{ Pa})^2 + \left(\dfrac{180 \text{ W m}^{-2}\text{ K}^{-1}}{2\cdot 5 \text{ W}}\right)^2 (5 \text{ W})^2 \\[4mm] + \left(\dfrac{-63 \text{ W m}^{-2}\text{ K}^{-1}}{2\cdot 0.37°\text{C}}\right)^2 (0.37°\text{C})^2 + \left(\dfrac{-71 \text{ W m}^{-2}\text{ K}^{-1}}{2\cdot 0.37°\text{C}}\right)^2 (0.37°\text{C})^2 \\[4mm] + \left(\dfrac{-13 \text{ W m}^{-2}\text{ K}^{-1}}{2\cdot 0.37°\text{C}}\right)^2 (0.37°\text{C})^2 + \left(\dfrac{-13 \text{ W m}^{-2}\text{ K}^{-1}}{2\cdot 0.37°\text{C}}\right)^2 (0.37°\text{C})^2 \\[4mm] + \left(\dfrac{-68 \text{ W m}^{-2}\text{ K}^{-1}}{2\cdot 0.37°\text{C}}\right)^2 (0.37°\text{C})^2 + \left(\dfrac{-39 \text{ W m}^{-2}\text{ K}^{-1}}{2\cdot 0.37°\text{C}}\right)^2 (0.37°\text{C})^2 \\[4mm] + \left(\dfrac{-88 \text{ W m}^{-2}\text{ K}^{-1}}{2\cdot 0.37°\text{C}}\right)^2 (0.37°\text{C})^2 + \left(\dfrac{-151 \text{ W m}^{-2}\text{ K}^{-1}}{2\cdot 0.37°\text{C}}\right)^2 (0.37°\text{C})^2 \end{array}} \quad \text{(C.22)}$$

$$U_{h_{\text{TS}}} = 170 \text{ W m}^{-2}\text{ K}^{-1} \quad \text{(C.23)}$$

REFERENCES

1. Armbruster, R., Mitrovic, J., 1994. Patterns of falling film over horizontal smooth tubes, 10th International Heat Transfer Conference, Brighton, pp. 275-280.
2. Armbruster, R., Mitrovic, J., 1995. Heat transfer in falling film on a horizontal tube, National Heat Transfer Conference, Portland, pp. 13-21.
3. Armbruster, R., Mitrovic, J., 1998. Evaporative cooling of a falling water film on horizontal tubes. Experimental Thermal and Fluid Science 18, 183-194.
4. Barba, D., Di Felice, R., 1984. Heat transfer in turbulent flow on a horizontal tube falling film evaporator. a theoretical approach. Desalination 51, 325-333.
5. Bellman, R., Pennington, R.H., 1954. Effects of Surface Tension and Viscosity on Taylor Instability. Quarterly Applied Mathematics 12, 151-162.
6. Bohn, M.S., Davis, S.H., 1993. Thermocapillary breakdown of falling liquid films at high Reynolds numbers. Int. J. Heat Mass Transfer 36, 1875-1881.
7. Bourouni, K., Chaibi, M.T., Tadrist, L., 2001. Analytical analysis of heat transfer in liquid film dripping around a horizontal tube. Desalination 141, 7-13.
8. Brumfield, L.K., Theofanous, T.G., 1976. On the Prediction of Heat Transfer Across Turbulent Liquid Films. J. Heat Transfer 98, 496-502.
9. Bukin, V.G., Danilova, G.N., Dyundin, V.A., 1982. Heat transfer from freons flowing over bundles of horizontal tubes that carry a porous coating. Heat Transfer - Soviet Research 14, 98-103.
10. Bustamante, J.G., Garimella, S., 2012. Dominant Flow Mechanisms in Falling-Film and Droplet Mode Evaporation over Horizontal Rectangular Tube Banks, International Refrigeration and Air Conditioning Conference, Purdue.
11. Canny, J., 1986. A Computational Approach to Edge Detection. Pattern Analysis and Machine Intelligence, IEEE Transactions on PAMI-8, 679-698.
12. Carey, V.P., 2008. Liquid-Vapor Phase-Change Phenomena, 2nd ed. Taylor & Francis Group, New York, NY.
13. Cerza, M., Sernas, V., 1985. Boiling nucleation criteria for a falling water film, 23rd National Heat Transfer Conference: Multiphase Flow and Heat Transfer. ASME HTD, Denver, CO, pp. 111-116.
14. Chang, T.-B., 2006. Effects of nozzle configuration on a shell-and-tube spray evaporator with liquid catcher. Applied Thermal Engineering 26, 814-823.
15. Chang, T.-B., Chiou, J.-S., 2005. Heat Transfer Enhancement in a Spray Evaporator. Journal of Enhanced Heat Transfer 12, 85-100.
16. Chang, T.-B., Li, J.-C., Liang, C.-C., 2011. Heat Transfer Enhancement of Square-Pitch Shell-and-Tube Spray Evaporator Using Interior Spray Nozzles. Heat Transfer Engineering 32, 14-19.
17. Chang, T.-B., Lu, C.-C., Li, J.-C., 2009. Enhancing the heat transfer performance of triangular-pitch shell-and-tube evaporators using an interior spray technique. Applied Thermal Engineering 29, 2527-2533.
18. Chang, T.B., Chiou, J.S., 1999. Spray evaporation heat transfer of R-141b on a horizontal tube bundle. Int. J. Heat Mass Transfer 42, 1467-1478.
19. Chen, I.Y., Kocamustafaogullari, G., 1989. An Experimental Study and Practical Correlations for Overall Heat Transfer Performance of Horizontal Tube Evaporator Design, National Heat Transfer Conference, p. 10.

20. Chien, L.-H., Chen, R.-H., 2012. An experimental study of falling film evaporation on horizontal tubes using R-134a. Journal of Mechanics 28, 319-327.

21. Chien, L.-H., Cheng, C.-H., 2006. A Predictive Model of Falling Film Evaporation with Bubble Nucleation on Horizontal Tubes. HVAC&R Research 12, 69-87.

22. Chien, L.-H., Tsai, Y.-L., 2011. An experimental study of pool boiling and falling film vaporization on horizontal tubes in R-245fa. Applied Thermal Engineering 31, 4044-4054.

23. Christians, M., 2010. Heat transfer and visualization of falling film evaporation on a tube bundle, Laboratory of Heat and Mass Transfer. École Polytechnique Fédérale de Lausanne.

24. Christians, M., Thome, J.R., 2012a. Falling film evaporation on enhanced tubes, part 1: Experimental results for pool boiling, onset-of-dryout and falling film evaporation. Int. J. Refrigeration 35, 300-312.

25. Christians, M., Thome, J.R., 2012b. Falling film evaporation on enhanced tubes, part 2: Prediction methods and visualization. Int. J. Refrigeration 35, 313-324.

26. Chun, K.R., Seban, R.A., 1971. Heat Transfer to Evaporating Liquid Films. J. Heat Transfer, 6.

27. Chun, K.R., Seban, R.A., 1972. Performance Prediction of Falling-Film Evaporators. J. Heat Transfer, 5.

28. Chyu, M.-C., 1984. Falling film evaporation on horizontal tubes with smooth and structured surfaces. Iowa State University.

29. Chyu, M.-C., Bergles, A.E., 1985. Enhancement of horizontal tube spray film evaporators by structured surfaces, Advances in Enhanced Heat Transfer-1985, ASME HTD, pp. 39-47.

30. Chyu, M.-C., Bergles, A.E., 1987. An Analytical and Experimental Study of Falling-Film Evaporation on a Horizontal Tube. J. Heat Transfer 109, 8.

31. Chyu, M.-C., Bergles, A.E., Mayinger, F., 1982. Enhancement of horizontal tube spray film evaporators, 7th International Heat Transfer Conference, Munich, pp. 275-280.

32. Chyu, M.C., Bergles, A.E., 1989. Horizontal-Tube Falling-Film Evaporation With Structured Surfaces. J. Heat Transfer 111, 518-524.

33. COMSOL, 2013. COMSOL Multiphysics, 4.3.2.189 ed.

34. Conti, R.J., 1978. Experimental investigation of horizontal tube ammonia film evaporators with small temperature differentials, Fifth Ocean Thermal Energy Conversion (OTEC) Conference, Miami Beach, pp. VI-161-180.

35. Danilova, G.N., Burkin, V.G., Dyundin, V.A., 1976. Heat transfer in spray-type refrigerator evaporators. Heat Transfer - Soviet Research 8, 105-113.

36. deBoor, C., 1978. A Practical Guide to Splines. Springer-Verlag, New York.

37. Dhir, V., Taghavi-Tafreshi, K., 1981. Hydrodynamic transition during dripping of a liquid from underside of a horizontal tube, ASME Paper 1981; [No 81-WA/HT-12].

38. Dukler, A., 1960. Fluid Mechanics and Heat Transfer in Vertical Falling-Film Systems, Chemical Engineering Progress Symposium Series, pp. 1-10.

39. El-Genk, M.S., Saber, H.H., 2001. Minimum thickness of a flowing down liquid film on a vertical surface. Int. J. Heat Mass Transfer 44, 2809-2825.

40.   Fernández-Seara, J., Pardiñas, Á.A., 2013. Refrigerant falling film evaporation review: Description, fluid dynamics and heat transfer. Applied Thermal Engineering.

41.   Fletcher, L.S., Sernas, V., Galowin, L.S., 1974. Evaporation from Thin Water Films on Horizontal Tubes. Industrial & Engineering Chemistry Process Design and Development 13, 265-269.

42.   Fletcher, L.S., Sernas, V., Parken, W.H., 1975. Evaporation Heat Transfer Coefficients for Thin Sea Water Films on Horizontal Tubes. Industrial & Engineering Chemistry Process Design and Development 14, 411-416.

43.   Fujita, T., Ueda, T., 1978. Heat transfer to falling liquid films and film breakdown--I: Subcooled liquid films. Int. J. Heat Mass Transfer 21, 97-108.

44.   Fujita, Y., Tsutsui, M., 1995a. Evaporation heat transfer of falling films on horizontal tube. Part 1. analytical study. Heat Transfer - Japanese Research 24, 1-16.

45.   Fujita, Y., Tsutsui, M., 1995b. Evaporation heat transfer of falling films on horizontal tube. Part 2. experimental study. Heat Transfer - Japanese Research 24, 17-31.

46.   Fujita, Y., Tsutsui, M., 1996. Experimental and analytical study of evaporation heat transfer in falling films on horizontal tubes, 10th International Heat Transfer Conference, Brighton, pp. 175-180.

47.   Fujita, Y., Tsutsui, M., 1998. Experimental investigation of falling film evaporation on horizontal tubes. Heat Transfer - Japanese Research 27, 609-618.

48.   Ganić, E.N., Getachew, D., 1986. Effects of surface condition and working fluid on liquid film breakdown during heat transfer, Eighth International Heat Transfer Conference, San Francisco, pp. 1931-1936.

49.   Ganić, E.N., Roppo, M.N., 1980. An Experimental Study of Falling Liquid Film Breakdown on a Horizontal Cylinder During Heat Transfer. J. Heat Transfer 102, 342-346.

50.   Garcia, J.M.G., Jabardo, J.M.S., Stoecker, W.F., 1992. Falling film ammonia evaporators, ACRC Technical Report, University of Illinois, Urbana.

51.   Garimella, S., Brown, A.M., Nagavarapu, A.K., 2011. Waste heat driven absorption/vapor-compression cascade refrigeration system for megawatt scale, high-flux, low-temperature cooling. Int. J. Refrigeration 34, 1776-1785.

52.   Gross, U., 1994. Falling Film Evaporation inside a Closed Thermosyphon, 10th International Heat Transfer Conference, Brighton, UK, pp. 443-448.

53.   Gstoehl, D., Roques, J.F., Crisinel, P., Thome, J.R., 2004. Measurement of Falling Film Thickness Around a Horizontal Tube Using a Laser Measurement Technique. Heat Transfer Engineering 25, 28-34.

54.   Habert, M., 2009. Falling film evaporation on a tube bundle with plain and enhanced tubes, Laboratory of Heat and Mass Transfer. École Polytechnique Fédérale de Lausanne, Lausanne, Switzerland.

55.   Habert, M., Thome, J.R., 2010a. Falling-Film Evaporation on Tube Bundle with Plain and Enhanced Tubes—Part I: Experimental Results. Experimental Heat Transfer 23, 259-280.

56. Habert, M., Thome, J.R., 2010b. Falling-Film Evaporation on Tube Bundle with Plain and Enhanced Tubes—Part II: New Prediction Methods. Experimental Heat Transfer 23, 281-297.

57. Hartley, D.E., Murgatroyd, W., 1964. Criteria for the break-up of thin liquid layers flowing isothermally over solid surfaces. Int. J. Heat Mass Transfer 7, 1003-1015.

58. He, Y., Bi, Q., Zhang, J., Hou, H., 2011. Experimental Study on the Heat Transfer Characteristics of an Evaporating Falling Film on a Horizontal Plain Tube. Heat Transfer Engineering 32, 936-942.

59. Honda, H., Nozu, S., Takeda, Y., 1987. Flow characteristics of condensate on a vertical column of horizontal low finned tubes, ASME/JSME Thermal Engineering Joint Conference, Honolulu, pp. 517-524.

60. Honda, H., Uchima, B., Nozu, S., Nakata, H., Torigoe, E., 1991. Film Condensation of R-113 on In-Line Bundles of Horizontal Finned Tubes. J. Heat Transfer 113, 479-486.

61. Hu, X., 1995. The intertube falling-film modes: transition, hysteresis and effect on heat transfer. University of Illinois.

62. Hu, X., Jacobi, A.M., 1996a. The Intertube Falling Film: Part 1---Flow Characteristics, Mode Transitions, and Hysteresis. J. Heat Transfer 118, 616-625.

63. Hu, X., Jacobi, A.M., 1996b. The Intertube Falling Film: Part 2---Mode Effects on Sensible Heat Transfer to a Falling Liquid Film. J. Heat Transfer 118, 626-633.

64. Hu, X., Jacobi, A.M., 1998. Departure-site spacing for liquid droplets and jets falling between horizontal circular tubes. Experimental Thermal and Fluid Science 16, 322-331.

65. Incropera, F.P., DeWitt, D.P., Bergman, T.L., Lavine, A.S., 2007. Fundamentals of Heat and Mass Transfer, Sixth ed. John Wiley and Sons.

66. Killion, J., 2003. An investigation of droplets and films falling over horizontal tubes, Mechanical Engineering. Iowa State University.

67. Killion, J.D., Garimella, S., 2003. Gravity-driven flow of liquid films and droplets in horizontal tube banks. Int. J. Refrigeration 26, 516-526.

68. Killion, J.D., Garimella, S., 2004a. Pendant droplet motion for absorption on horizontal tube banks. Int. J. Heat Mass Transfer 47, 4403-4414.

69. Killion, J.D., Garimella, S., 2004b. Simulation of Pendant Droplets and Falling Films in Horizontal Tube Absorbers. J. Heat Transfer 126, 1003-1013.

70. Klein, S.A., 2013. Engineering Equation Solver, Academic Professional V9.452 ed. F-Chart Software.

71. Kocamustafaogullari, G., Chen, I.Y., 1988. Falling film heat transfer analysis on a bank of horizontal tube evaporator. AIChE Journal 34, 1539-1549.

72. Kutateladze, S.S., Gogonin, I.I., 1979. Heat transfer in film condensation of slowly moving vapour. Int. J. Heat Mass Transfer 22, 1593-1599.

73. Kuwahara, H., Yasukawa, A., Nakayama, W., Yanagida, T., 1990. Evaporative heat transfer from horizontal enhanced tubes in thin film flow. Heat Transfer - Japanese Research 19, 83-97.

74. Lee, S., Köroğlu, B., Park, C., 2012. Experimental investigation of capillary-assisted solution wetting and heat transfer using a micro-scale, porous-layer

coating on horizontal-tube, falling-film heat exchanger. Int. J. Refrigeration 35, 1176-1187.

75. Lel, V., Al-Sibai, F., Leefken, A., Renz, U., 2005. Local thickness and wave velocity measurement of wavy films with a chromatic confocal imaging method and a fluorescence intensity technique. Experiments in Fluids 39, 856-864.

76. Li, W., Wu, X.-Y., Luo, Z., Webb, R.L., 2011a. Falling water film evaporation on newly-designed enhanced tube bundles. Int. J. Heat Mass Transfer 54, 2990-2997.

77. Li, W., Wu, X.-Y., Luo, Z., Yao, S.-c., Xu, J.-L., 2011b. Heat transfer characteristics of falling film evaporation on horizontal tube arrays. Int. J. Heat Mass Transfer 54, 1986-1993.

78. Li, W., Wu, X., Luo, Z., 2010. Falling Film Evaporation of Water on Horizontal Configured Tube Bundles. ASME Conference Proceedings 2010, 495-502.

79. Lienhard, J.H., Wong, P.T.Y., 1964. The dominant unstable wavelength and minimum heat flux during film boiling on a horizontal cylinder. J. Heat Transfer 86, 220-226.

80. Liu, P.J.P., 1975. The evaporating falling film on horizontal tubes. University of Wisconsin-Madison.

81. Liu, Z.-H., Yi, J., 2001. Enhanced evaporation heat transfer of water and R-11 falling film with the roll-worked enhanced tube bundle. Experimental Thermal and Fluid Science 25, 447-455.

82. Liu, Z.-H., Yi, J., 2002. Falling film evaporation heat transfer of water/salt mixtures from roll-worked enhanced tubes and tube bundle. Applied Thermal Engineering 22, 83-95.

83. Liu, Z.-H., Zhu, Q.-Z., 2005. Heat Transfer in a Subcooled Water Film Falling Across a Horizontal Heated Tube. Chemical Engineering Communications 192, 1334-1346.

84. Liu, Z.-H., Zhu, Q.-Z., Chen, Y.-M., 2002. Evaporation heat transfer of falling water film on a horizontal tube bundle. Heat Transfer - Asian Research 31, 42-55.

85. Lorenz, J.J., Yung, D., 1979. A Note on Combined Boiling and Evaporation of Liquid Films on Horizontal Tubes. J. Heat Transfer 101, 178-180.

86. Lorenz, J.J., Yung, D., 1982. Film Breakdown and Bundle-Depth Effects in Horizontal-Tube, Falling-Film Evaporators. J. Heat Transfer 104, 569-571.

87. Lorenz, J.J., Yung, D.T., 1978. Combined boiling and evaporation of liquid films on horizontal tubes, Fifth ocean thermal energy conversion (OTEC) conference, Miami Beach, pp. VI-46-70.

88. Mathworks, I., 2010. MATLAB, Version 7.11.0.584 (R2010b) ed, Natick, Massachusetts.

89. Mitrovic, J., 1986. Influence of tube spacing and flow rate on heat transfer from a horizontal tube to a falling liquid film, Eighth international heat transfer conference, San Francisco, pp. 1949-1956.

90. Mitrovic, J., 2005. Flow Structures of a Liquid Film Falling on Horizontal Tubes. Chemical Engineering & Technology 28, 684-694.

91. Miyasaka, Y., Inada, S., 1980. Effect of Pure Forced Convection on the Boiling Heat Transfer Between a Two-Dimensional Subcooled Water Jet and a Heated Surface. Journal of Chemical Engineering of Japan 13, 22-28.

92. Moeykens, S.A., 1994. Heat transfer and fluid flow in spray evaporators with application to reducing refrigerant inventory. Iowa State University.

93. Moeykens, S.A., Huebsch, W.W., Pate, M.B., 1995a. Heat transfer of R-134a in single-tube spray evaporation including lubrificant effects and enhanced surface results, ASHRAE Transactions, pp. 111-123.

94. Moeykens, S.A., Kelly, J.E., Pate, M.B., 1996. Spray evaporation heat transfer performance of R-123 in tube bundles, ASHRAE Transactions, pp. 259-272.

95. Moeykens, S.A., Newton, B.J., Pate, M.B., 1995b. Effects of surface enhancement, film-feed supply rate, and bundle geometry on spray evaporation heat transfer performance, ASHRAE Transactions, pp. 408-419.

96. Moeykens, S.A., Pate, M.B., 1994. Spray evaporation heat transfer of R-134a on plain tubes, ASHRAE Transactions, pp. 173-184.

97. Moeykens, S.A., Pate, M.B., 1995. The effects of nozzle height and orifice size on spray evaporation heat transfer performance for a low-finned, triangular-pitch tube bundle with R-134a, ASHRAE Transactions, pp. 420-433.

98. Moeykens, S.A., Pate, M.B., 1996. Effect of lubricant on spray evaporation heat transfer performance of R-134a and R-22 in tube bundles, ASHRAE Transactions, pp. 410-426.

99. Nusselt, W., 1916. Die Oberflachenkondensation des Wasserdampfes. Zetschrift des Vereins Deutscher Ininuere 60, 541-575.

100. Owens, W.L., 1978. Correlation of thin film evaporation heat transfer coefficients for horizontal tubes, Fifth Ocean Thermal Energy Conversion Conference, Miami Beach, pp. VI-71-89.

101. Parken, W.H., 1975. Heat transfer to thin films on horizontal tubes. Rutgers University.

102. Parken, W.H., Fletcher, L.S., 1982. Heat transfer in thin liquid films flowing over horizontal tubes, Seventh International Heat Transfer Conference, Munich, pp. 415-420.

103. Parken, W.H., Fletcher, L.S., Sernas, V., Han, J.C., 1990. Heat Transfer Through Falling Film Evaporation and Boiling on Horizontal Tubes. J. Heat Transfer 112, 744-750.

104. Patnaik, V., Perez-Blanco, H., 1996. Roll waves in falling films: an approximate treatment of the velocity field. Int. J. Heat Fluid Flow 17, 63-70.

105. Putilin, J.V., Podberezny, V.L., Rifert, V.G., 1996. Evaporation heat transfer in liquid films flowing down horizontal smooth and longitudinally profiled tubes. Desalination 105, 165-170.

106. Ribatski, G., Jacobi, A.M., 2005. Falling-film evaporation on horizontal tubes--a critical review. Int. J. Refrigeration 28, 635-653.

107. Ribatski, G., Thome, J.R., 2007. Experimental study on the onset of local dryout in an evaporating falling film on horizontal plain tubes. Experimental Thermal and Fluid Science 31, 483-493.

108. Rifert, V.G., Podberezny, V.I., Putilin, J.V., Nikitin, J.G., Barabash, P.A., 1989. Heat transfer in thin film-type evaporator with profile tubes. Desalination 74, 363-372.

109. Rifert, V.G., Putilin, J.V., Podberezny, V.L., 1992. Evaporation heat transfer in liquid films flowing down the horizontal smooth and longitudinally-profiled

tubes, Heat Transfer: 3rd UK National Conference Incorporating 1st European Conference of Thermal Sciences. Taylor & Francis, pp. 1283-1289.

110. Rogers, J.T., 1981. Laminar falling film flow and heat transfer characteristics on horizontal tubes. The Canadian Journal of Chemical Engineering 59, 213-222.

111. Rogers, J.T., Goindi, S.S., 1989. Experimental laminar falling film heat transfer coefficients on a large diameter horizontal tube. The Canadian Journal of Chemical Engineering 67, 560-568.

112. Rogers, J.T., Goindi, S.S., Lamari, M., 1995. Turbulent falling film flow and heat transfer on horizontal tube, National Heat Transfer Conference, Portland, pp. 3-12.

113. Rohsenow, W.M., 1951. A method of correlating heat transfer data for surface boiling of liquids, Heat Transfer Laboratory Technical Reports. M.I.T. Division of Industrial Cooperation, Cambridge, Massachusetts.

114. Roques, J.-F., 2004. Falling Film Evaporation on a Single Tube and on a Tube Bundle, Laboratory of Heat and Mass Transfer. École Polytechnique Fédérale de Lausanne, Lausanne, Switzerland.

115. Roques, J.-F., Thome, J.R., 2003. Falling Film Transitions Between Droplet, Column, and Sheet Flow Modes on a Vertical Array of Horizontal 19 FPI and 40 FPI Low-Finned Tubes. Heat Transfer Engineering 24, 40-45.

116. Roques, J.-F., Thome, J.R., 2007a. Falling Films on Arrays of Horizontal Tubes with R-134a, Part I: Boiling Heat Transfer Results for Four Types of Tubes. Heat Transfer Engineering 28, 398 - 414.

117. Roques, J.-F., Thome, J.R., 2007b. Falling Films on Arrays of Horizontal Tubes with R-134a, Part II: Flow Visualization, Onset of Dryout, and Heat Transfer Predictions. Heat Transfer Engineering 28, 415 - 434.

118. Roques, J.F., Dupont, V., Thome, J.R., 2002. Falling Film Transitions on Plain and Enhanced Tubes. J. Heat Transfer 124, 491-499.

119. Ruan, B., Jacobi, A.M., 2011. Investigation on Intertube Falling-Film Heat Transfer and Mode Transitions of Aqueous-Alumina Nanofluids. J. Heat Transfer 133, 051501.

120. Ruan, B., Jacobi, A.M., 2012. Heat transfer characteristics of multiwall carbon nanotube suspensions (MWCNT nanofluids) in intertube falling-film flow. Int. J. Heat Mass Transfer 55, 3186-3195.

121. Ruan, B., Jacobi, A.M., Li, L., 2009. Effects of a countercurrent gas flow on falling-film mode transitions between horizontal tubes. Experimental Thermal and Fluid Science 33, 1216-1225.

122. Ruan, B., Li, H., Wang, Q., 2011. Theoretical analysis on film thickness of intertube falling-film flow with a countercurrent gas flow, ASME International Mechanical Engineering Congress & Exposition. IMECE2011-64425, Denver, Colorado.

123. Sabin, S.M., Poppendiek, H.F., 1978. Film evaporation of ammonia over horizontal round tubes, Fifth Ocean Thermal Energy Conversion Conference, Miami Beach, pp. VI-237-260.

124. Semiat, R., Moalen, S.S., Maron, D., 1978. Turbulent film evaporation on and condensation in horizontal elliptical conduits, Sixth international heat transfer conference, Toronto, pp. 361-366.

125. Sernas, V., 1979. Heat Transfer Correlation for Subcooled Water Films on Horizontal Tubes. J. Heat Transfer 101, 176-178.
126. Sideman, S., Pinczewski, W.V., 1975. Topics in Transport Phenomena. John Wiley & Sons, NY.
127. Slesarenko, V., 1979. Investigation of heat exchange during sea water boiling in a horizontal thin film desalination plant. Desalination 29, 311-318.
128. Tan, Y., Wang, G., Wang, S., Cui, N., 1990. An experimental research on spray falling film boiling on the second generation mechanically made porous surface tubes, Ninth International Heat Transfer Conference, Jerusalem, pp. 269-273.
129. Tatara, R.A., Payvar, P., 2001. Measurement of spray boiling refrigerant coefficients in an integral-fin tube bundle segment simulating a full bundle. Int. J. Refrigeration 24, 744-754.
130. Thome, J.R., 1999. Falling Film Evaporation: State-of-the-Art Review of Recent Work. Enhanced Heat Transfer 6, 263-277.
131. Thome, J.R., 2009. Falling Film Evaporation, Engineering Data Book III. Wolverine Tube, Inc., http://www.wlv.com/products/databook/db3/data/db3ch14.pdf.
132. Wang, X., Hrnjak, P.S., Elbel, S., Jacobi, A.M., He, M., 2012. Flow Modes and Mode Transitions for Falling Films on Flat Tubes. J. Heat Transfer 134, 021801.
133. Wang, X., Jacobi, A.M., 2014. A Thermodynamic Basis for Predicting Falling-Film Mode Transitions. Int. J. Refrigeration.
134. Wang, X.F., Hrnjak, P.S., Elbel, S., Jacobi, A.M., He, M.G., 2010. Flow Patterns and Mode Transitions for Falling-Films on Flat Tubes, International Refrigeration and Air Conditioning Conference at Purdue, Purdue, IL.
135. Wang, X.F., Hrnjak, P.S., Elbel, S., Jacobi, A.M., He, M.G., 2011. Heat Transfer Performance for a Falling-film on Horizontal Flat Tubes, ASME 2011 International Mechanical Engineering Congress & Exposition, Denver, Colorado.
136. Wei, Y., Jacobi, A.M., 2002. Vapor-shear, geometric, and bundle-depth effects on the intertube falling-film modes, First International Conference on Heat Transfer, Fluid Mechanics, and Thermodynamics, Kruger National Park, South Africa, pp. 40-46.
137. Xu, L., Wang, S., Wang, Y., Ling, Y., 2003. Flowing state in liquid films over horizontal tubes. Desalination 156, 101-107.
138. Yang, L., Shen, S., 2008. Experimental study of falling film evaporation heat transfer outside horizontal tubes. Desalination 220, 654-660.
139. Yung, D., Lorenz, J.J., Ganic, E.N., 1980. Vapor/Liquid Interaction and Entrainment in Falling Film Evaporators. J. Heat Transfer 102, 20-25.
140. Zeng, X., Chyu, M.-C., Ayub, Z.H., 1995. Evaporation heat transfer performance of nozzle-sprayed ammonia on a horizontal tube, ASHRAE Transactions, pp. 136-149.
141. Zeng, X., Chyu, M., Ayub, Z.H., 1998. Ammonia spray evaporation heat transfer performance of single low-fin and corrugated tubes / Discussion. ASHRAE Transactions 104, 185-185.
142. Zeng, X., Chyu, M.C., Ayub, Z.H., 2001a. Experimental investigation on ammonia spray evaporator with triangular-pitch plain-tube bundle, Part I: tube bundle effect. Int. J. Heat Mass Transfer 44, 2299-2310.

143. Zeng, X., Chyu, M.C., Ayub, Z.H., 2001b. Experimental investigation on ammonia spray evaporator with triangular-pitch plain-tube bundle, Part II: evaporator performance. Int. J. Heat Mass Transfer 44, 2081-2092.

144. Zeng, X., Ming, C.C., Ayub, Z.H., 1997. Performance of Nozzle-Sprayed Ammonia Evaporator with Square-Pitch Plain-Tube Bundle. ASHRAE Transactions 103, 68-68.